UNIVERSITY OF LONDON THESIS

Degree phd Year 2007 Name of Author KIERAN ISHTAR MOIRA INGRAM

COPYRIGHT

This is a thesis accepted for a Higher Degree of the University of London. It is an unpublished typescript and the copyright is held by the author. All persons consulting the thesis must read and abide by the Copyright Declaration below.

COPYRIGHT DECLARATION

I recognise that the copyright of the above-described thesis rests with the author and that no quotation from it or information derived from it may be published without the prior written consent of the author.

LOAN

Theses may not be lent to individuals, but the University Library may lend a copy to approved libraries within the United Kingdom, for consultation solely on the premises of those libraries. Application should be made to: The Theses Section, University of London Library, Senate House, Malet Street, London WC1E 7HU.

REPRODUCTION

University of London theses may not be reproduced without explicit written permission from the University of London Library. Enquiries should be addressed to the Theses Section of the Library. Regulations concerning reproduction vary according to the date of acceptance of the thesis and are listed below as guidelines.

A. Before 1962. Permission granted only upon the prior written consent of the author. (The University Library will provide addresses where possible).

B. 1962 - 1974. In many cases the author has agreed to permit copying upon completion of a Copyright Declaration.

C. 1975 - 1988. Most theses may be copied upon completion of a Copyright Declaration.

D. 1989 onwards. Most theses may be copied.

This thesis comes within category D.

☐ This copy has been deposited in the Library of UCL

☐ This copy has been deposited in the University of London Library, Senate House, Malet Street, London WC1E 7HU.

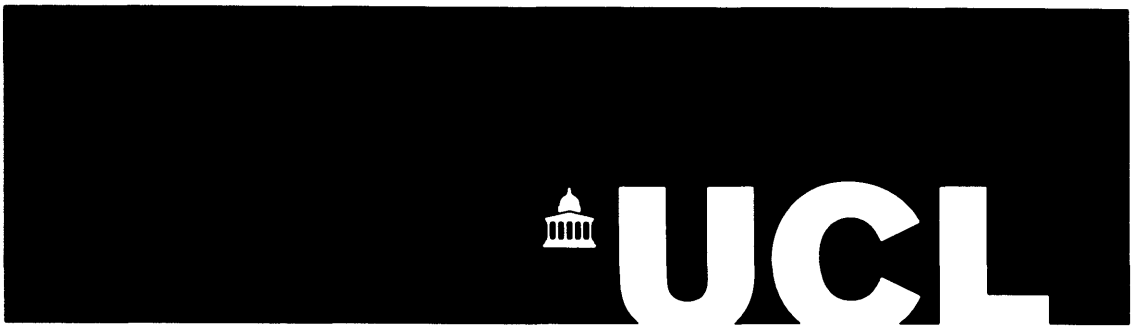

Computational Studies of Molecular Actinide and Lanthanide complexes

Kieran I M Ingram

A dissertation submitted in partial fulfillment

of the requirements for the degree of

Doctor of Philosophy

of the

University of London.

Department of Chemistry

University College London

July 8, 2007

ProQuest LLC
789 East Eisenhower Parkway
P.O. Box 1346
Ann Arbor, MI 48106-1346

I, Kieran I M Ingram, confirm that the work presented in this thesis is my own.

Where information has been derived from other sources, I can confirm that his has been indicated in this thesis.

Signed

Abstract

This thesis reports computational DFT studies of three families of complexes (see below). Before presenting the results from these studies, the first chapter introduces the lanthanides and actinides and investigates their similarities and differences through a discussion of selected compounds of each of the series of metals. The second chapter introduces the electronic structure methods that were used in this research and mentions some of the relevant computational utilities.

Chapter 3 discusses DFT studies of mixed water/hydroxide uranyl systems, $[UO_2(H_2O)_{a-x}(OH)_x]^{(2-x)+}$ for $x = 0, 1, 2, 3, 4, 5$ with $a = 5$, and some $a = 3, 4$. The reasons for the observed lengthening, and resultant weakening, of U O_{yl} as x increases are investigated. These studies show that this lengthening appears to be predominantly due to a reduction in ionic character stemming from charge build up on the U centre, and not from hydroxide / O_{yl} competition for U 6*d*, as has been previously suggested.

Time-Dependent DFT is used in chapter 4 to simulate the electronic spectra of $[UO_2(NCN)_2]$ and $[UO_2(NPN)_2]$ in order to investigate why these complexes are coloured red rather than the normally observed green/yellow of uranyl systems. This chapter involves some preliminary benchmarking calculations on three other uranyl complexes, $[UO_2Cl_2(TBP)_2]$, $[UO_2Cl_2(THF)_2]$, $[UO_2(NO_3)_2(TBP)_2]$, as there is as yet no literature suggesting suitable exchange potentials and/or basis sets for TD-DFT calculations on actinides. The conclusion was reached that the unusual colour of the nitrogen donor complexes is due to a small HOMO–LUMO gap resulting from the relatively low energy nitrogen based ligand MOs compared with usual uranyl ligands such as O and Cl.

Chapter 5 systematically investigates $[M(N(EPR_2)_2)_3]$, M = Ln (Ln = La, Ce, Pr, Pm, Eu), An (An = U, Np, Pu, Am, Cm); E = O, S, Se, Te; R = H to investigate the ligands' suitability for extraction of An(III) from Ln(III), and also to test the suitability of La and U as models for Eu and Am/Cm respectively. The results lead me to conclude that chalcogen donor ligands are extremely promising for successful separation of Cm from Am and Eu, but good separation factors of Am from Eu seem unlikely. Furthermore I conclude that La and U are not suitable models for Eu and Am/Cm as the 2+ capability of Eu seems present in with S, Se, Te; U shows considerable covalency in M–E with the heavier chalcogens and there is no evidence of covalency in any Am–E or Cm–E.

Acknowledgements

Firstly I would like to thank my supervisor, Nik Kaltsoyannis, for his constant encouragement, advice, and help in untangling my results, without which this thesis would not have been possible. I would like to extend my thanks to the chemistry department, specifically the members of G19 past and present. I feel very lucky to have spent 3 years working with such intelligent and interesting people and will miss them all. A special thank you must go to my three good friends Luke, Andrea, and Dervise, who have played a larger role in my PhD than anyone else; their constant enthusiasm for science has been inspirational and their (almost!) unfailing good humour, not to mention the excellent technical help from Luke in particular, has been a huge comfort to me.

I have received an enormous amount of support from my family and would like to specifically thank Mix and Julia as well as Bill, Jean, Marty and Clare, each of whom has helped me financially at some point and made the whole experience a lot easier than it would otherwise have been. My brothers Rendel and Estel have both listened with enthusiasm to endless accounts of my work and for this I am grateful, I only hope my words will filter down and influence my nieces' career choices!

Finally I wish to thank my dear friends, you're the reason I've loved living in London and therefore you're a large part of this thesis. Kate, Helen, Sarah, Maria, Noel, Richard, John, Jamie, Greg, Andy, and finally Ed, thanks. I love you all.

Contents

1 Introduction **17**

1.1 The electronic structures of the *f* elements 18

1.1.1 Lanthanides 18

1.1.2 Actinides 21

1.1.3 Comparing Ln with An compounds 24

1.2 Research Projects 27

1.2.1 A Density Functional Theory investigation of the geometric and electronic structures of $[UO_2(H_2O)_{a-x}(OH)_x]^{(2-x)+}$ for $x = 0 \rightarrow 5$ with $a = 5$, and some $a = 3, 4$. 28

1.2.2 The Performance of Time-Dependent Density Functional Theory in the simulation of the electronic spectra of molecular uranium complexes 28

1.2.3 Covalency in the *f*-element–chalcogen bond. Computational studies of $[M(N(EPR_2)_2)_3]$, M = Ln (Ln = La, Ce, Pr, Pm, Eu), An (An = U, Np, Pu, Am, Cm); E = O, S, Se, Te; R = H, Me, ^{i}Pr 29

2 Electronic Structure Theory **31**

2.1 Density Functional Theory (DFT) 31

2.1.1 Exchange-Correlation Functionals 34

2.1.2 Time Dependent-Density Functional Theory (TD-DFT) 37

2.2 Basis Functions 38

2.2.1 Satisfying the Pauli Principle 38

2.2.2 Slater Type Orbitals 41

2.2.3 Gaussian Type Orbitals 41

2.2.4 Basis Sets and Nomenclature 42

2.2.5 Effective Core Potentials and the Frozen Core Approximation . . 44

2.3 Relativity 45

2.3.1 Relativistic ECPs 47
2.3.2 Quasi-Relativistic methods 47
2.4 Computational Methods 53
2.4.1 Amsterdam Density Functional 53
2.4.2 Gaussian 03 53
2.4.3 Computational Utilities 54

3 Density Functional Theory investigation of the geometric and electronic structures of $[UO_2(H_2O)_{a-x}(OH)_x]^{(2-x)+}$ for $x = 0 \rightarrow 5$ with $a = 5$, and some $a = 3$, 4 60

3.1 Introduction 60
3.2 Literature Review of Mixed Water-Hydroxide Uranyl systems 61
3.3 Computational Details 66
3.3.1 ADF 66
3.3.2 G03 67
3.3.3 Solvent Effects 67
3.4 Results 68
3.4.1 Geometries 68
3.4.2 Uranyl vibrations 75
3.4.3 Bond Strengths 80
3.4.4 Molecular orbital analysis 82
3.4.5 Mulliken and Hirshfeld charges, and Mulliken populations 87
3.5 Conclusions 93

4 The performance of Time-Dependent Density Functional Theory (TD-DFT) in the simulation of the electronic spectra of molecular uranium complexes 95

4.1 Introduction 95
4.2 Literature Review 97
4.3 Computational Details 101
4.4 Results 102

4.4.1 Optimised geometries: $[UO_2Cl_2(TBP)_2]$, $[UO_2Cl_2(THF)_2]$, and $[UO_2(NO_3)_2(TBP)_2]$. 102
4.4.2 Electronic spectra: $[UO_2Cl_2(TBP)_2]$, $[UO_2Cl_2(THF)_2]$, and $[UO_2(NO_3)_2(TBP)_2]$. 102
4.4.3 Conclusions: $[UO_2Cl_2(TBP)_2]$, $[UO_2Cl_2(THF)_2]$, and $[UO_2(NO_3)_2(TBP)_2]$ 109
4.4.4 Geometries: $[UO_2(NCN)_2]$ and $[UO_2(NPN)_2]$ 109
4.4.5 Electronic spectra: $[UO_2(NCN)_2]$ and $[UO_2(NPN)_2]$ 109
4.5 Conclusions 117

5 Covalency in the *f*-element – chalcogen bond; computational studies of $[M(N(EPR_2)_2)_3]$, M = Ln (Ln = La, Ce, Pr, Pm, Eu), An (An = U, Np, Pu, Am, Cm); E = O, S, Se, Te; R = H, Me, ^{i}Pr 119
5.1 Introduction 119
5.2 Literature Review 120
5.3 Computational Details 125
5.3.1 ADF 126
5.4 Results 127
5.4.1 Geometries of the La and U complexes 127
5.4.2 Charge analysis of the La / U complexes 133
5.4.3 Conclusions from the initial La / U comparison 135
5.4.4 Extending the project to $[M(N(EPH_2)_2)_3]$, M = Ce, Pr, Pm, Eu; Np, Pu, Am, Cm 135
5.4.5 Geometries of $[M(N(EPH_2)_2)_3]$, M = La, Ce, Pr, Pm, Eu; U, Np, Pu, Am, Cm 136
5.4.6 Natural Charge Analysis of $[M(N(EPH_2)_2)_3]$ M = La, Ce, Pr, Pm, Eu, U, Np, Pu, Am, Cm; E = O, S, Se, Te 139
5.4.7 Natural Population Analysis 143
5.4.8 Mulliken Overlap Populations 147
5.4.9 Molecular Orbital Analysis 149
5.4.10 MOs containing *f*-electrons 157

5.5 Conclusions 167

Bibliography **172**

List of Figures

1.1 The *general set* of *f* orbitals 17

1.2 The variation of selected ionisation energies (I_n for n=3, 4, (1+2+3)) across the lanthanides 20

1.3 Accessible oxidation states for Ln; solid circles indicate the most common oxidation state in aqueous solution, open circles show other possible solution oxidation states 21

1.4 Accessible oxidation states for An; solid circles indicate the most common oxidation state in aqueous solution, open circles show other solution oxidation states and squares represent oxidation states only found in the solid state 22

1.5 Schematic of proposed structure of LnL_3 26

2.1 Approximating an STO with several GTOs 42

2.2 Non-relativistic and Relativistic solutions to the Dirac equation 49

2.3 Solvent Accessible Surface (SAS/asurf) and Solvent Excluding Surface (SES/esurf) 59

3.1 D_{5h} and C_1 $[UO_2(H_2O)_5]^{2+}$ structures 63

3.2 The four $[UO_2(H_2O)_3(OH)_2]^0$ starting configurations used by Oda *et al* . 64

3.3 Four $[UO_2(OH)_4]^{2-}$ starting configurations used by Schreckenbach *et al* . 66

3.4 Sonnenberg *et al*'s[1] proposed structure for $[UO_2(OH)_5]^{3-}$ 66

3.5 Ball + stick representations of the calculated geometries for **5W**, **4W1OH**, **2W2OH**, **1W3OH**, **4OH**, and **5OH** (ADF BP86 gas phase data) 68

3.6 Optimised structure of $[UO_2(H_2O)_3(OH)_2]$ (ADF/BP86/Gas phase), **3W2OH**, note the non-coordinated water molecule 69

3.7 The three $[UO_2(H_2O)_x(OH)_3]^-$ structures (ADF/BP86/Gas phase); x = 0 (a), 1(b), 2(c) 70

3.8 Selected calculated r(U–O_{yl}) /Å as a function of the number of coordinated OH^-, including selected previous experimental and theoretical results 71

3.9 Selected calculated r(U–O_{water}) /Å as a function of the number of coordinated OH^-, including selected previous experimental and theoretical results 74

3.10 Selected calculated r(U–$O_{hydroxide}$) as a function of the number of coordinated OH^-, including selected previous experimental and theoretical results 75

3.11 Selected calculated values for $\overline{\nu}_{sym}$(U–O_{yl}) compared with selected previous experimental and theoretical results 76

3.12 Selected calculated values for $\overline{\nu}_{asym}$(U–O_{yl}) compared with selected previous experimental and theoretical results 77

3.13 Calculated U–O_{yl} MBO as a function of the number of OH^- 81

3.14 MO energy level diagram for species UO_2^{2+}, **5W**, **4W1OH**, **2W2OH**, **1W3OH**, **4OH** and **5OH**. The energies of the σ_u MO for each complex has been set to zero 83

3.15 Three dimensional representations of the UO_2^{2+} HOMO (σ_u) and all **1W3OH** MOs which contain similar uranium–axial oxygen bonding character 84

3.16 Three dimensional representations of the UO_2^{2+} HOMO-1 and HOMO-2, a pair of π_u orbitals and the two analogous **1W3OH** MOs π_u MOs 85

3.17 Three dimensional representations of the UO_2^{2+} HOMO-3, HOMO-4, and HOMO-5, a pair of π_g orbitals and a σ_g orbital respectively, along with four similar **1W3OH** MOs, note how (c) contains a combination of π_g and σ_g character 85

3.18 Three-dimensional representations of the σ_g orbital of **5W** (D_{5h}) and **4OH** 86

3.19 Three-dimensional representation of the π_u and π_g orbitals of **5W**(D_{5h}) and **4OH** 87

3.20 Ligand-metal π bonding in **4OH**. Note the metal orbital is of the wrong symmetry to form a π-bond with O_{yl} (circled) 88

3.21 Calculated charge on U using the Mulliken charge analysis scheme 89

3.22 Calculated charge on O_{yl} using the Mulliken charge analysis scheme . . . 89

3.23 Mulliken population analysis of the *s*, *p*, *d*, and *f* orbitals of uranium (ADF/BP86/Gas phase data) 90
3.24 Calculated charge on U using the Hirshfeld charge analysis scheme 90
3.25 Calculated charge on O_{yl} using the Hirshfeld charge analysis scheme . . . 92

4.1 NCN and NPN ligands 96
4.2 Ball and stick representations of the optimised geometries of complexes **A**, **B**, and **C** 103
4.3 Calculated absorption spectra for **A** using PW91, LB94 and SAOP, 1-6 refer to the basis set combination used, as defined in table 4.1 104
4.4 Calculated absorption spectra for **B** using PW91, LB94 and SAOP. 107
4.5 Calculated absorption spectra for **C** using PW91, LB94 and SAOP. 108
4.6 Ball and stick representations of $[UO_2(NCN)_2]$ and $[UO_2(NPN)_2]$ 110
4.7 Calculated (a) and experimental (b) absorption spectra of D (red lines) and E (blue lines); all energies are given in nm and the cm^{-1} scale has been included to enable comparison with A, B, and C. 111
4.8 Schematic showing vibronic coupling; the quantised energies of the excited vibrational levels in the excited state lead to fine structure on the absorption band 113
4.9 Calculated MO diagram illustrating the component transitions of $\mathbf{D}_1$ (red), $\mathbf{D}_2$ (turquoise) and $\mathbf{D}_3$ (green), along with three dimensional representations of the relevant MOs, the line widths refer to the percentage contribution of each transition to that excitation 115
4.10 Calculated MO diagram illustrating the component transitions of $\mathbf{E}_1$ (red) and $\mathbf{E}_2$ (turquoise with a green shoulder), along with three dimensional representations of the relevant MOs, the line widths refer to the percentage contribution of each transition to that excitation 116
4.11 Calculated MO diagram illustrating the component transitions of $\mathbf{B}_1$ (red), $\mathbf{B}_2$ (turquoise) and $\mathbf{B}_3$ (green), along with three dimensional representations of the relevant MOs, the line widths refer to the percentage contribution of each transition to that excitation 117

5.1 Structure for Ln(III) and An(III) motexaphyrins, $(M\text{-motex})^{2+}$, R = $O(CH_2CH_2O)_3CH_3$ 122

5.2 Terpy and MeBtp ligands 124

5.3 Ball and stick representations of the D_3 optimised geometries of $[La(N(EPH_2)_2)_3]$; E = O (a), S (b), Se (c), Te (d) 130

5.4 Ball and stick representations of the D_3 optimised geometries of $[La(N(EPMe_2)_2)_3]$; E = O (a), S (b), Se (c), Te (d) 130

5.5 Calculated r(La–E) in $[La(N(EPR_2)_2)_3]$ for E = O, S, Se, Te; R = H, Me; both C_1 and D_3, together with the experimental data for $[La(N(EP^iPr_2)_2)_3]$ 130

5.6 Ball and stick representations of the D_3 optimised geometries of $[U(N(EPH_2)_2)_3]$; E = O (a), S (b), Se (c), Te (d) (D_3) 131

5.7 Ball and stick representations of the D_3 optimised geometries of $[U(N(EPMe_2)_2)_3]$; E = O (a), S (b), Se (c), Te (d) (D_3) 131

5.8 Calculated r(U–E) in $[U(N(EPR_2)_2)_3]$ for E = O, S, Se, Te; R = H, Me; both C_1 and D_3 together with the experimental data for $[U(N(EP^iPr_2)_2)_3]$ 131

5.9 Calculated r(M–E) in $[M(N(EPR)_2)_2)_3]$ for M = La, U; E = O, S, Se, Te; R = H, Me; D_3 symmetry, compared with experimental data 132

5.10 Calculated r(P–E) in $[M(N(EPR)_2)_2)_3]$ for M = La, U; E = O, S, Se, Te; R = H, Me; D_3 symmetry compared with experimental data 132

5.11 Natural charges for $[M(N(EPR)_2)_2)_3]$; M = La, U; E = O, S, Se, Te; R = H, Me; both D_3 and C_1 133

5.12 Calculated r(M-E) in $[Ln/An(N(EPH_2)_2)_3]$; An = U, Np, Pu, Am, Cm; Ln = La, Ce, Pr, Pm, Eu; E = O, S, Se, Te, at the optimised geometries 138

5.13 Normalised calculated r(M–E) in $[An/Ln(N(EPH_2)_2)_3]$; An = U, Np, Pu, Am, Cm; Ln = La, Ce, Pr, Pm, Eu; E = O, S, Se, Te, at the optimised geometries. r(M–O) has been set to zero for each metal 139

5.14 Natural charges of $[M(N(EPH_2)_2)_3]$ for M = La, Ce, Pr, Pm, Eu, U, Np, Pu, Am, Cm; E = O, S, Se, Te at the optimised geometries 140

5.15 $\Delta(q_M - q_{E_M})$ in $[M(N(EPH_2)_2)_3]$ for M = La, Ce, Pr, Pm, Eu, U, Np, Pu, Am, Cm; E = O, S, Se, Te at the optimised geometries 142

5.16 Natural populations of [An/Ln(N(EPH$_2$)$_2$)$_3$] for Ln = La, Ce, Pr, Pm, Eu; An = U, Np, Pu, Am, Cm; E = O, S, Se, Te, at the optimised geometries . 144

5.17 Natural *s*- and *d*- populations of [An/Ln(N(EPH$_2$)$_2$)$_3$] for Ln = La, Ce, Pr, Pm, Eu; An = U, Np, Pu, Am, Cm; E = O, S, Se, Te, at the optimised geometries *plotted as a function of the formal number of f-electrons*. Triangles indicate lanthanide data, circles indicate actinides 145

5.18 Mulliken M — E and M^{3+}— L_3^3 overlap populations in [An/Ln(N(EPH$_2$)$_2$)$_3$] for Ln = La, Ce, Pr, Pm, Eu; An = U, Np, Pu, Am, Cm; E = O, S, Se, Te . 148

5.19 MO energy level diagram for [Ln(N(EPH$_2$)$_2$)$_3$] Ln = La, Ce, Pr, Pm, Eu; E = O, S, Se, Te at the optimised D_3 geometries. The energies of orbitals 34 → 52 have been normalised to that of MO 53, which has been arbitrarily set to 0eV in all cases. Orbitals with a_1 symmetry are shown in red, a_2 in blue and e in black 151

5.20 MO energy level diagram for [An(N(EPH$_2$)$_2$)$_3$] An = U, Np, Pu, Am, Cm; E = O, S, Se, Te at the optimised D_3 geometries. The energies of orbitals 34 → 52 have been normalised to that of MO 53, which has been arbitrarily set to 0eV in all cases. Orbitals with a_1 symmetry are shown in red, a_2 in blue and e in black 152

5.21 Three dimensional representations (at the same space value, 0.375) of orbitals 39 and 40 in selected [Ln/An(N(SPH$_2$)$_2$)$_3$] Ln = Pr (turquoise), Eu (blue); An = U (green), Am (red) 153

5.22 Three dimensional representations (at the same space value, 0.375) of e symmetry orbital pairs 42 & 43 and 45 & 46 in selected [Ln/An(N(TePH$_2$)$_2$)$_3$] Ln = Pr (turquoise), Ce (yellow); An = U (green), Np (black) 155

5.23 Three dimensional representations (at same space value, 0.375) of a_1 orbital 44 in selected [Ln/An(N(SePH$_2$)$_2$)$_3$] Ln = Pr(turquoise), An = U(green) 156

5.24 % metal *d* contribution to a_1 symmetry orbital 44 in [Ln/An(N(EPH$_2$)$_2$)$_3$] Ln = La, Ce, Pr, Pm, Eu; An = U, Np, Pu, Am, Cm; E = O, S, Se, Te . . . 156

5.25 Three dimensional representations (at the same space value, 0.4) of a_1 symmetry orbital 38 in [Ln/An(N(TePH$_2$)$_2$)$_3$] Ln = Pr(turquoise), An = U(green) 157

5.26 % metal *s* contribution to a_1 symmetry orbitals in [Ln/An(N(EPH$_2$)$_2$)$_3$] Ln = La, Ce, Pr, Pm, Eu; An = U, Np, Pu, Am, Cm; E = O, S, Se, Te 157

5.27 Three dimensional representations (at the same space value, 0.4) of MOs 50, 51, 52 in [U(N(TePH$_2$)$_2$)$_3$] 158

5.28 Three dimensional representations (at the same space value, 0.4) of MOs 50, 51, 52 in [Np(N(TePH$_2$)$_2$)$_3$] 159

5.29 Three dimensional representations (at the same space value, 0.4) of MOs 50, 51, 52 in [Pu(N(TePH$_2$)$_2$)$_3$] 160

5.30 Three dimensional representations (at the same space value, 0.4) of MOs 47, 48, 49, 50 in [Am(N(TePH$_2$)$_2$)$_3$] 161

5.31 Three dimensional representations (at the same space value, 0.4) of the six main U^{3+} and L_3^{3-} components of MO 45 in [U(N(TePH$_2$)$_2$)$_3$], as seen relative to three different Cartesian axes defined in 5.31(a) 162

5.32 Three dimensional representations (at the same space value, 0.4) of the six main Am^{3+} and L_3^{3-} components of MO 45 in [Am(N(TePH$_2$)$_2$)$_3$], as seen relative to three different Cartesian axes defined in 5.31(a) 164

5.33 Three dimensional representations (at same space value, 0.4) of orbitals 35 → 59 in [Cm(N(TePH$_2$)$_2$)$_3$] 166

List of Tables

1.1 Electronic configuration data for the neutral Ln and An atoms 19

3.1 Hay *et al*'s results: Selected data for DFT optimised $[AnO_2(H_2O)_5]^{2+}$ (An = U, Np, Pu) with various functionals along with previous experimental results 62

3.2 Oda *et al*'s results: Selected data for DFT optimised $[UO_2(H_2O)_{5-x}(OH)_x]^{(2-x)+}$ (x = 0, 1, 2); †H_2O next to OH^-, ‡H_2O between OH^-s, i.e. *meta-trans*, see below 63

3.3 Spencer *et al*'s results: Selected data for DFT optimised AnO_2^{2+} and $[AnO_2(H_2O)_5]^{2+}$ (An = U, Pu) in gas and solvent phases 65

3.4 Total bonding energies of $[UO_2(OH)_5]^{3-}$ *vs.* ($[UO_2(OH)_4]^{2-}$ + $[OH]^-$) from ADF/PBE/gas phase calculations (Häller's data) 71

3.5 Calculated r(U–O_{yl}) /Å as a function of the number of coordinated OH^-, including previous experimental and theoretical results 72

3.6 Calculated values for r(U–O_{water}) /Å as a function of the number of coordinated OH^-, including previous experimental and theoretical results . . . 73

3.7 Calculated values for r(U–$O_{hydroxide}$) /Å as a function of the number of coordinated OH^-, including previous experimental and theoretical results 74

3.8 Calculated values for $\overline{\nu}_{sym}$(U–O_{yl}) /cm^{-1} as a function of the number of OH^-, including previous results. MAE = Mean Absolute Error of calculated values compared with experimental data from refs 2[2] and 3[3] 78

3.9 Calculated values for $\overline{\nu}_{asym}$(U–O_{yl}) /cm^{-1} as a function of the number of OH^-, including previous results 79

3.10 Calculated bonding energies using charged and neutral fragments along with calculated Coulomb attraction energies 80

3.11 Calculated percentage contributions of U and O_{yl} (i.e. the uranyl unit) to, and absolute/normalised energies of **1W3OH** MOs, all energies given in eV 84

3.12 Calculated charges on U and O using the **Mulliken** charge analysis scheme 88

3.13 Mulliken population analysis of the *s*, *p*, *d*, and *f* orbitals of uranium (ADF/BP86/Gas phase data) 91

3.14 Calculated charges on U and O using the Hirshfeld charge analysis scheme 92

3.15 Calculated charge difference between uranium and O_{yl} (q_U - $q_{O_{yl}}$) in **5W** and **4OH** using the Mulliken and Hirshfeld charge analysis schemes (ADF/BP86/Gas phase data) 93

4.1 Basis set combinations used, 'inner' atoms includes O_{yl}, $O_{TBP/THF}$, Cl, NO_3 (see figure 4.2) 101

4.2 Selected bond length data for complexes **A**, **B**, and **C** 102

4.3 Calculated and experimental absorption data for **A** 105

4.4 Calculated and experimental absorption data for **B**, 1-6 refer to the basis set combination used, as defined in table 4.1 106

4.5 Calculated and experimental absorption data for **C**, 1-6 refer to the basis set combination used, as defined in table 4.1 106

4.6 Calculated bond lengths and angles for **D** and **E**, for definitions of N_1, N_{1a}, and N_2 see figure 4.6. 110

4.7 Selected calculated electronic transition data for **D** and **E** 112

5.1 Non-default convergence criteria used for some $[M(N(EPH_2)_2)_3]$ 126

5.2 The total energies (kJ/mol) of the La and U complexes calculated with (D_3) and without (C_1) symmetry constraints. $\Delta E = E(C_1) - E(D_3)$ 128

5.3 Selected bond lengths and angles (see figure 5.3(d) for definitions of α, β, γ) from the D_3 and C_1 optimised geometries of $[M(N(EPR_2)_2)_3]$ (M = La, U; E = O, s, Se, Te; R = H, Me), together with experimental data (M = La, U, E = S, Se, Te; R = ^{i}Pr) 129

5.4 Natural charges of selected atoms in $[M(N(EPH_2)_2)_3]$, M = La, U; E = O, S, Se, Te, at the optimised D_3 geometries 134

5.5 Selected bond lengths and angles (see figure 5.3(d) for definitions of α, β, γ) from the optimised geometries of the target molecules, together with experimental data in italics (from ref 4) 137

5.6 Natural charges of [Ln/An(N(EPH$_2$)$_2$)$_3$] Ln = La, Ce, Pr, Pm, Eu; An = U, Np, Pu, Am, Cm; E = O, S, Se, Te 141

5.7 Natural population data for Ln, An in [Ln/An(N(EPH$_2$)$_2$)$_3$] Ln = La, Ce, Pr, Pm, Eu; An = U, Np, Pu, Am, Cm; E = O, S, Se, Te 146

5.8 Selected Mulliken overlap populations in [An/Ln(N(EPH$_2$)$_2$)$_3$] for Ln = La, Ce, Pr, Pm, Eu, U, Np, Pu, Am, Cm; E = O, S, Se, Te 149

5.9 $\Delta(E_{HO_{LB}MO} - E_{LL_{f_e}})$ for [Ln/An(N(EPH$_2$)$_2$)$_3$] Ln = La, Ce, Pr, Pm, Eu; An = U, Np, Pu, Am, Cm; E = O, S, Se, Te 150

5.10 % metal *d* contribution to, and normalised energy of *e* orbitals 39 and 40 in [Ln/An(N(SPH$_2$)$_2$)$_3$] Ln = La, Ce, Pr, Pm, Eu; An = U, Np, Pu, Am, Cm 153

5.11 % metal *d* and *f* contribution to orbitals 45 and 46 in [An(N(SPH$_2$)$_2$)$_3$] An = U, Np, Pu, Am 163

Chapter 1

Introduction

Not only is the chemistry of the 5*f* elements comparatively little understood, but it is also related to one of the most pressing environmental challenges of our time, the radioactive waste and contamination that have resulted from decades of atomic weapons production and nuclear power generation. Expertise in the chemistry and physics of the actinides is highly sought after in the aforementioned industries in order to develop new technologies.

In addition to the actinides, knowledge of the 4*f* metals is extremely important to the nuclear power problem; current research in the field of nuclear waste reprocessing aims at separating long lived radionuclides, specifically the trivalent actinide ions, An^{3+}, from the trivalent lanthanide ions, Ln^{3+}, and so a detailed knowledge of both the 4*f* and 5*f* metals is essential to the industry.

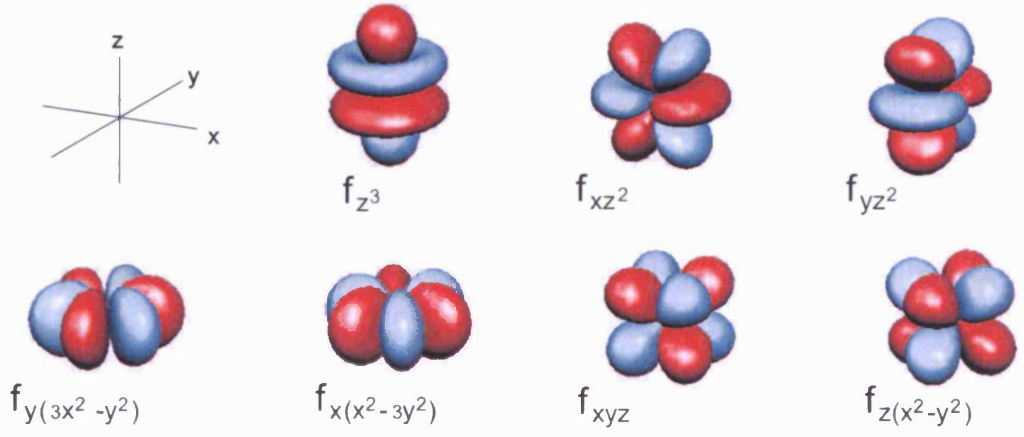

Figure 1.1: The *general set* of *f* orbitals

Heavy metals such as the actinides present a challenge for experimental and theoretical chemists alike. Thorium and uranium form many stable complexes[4-6] and so it is relatively easy to obtain experimental information about them; however due to the scarcity and/or the extreme radioactivity and instability of protactinium and the heavier actinides, special facilities are required for the limited chemistry carried out on them. Since the chemical properties of a given oxidation state often vary in a predictable way, one can combine the available experimental data with theoretical results to predict properties that could not be easily experimentally produced.

Several problems arise to the theoretician studying heavy metal chemistry. The high nuclear charge number means that relativistic effects are important and must be treated accordingly, while the number of electrons means correlation is also a significant effect. In addition to this the large numbers of electrons also makes calculations on lanthanide/actinide systems expensive, and so computational simplifications must be used to achieve a satisfactory level of accuracy on a manageable timescale in such calculations. Both of these issues will be discussed in detail later.

1.1 The electronic structures of the *f* elements

As can be seen from table 1.1, the filling of the $4f$ and $5f$ shells is the primary electronic trend as each metal series is crossed. Anomalies in this trend are seen in the lanthanides (Ce, Gd) and in the actinides (Pa $\rightarrow$ Np, Cm) but generally a $ns^2\ (n-1)d^0\ (n-2)f^x$ electronic structure is seen (in the anomalous metals named above $(n-1)d^1$ is seen); n is the primary quantum number and $(x+2)$ is the number of valence electrons.

It is clear that the *f* orbitals (pictured in figure 1.1) have an important role in determining the physicochemical properties of Ln and An; irregularities in the filling of the *f* shells hint to differences between the metals and I shall now look in more detail at what those differences are and how they manifest themselves.

1.1.1 Lanthanides

There are different definitions of which elements comprise the *f*-block series depending on whether to include the elements which begin the series, and from which the series get their names, lanthanum and actinium for the lanthanides and actinides respectively, and whether

LANTHANIDES				ACTINIDES			
Element	Symbol	Atomic number	Electronic configuration	Element	Symbol	Atomic number	Electronic configuration
Lanthanum	La	57	$[Xe]\,5d^16s^2$	Actinium	Ac	89	$[Rn]\,6d^17s^2$
Cerium	Ce	58	$[Xe]\,4f^15d^16s^2$	Thorium	Th	90	$[Rn]\,6d^27s^2$
Praseodymium	Pr	59	$[Xe]\,4f^36s^2$	Protactinium	Pa	91	$[Rn]\,5f^26d^17s^2$
Neodymium	Nd	60	$[Xe]\,4f^46s^2$	Uranium	U	92	$[Rn]\,5f^36d^17s^2$
Promethium	Pm	61	$[Xe]\,4f^56s^2$	Neptunium	Np	93	$[Rn]\,5f^46d^17s^2$
Samarium	Sm	62	$[Xe]\,4f^66s^2$	Plutonium	Pu	94	$[Rn]\,5f^67s^2$
Europium	Eu	63	$[Xe]\,4f^76s^2$	Americium	Am	95	$[Rn]\,5f^77s^2$
Gadolinium	Gd	64	$[Xe]\,4f^75d^16s^2$	Curium	Cm	96	$[Rn]\,5f^76d^17s^2$
Terbium	Tb	66	$[Xe]\,4f^96s^2$	Berkelium	Bk	97	$[Rn]\,5f^97s^2$
Dysprosium	Dy	66	$[Xe]\,4f^{10}6s^2$	Californium	Cf	98	$[Rn]\,5f^{10}7s^2$
Holmium	Ho	67	$[Xe]\,4f^{11}s^2$	Einsteinium	Es	99	$[Rn]\,5f^{11}7s^2$
Erbium	Er	68	$[Xe]\,4f^{12}6s^2$	Fermium	Fm	100	$[Rn]\,5f^{12}67s^2$
Thulium	Tm	69	$[Xe]\,4f^{13}6s^2$	Mendelevium	Md	101	$[Rn]\,5f^{13}7s^2$
Ytterbium	Yb	70	$[Xe]\,4f^{14}6s^2$	Nobelium	No	102	$[Rn]\,5f^{14}7s^2$
Lutetium	Lu	71	$[Xe]\,4f^{14}5d^16s^2$	Lawrencium	Lr	103	$[Rn]\,5f^{14}6d^17s^2$

Table 1.1: Electronic configuration data for the neutral Ln and An atoms

or not to include the elements which terminate the series, lutetium and lawrencium respectively for the two series; in this thesis I include both. Thus the lanthanide series of metals comprises the 15 elements with atomic numbers 57 to 71, from lanthanum to lutetium; all except the two aforementioned metals are *f*-block elements with an increasingly occupied $4f$ electron shell (see table 1.1). The lanthanides, together with scandium and yttrium, are sometimes referred to by the trivial name *rare earths*, although this name is not approved by IUPAC, as they are neither rare (even the least abundant, lutetium, is more abundant in the Earth's crust than gold), nor are they 'earths' (an obsolete term for oxides). Two of the lanthanides have radioactive isotopes with long half-lives (^{147}Sm and ^{176}Lu) and this property is very useful to date minerals and rocks from Earth, the Moon and meteorites.

The chemistry of the lanthanides is well known to be dominated by the +3 oxidation state. As electrons are removed from the neutral metal, Z_{eff} increases and so the electrons are more strongly attracted to the nucleus: the orbitals become stabilised. The $4f$ shell is stabilised considerably more than the $5d$, which in turn is stabilised more than $6s$. This ordering arises from the enhanced ability of the $4f$ shell with no radial nodes (and to a lesser extent $5d$ with two radial node, compared with the five radial nodes of $6s$) to penetrate the inner core electrons. Following this rationale, electrons are removed first from the $6s$ and $5d$ levels and, only when these are empty, from the $4f$; as figure 1.2 shows,

once three electrons have been removed, the additional stabilisation of the 4*f* orbitals results in an I_4 larger than $I_1 + I_2 + I_3$ and so the +4 oxidation state is unfavourable.

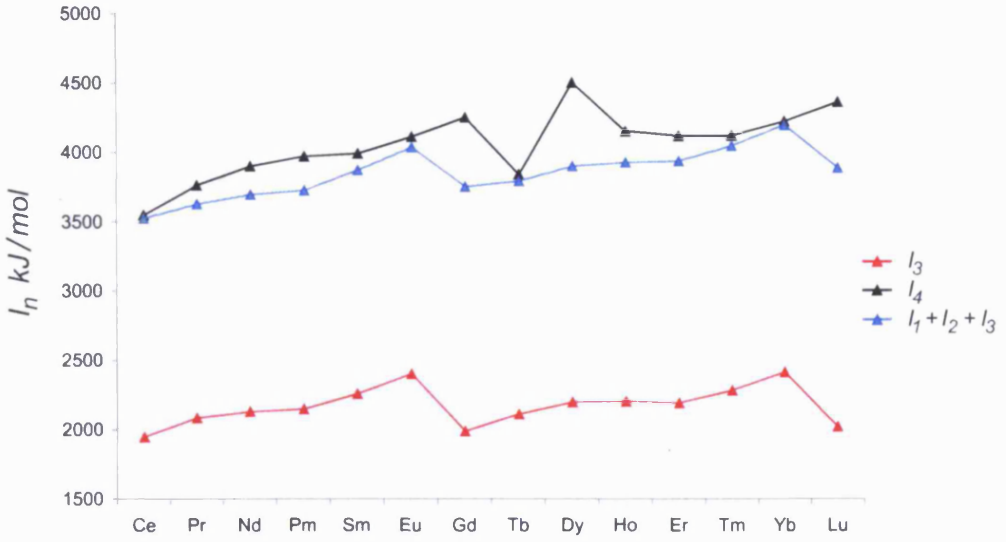

Figure 1.2: The variation of selected ionisation energies (I_n for n=3, 4, (1+2+3)) across the lanthanides

In contrast to the wide variation of properties across each series of *d* elements, the chemical properties of the lanthanides are highly uniform. However, superimposed on this uniformly 3+ behaviour are some atypical oxidation states that are most prevalent when the ion can attain an empty (f^0), half-filled (f^7) or filled (f^{14}) subshell (see figure 1.3). Thus Ce^{3+} (f^1) can be oxidised to the f^0 ion Ce^{4+}, a strong and useful oxidising agent. The next most common of the atypical oxidation states is Eu^{2+}, an f^7 ion that readily reduces water.

Although some other oxidation states are possible, the lanthanides generally occur as trivalent cations in nature. As a consequence, their chemical behaviour is a function of ionic radius. The ionic radii of the lanthanides decrease through the period, the so-called *lanthanide contraction*. The lanthanide contraction is caused by the increase in effective nuclear charge across the series, in turn due to the poor shielding ability of 4*f* electrons. Therefore much of the chemistry of the lanthanides depends markedly on atomic number. Furthermore the isolation of pure lanthanide metals from a mixed Ln ore (such as monazite or xenotime) is not trivial; Ce which can be oxidised to Ce^{4+} and Eu, reducible to Eu^{2+} are chemically separable from the other lanthanides, but separation of the remaining

lanthanides requires more refined techniques. A multi step liquid-liquid extraction process with different ligands in the aqueous and organic phases shows some success; for high purity an ion exchange chromatography system may be used. Electrolysis of molten Ln halides can also show good separation factors.

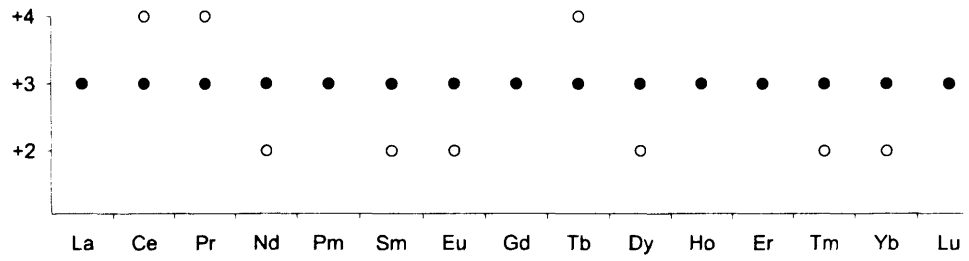

Figure 1.3: Accessible oxidation states for Ln; solid circles indicate the most common oxidation state in aqueous solution, open circles show other possible solution oxidation states

1.1.2 Actinides

The actinide series of metals comprises the 15 elements with atomic numbers 89 to 103, from actinium to lawrencium; all except the two named metals are *f*-block elements with an increasingly occupied 5*f* electron shell (see table 1.1). It is commonly believed that of the actinides, only the first four (Ac → U) are naturally occurring; this isn't strictly true.

Commercially, neptunium and plutonium are created from uranium in nuclear reactors. ^{235}U accepts a neutron to be converted to an excited state of ^{236}U. Some of the excited ^{236}U nuclei undergo fission, but some decay to the ground state of ^{236}U by emitting gamma radiation. Further neutron capture creates ^{237}U (half-life 7 days) which quickly decays to ^{237}Np. Alternatively, when ^{238}U absorbs a neutron, it becomes ^{239}U which ultimately decays to ^{239}Pu. Different isotopes of uranium and different combinations of neutron absorptions and radioactive decay create different isotopes of neptunium/plutonium.

In extremely rare cases, rocks with a high localised concentration of uranium can provide the right conditions for making small amounts of heavier elements naturally. Trace quantities of Np and Pu are found in nature due to transmutation reactions in uranium ores produced by the neutrons which are present.[7] One such example is muromontite, which is a mixture of uranium and beryllium. Putting beryllium near uranium is generally considered a bad idea because the alpha particles from the decay of uranium are captured by

the beryllium atoms, which in turn release neutrons. In the case of this mineral, however, the neutrons are in turn re-captured by the uranium, which then undergoes further decay and is transformed into plutonium. The result is that this mineral contains the highest known naturally occurring concentration of plutonium;[8] neptunium has also been found in small quantities in uranium ores[9] as a result of similar processes. The remaining actinides, Am → Lr (and the transactinide elements, currently numbers 104 → 116 excluding 113, 115, and a later retracted discovery of 118) are all the result of artificial synthesis using techniques such as neutron or light-atom bombardment.

As the actinides are defined by the filling of the *5f* shell, they are in a sense analogues of the lanthanides. Similarly to the lanthanides, the ionic radii of the actinides decrease as the series is crossed, defining an *actinide contraction*; although while the lanthanide contraction is primarily an orbital shielding effect rather than a relativistic one, the actinide contraction is thought to be an almost exclusively relativistic effect[10] (see discussion of relativity in section 2.3).

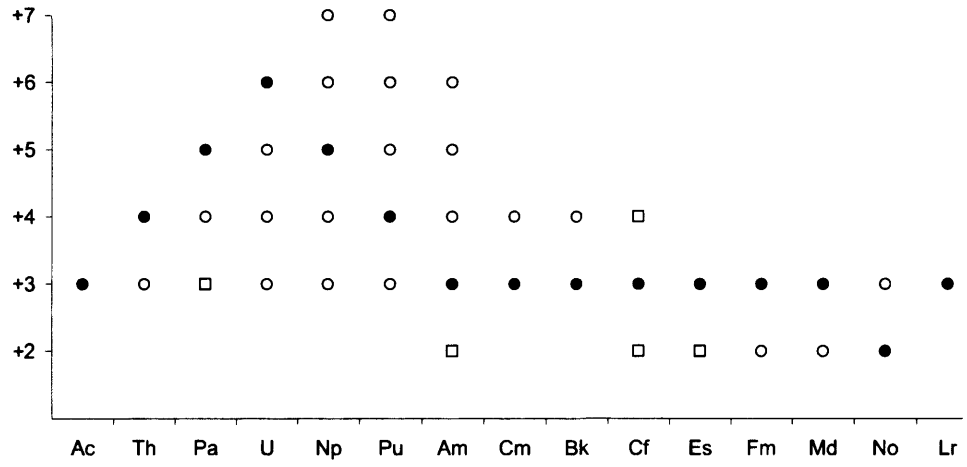

Figure 1.4: Accessible oxidation states for An; solid circles indicate the most common oxidation state in aqueous solution, open circles show other solution oxidation states and squares represent oxidation states only found in the solid state

Despite the fact that both series are defined by progressive filling of the *f* levels, the actinides do not exhibit the chemical uniformity of Ln. The early actinides occur in a rich variety of oxidation states while the later actinides show a more limited, +3 dominated chemistry, as can be seen in figure 1.4. It has been said that the early actinides

resemble transition metals while the later actinides display lanthanide-like behaviour. Although there are many examples of actinide chemsitry differing significantly from that of the transition metals,[11] certainly the range of achieveable oxidation states and the variety of coloured complexes[12] formed by the early actinides does echo the *d* block. Exactly where the changeover between TM-like/'varied' and Ln-like/'unvaried' behaviour comes has been much disputed, and this fascinating characteristic of the actinides is investigated in chapter 5 of this thesis.

The reader may recall that the +3 oxidation state strongly dominates the chemistry of the lanthanides because the 4*f* orbital is so stabilised by the removal of three electrons that a 4^{th} electron is near impossible to remove except in a few exceptional cases. The actinides contrast with the lanthanides dramatically in this respect, indeed where Ce is the only lanthanide capable of losing all its valence electrons, thorium, protactinium, uranium and neptunium can all achieve 'group valence'. Where the 4*f* shell lacks any radial nodes and therefore is able to penetrate the inner electrons efficiently, the 5*f* shell has a single radial node and as a consequence is significantly higher in energy than 4*f*.

In most cases the electronic structure of an actinide complex involves a partially filled *f*-shell; the *f*-shell is more diffuse in the actinides than the lanthanides (see discussion of relativity later), and consequently can participate in bonding to a greater extent. An interesting property of the actinides is, as pointed out by Pyykkö,[13] that the 6*s* and 6*p* atomic orbitals are highly polarizable and must be treated as valence orbitals (or at least semi-core), whereas in transition metal chemistry equivalent orbitals would be treated in the core. Practically this means that the 6*p*, 6*d* and 5*f* atomic orbitals have a similar radial extent in actinide compounds, thus the number of electrons which need to be treated explicitly in a calculation can become quite large. The 5*f* participation in actinide bonding in nicely illustrated by the actinyl (VI) ions, symmetric linear di-oxygen ions with a VI-valent actinide centre. Stable ions of this kind are found for the sequence uranium, neptunium, plutonium and americium. The increased nuclear charge stabilises the 5*f* orbital along this series; thorium has a $6d^2 7s^2$ ground state and the 5*f* orbital is not stable enough to form a doubly charged dioxo-ion, (although Th(VI) implies $2e^-$ into the [Rn] core so this would not seem a likely species anyway!). The electronic configurations of the ground states for

U, Np, Pu, Am are: U $5f^3 6d^1 7s^2$, Np $5f^4 6d^1 7s^2$, Pu $5f^6 6d^0 7s^2$, Am $5f^7 6d^0 7s^2$. A gradual stabilisation of the 5*f* orbitals as the series is crossed results from the increased effective nuclear charge, a result of the 5*f* electrons' poor nuclear shielding, and after americium the 5*f* orbitals have become so stabilised that removal of the *f* electrons is energetically very unlikely, so ions of this type can no longer be formed.

1.1.3 Comparing Ln with An compounds

This section summarises trends among the lanthanides and among the actinides, firstly within metal halides and metal oxides and then among some larger complexes with Ln / An –E bonds (E = S, Se), and as such provides a good comparison of the series' respective behaviour.

M–X (X = F, Cl, Br, I) and M–O

Trihalides, LnX_3 (X = F, Cl, Br, I) are known for all the lanthanides, and as might be expected they are ionic salts with crystalline structures. The coordination number of X around Ln depends heavily on the size of the metal (i.e. the atomic number) and also, of course, on the halide. For example, within the lanthanide fluorides, La → Pm adopt a 9-coordinate structure and the remaining metals an 8-coordinate one. Among the chlorides La → Gd take 9-coordinate structures, Tb is 8-coordinate and all other Lns are 6-coordinate, and of the bromides La → Pr are 9-coordinate with Nd 8-coordinate and the rest all 6-coordinate; all LnI_3 are either 8- or 6- coordinate salts. The trihalides are primarily useful as starting materials for the synthesis of either pure Ln or else other Ln complexes. Dihalides are significantly scarcer than trihalides among the lanthanides, only Sm and Yb form dihalides with F, Cl, Br and I, and Tb, Ho, Er and Lu have no known LnX_2 at all. Other Ln halides include the three tetravalent fluorides of Ce, Pr and Tb and a number of Ln_2Cl_3.

In contrast with this, the halides of the actinides are myriad. As mentioned previously, 'group valence' is possible up to U and thus ThX_4, PaX_5 (X = F, Cl, Br, I) and UX_6 (X = F, Cl) are all known; other hexahalides include NpF_6 and PuF_6. The pentahalides are slightly more common, PaX_5 and UX_5 are known for all X as well as NpF_5. Tetrafluorides in the actinides are widespread and include ThX_4 → NpX_4 for all X, as well as PuX_4 → CfX_4 for X = F. AnX_3 for all X are known for U → Es, Th and Pa are only known in trihalide

complexes with I. Finally, AnX_2 are known for Am → Es with X = Cl, Br and I, and for Th with I only. The many coordination numbers of the actinide halides are not detailed here but to briefly compare with the lanthanide halides, the early AnF_3 take a 9-coordinate environment and there is a changeover to 8-coordinate with BkF_3, three metals further than the analogous changeover in the lanthanides (at Pm). Similarly, $AcBr_3$ → $NpBr_3$ take a 9-coordinate structure and $PuBr_3$ → $BkBr_3$ an 8-coordinate one, in contrast to $LnBr_3$ mentioned above.

As well as differences in the abundance and variety of lanthanide and actinide halides, there are significant differences in the synthesis of these compounds. Lanthanide fluorides are generally made via a metathesis reaction of $Ln(NO_3)_3$ with HF and further heating of the hydrated fluoride product. More complicated synthetic routes are needed for the heavier halides, as the heating step mentioned above instead involves other reagents and conditions. In contrast with this, direct combination of An and X will react to give the early actinide halides.

Next I will mention lanthanide and actinide oxides. The most commonly occurring lanthanide oxides have the formula Ln_2O_3 for all Ln with the exceptions of Ce, Pr and Tb which form LnO_2 initially but can be reduced to Ln_2O_3 with hydrogen gas. Ln_2O_3 can be reduced with Ln metal to form LnO for Ln = Np → Yb; this covers the range of lanthanide oxides. Unsurprisingly the variety of An oxides is richer, uranium alone forms UO_2, U_4O_9, U_3O_8, and UO_3. The most stable oxides of Th → Es are as follows: ThO_2, Pa_2O_5, U_3O_8, NpO_2, PuO_2, AmO_2, Cm_2O_3, BkO_2, Cf_2O_3 and Es_2O_3 with oxidation states +4, +5, +5.$\dot{3}$, +4, +4, +4, +3, +4, +3 and +3 respectively (note how as the series is crossed, the dominant lanthanide oxide formula begins to dominate the actinides too).

Some larger Ln complexes with the formula $LnL_3.nH_2O$ with L = 2-(((4.6-dimethyl)-2-pyrimidinyl)thio) acetic acid, Ln = La, Ce, Pr, Nd, Sm, Eu, Gd, Tb and n = 4, 5 were synthesised as potential anti-tumour agents.[14] The eight metal structures were found to all have similar structures, and furthermore these structures show similarities to the complexes studied in this chapter, see figure 1.5; the homoleptic structures consist of three bidentate oxygen donor ligands around a trivalent metal centre.

Although no bond length data is given, the I.R. absorption of Ln–O was measured

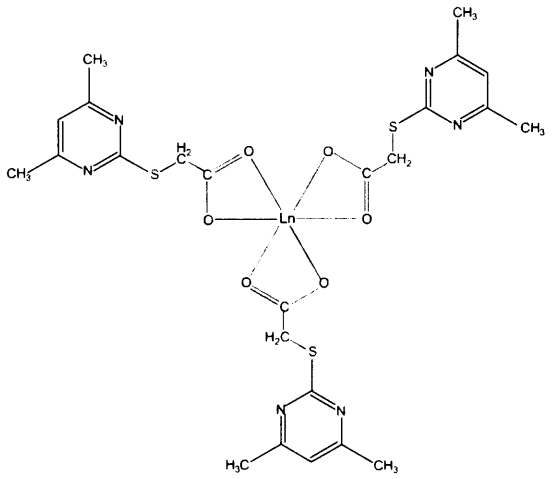

Figure 1.5: Schematic of proposed structure of LnL_3

and Qu *et al* found that all eight complexes have the same value to within $3cm^{-1}$ (404 - 407 cm^{-1}), an indication that the Ln–O bond is of a very similar strength in each complex. In addition to this, thermal stabilities for the complexes were found to all be similar. Unfortunately no actinide complexes of this type have been synthesised yet.

M–E (E = S, Se)

Few Ln–X complexes are known for X = S, Se, and significantly fewer An–X. The first thiolates of the *f* elements, $U(SEt)_4$ and $U(S^nBu)_4$ were prepared in 1956 by Gilman *et al*,[15] although they were largely ignored until the 1990s when Tatsumi *et al* isolated the tetrakis dithiolate $[Li(dme)]_4U(edt)_4$.[16] Since then other heterobimetallic homoleptic thiolate and dithiolate compounds of uranium (IV) have been produced. It is noteworthy that since the discovery of $U(SEt)_4$ and $U(S^nBu)_4$ (both pyrophoric powders), there have been no reports of structural characterization of any neutral homoleptic uranium (IV) thiolate compound. There have, however, been preparations of a variety of uranium (IV) compounds containing thiolate or dithiolene ligands along with inorganic[17–19] and organic[17,19–24] ligands, and the complexes clearly demonstrate the stability of the U–S bond. r(U–S) varies in length from approx. 2.46 Å in [Na(18-crown-6)][$U(Cp^*)_2(SBu^t)$(S)] to approx. 2.88 Å in $[\{U(cot)(\mu\text{-}SPr^i)_2\}_2]$. Comparative studies of U(III)–S with Ln(III)–S have been limited, but a shortening of the uranium–sulphur bond (2.63-2.65 Å) compared with lanthanide–sulphur (2.83-2.85 Å, Ln = Ce) has been observedby Roger *et al*[24] and has been cited

as evidence for a stronger metal–sulphur interaction in the uranium complex due to the presence of covalent character in the U–S bond; Roger's research will be more extensively reviewed in the literature section of chapter 5. Recent work to synthesise metal tri-thiolates, $M(SMes^*)_3$, for M = La, Ce, Pr, Nd and U ($SMes^*$ = S-2,4,6-$^t Bu_3C_6H_2$) have yielded M–S of 2.741 Å (La), 2.703 Å (Ce), 2.709 Å (Pr), 2.695 Å (Nd) and 2.723 Å (U), although since the ionic radius for U(III) is similar to that of La(III) and somewhat larger than any of the other Ln(III)[25,26] this still implies a *relative* shortening of U–S compared with Ln–S.

There have been a number of reports of Ln–E bonds in crystals such as Ln_2SnS_4 (Ln = Eu, Sr) and Sr_2GeSe_4,[27] $Pr_4N_2E_3$ (E = S, Se),[28] $Ln_4N_2Se_3$ (Ln = Nd, Tb)[29] and $CsCu_3Ln_2Se_5$ (Ln = Sm, Gd – Lu).[30] The Ln–S distances vary from 2.833 Å ($Pr_4N_2S_3$) to 3.416 Å (Sr_2SnS_4) with typical values falling around 2.9-3.1 Å. Unsurprisingly Ln–Se is generally longer than Ln–S, the range spanning 2.770 Å ($CsCu_3Lu_2Se_5$) to 3.568 Å (Sr_2GeSe_4) with typical values falling around 3.0-3.3 Å, in reasonable agreement with the difference between the ionic radii of the two chalcogen dianions (S^{2-} = 1.84 Å, Se^{2-} = 1.98 Å[26])

The few reports of U–Se bonds indicate that, as expected by the larger ionic radius of Se *vs.* S, *r*(U–Se) is appreciably longer than U–S, values of approx. 3 Å have been recorded by Gaunt *et al*[31] in $[U(SePh)_2(\mu_2\text{-}SePh)_2(CH_3CN)_2]_2$ and a range of *r*(U–Se) from 2.79 Å to 3.12 Å have been measured in $[U(py)_2(SePh)(\mu_3\text{-}Se)_2(\mu\text{-}SePh)]_4 \cdot 4py$ (both U(IV)).

Thus it is clear that the range of chemistry exhibited by the actinides is larger than that of their homologous 4*f* cousins, although the chemistry of the former is largely unexplored due to the practical problems of safety and expense.

1.2 Research Projects

The following sections will introduce each of the projects undertaken during this PhD.

1.2.1 A Density Functional Theory investigation of the geometric and electronic structures of $[UO_2(H_2O)_{a-x}(OH)_x]^{(2-x)+}$ for $x = 0 \rightarrow 5$ with a = 5, and some a = 3, 4.

Complexes belonging to this family have been studied previously (mainly $[UO_2(H_2O)_5]^{2+}$ and $[UO_2(OH)_4]^{2-}$) both computationally, e.g.[32-39] and experimentally[1-3,32,40-43] but this is the first systematic treatment of all species with one method. It has been observed that as charged hydroxide ions replace neutral water ligands in these systems, r(U–O) lengthens; the reason for this lengthening is not known. There is dispute over whether it is a purely ionic effect: as electron density is pushed onto the metal centre then the charge difference between uranium and oxygen is reduced and therefore an ionic bond could be expected to lengthen and weaken. However a covalent argument has also been proposed: hydroxide ions are π-donors and can therefore be expected to compete with the π-orbitals of uranyl oxygens for metal d and f orbitals. The π-bonds, along with a σ-bond, constitute the formally triple bond between uranium and oxygen in the bare uranyl ion UO_2^{2+} and so ligand competition for the metal orbitals involved may weaken the uranyl bonds.

The first chapter of results details work modelling the family of complexes and performing analyses of bond lengths, vibrational wavenumbers, atomic charges and the molecular orbitals involved in bonding to attempt to validate either the ionic or the covalent argument.

1.2.2 The Performance of Time-Dependent Density Functional Theory in the simulation of the electronic spectra of molecular uranium complexes

A group at Manchester's Centre for Radiochemistry Research (CRR) has synthesised two uranyl complexes with soft, nitrogen-donating ligands: $[UO_2\{(NSiMe_3)_2C\text{-}Ph\}_2]$ and $[UO_2\{(NSiMe_3)_2P\text{-}Ph_2\}_2]$. It was observed that these two complexes were orange/red and showed significantly longer wavelength *UV/Vis* absorption peaks than typical uranyl complexes, which are green/yellow coloured. The question here was: do these complexes show longer wavelength (and therefore lower energy) absorptions because the soft, N-donor ligands lead to significantly different molecular orbitals around the HOMO of the

molecule and therefore a different type of electronic transition, or is it simply a case of the ligands interacting with uranyl to give an unusually small HOMO-LUMO gap?

Computationally, modelling these complexes (~100 atoms) was significantly more demanding than the ~15 atoms in the mixed water/OH systems. This stretched computational resources and lead to a sidestep from the main project in the form of an investigation into the best method to model electronic spectra of heavy metal complexes. Time dependent DFT (TD-DFT) was used and a number of different functionals and basis sets were tested on simpler, well characterised uranyl complexes. Once a reliable method which showed good agreement with experiment had been decided on, the two soft N-donor ligand complexes were addressed.

1.2.3 Covalency in the *f*-element–chalcogen bond. Computational studies of $[M(N(EPR_2)_2)_3]$, M = Ln (Ln = La, Ce, Pr, Pm, Eu), An (An = U, Np, Pu, Am, Cm); E = O, S, Se, Te; R = H, Me, ^{i}Pr

Current work at the Los Alamos National Lab (LANL), USA is focusing on the synthesis and characterization of a range of homoleptic, trivalent lanthanum and uranium complexes with S-, Se-, and Te- donor ligands. The principal aim of the research is to explore the differences in *f*-element–ligand bonding between Ln(III) and An(III) with soft donor ligands such as S, Se, and Te in the anticipation that the actinide bond with heavier chalcogens will be more covalent than the analogous lanthanide bond. The motivation for this work is the need for effective ligands for the separation of minor actinides (Am, Cm) from lanthanide fission products in nuclear reactor waste.

I have initially modelled the La and U complexes, testing R = H, Me as approximations to the bulky R = ^{i}Pr ligand synthesised experimentally; I have also tested the validity of idealising these complexes to D_3 symmetry, to cut computational cost and also to facilitate MO analysis of these complexes. Having validated both approximations, I next extended the study to include all $[M(N(EPH_2)_2)_3]$ for M = Ln, An, for Ln = La, Ce, Pr, Pm, Eu; An = U, Np, Pu, Am, Cm with E = O, S, Se, Te, with a focus on comparing Ln–E and An–E both along the respective metal series and down group 16, as well as comparing the lanthanide data with that of the actinides. Bond lengths, calculated charges and atomic

populations as well as atom-atom overlap populations, Mayer bond orders and molecular orbital energy and composition analysis are among the methods used to compare Ln–E and An–E.

Chapter 2

Electronic Structure Theory

This research has used a variety of aspects of electronic structure theory as well as different resources and software to implement the theory. In this chapter I will discuss many of those aspects of electronic structure theory most relevant to the study of heavy metal complexes.

2.1 Density Functional Theory (DFT)

Traditional methods in electronic structure theory (such as Hartree-Fock, Coupled Cluster, Møller-Plesset perturbation theory to name a few) are based on the many electron wavefunction, which can get very complicated very quickly as the number of electrons increases. The main objective of DFT is to replace the many body electronic wavefunction with the electronic density, and to subsequently compute molecular properties with the electron density as the main variable rather than the electronic wavefunction.

The basis for DFT is the proof by Hohenberg and Kohn that the ground state electronic energy is determined by the electron density. This approach is fundamentally different from the wavefunction approach of expanding the one-electron Schrödinger equation to account for many electrons, resulting in a wavefunction which requires $3N$ coordinates to describe N electrons. Instead the electron density of a system depends on only three coordinates, regardless of the system size, and herein lies the power of DFT.

Following on from Hohenberg and Kohn's first theorem:[44]

The electron density determines the external potential (to within an additive constant)

comes: *The electron density uniquely determines the Hamiltonian operator.*

If the system in question is a molecule we can break its energy down into its component

parts as functionals* of ρ, the electron density:

$$E[\rho] = T[\rho] + V_{e\ /e}\ [\rho] + V_{nuc/e}\ [\rho] \tag{2.1}$$

where $T[\rho]$ is the kinetic energy of the system as a functional of $[\rho]$, the electron density, and $V_{e\ /e}\ [\rho]$ and $V_{nuc/e}\ [\rho]$ are the electron/electron and nucleus/electron interaction energies respectively, both also as functionals of ρ.

Hohenberg and Kohn's second theorem establishes a variational principle:

For any trial charge density ρ_{trial} *such that* $\int \rho_{trial}\ (r)\ dr = N$, *then* $E\ [\rho_{true}] \leq E\ [\rho_{trial}]$

We consider a molecule in which the electrons move in an external nuclear potential $V(r)$. Now consider a fictitious system with the same $V(r)$ in which *the electrons do not interact with one another*. This system may be described by a single determinant:

$$\Psi_{non-int} = \frac{1}{\sqrt{n!}} \mid \phi_1\ \phi_2\ \phi_3\ \ldots\ \phi_n \mid \tag{2.2}$$

ϕ_i are the n lowest eigenstates of

$$\hat{H}_{non\ int}\ \phi_i = \left(-\frac{1}{2}\nabla^2 + V\ (r) \right) \phi_i = \varepsilon_i \phi_i \tag{2.3}$$

note there are no e^-/e^- terms in this expression, as defined above.

If ϕ_i (the molecular orbitals, see discussion later) are known then the charge density is simply:

$$\rho = \sum_{i=1}^{n} \mid \phi_i\ (r) \mid^2 \tag{2.4}$$

The kinetic energy (K.E.) of the fictitious system with charge density ρ is:

$$T_{non\ int}[\rho] = \left\langle \Psi_{non\ int} \left| \sum_i^n \left(-\frac{1}{2}\nabla^2 \right) \right| \Psi_{non\ int} \right\rangle \tag{2.5}$$

$$= \sum_i^n \left\langle \phi_i \left| \ \frac{1}{2}\nabla^2 \right| \phi_i \right\rangle \tag{2.6}$$

* Nomenclature: a functional is a function of a function, so just as $\rho(r)$ indicates ρ is a *function* of r, $E[\rho]$ defines E as a *functional* of ρ

$T_{non-int}[\rho] \neq T[\rho]$ of (2.1), but given ϕ_i it is easy to evaluate.

Kohn and Sham noticed that a system of non-interacting electrons is equivalent to a real system experiencing a modified potential and therefore stated that $T_{non-int}[\rho]$ is the K.E. of a real system. To continue we must rewrite equation 2.1 as:

$$E[\rho] = T_{non-int}[\rho] + J[\rho] + E_{XC}[\rho] + V_{nuc/e}[\rho] \tag{2.7}$$

where $J[\rho]$ is the classical coulomb term, and $E_{XC}[\rho]$ the exchange and correlation term, further defined as:

$$E_{XC}[\rho] = T[\rho] - T_{non-int}[\rho] + V_{e/e}[\rho] - J[\rho] \tag{2.8}$$

In the above expression (2.8), $(T[\rho] - T_{non-int}[\rho])$ is the difference between the K.E.s of the real and fictitious systems and $(V_{e/e}[\rho] - J[\rho])$ accounts for the non-coulomb e/e term. Next we can work out the energy of the non-interacting system:

$$E_{non-int}[\rho] = T_{non-int}[\rho] + V_{nuc/e}[\rho] \tag{2.9}$$

$$V_{nuc/e}[\rho] = \int \rho(r) V(r)\, dr \tag{2.10}$$

$$\Longrightarrow E_{non-int}[\rho] = T_{non-int}[\rho] + \int \rho(r) V(r)\, dr \tag{2.11}$$

If we know $[\rho]$ we can calculate $E_{non-int}[\rho]$. We can get $[\rho]$ from (2.3) and (2.4), and thus the total energy of the real system is:

$$E[\rho] = T_{non-int}[\rho] + J[\rho] + E_{XC}[\rho] + \int \rho(r) V(r)\, dr \tag{2.12}$$

If we know $[\rho]$ we can calculate $E[\rho]$; how do we get $[\rho]$ for a real system? We can get it from a one-electron eigenvalue equation similar to eq. 2.3 in which $V(r)$ is replaced by a modified external potential, $V_{eff}(r)$:

$$\hat{h}\,\phi_i = \left(-\frac{1}{2}\nabla^2 + \underbrace{V_{eff}(r)}_{\uparrow \text{ Kohn-Sham effective potential}}\right)\phi_i = \varepsilon_i\,\phi_i \tag{2.13}$$

$$V_{eff}(r) = \underbrace{V(r)}_{\uparrow \text{ nuclear field}} + \underbrace{\int \frac{\rho(r')}{|r-r'|}\,dr'}_{\uparrow \text{ coulomb term}} + \underbrace{V_{XC}(r)}_{\uparrow \text{ exchange-correlation potential}} \tag{2.14}$$

$$\Longrightarrow \left(\left[-\frac{1}{2}\nabla^2 + V(r)\right] + \int \frac{\rho(r')}{|r-r'|}\,dr' + V_{XC}(r)\right)\phi_i = \varepsilon_i\,\phi_i \tag{2.15}$$

The key to equation 2.15 is $V_{XC}(r)$; we get this term from $E_{XC}[\rho]$ from the calculus of functionals:

$$V_{XC}(r) = \frac{\partial E_{XC}[\rho]}{\partial \rho(r)} \tag{2.16}$$

2.1.1 Exchange-Correlation Functionals

Exchange-Correlation functionals essentially try to model the exchange-correlation hole. This is done with varying degrees of sophistication depending on the approach taken. However, all XC functionals can be written in the following general form

$$E_{XC}[\rho(r)] = \int \rho(r)\,\varepsilon_{XC}(r)\,dr \tag{2.17}$$

where $\varepsilon_{XC}(r)$ is the exchange-correlation energy per particle. Functionals can be characterised by the way in which the density surrounding each electron is sampled in order to construct $\varepsilon_{XC}(r)$. Currently five principal types of functional have been proposed; these are examined in the section below.

Local Density Approximation (LDA)

The oldest and simplest XC functional is the Local Density Approximation (LDA) (for high-spin systems this is called the local spin density approximation (LSDA)), which was

proposed by Hohenberg and Kohn in their original DFT paper.[44] The LDA consists of approximating the density locally as a homogeneous electron gas, that is to say the variation of electron density over the molecule or system is zero. The exchange and correlation energies are computed as functionals of the electron density, and the total energy is commonly written as:

$$E_{XC}^{LDA}[\rho(r)] = \int \rho(r)\,\varepsilon_{XC}^{hom}[\rho(r)]\,dr \tag{2.18}$$

where $\varepsilon_{XC}^{hom}[\rho(r)]$ is the exchange-correlation energy density corresponding to a homogeneous electron gas of density $\rho(r)$. Despite its simplicity, the LDA works well for solid systems and has been used in solid state calculations for many years, however its success does not transfer well to chemistry; the LDA has a notorious tendency to overbind. In recent years, LDA, LSDA, and VWN (the Vosko, Wilks, and Nusair functional[45]) have become synonymous in the literature.

Generalized Gradient Approximation (GGA)

Advancements in DFT lead to the development of GGA functionals, in which the density is considered to be a non-uniform electron gas, in contrast with the LDA. This is achieved by making the exchange and correlation energies dependent not only on the electron density, but on derivatives of the density too. Computationally this is normally implemented by writing the GGA in terms of an analytic function known as the enhancement factor, $F_{XC}[\rho(r), \nabla\rho(r)]$, that directly modifies the LDA energy density.

$$E_{XC}^{GGA}[\rho(r)] = \int \rho(r)\;\varepsilon_{XC}^{hom}[\rho(r)]\;F_{XC}\;[\rho(r)\,\nabla\rho(r)]\;dr \tag{2.19}$$

The most notable outcome of the development of the GGA was the significant reduction in the LDA over-binding error for solids and molecules. It has been said that the success of the GGA for molecular properties was a major factor in the awarding of the Nobel Prize in chemistry to Kohn in 1998. Two popular GGA functionals have been used in this work, PW91[46] and PBE,[47,48] the former, older and more complicated functional has long been a favourite GGA functional with the computational physics and chemistry communities

alike. The enhancement factor for PW91 is:

$$F_X^{PW91}(s) = \frac{1 + 0.19645s \sinh^{-1}(7.7956s) + \left(0.2743 - 0.15084e^{-100s^2}\right)s^2}{1 + 0.19645s \sinh^{-1}(7.7956s) + 0.004s^4} \quad (2.20)$$

where s is a function $s(r)$ which represents the dimensionless reduced density gradient.[49]

I have included the enhancement factor above in order to compare this older functional with the newer PBE, with the enhancement factor below:

$$F_X^{PBE}(s) = 1 + \kappa - \frac{\kappa}{1 + \mu s^2/\kappa} \quad (2.21)$$

where $\mu = 0.21951$ and $\kappa = 0.804$. PBE was designed to give a simpler functional form by retaining only the most energetically important conditions satisfied by PW91. However since the PBE and PW91 enhancement factors are virtually indistinguishable for $0 < s < 3$, (the range exhibited by most physical systems), they yield essentially the same physical properties.

With the exception of some preliminary LDA calculations and a small number of calibration calculations using the hybrid B3LYP[50,51] functional, all calculations in this thesis were performed with GGA functionals; hence whilst the remaining types of functional are mentioned below, they have not been explained in detail. For a deeper understanding or recent research into Meta-GGA, Hybrid, and WDA functionals, the reader is directed to the literature, e.g.[52–56]

Meta-GGA, Hybrid functionals and Non-local Functionals

Meta-GGA functionals use the Laplacian (second derivative) of the density in addition to the density and the gradient of the density. Just as a GGA functional is an LDA functional modified with additional terms, so a meta-GGA functional can be constructed by adding terms to a GGA functional.

There are several meta-GGA functionals now in existence and some improvement has been obtained over the GGA in a limited number of tests. However a few cautionary words should be said about the meta-GGA. At present, meta-GGA calculations do not perform consistently because they rely on the utilisation of GGA orbitals and densities. To achieve self-consistency computationally expensive methods must be invoked; this has yet

to be implemented - indeed it may eventually prove too costly for practical computations. Another point to highlight is that all meta-GGA forms are constructed using experimental molecular data to define the form. This will have the effect of introducing an element of bias into the character of the functional.

Hybrid functionals combine exact (Hartree-Fock) exchange with conventional GGAs. They take the general form:

$$E_{XC}^{hybrid} = a(E_X^{HF} - E_X^{GGA}) + E_{XC}^{GGA} \tag{2.22}$$

Hybrid functionals give impressive agreement with experiment for many molecular properties, outperforming GGA functionals for the lighter elements; the well known B3LYP[50,51] is possibly the best performing of all the currently known functionals for the top part of the periodic table. However, an extensive study of the literature indicates that these two types of functional perform more similarly for heavy metal calculations,[57 64] with the GGA method often outperforming hybrid functionals by varyingly sized margins.

The final class of functionals to consider are fully non-local approximations such as the average density approximation (ADA[65]) and weighted density approximation (WDA[56]), which were created in the 1970s. The advantage of the non-local approach is that the number and severity of the approximations are kept to a minimum, and so the functionals retain many of the correct features of the exact functional such as self-interaction effects and correct asymptotic characteristics. However, the main disadvantage is the increase in computational expense due to the double integral form of these functionals (see ref 56 for further details). An unfortunate consequence of this downside is that fully non-local functionals such as the ADA and WDA are relatively unknown and little explored in comparison to the functionals described previously, despite possessing several desirable features.

2.1.2 Time Dependent-Density Functional Theory (TD-DFT)

TD-DFT extends the concept of stationary ('normal') DFT to time-dependent situations. In basic terms, TD-DFT employs the fact that the frequency dependent linear response of a finite system with respect to a time-dependent perturbation has discrete poles at the exact

correlated excitation energies of the unperturbed system.

The frequency dependent mean polarisability $\alpha(\omega)$ describes the response of the dipole-moment to a time-dependent electric field of frequency $\omega(t)$. It can be shown (not given) that $\alpha(\omega)$ is related to the electronic spectrum according to:

$$\alpha(\omega) = \sum_{I} \frac{f_I}{\omega_I^2 - \omega^2} \tag{2.23}$$

where ω_I is the excitation energy E_I-E_0. Equation 2.23 tells us that $\alpha(\omega)$ diverges when $\omega_I = \omega$, i.e. it has poles at the electronic excitation energies ω_I with corresponding oscillator strengths f_I. Within the Kohn-Sham scheme, the exact linear response can be expressed as the linear density of a non-interacting system to an effective perturbation. The orbital eigenvalue differences of the ground state KS orbitals enter this formalism as a first approximation to the excitation energies.

TD-DFT Functionals

For properties that depend strongly on the outer region of the molecule such as high-lying excitation energies and (hyper) polarisabilities, it may be important to use a XC potential with correct asymptotic behaviour. Chapter 4 details benchmarking two such potentials, LB94[66] and SAOP,[67] alongside three 'regular' functionals (VWN,[45] PBE,[47,48] and PW91[46]) and a sixth functional, rev-PBE,[68] a revised version of PBE which has been used with some success for TD-DFT calculations.[69]

2.2 Basis Functions

2.2.1 Satisfying the Pauli Principle

Section 2.1 formulates the DFT equations starting from a basic breakdown of the energy of a system into kinetic and Coulombic contributions, a detailed breakdown of these components by the use of a fictitious non-interacting electron gas, and subsequent evaluation of the real and fictitious parts until an expression is arrived at which contains all the known quantities as well as the exchange-correlation energy, all expressed in terms of the electron density. Equation 2.4 gives an expression for the density in terms of $\phi_i(r)$, but what does this quantity signify? To answer this I will leave the confines of DFT for a moment and

move into more general quantum chemistry.

An electronic wavefunction for N particles must be a function of $4N$ coordinates: for each electron, there are x, y, and z Cartesian coordinates plus a spin coordinate s. The Cartesian coordinates for electron i are usually denoted by a collective index $\mathbf{r}_i$, and the set of Cartesian plus spin coordinates is often denoted $\mathbf{x}_i$.

What is an appropriate form for an N-electron wavefunction? The simplest solution is a product of one-particle functions, *orbitals*:

$$\Psi(\mathbf{x}_1, \mathbf{x}_2, \cdots, \mathbf{x}_N) = \chi_1(\mathbf{x}_1)\chi_2(\mathbf{x}_2)\cdots\chi_N(\mathbf{x}_N) \tag{2.24}$$

This is referred to as a *Hartree Product*. Since the orbitals $\chi_i(\mathbf{x}_i)$ depend on spatial and spin coordinates, they are called *spin orbitals*, and are simply a spatial orbital multiplied by a spin function.

Unfortunately, the Hartree Product is not a suitable wavefunction because it ignores the Pauli antisymmetry principle. Since electrons are fermions, the electronic wavefunction must be antisymmetric with respect to the interchange of coordinates of any pair of electrons. This is not the case for the Hartree Product. Simplifying to the case of two electrons, the wavefunction can be easily made antisymmetric:

$$\Psi(\mathbf{x}_1, \mathbf{x}_2) = \frac{1}{\sqrt{2}}\left[\chi_1(\mathbf{x}_1)\chi_2(\mathbf{x}_2) - \chi_1(\mathbf{x}_2)\chi_2(\mathbf{x}_1)\right]. \tag{2.25}$$

Where $1/\sqrt{2}$ is a normalisation factor. The expression above can be rewritten as a determinant:

$$\Psi(\mathbf{x}_1, \mathbf{x}_2) = \frac{1}{\sqrt{2}}\begin{vmatrix} \chi_1(\mathbf{x}_1) & \chi_2(\mathbf{x}_1) \\ \chi_1(\mathbf{x}_2) & \chi_2(\mathbf{x}_2) \end{vmatrix} \tag{2.26}$$

Note a nice feature of this; if two electrons are put in the same orbital at the same time (i.e., set $\chi_1 = \chi_2$), then $\Psi(\mathbf{x}_1, \mathbf{x}_2) = 0$. This is just a statement of the Pauli exclusion principle.

This strategy can be generalized to N electrons using *determinants*.

$$\Psi = \frac{1}{\sqrt{N!}} \begin{vmatrix} \chi_1(\mathbf{x}_1) & \chi_2(\mathbf{x}_1) & \cdots & \chi_N(\mathbf{x}_1) \\ \chi_1(\mathbf{x}_2) & \chi_2(\mathbf{x}_2) & \cdots & \chi_N(\mathbf{x}_2) \\ \vdots & \vdots & \ddots & \vdots \\ \chi_1(\mathbf{x}_N) & \chi_2(\mathbf{x}_N) & \cdots & \chi_N(\mathbf{x}_N) \end{vmatrix} \tag{2.27}$$

A determinant of spin orbitals is known as a *Slater* determinant. By expanding the determinant, $N!$ Hartree Products are obtained, each with a different sign; the N electrons are arranged in all $N!$ possible ways among the N spin orbitals. This ensures that the electrons are indistinguishable as required by the antisymmetry principle. The leading term of the Slater determinant ($\chi_1(\mathbf{x}_1)\ \chi_2(\mathbf{x}_2) \cdots \chi_N(\mathbf{x}_N)$) can be written as shorthand for the whole expression, and this can be further simplified to give:

$$\Psi_{atom} = \chi_1\ \chi_2\ \chi_3 \cdots \chi_n \tag{2.28}$$

as a wavefunction for an atom; the χ_i in equation 2.28 are atomic orbitals (AOs). If this is extended to the molecular situation then the following can be written:

$$\Psi_{molecule} = \phi_1\ \phi_2\ \phi_3 \cdots \phi_n \tag{2.29}$$

In this manner we can think of ϕ_i as single-electron molecular orbitals (MOs); ϕ_i can be written in the Linear Combination of Atomic Orbitals (LCAO) approach as:

$$\phi_i = \sum_k c_{ik}\ \chi_k \tag{2.30}$$

c is a coefficient, i is the label for the one electron MO and k is a label running from 1 to the total number of AOs, so equation 2.30 sums a weighted contribution of all AOs (c_{ik} can be zero) to give each MO.

The χ_k wavefunctions defined in equations 2.28 and 2.30 are called *basis functions* and sum over the whole molecule to give the *basis set*. The mathematical form of χ_k is a problem; as χ_i are likened above to atomic orbitals, an obvious answer is for each χ_k to

take the solution to the hydrogenic Schrödinger equation. Unfortunately the mathematics involved with such a basis function render this problematic and so two alternatives are widely used. These are Slater Type Orbitals (STOs) and Gaussian Type Orbitals (GTOs).

2.2.2 Slater Type Orbitals

STOs take the form:

$$\chi^{STO}_{\zeta,n,l,m}(r,\theta,\varphi) = N\,Y_{l,m}(\theta,\varphi)\,r^{n-1}\,e^{-\zeta r} \tag{2.31}$$

where N is a normalization constant, $Y_{l,m}$ describes the angular part of the function and ζ is the Slater exponent. The Slater exponent has a definition: $\zeta = \frac{Z^*}{n} = \frac{Z-s}{n}$ where Z^* is the effective nuclear charge, calculated by subtracting the screening constant s from the formal nuclear charge Z, and r and n are the $nuc-e^-$ distance and the principal quantum number respectively. However when designing basis sets instead of using this formula, high-level atomic calculation data are used to empirically choose values for ζ.

The radial part of the function in equation 2.31, $e^{-\zeta r}$ means that from a computational point of view, while the STOs describe the AOs well, they cannot be integrated analytically and therefore must be calculated numerically, which drastically decreases the speed of a computation.

2.2.3 Gaussian Type Orbitals

An alternative to STOs are Gaussian Type Orbitals (GTOs), which take the form:

$$\chi^{GTO}_{\alpha,n,l,m}(r,\theta,\varphi) = N\,Y_{l,m}(\theta,\varphi)\,r^{2n-2-l}\,e^{-\alpha r^2} \tag{2.32}$$

with the parameter α calculated in the same way as ζ above, i.e. by comparing the performance of different α s with high-level calculation data.

The main difference between STOs and GTOs is that while the former has the computationally awkward e^{-r} dependency, GTOs have a much simpler e^{-r^2} dependency and can be calculated analytically; hence GTOs are often preferred over STOs. However, GTOs do not describe AOs as well as STOs because unlike STOs, they do not describe the cusp behaviour at the nucleus, and furthermore they tend to fall off too rapidly at large r. One way

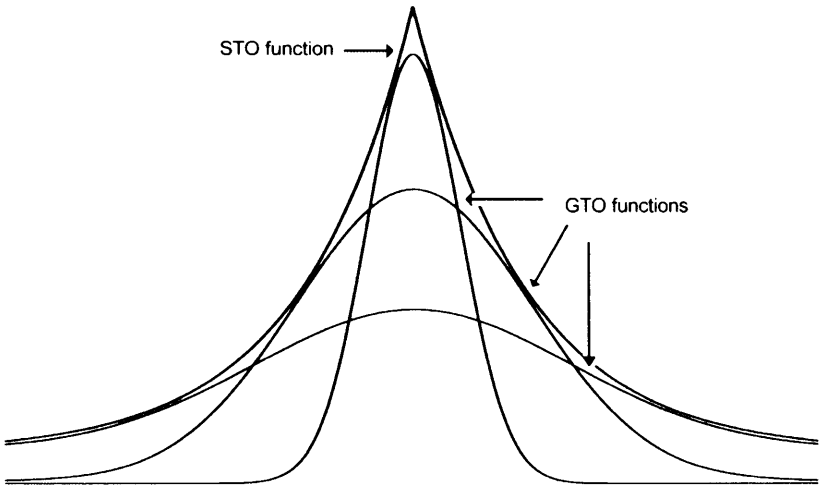

Figure 2.1: Approximating an STO with several GTOs

to sidestep this problem with GTOs is to linearly combine a number of GTOs to mimic STO behaviour (see figure 2.1). The combination of GTOs is called a contracted Gaussian function (CGF) and it is said to be made up of primitive Gaussian functions (PGF).

2.2.4 Basis Sets and Nomenclature

I have shown above the form of the basis functions which make up a basis set. This next section will deal with how many basis functions to combine and what quality of basis set is obtained by different combinations of basis functions.

The simplest basis set consists of one STO or one CGF per filled AO (i.e. per electron). One such minimal basis set is the STO-3G set. The notation defines the basis set as consisting of an STO mimic of a single CGF comprising three PGFs to describe the AO, i.e. the example shown in figure 2.1. To describe molecules a more complex basis set is needed for each atom; one function, be it an STO or a CGF, is not sufficient to describe the electron density distribution in a molecule, and so basis sets which put two or more functions on each atom are much more commonly used. 6-31G is a commonly used basis set which breaks down as follows: each core orbital is described by a single CGF consisting of six PGFs and each valence orbital is described by two CGFs, one with a single PGF component and the other with three PGFs. These basis sets are particularly popular for organic molecules and are named Pople basis sets after their creator; other Pople basis sets

commonly used are 3-21G, 4-31G, 4-22G, 6-21G, 6-311G and 7-41G; this notation is used in the *Gaussian* programs, see later. *ADF* (see later) implements basis sets with the more expensive STO functions and uses the following notation: double ζ, triple ζ, quadruple ζ (DZ, TZ, QZ) etc according to how many STOs they contain. Doubling/tripling etc causes the computational cost of DZ $\rightarrow$ QZ molecular calculations to increase, to unmanageable levels if studying a large complex and/or one containing heavy atoms. To get around this problem the basis set can be 'split'. In a molecule, the valence electrons are involved in bonding and reactions, and the core electrons are largely unaltered (the extent to which they are involved varies between atoms and complexes). A split valence basis set models the core electrons with a single function and only uses the higher quality double-, triple- etc for valence electrons (VDZ, VTZ...), in the same way that 6-31G uses one CGF for the core electrons and two CGFs for each valence e . Like DZ, VDZ is a significant improvement over the minimum basis set but it is more efficient that the full DZ basis set. This kind of basis set is particularly useful for heavy elements which have a large number of chemically inactive core electrons.

Chemical bonds are not generally isotropic. To account for potentially asymmetric electron density around an H atom in a molecule we must use more than a spherically symmetric 1*s* AO, typically we add *p* functions to H (or He). Similarly, to describe anisotropic interactions on heavier atoms *d* functions are added to the *p* block, *f* functions to the *d* block etc. These polarisation functions, so called because they allow the wavefunction to change shape, are notated by 'P' in the ADF scheme (DZP, VTZP etc, multiple polarisation functions added are denoted by e.g. DZ2P, QZ4P) and by '*' in the Gaussian scheme (a single asterisk means that a set of *d* primitives have been added to atoms other than H, two asterisks mean that a set of *p* primitives have been added to H as well).

The final augmentation to the minimal basis set is the addition of diffuse functions, mainly used in anions or for describing interactions at large distances, or for TD-DFT applications, as they enhance the description of the wavefunction far from the nucleus. Diffuse functions are notated with a '+' sign in both schemes, e.g TZ2P+, 7-41G**++ (to describe diffuse functions on just atoms heavier than H (first +) as well as on H (second +)).

2.2.5 Effective Core Potentials and the Frozen Core Approximation

A step further than splitting the basis set into valence and core electrons is the use of either Effective Core Potentials (ECPs, or pseudopotentials) or the frozen core approximation. Both methods reduce the computational cost of a calculation by replacing the individual core electrons of specified atoms with functions that describe the core electrons as a whole.

ECPs

Effective core potentials are a useful means of replacing the core electrons in a calculation with an effective potential, thereby eliminating the need for the core basis functions. There are four main steps to designing an ECP. First a high quality all-electron wave function is generated for the atom; this is typically a Hartree-Fock (or Relativistic Hartree-Fock, see later) calculation. Next the valence orbitals are replaced by a set of nodeless pseudo-orbitals; this is done to rid the basis set of the valence electrons' core nodes, e.g. uranium's five 6*s* core radial nodes. The next step is to replace the core electrons with a potential that enables the Schrödinger (or Dirac, see later) equation to produce valence orbitals that match the pseudo-orbitals described above. The final step requires the fitting of this numerical potential to a suitable set of analytical functions, often GTOs:

$$U_{ECP}(r) = \sum_i a_i r^{n_i} e^{-\alpha_i r^2} \tag{2.33}$$

a_i, n_i and α_i depend on angular momentum, typically between two and seven GTOs are used in the fit; more GTOs improve the result but increase the computational cost. The size of the core can vary, 'small core' and 'large core' ECP basis sets are available for many atoms and much comparison of the two has been carried out.[58,64,70,71] Typically a large core basis set will contain all except the valence electrons (e.g. 1*s*, 2*s*, 2*p*, 3*s*, 3*p*, 3*d*, 4*s*, 4*p*, 4*d*, and 4*f*, 5*s*, 5*p*, 5*d*, 6*s* and 6*p* = 86 electrons in the core and only the 5*f* = 3 in the valence for U^{3+}), while the small core approach leaves the valence and the 'shell beneath' the valence to be treated explicitly (e.g. 1*s*, 2*s*, 2*p*, 3*s*, 3*p*, 3*d*, 4*s*, 4*p*, 4*d*, and 4*f*, 5*s*, 5*p* and 5*d* = 78 electrons in the core and 6*s*, 6*p*, and 5*f* = 11 in the valence for U^{3+}); smaller core calculations are found to be considerably more accurate (see refs mentioned above).

The Frozen Core

A second approach is to use the frozen core approximation. Like the ECP approach, the frozen core approximation starts with a high quality all-electron calculation. The core orbitals are considered first and are replaced by a linear combination of fixed functions which solve the all-electron calculation in this region. Next the valence orbitals are considered and core-valence orthogonality is ensured. So in the frozen core approximation the lowest-lying molecular orbitals (occupied by the inner-shell electrons) are constrained to remain doubly-occupied in all configurations. The frozen core for Li – Ne typically consists of the $1s$ atomic orbital, while that for atoms Na – Ar consists of the atomic orbitals $1s$, $2s$, & $2p$; the frozen molecular orbitals are primarily these inner-shell atomic orbitals (or linear combinations thereof). Larger atoms can take a variety of frozen cores, the small core ECP mentioned above is similar to U with a $5d$ frozen core, while the large core is equivalent to U with a $6p$ core.

A justification for this approximation is that since the inner-shell electrons of an atom are less sensitive to their environment than are the valence electrons, the error introduced by freezing the core orbitals is nearly constant for molecules containing the same types of atoms. In fact, it is sometimes recommended that one employ the frozen core approximation as a general rule because most of the basis sets commonly used in quantum chemical calculations do not provide sufficient flexibility in the core region to accurately describe the correlation of the core electrons.

The frozen core approximation is often preferred over the use of ECPs because it is in essence an all-electron calculation. Instead of approximately mimicking the effects of the core orbitals on the valence shells (as ECPs do), the frozen core approximation is only less accurate than an all-electron calculation by the amount that the core orbitals *change* on formation of a chemical bond, i.e. a negligible amount.

2.3 Relativity

As mentioned in chapter 1, relativity is an important factor in calculations involving the lanthanides and actinides; anything containing atoms heavier than caesium ($Z = 55$) will have considerable relativistic effects to consider, and for high accuracy relativity must

be included for the atoms heavier than krypton ($Z = 36$). Relativity is not normally so important when considering the chemistry of the top 4 rows of the periodic table (H to Kr) unless extremely high accuracy is required.

Relativistic effects can be considered as anything arising from the fact that c (*speed of light*) = 137.0359 atomic units (au) as compared to $c = \infty$, at which limit relativity 'disappears'. As c approaches ∞, the Dirac equation (see later), which can be used to describe relativistic effects, reduces to the familiar Schrödinger equation.

One of the consequences of relativity is that mass increases with velocity. This increase is only noticeable if an object is moving at an appreciable percentage of the speed of light, as shown by the equation for relativistic mass increase[72]

$$m = m_0 \left[\sqrt{1 - \frac{v^2}{c^2}} \right]^{-1}. \tag{2.34}$$

The energy of a $1s$ electron in a hydrogenic system is $Z^2/2$, classically equal to -T (T = kinetic energy) according to the virial theorem, E = -T = $1/2\,V$. The classically calculated velocity of a $1s$ electron is Z, and $m = 1$ (both in au); thus remembering that $c \sim 137au$, one sees that relativistic effects cannot be neglected for the core electrons of heavy nuclei. Because of the high velocities achieved by the $1s$ electrons of heavy nuclei, these electrons have a greater effective mass according to the relativistic mass equation, 2.34. This leads to a contraction of the $1s$ orbitals (by the same factor which the mass increases by), which in turn implies a contraction of the higher s orbitals. The nucleus of the atom is more effectively shielded by contracted s orbitals, and so an additional effect of relativity is that the higher l number orbitals expand. The net effect of this on the p orbitals is negligible, but d and f orbitals are certainly more diffuse than they would be in the fictitious non-relativistic case, particularly so in the actinides.

Relativity is not accounted for by the Schrödinger equation, and so to perform a quantum mechanics calculation on a heavy atom requires some additional description of its wavefunction. This can be achieved in a variety of ways. Relativistic effects are normally included in heavy element calculations by one of two commonly used approaches: the use of a fully relativistic frozen core combined with a quasi-relativistic treatment of the

valence orbitals, and an approach based on relativistic effective core potentials (RECPs). Furthermore there are two popularly used quasi-relativistic methods, the first based on the Pauli Hamiltonian[73] and a second more recently developed zero-order regular approximation (ZORA).[74–77] Both of these methods also decrease the computational effort of heavy metal calculations.

2.3.1 Relativistic ECPs

In addition to replacing the core, ECPs may be used to represent relativistic effects, which are largely confined to the core. Relativistic ECPs (RECPs) are constructed as described in section 2.2.5 with an initial relativistic Dirac-Hartree-Fock calculation and a further subsequent Dirac calculation to determine the valence electron potential.

2.3.2 Quasi-Relativistic methods

The Dirac equation

The central theme in relativity is that the speed of light, c, is constant in all inertial frames, that is to say all coordinate systems which move with respect to each other. When one considers that all physical laws should be identical in such frames, the result is that time and space coordinates become equivalent. Therefore a relativistic description of a particle needs four coordinates to fully describe it, three space and one time coordinate.[72] To achieve all four coordinates in the same units, time is often multiplied by c (ms^{-1}).

Changes between different coordinate systems are described by a *Lorentz Transformation*, which may mix space and time coordinates. The previous requirement that physical laws should be identical in all coordinate systems is equivalent to saying that equations describing the physics must be invariant to a Lorentz transformation.

Consider the time-dependent Schrödinger equation:

$$\left[-\frac{1}{2m}\left(\frac{\partial^2}{\partial x^2}+\frac{\partial^2}{\partial y^2}+\frac{\partial^2}{\partial z^2}\right)V\right]\Psi = i\frac{\partial\Psi}{\partial t} \tag{2.35}$$

The partial derivatives of the space coordinates are second order, while the time coordinates are only first order; this is clearly not Lorentz invariant. This leads us to conclude that the fundamental structure of the Schrödinger equation is not relativistically correct.

For a free electron Dirac proposed an alternative to the time-dependent Schrödinger

equation:

$$\left[c\alpha \cdot p + \beta mc^2\right] \Psi = i\frac{\partial \Psi}{\partial t} \tag{2.36}$$

where α and β are 4×4 matrices. α is written in terms of the three Pauli 2×2 spin matrices σ:

$$\sigma_x = \begin{pmatrix} 0 & 1 \\ 1 & 0 \end{pmatrix} \quad \sigma_y = \begin{pmatrix} 0 & -i \\ -i & 0 \end{pmatrix} \quad \sigma_z = \begin{pmatrix} 1 & 0 \\ 0 & -1 \end{pmatrix} \quad \alpha_{x,y,z} = \begin{pmatrix} 0 & \sigma_{x,y,z} \\ \sigma_{x,y,z} & 1 \end{pmatrix} \tag{2.37}$$

and β is written in terms of a 2×2 unit matrix I:

$$I = \begin{pmatrix} 1 & 0 \\ 0 & 1 \end{pmatrix} \quad \beta = \begin{pmatrix} I & 0 \\ 0 & I \end{pmatrix} \tag{2.38}$$

The Dirac equation is of the same order in all variables since the momentum operator $p\ (= -i\nabla)$ involves a first order differentiation with respect to the space variables. The free electron rest energy in the Dirac equation (see eq. 2.36) is mc^2, = 0.511MeV. This situation is defined as zero in the non-relativistic case; the zero point of the energy scale is therefore shifted by 0.511 MeV, a large amount. The two energy scales can be aligned by subtracting the electron rest energy. This is achieved by replacing β by β'.

$$\beta' = \begin{pmatrix} 0 & 0 \\ 0 & -2I \end{pmatrix} \tag{2.39}$$

The Dirac equation (eq. 2.36) satisfies the requirement of special relativity in connection with quantum behaviour of the electron. Special relativity considers only systems which move with a constant velocity with respect to each other, this is not a valid model for movement of an electron around a nucleus.

Relativistic treatment of accelerated systems is described by general relativity. The *nuclei/e* or *e /e* gravitational interaction is negligible compared with the electrostatic interaction (a consistent theory describing the quantum aspects of gravitation has not yet been developed).

The Dirac equation is four-dimensional so the relativistic wavefunction contains four

components, normally written as:

$$\Psi = \begin{pmatrix} \Psi_{L\alpha} \\ \Psi_{L\beta} \\ \Psi_{S\alpha} \\ \Psi_{S\beta} \end{pmatrix} \tag{2.40}$$

where Ψ_L are the large components, Ψ_S the small components, and α, β the spins. As $c \to \infty$, for the electrons the large component reduces to solutions to the Schrödinger equation and the small component disappears, and for the positrons the small component reduces to solutions to the Schrödinger equation and the large component disappears. Therefore the small component of the electronic wavefunction corresponds to coupling with the positron states (see also figure 2.2).

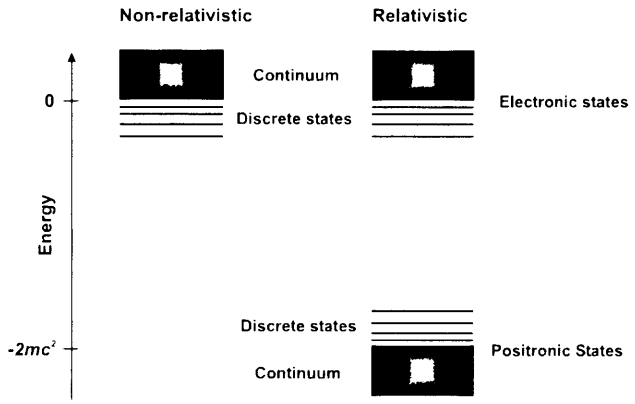

Figure 2.2: Non-relativistic and Relativistic solutions to the Dirac equation

Relating the Dirac and Schrödinger equations

In electric and magnetic fields the Dirac equation is modified to:

$$\left[c\boldsymbol{\alpha} \cdot \boldsymbol{\pi} + \beta' mc^2 + V\right] \Psi = i\frac{\partial \Psi}{\partial t} \tag{2.41}$$

V is the electrostatic potential, and the generalized momentum operator $\boldsymbol{\pi}$ includes the

vector potential $\boldsymbol{A}$ associated with the magnetic field $\boldsymbol{B}$ ($\nabla\times$ is the curl operator).

$$\pi = p + A. \qquad B = \nabla \times A \tag{2.42}$$

The time-independent Dirac equation can be written:

$$\left[c\alpha\cdot\pi + (\beta' mc^2 + V)\right]\Psi = i\frac{\partial\Psi}{\partial t} \tag{2.43}$$

α and β are block matrices in terms of σ and i so eq. 2.43 can be factored out into two further equations:

$$\begin{aligned} c(\sigma\cdot\pi)\Psi_S + V\Psi_L &= E\Psi_L \\ c(\sigma\cdot\pi)\Psi_L + (-2mc^2 + V)\Psi_S &= E\Psi_S) \end{aligned} \tag{2.44}$$

Solving the equation in Ψ_S:

$$\longrightarrow \quad \Psi_S = \left(E + 2mc^2 - V\right)^{-1} c(\sigma\cdot\pi)\Psi_L \tag{2.45}$$

Factorising the E^{-1} term you can get

$$\longrightarrow \quad \left(E + 2mc^2 - V\right)^{-1} = \left(2mc^2\right)\left(1 + \frac{E-V}{2mc^2}\right)^{-1} = \left(2mc^2\right)^{-1}\mathbf{K} \tag{2.46}$$

Rewrite eq. 2.45 as

$$\longrightarrow \quad \Psi_S = \mathbf{K}\frac{\sigma\cdot\pi}{2mc}\Psi_L \tag{2.47}$$

Substitute (2.47) into (2.44) and rewrite the term in Ψ_L:

$$\left[\frac{1}{2m}(\sigma\cdot\pi)\mathbf{K}(\sigma\cdot\pi) + (-E+V)\right]\Psi_L = 0 \tag{2.48}$$

In the non-relativistic limit ($c \longrightarrow \infty$), the $\mathbf{K}$ factor is 1, so the first term is $(\sigma\pi)(\sigma\pi)$.

Using vector identities this can be rewritten as:

$$\left[\frac{1}{2m}\left(\pi\cdot\pi+i\sigma\cdot(\pi\times\pi)\right)+V\right]\Psi_L=E\Psi_L \tag{2.49}$$

More vector manipulation using the identity $\pi = p + A$ and also $p = -i\nabla$ leads to:

$$\left[\frac{\pi^2}{2m}+V+\frac{\sigma\cdot B}{2m}\right]\Psi_L=E\Psi_L \tag{2.50}$$

Except for the $\sigma\cdot B$ term (the Zeeman interaction) this is exactly the Schrödinger equation; the former term relates to the interaction of an external magnetic field with the intrinsic magnetic moment associated with an electron, i.e. the electron spin.

In the non-relativistic limit the small component of the wavefunction is $\frac{\sigma\cdot\pi}{2mc}\Psi_L$ (see eq. 2.47 when K=1). For a hydrogenic wavefunction ($\Psi_L\sim e^{-Zr}$) this gives $\Psi_S\sim\frac{Z}{2c}\Psi_L$. Comparing a hydrogen atom with a uranium atom we can see that the small component, i.e. the relativistic correction, accounts for 0.4% of the total wavefunction and 10^{-3}% of the electron density of a H $1s$ electron, but 33% of the total wavefunction and 10% of the electron density of a U $1s$ electron, a significant quantity[†].

The Pauli equation

Remember in the non-relativistic limit, the K factor is 1; thus by expanding the K factor relativistic corrections can be found...

$$K=\left(1+\frac{E-V}{2mc^2}\right)^{-1}\approx 1-\frac{E-V}{2mc^2}+\cdots \tag{2.51}$$

This is only valid if $EV << 2mc^2$, although all atoms have a region close to the nucleus where this is not true since $V\longrightarrow-\infty$ as $r\longrightarrow 0$. By inserting (2.51) into (2.48) and rearranging then renormalizing, the Pauli equation is achieved:

$$\left[\frac{\pi^2}{2m}+V-\frac{\pi^4}{8m^3c^2}+\frac{Zs\cdot L}{2m^2c^2r^3}+\frac{Z\pi\delta(r)}{2m^2c^2}\right]\Psi_L=E\Psi_L \tag{2.52}$$

The first two terms of this equation are the non-relativistic terms, the K.E. and P.E.

[†]This elegant calculation, presented by Jensen[72] must be approached cautiously as it uses non-relativistic limit approximations to consider relativity.

operators. The term with π^4 is the mass velocity correction which is due to the (relativistic) dependence of the electron mass on its velocity. A spin orbit term (fourth term) corresponds to an interaction of the intrinsic magnetic moment (spin) with the magnetic field generated by the movement of the electron, and the final term is known as the Darwin correction; it can be interpreted as the electron making a high frequency oscillation around its mean position.

The Zeroth-Order Regular Approximation (ZORA)

The Pauli Hamiltonian contains the first-order relativistic correction terms. It presents a fundamental problem as the expression is not bound from below, and as a result diverges near the nucleus. To use the Pauli equation to include relativity into a basis set, it is essential that the valence basis is limited to avoid a variational collapse. Indeed it is sometimes found counter-intuitively that Pauli relativistic calculations give worse results when a larger basis set is applied, or when a smaller frozen core is used. To relieve this problem the expression can be partitioned:

$$(E - 2mc^2 - V)^{-1} = (2mc^2 - V)^{-1}\left(1 + \frac{E}{2mc^2 - V}\right)^{-1} = (2mc^2 - V)^{-1} K' \tag{2.53}$$

We have already mentioned that the K expansion only works when $EV << 2mc^2$, and near the nucleus this is not true: the expansion diverges. In contrast to K in equation 2.46, using K' above gives $E/(2mc^2 - V)$, which $<< 1$ so there will be no divergence near the nucleus when we expand K' and insert this new expression into the large component wavefunction, which on rearrangement and renormalization now gives:

$$\left[\pi \frac{c^2}{2m^2c^2 - V}\pi + \left(\frac{c^2}{2m^2c^2 - V}\right)^2 \frac{2Zs \cdot L}{r^3}\right]\Psi_L = E\Psi_L \tag{2.54}$$

the ZORA equation. Only the zeroth order terms of this expression are kept and so a bound expression that can be easily computed and includes relativistic effects (via the Dirac equation which is key to the derivation) is obtained. Thus the above-mentioned problems with the Pauli equation are eliminated and basis set saturation within the available computational resources can be reached. For this reason the ZORA method is usually found to give more accurate results.

2.4 Computational Methods

I have used two codes for the calculations in this thesis, Amsterdam Density Functional[78 81] (ADF) and Gaussian 03[82] (G03).

2.4.1 Amsterdam Density Functional

The ADF program has been being developed for over thirty years with the aim of exploiting the computational advantages of DFT. Currently available functions of ADF include the computation of energy minima, transition states, reaction paths and harmonic frequencies. Solvation and electric field effects can also be accounted for and as such allow the further computation of NMR shifts, ESR, and various response properties using the time-dependent density functional theory (TD-DFT): excitation energies, frequency-dependent (hyper) polarisabilities, Raman intensities and dispersion coefficients. Numerical precision is controlled by a flexible numerical integration scheme for the evaluation of integrals, QM/MM and linear scaling techniques are available for the treatment of very large systems, and parallelisation speeds up the execution on multi-CPU systems. ADF supports a wide variety of XC functionals, within both the LDA and GGA, and more recently meta-GGA and hybrid density functionals have been added.

ADF uses Slater type orbitals in its basis sets (enabled by the numerical integration functionality mentioned above), cuts computational expense by employing the frozen core approximation, and includes relativity with the ZORA.

Analysis carried out in ADF for this thesis includes geometry optimizations, frequency calculations, Mulliken charge, population, and overlap population analysis; Hirshfeld and Voronoi charge analysis, the Bond Energy Decomposition scheme and Mayer bond orders; within the TD-DFT package of ADF I have calculated Excitation energies and Oscillator strengths (described previously in section 2.1.2).

2.4.2 Gaussian 03

G03 represents further development of the Gaussian 70 → Gaussian 98 systems and is a connected system of programs for performing a variety of calculations including molecular structures and energies, energies and structures of transition states, vibrational frequencies, IR and Raman spectra, bond and reaction energies, NMR shielding and magnetic suscepti-

bilities and many more. G03 is a much more comprehensive package than ADF and allows energy and other calculations to be performed in a number of different methods. As well as DFT used here, G03 also performs, among others: Hartree-Fock, Møller-Plesset, CISD, QCISD, CCSD, CASSCF and ONIOM calculations. G03 was used for comparison with ADF results in chapters 4 and 5; and for the main geometry optimisations on the complexes in chapter 5 (subsequent single point calculations in ADF completed the analysis for this family of molecules). The analysis methods used include geometry optimisation as mentioned above, Natural charge and population analysis and excitation energies and oscillator strengths from G03 TD-DFT calculations. Unlike ADF, G03 uses Gaussian type orbitals, RECPs to include relativity and increase the efficiency of the calculations and implements analytic gradients in the calculation of first and second derivatives. There are numerous other calculational differences between the two codes, I have mentioned the relevant ones below.

2.4.3 Computational Utilities

This section describes the utilities (e.g. geometry optimization, frequency calculation, charge analysis) used in this thesis.

Geometry Optimizations and Frequency Calculations

I have carried out geometry optimisations using both Cartesian and Z-matrix coordinates; an initial geometry is input, an SCF calculation is carried out and then the first derivatives of the energy with respect to nuclear displacements are calculated. These gradients are used to identify stationary points on the energy surface. ADF employs a Newton-type iterative proceedure[83 85] via the BFGS algorithm;[86 89] it uses the second derivative matrix (the *Hessian* matrix) for computing changes in the geometry so as to make the gradients vanish. The Hessian itself is initialized (e.g. based on a force field) and updated in the process of optimization.

The default optimization algorithm in G03 is the *Berny algorithm* developed by Bernhard Schlegel.[90] This algorithm uses forces acting on the atoms of a given structure together with the Hessian to predict energetically favourable structures and thus optimize the molecular structure towards the next local minimum on the potential energy surface. As explicit calculation of the second derivative matrix is quite costly, the Berny algorithm

constructs an approximate Hessian at the beginning of the optimization procedure through application of a simple valence force field, and then uses the energies and first derivatives calculated along the optimization pathway to update this approximate Hessian matrix. Often it is sufficient to calculate the Hessian matrix explicitly once at the beginning of the calculation and then use the standard updating scheme of the Berny algorithm.

Frequencies are calculated in ADF by computing second derivatives of the energy with respect to nuclear displacements in both directions along all three Cartesian axes. The second derivatives are calculated numerically from the first derivatives and a full SCF calculation is carried out on each displacement, so frequency calculations in ADF are time consuming, although ADF only displaces symmetry unique atoms to cut computational effort (similarly symmetry is made use of to reduce cost in all ADF calculations).

Unlike in ADF, frequency calculations in G03 are done by analytical computation of the second derivative of the energy with respect to nuclear displacements; numerical second derivatives can be called if desired but are not the default.

Mulliken Charge, Population and Overlap Population analysis

The i^{th} MO (ψ_i^{KS}) can be occupied by 0, 1 or 2 electrons (in the spin restricted case, in spin unrestricted calculations each MO has an α and β component, each of which can be occupied by 0 or 1 electron) and the occupation number, n_i, is defined as:

$$\begin{aligned} n_i &= n_i \int \rho_i(r)\, dr = \sum_{A,B}^{AO} n_i\, c_{iA}\, c_{iB} \int \phi_A^* \phi_B\, dr \\ &= \sum_{A,B}^{AO} n_i\, c_{iA}\, c_{iB}\, S_{AB} \\ &= n_i c_{iA}^2 + n_i c_{iB}^2 + 2 \sum_{A \neq B}^{AO} n_i\, c_{iA}\, c_{iB}\, S_{AB} \end{aligned} \tag{2.55}$$

By using the above equations, the total occupation of the i^{th} MO can be divided into each atom's partial occupation number: occupation on A = $n_i c_{iA}^2$, occupation on B = $n_i c_{iB}^2$, and the overlap population between the two is $\sum_{A \neq B}^{AO} n_i c_{iA} c_{iB} S_{AB}$; large positive overlap populations between basis functions on different atoms are an indication of a chemical bond.

To get the total population for each atom in a molecule, in addition to summing the atomic populations from each MO, half of the overlap population in each MO is attributed to the atom, so the gross population of atom A is defined as:

$$p_A = \sum_i n_i c_{iA}^2 + \frac{1}{2} \sum_{A \neq B} \sum_i n_i \left(2 c_{iA} c_{iB} S_{AB}\right) \tag{2.56}$$

Mulliken charges arise from the Mulliken population analysis. They provide a means of estimating partial atomic charges from calculations. The n_i terms sum to N as do the n_{iA} terms. The charge, q_A, is then defined as the difference between the number of electrons on the isolated free atom, which is the atomic number Z_A, and the gross atom population:-

$$q_A = Z_A - n_{iA} \tag{2.57}$$

There are a number of common problems associated with using this approach; Mulliken populations can give unphysical negative values which are sometimes quite significant, furthermore Mulliken analysis is very basis set dependent so Mulliken populations and charges are only really of use when comparing systems with consistent basis sets. In ADF two alternative charge analysis schemes are implemented, as described below. A further method, also described below, is Natural population/charge analysis, as used in Gaussian 03.

Voronoi and Hirshfeld Charge analysis

ADF implements the Voronoi deformation density[91 93] (VDD) and the Hirshfeld scheme[94,95] for atomic charge analysis. The VDD method partitions the density into cells, the cell on atom A is the region of space closer to cell A than to any other atom. The VDD charge of an atom is a measure of the difference between how much charge the atomic Voronoi cell contains before and after the converged SCF is achieved and is therefore a measure of charge redistribution due to chemical bonding.

The Hirshfeld charge on an atom is defined as the integral of the SCF charge density weighted by the relative contribution (in each point in space) of the initial unperturbed charge density of an atom compared with the density of a pro-molecule, a superposition

of the initial unperturbed atomic densities.

$$Q_A^{Hirshfeld} = Z_A \int \rho(r) \frac{\rho_A(r)}{\sum_B \rho_B(r)} dr \tag{2.58}$$

This is described by G. te Velde *et al* as *'picking from the SCF density the parts that "belong" (according to the unperturbed densities) to the atom at hand'*.[79]

The VDD and Hirshfeld charges are reported as being similar to each other numerically, chemically significant, and more reliable/less prone to basis set dependency than Mulliken charges[78,79,93] and are recommended over the latter.

Natural Charges

Developed by Weinhold and coworkers[96,102] in the 80s, Natural population analysis was proposed as an alternative to the unreliable Mulliken method. It is based on the construction of a set of *Natural Atomic Orbitals* (NAOs) for a given molecule in an arbitrary atomic orbital basis set. The *Natural Population Analysis* (NPA) represents the occupancies of these NAOs in the system of interest.

In an initial step, orbitals which are associated almost entirely with a single atom, e.g. core orbitals and lone pairs, are localized, → NAOs. Next, orbitals involving bonding or antibonding between pairs of atoms are localized by using only the basis set AOs of those atoms. Finally the remaining Rydberg-like orbitals are identified, and all orbitals are made orthogonal to one another.[103] The result of this is that apart from very small contributions from other AOs to ensure orthogonality, all NAOs and Rydberg orbitals are described using the basis-set AOs of a single atom, and all NBOs are described using the basis-set AOs of two atoms (thus when delocalisation effects require consideration this method is not sufficient). Thus Natural analysis provides an orbital picture which is as close as possible to a classical Lewis structure for a molecule. Natural charges are obtained from the NAOs by way of the NPA.

Mayer Bond Order

The Mayer Bond Order (MBO)[104] is related strongly to Mulliken populations, and is calculated from the former along with the density matrix (containing all the orbital coefficients); it can be called as a subroutine in an ADF calculation. MBOs have similar basis set prob-

lems to Mulliken analysis, but just as with the Mulliken analysis, MBOs can be useful in comparing families of molecules calculated with the same basis sets.

Energy Decomposition Scheme

The Energy Decomposition scheme implemented in ADF was used to analyse the bonding in chapter 3. ADF defines the molecular interaction energy as the energy difference between the molecular fragments (e.g. M^{3-} and L_3^{3-} as in chapter 6) in their final positions and at infinite separation. The fragments are placed at their final positions within the molecule. At this point there is an electrostatic interaction between them, comprising the nucleus/nucleus, nucleus/electron and electron/electron Coulombic interactions. This electrostatic interaction is computed from the unperturbed and superimposed charge densities of the separate fragments. Next it is ensured that the overall molecular wavefunction satisfies the Pauli principle. This is done by requiring that the one electron orbitals of the combined fragments form a correct single determinantal wavefunction. It is extremely unlikely, however, that this will be the case for the fragment orbitals when the fragments are simply placed at their positions within the molecule because the orbitals on the different fragments will not be orthogonal to one another. Thus the next step is to orthogonalise the occupied fragment orbitals to obtain a correct single determinantal, antisymmetrised molecular wavefunction. This will result in a change in the molecular charge density, and the accompanying energy change is known as the Pauli, or exchange, repulsion. The final part of the process is to allow the fragment orbitals to relax to self consistency, and this interaction energy between the orbitals of the various fragments is defined as the electronic (or orbital) interaction within ADF.[105,106]

Solvent effects

Solvent effects have been incorporated by ideal screening models which mimic the effects of solvent by building a cavity around the solute and placing electrical charges on the cavity walls. The cavity is built by placing spheres around the atomic nuclei,[107] and then discarding the overlapping parts of the spheres. The surface of the cavity is smoothed, a process which can be performed in a number of ways. In this work the Solvent Accessible Surface (SAS in G03 or asurf in ADF) and the Solvent Excluding Surface (SES in G03 or esurf in ADF) have been used.[108] The principal difference between the SAS and SES is

that the size of the cavity is significantly larger for SAS, see figure 2.3.

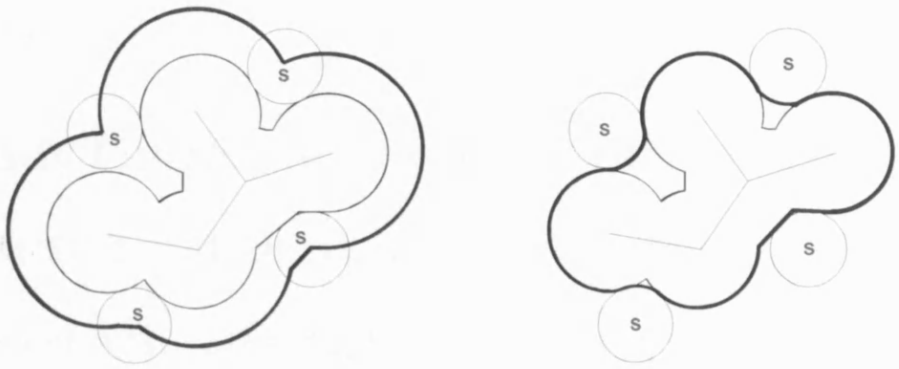

(a) **sas** (b) **ses**

Figure 2.3: Solvent Accessible Surface (SAS/asurf) and Solvent Excluding Surface (SES/esurf)

Each charge is placed on a small triangular surface (tessera) which can be of variable size. The magnitudes of the charges are determined by solving variations of the Poisson-Boltzmann equation. This equation does not have an analytic solution for complicated geometries and so the tesserae are needed to form a triangular grid which approximates the smooth surface, enabling a numerical solution.

Chapter 3

Density Functional Theory investigation of the geometric and electronic structures of $[UO_2(H_2O)_{a-x}(OH)_x]^{(2-x)+}$ for $x = 0 \rightarrow 5$ with a = 5, and some a = 3, 4

3.1 Introduction

The linear uranyl ion $[O_{yl} - U - O_{yl}]^{2+}$ features in approximately half of all known uranium complexes.[109] In complexes of uranyl, ligands coordinate in the equatorial plane (perpendicular to UO_2^{2+}); typically these equatorial ligands bond to the uranium centre through hard donor atoms such as oxygen, although the effects of such fields are generally much weaker (and with correspondingly longer U–O bond lengths) than the strongly bound O_{yl} atoms.

This chapter presents calculations on geometries, vibrational frequencies and bonding properties of the family of molecules $[UO_2(H_2O)_{a-x}(OH)_x]^{(2-x)+}$ for $x = 0 \rightarrow 5$ with a = 5, and some a = 3, 4. These targets have been chosen for three main reasons. First, some members of the series have previously received considerable experimental and theoretical attention, thus allowing the methods used in this study to be benchmarked. As part of this benchmarking exercise the performance of continuum methodologies for including solvent effects is tested as many of the experimental data for uranyl complexes such as those studied here are generated in solution. Second, it may be expected that the interactions between the equatorial ligands and the U atom will change as the essentially σ-donor water ligands are gradually replaced by hydroxide ligands, for which π-donation is also possible, thus raising interesting bonding questions. In particular, it is known that the

U-O_{yl} bond lengthens and the vibrational wavenumbers of the uranyl unit decrease as H_2O is replaced by OH^-,[2] and this work probes the origins of these changes. Finally, to the best of my knowledge there have been no systematic studies of all the targets using a consistent computational approach, and trends across the series would be best explored by such a study.

3.2 Literature Review of Mixed Water-Hydroxide Uranyl systems

While this thesis presents the first systematic study of $[UO_2(H_2O)_{5-x}(OH)_x]^{(2-x)+}$ for $x = 0 \rightarrow 5$ including some $[UO_2(H_2O)_{4-x}(OH)_x]^{(2-x)+}$ ($x = 2 \rightarrow 4$) and a singular $[UO_2(H_2O)_{3-x}(OH)_x]^{(2-x)+}$ ($x = 3$), some members of the series have been studied in the past. The dominance of the literature by two members of the family of complexes, $[UO_2(H_2O)_5]^{2+}$ and $[UO_2(OH)_4]^{2-}$, reflects the most commonly found experimental species. Below I discuss research into systems similar to the ones I am studying here. Each paper raises points which are of interest in relation to my work. There are many more references in the literature to both experimental and computational studies of water/hydroxide uranyl systems and a greater range of literature results are presented alongside my own results in the results section (section 3.4).

Generally speaking, in aqueous solution uranyl coordinates water or hydroxide ligands in the equatorial plane, and the number of each ligand depends on the pH. Five water ligands are coordinated in acidic solution,[32,33] a mixture of water and hydroxide ligands in neutral solution[3] and four or five hydroxide ligands in highly alkaline solutions.[1,2] Clark *et al*[2] have investigated the uranyl ion in high pH solution and interpret their results as a mixture of species with four and five hydroxide ligands coordinated to the uranyl ion. This was later questioned by Wahlgren *et al*[32] who performed similar experiments but concluded that only a tetra-hydroxide compound was present in alkali solution. More recent computational studies have also found the tetra-hydroxide compound to be more stable than one with five hydroxides.[1]

Hay and co-workers used Gaussian 98[110] to compare the performance of different functionals on $[AnO_2(H_2O)_5]^{2+}$ (An = U, Np, Pu).[33] The group used a 5*d* (large) core[111]

for uranium, leaving the valence orbitals to be described by a [3*s* 3*p* 2*d* 2*f*] contracted Gaussian basis; the 6-31G* basis set is used for the lighter atoms and a variety of functionals were used. This work illustrates how varying the (type of) functional affects the computational results; B3LYP was found to give the best results compared with HF-SCF, LDA, and BLYP (see table 3.1). Although the LDA gave similar quality results to the hybrid functional, the group chose to perform further analysis using B3LYP instead of the LDA as the latter is known to overestimate energetic quantities.

Complex	XC functional	r(An-O_{yl})	r(An-O_{water})	υ_{sym}(An-O_{yl})	υ_{asym}(An-O_{yl})
$UO_2(H_2O)_5]^{2+}$	HF	1.694	2.545	1091	1149
$UO_2(H_2O)_5]^{2+}$	LDA	1.778	2.423	854	945
$UO_2(H_2O)_5]^{2+}$	BLYP	1.803	2.516	787	893
$UO_2(H_2O)_5]^{2+}$	B3LYP	1.756	2.516	910	1003
$[UO_2(H_2O)_5]^{2+}$	*expt*	*1.76*,[112] *1.78*[32]	*2.41*[32,112]	*869*,[41] *870*[113]	*962*,[114] *965*[115]
$NpO_2(H_2O)_5]^{2+}$	B3LYP	1.752	2.500	854	983
$[NpO_2(H_2O)_5]^{2+}$	*expt*	*1.75*[116,117]	*2.42*[116,117]	*854*,[118] *863*[113]	*969*[114]
$PuO_2(H_2O)_5]^{2+}$	B3LYP	1.742	2.485	805	951
$[PuO_2(H_2O)_5]^{2+}$	*expt*	*1.74*[119]	*2.41*[119]	*833*,[118] *835*[113]	*962*[114]

Table 3.1: Hay *et al*'s results: Selected data for DFT optimised $[AnO_2(H_2O)_5]^{2+}$ (An = U, Np, Pu) with various functionals along with previous experimental results

A thorough treatment of symmetry was made in Hay's work and a $[UO_2(H_2O)_5]^{2+}$ structure with four water molecules perpendicular to the equatorial plane and the fifth in the plane was found to lie lowest in energy, although it was calculated to lie only 0.4 kJ mol^{-1} lower than the D_5 structure, (i.e. all water molecules orientated similarly, near perpendicular to the equatorial plane but slightly canted), and 2.4 kJ mol^{-1} lower than the D_{5h} structure (see figure 3.1). Hay *et al* conclude that r(An-O_{yl}) is well reproduced by DFT but r(An-O_{water}) is typically overestimated by *ca.* 0.1Å. Hay notes that r(An-O_{yl}) decreases from U $\rightarrow$ Pu as do υ_{sym}(An-O_{yl}) and υ_{asym}(An-O_{yl}); the data seem contradictory. Hay concludes that as a result of the actinide contraction there is less overlap between the oxygen *p* and actinide 5*f* so although the bonds are becoming shorter, they are also becoming weaker, as indicated by the vibrational frequencies.

Oda and Aoshima[120] performed DFT calculations on $[UO_2(H_2O)_5]^{2+}$, $[UO_2(H_2O)_4(OH)]^{+}$ and $[UO_2(H_2O)_3(OH)_2]^{0}$ (among other species) using Gaussian98 and the B3LYP functional with a standard 5*d* uranium RECP[111] describing the core and a [3*s* 3*p* 2*d* 2*f*]

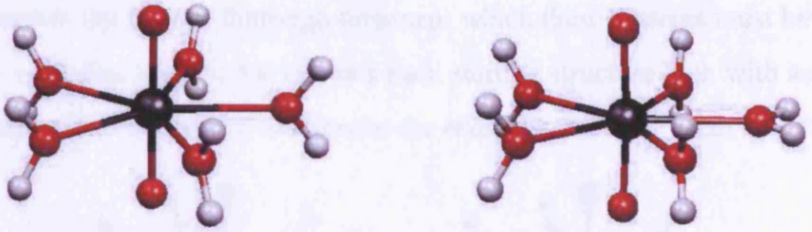

(a) D_{5h} symmetry (b) C_1 symmetry

Figure 3.1: D_{5h} and C_1 $[UO_2(H_2O)_5]^{2+}$ structures

contracted Gaussian basis for uranium's valence shells, 6-311G(*d,p*) basis sets were used for oxygen and hydrogen. Symmetry constraints were used where applicable. Table 3.2 below shows their calculated r(U–O_{yl}) and other selected data as H_2O ligands are replaced by OH^- in the complex.

Complex	r(U–O_{yl})	∠(O–U–O)	r(U–O_{water})	r(U–$O_{hydroxide}$)	v_{sym}(U–O_{yl})
$UO_2(H_2O)_5]^{2+}$	1.752	180°	2.522	-	902
$UO_2(H_2O)_4(OH)]^+$	1.781, 1.792	166.7°	2.571†, 2.583	2.155	848
$UO_2(H_2O)_3(OH)_2]^0$	1.795	178.1°	2.576‡, 2.670	2.250	831

Table 3.2: Oda *et al*'s results: Selected data for DFT optimised $[UO_2(H_2O)_{5-x}(OH)_x]^{(2-x)+}$ (x = 0, 1, 2); †H_2O next to OH^-, ‡H_2O between OH^-s, i.e. *meta-trans*, see below

The data show that as OH^- ions replace water molecules in the coordination sphere of uranyl, r(U–O_{yl}) lengthens; this result has been seen before. As discussed above, An–O becomes weaker on moving from U to Pu as shown by the vibrational data, although r(An–O_{yl}) shortens. However in Oda's work on mixed water/hydroxide systems of uranyl the vibrational data 'agree' with the bond length data in the expected manner, as r(U–O_{yl}) lengthens so v_{sym}(U–O_{yl}) decreases; both data suggest a weakening of the U–O_{yl} bond. In this work Oda *et al* also investigate the precise nature of the coordination geometry of $[UO_2(H_2O)_3(OH)_2]^0$, as there are a number of different configurations this species can take, as shown in figure 3.2.

Oda calculates the structure in figure 3.2(d) to lie lowest in energy, the so-called *meta-trans* (i.e. OH^- ions not adjacent, one pointing up and one down with respect to the equatorial plane of uranyl), although the calculated energy difference between 3.2(d) and 3.2(c) is less than 1 kJ mol^{-1}. This treatment of all combinations of H_2O and OH^-

ligands illustrates the type of thorough treatment which these systems must be subjected to; my own work (see section 3.4.1) treats each starting structure both with and without symmetry constraints in order to fully probe the energy surface.

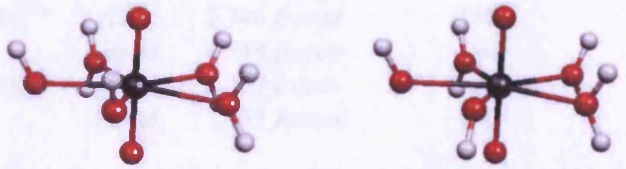

(a) ***ortho-cis*** (b) ***ortho-trans***

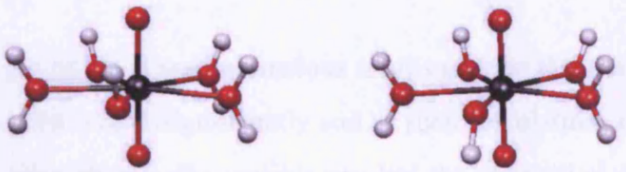

(c) ***meta-cis*** (d) ***meta-trans***

Figure 3.2: The four $[UO_2(H_2O)_3(OH)_2]^0$ starting configurations used by Oda *et al*

Spencer and co-workers[35] also applied DFT to this problem using the MAGIC[121] code (in development by the same authors). Solvent effects were included by a simple model which calculates the effect of a liquid environment on the electronic structure of the solute molecule, and so a comparative picture of gas phase and aqueous $[UO_2(H_2O)_5]^{2+}$ and $[PuO_2(H_2O)_5]^{2+}$ has been obtained. Their work uses Hay's RECPs[111] to represent the $5d$ core of each actinide; the BLYP functional was used with DZP basis sets for the light atoms, D_{5h} symmetry calculations were performed.

As table 3.3 suggests, a geometry optimisation was carried out on each actinyl ion in both gas and solvent phases; the optimised data are shown in the top part of table 3.3. Water molecules were added to these optimised actinyl ions and all coordinates were frozen except the An–O_{water} bond length, the optimised values of which are presented in the lower part of table 3.3. Comparing these values with Hay's results in table 3.1, the striking difference between the two data sets is that while r(U–O_{yl}) > r(Pu–O_{yl}) both experimentally and according to Hay, the reverse is true for Spencer's results. Furthermore Spencer calculates similar r(U–O_{yl}) in both the gas and solvent phase but a larger r(Pu–O_{yl}) in the gas phase; the same data reveal similar gas/solvent r(Pu–O_{water}) but a larger

Complex	state	r(An-O_{yl})	∠ (O–An–O)	r(An-O_{water})
UO_2^{2+}	gas	1.746 *optimised*	180°	-
	solvent	1.748 *optimised*	180°	-
PuO_2^{2+}	gas	1.767 *optimised*	180°	-
	solvent	1.757 *optimised*	180°	-
$UO_2(H_2O)_5]^{2+}$	gas	1.746 *frozen*	180°	2.550
	liquid	1.748 *frozen*	180°	2.502
$PuO_2(H_2O)_5]^{2+}$	gas	1.767 *frozen*	180°	2.522
	liquid	1.757 *frozen*	180°	2.523

Table 3.3: Spencer *et al*'s results: Selected data for DFT optimised AnO_2^{2+} and $[AnO_2(H_2O)_5]^{2+}$ (An = U, Pu) in gas and solvent phases

r(U–O_{water}) in the gas phase. These anomalous results suggest that the coordinated water molecules affect the actinyl ion significantly and as such calculations on 'frozen' AnO_2^{2+} do not necessarily yield chemically sensible results: the interaction of water molecules with actinyl MOs is significant (see my results later) and neglecting this may produce chemically-unlikely species.

A study by Schreckenbach[37] *et al* investigates $[UO_2(OH)_4]^2$ using Gaussian94[122] to apply the B3LYP functional to the problem. An initial survey of the four symmetrical configurations for this anionic complex was made; all four species were found to lie close in energy to one another, with a 6 kJ mol ^{1} separation between the most stable (*udud*, fig. 3.3(d)) and the least stable (*uuuu*, fig. 3.3(a)) suggesting that the interconversion of structures may be facile in solution.

While *uuuu* is the least stable configuration, the potential surface describing the transition from *udud* to *uuuu*, via *uudd* and *uuud* (see figures 3.3(c) and 3.3(b)), is very shallow indeed. Further to these four structures of $[UO_2(OH)_4]^{2-}$ Schreckenbach investigated some additional $[UO_2(OH)_4]^{2-}$ with the difference that the uranyl ion is bent. Five structures were found, the most stable of which showed a ∠ (O–U–O) of 128.4°, lying 76 kJ mol^{-1} higher in energy than the symmetrical *udud* structure. A maximum bond angle of 112.7° was predicted lying 81 kJ mol^{-1} above *udud*. Schreckenbach predicts these structures to be stable as they relate to local minima on the potential surface.

Whether the $[UO_2(OH)_5]^{3-}$ species exists in solution or not has been investigated by a number of groups, both experimentally[2,39] and theoretically.[1,32,39] Vallet concludes than

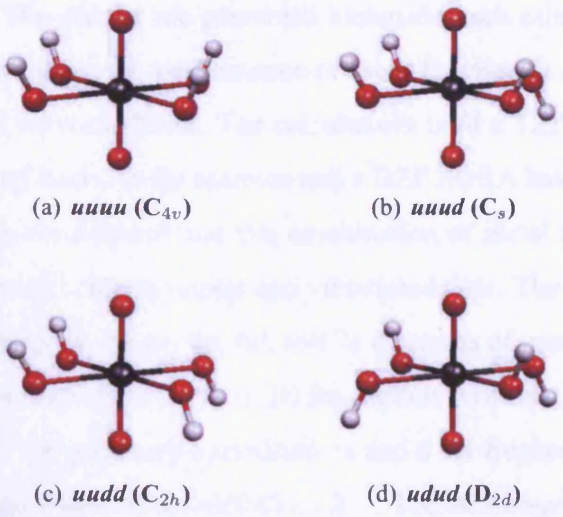

(a) ***uuuu*** (C_{4v}) (b) ***uuud*** (C_s)

(c) ***uudd*** (C_{2h}) (d) ***udud*** (D_{2d})

Figure 3.3: Four $[UO_2(OH)_4]^{2-}$ starting configurations used by Schreckenbach *et al*

a penta-hydroxide uranyl species is unlikely to exist in solution; computationally forcing this structure by use of symmetry constraints leads to U–$O_{hydroxide}$ bond lengths which do not agree well with experiment. Sonnenberg *et al*'s recently reported $[UO_2(OH)_5]^{3-}$ structure is shown in figure 3.4, in which all bar one of the hydroxides lies in the equatorial plane. They calculate this structure to be *ca.* 5 kJ mol^{-1} less stable than that reported by Vallet *et al*, in which all five OH^- ligands lie in the equatorial plane.[39]

Figure 3.4: Sonnenberg *et al*'s[1] proposed structure for $[UO_2(OH)_5]^{3-}$

3.3 Computational Details

3.3.1 ADF

I have used two functionals, BP86[123,124] and PW91,[46] to investigate these complexes in ADF; my colleague Jonas Häller performed complementary calculations using the

PBE[47,48] functional. The results are presented alongside each other as this was a collaborative project to compare the performance of these functionals on uranyl complexes both with and without solvent effects. The calculations used a TZP Zero Order Regular Approximation (ZORA) basis set for uranium and a DZP ZORA basis set for oxygen and hydrogen. Test calculations reveal that this combination of metal and ligand basis sets achieves basis set saturation for structural and vibrational data. The frozen core approximation was used, leaving the 5*f*, 6*s*, 6*p*, 6*d*, and 7*s* electrons of uranium, and the 2*s* and 2*p* electrons of oxygen (as well as the 1*s* of H) for explicit treatment. The integration grid parameter was set to 5 for geometry optimizations and 6 for frequency calculations, and the geometry convergence was set to $0.00045\,au\,\mathring{A}^{-1}$. The SCF convergence criterion was 10^{-7}. Mayer bond orders[104] were calculated from the optimized ADF electronic structure using the MAYER program.[125] Mulliken[126,127] and Hirshfeld[94,95] charge analyses were also carried out on optimized structures.

3.3.2 G03

As with ADF, three GGA functionals, BP86, PW91 (my work) and PBE (Häller's work) were used, together with the hybrid functional B3LYP[50,51] (also Häller). All atoms except uranium were assigned a 6-31G** basis set, and a (14*s* 13*p* 10*d* 8*f* 6*g*)/[10*s* 9*p* 5*d* 4*f* 3*g*] segmented valence basis set with a relativistic pseudopotential of the Stuttgart-Bonn variety[128] was employed for U. The integration grid used was pruned, with 99 radial shells and a maximum of 590 angular points per shell (i.e. the "ultrafine" grid).

3.3.3 Solvent Effects

For G03, solvent effects were accounted for by the Conductor Polarizable Continuum Model (CPCM),[129] with the United Atom Kohn Sham[130] (UAKS) formula for the atomic radii. The default values for the tesserae area and smoothing parameters (TSARE = 0.2, OFAC = 0.89) were used for all except one calculation. For Häller's $[UO_2(H_2O)_2(OH)_2]$ /G03/PBE/solvent, the CPCM parameters TSARE and OFAC had non-default values of 0.4 and 0.96 respectively due to problems with the default values. For ADF, solvent effects were accounted for using the COnductor-like Screening MOdel (COSMO),[131-133] using asurf with the following values for the atomic radii; U = 2.0 Å, O = 1.4 Å and H = 1.2 Å.

3.4 Results

3.4.1 Geometries

Overview

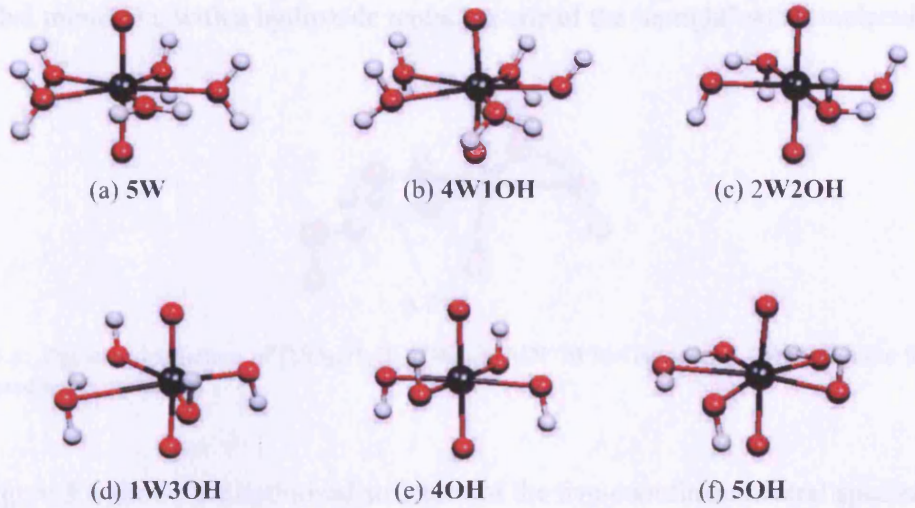

(a) **5W** (b) **4W1OH** (c) **2W2OH**

(d) **1W3OH** (e) **4OH** (f) **5OH**

Figure 3.5: Ball + stick representations of the calculated geometries for **5W**, **4W1OH**, **2W2OH**, **1W3OH**, **4OH**, and **5OH** (ADF BP86 gas phase data)

By initially considering all $[UO_2(H_2O)_{5-x}(OH)_x]^{(2-x)+}$ for $x = 0 \rightarrow 5$, geometry optimizations for each of the target molecules were carried out from a variety of starting structures including all possible *cis*/*trans* H_2O/OH^- combinations as well as different orientations for both water and hydroxide ligands, to try to ensure that global minima were achieved. All calculations were performed both with and without symmetry constraints (where symmetry was applicable). The lowest energy structures for each of the 2+, 1+, neutral, 1-, 2- and 3- complexes are shown in figure 3.5 (generated using Molekel[134,135] from ADF/BP86/Gas phase data), and structural data for my results along with Häller's are collected in tables 3.5 - 3.9, together with previous theoretical and experimental data. A discussion of the structures follows.

In $[UO_2(H_2O)_5]^{2+}$ (**5W**, figure 3.5(a)), the five water molecules are arranged in a pentagonal geometry in a plane perpendicular to the almost linear uranyl ion. Four of these water ligands are 'upright', i.e. co-planar with the uranyl axis, while the fifth is rotated by 90° from this orientation. This structure has been noted before in computa-

tional studies, although there is some disagreement as to whether it is indeed the lowest energy structure,.[33,35] In addition to Hay's study of $[UO_2(H_2O)_5]^{2+}$, Wahlgren *et al*[32] have calculated the rotational barrier for a water molecule in this complex to be 1.5 kJ mol^{-1}. $[UO_2(H_2O)_4(OH)]^+$ (**4W1OH** figure 3.5(b)) has a very similar structure to **5W** at the global minimum, with a hydroxide replacing one of the 'upright' water molecules.

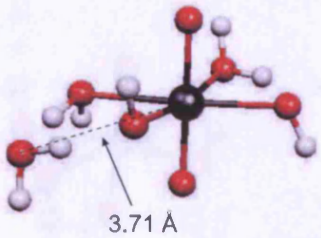

Figure 3.6: Optimised structure of $[UO_2(H_2O)_3(OH)_2]$ (ADF/BP86/Gas phase), **3W2OH**, note the non-coordinated water molecule

Figure 3.6 shows the optimised structure of the five-coordinate neutral species. Unlike in the paper by Oda *et al*[34] mentioned previously, I have carried out geometry optimisations from each starting structure shown in figure 3.2 both with and without symmetry constraints. The symmetry-restricted structures were generally higher in energy than their no-symmetry analogues. Furthermore, in the absence of symmetry restrictions, optimizations of $[UO_2(H_2O)_3(OH)_2]$, **3W2OH** led to the expulsion of one water molecule from the primary coordination sphere. Hence one water ligand was removed from the starting structures in subsequent optimizations, performed in order to locate the global minimum for **2W2OH** (see figure 3.5(c)). The non-O_{yl} ligands in **2W2OH** are in a near-square-planar arrangement around a linear uranyl unit giving the molecule C_i symmetry. The two hydroxide ligands are *trans* to one another and the hydrogens of the hydroxide ligands lie on opposite sides of the equatorial plane. Since only two of the three water ligands stay in the first sphere of coordination for **3W2OH**, and the geometry optimised structure of **3W2OH** is effectively **2W2OH** around the uranyl ion, the latter structure will be analysed further instead of the former.

In both my calculations and Häller's, species with zero, one and two OH^- ligands have two or more water molecules in the primary coordination sphere. The **4OH** and **5OH** systems have no such water molecules (see below). The complex bridging these

two behaviours, the three-hydroxide complex, lies on the border between the coordinated water and non-coordinated water cases. Having investigated a variety of species with 3 hydroxide ligands (see figures 3.7(a)-3.7(c)), the favoured system, $[UO_2(H_2O)(OH)_3]^-$ **1W3OH**, is shown in figure 3.7(b) (and also 3.5(d)), and features a comparatively long U–O_{water} bond. This species was chosen for the more rigorous analysis in the coming

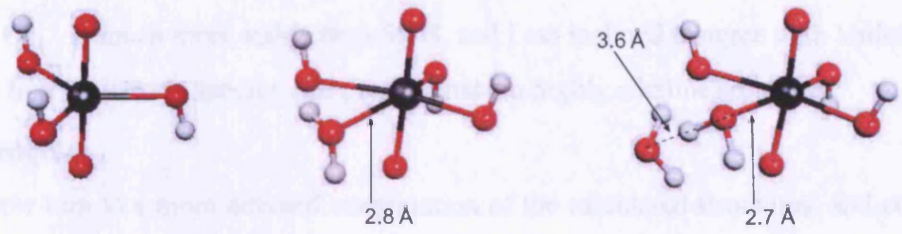

(a) **3OH** (b) **1W3OH** (c) **2W3OH**

Figure 3.7: The three $[UO_2(H_2O)_x(OH)_3]^-$ structures (ADF/BP86/Gas phase); x = 0 (a), 1(b), 2(c)

sections for a number of reasons. Firstly, in **1W3OH** the uranyl ion is 4-coordinate, as it is in the two 'neighbouring' species, **2W2OH** and **4OH**. Secondly, while in figure 3.7(c) the second water molecule is clearly dissociated, in both 3.7(b) and 3.7(c), r(U–O_{H_2O}), while long, is still short enough to suggest a chemical bond between the two, and I therefore decided that the **3OH** complex was insufficiently hydrated and not the most likely species. Since **2W3OH** and **1W3OH** are effectively the same species, the only difference being the extra H_2O molecule in the second coordination sphere of **2W3OH**, **1W3OH** was chosen as the most chemically sensible of the neutral species.

$[UO_2(OH)_4]^{2-}$ (**4OH**, figure 3.5(e)) shows similarities to **2W2OH**, having an approximately square planar arrangement of hydroxide ligands around a linear uranyl ion centre, and showing an alternating arrangement of hydrogen atoms above and below the equatorial plane. This alternating arrangement has been noted previously for the **4OH** system.[1] It was not possible to obtain a structure with four hydroxides and a water molecule bonded to the U atom, this conclusion was also reached by Vallet *et al.*[39]

The **5OH** structure presented here (figure 3.5(f)) is similar to those of Sonnenberg *et al* and Vallet *et al*, but has two H atoms out of the plane, one above and one below. Häller compared the energy of **5OH** *vs.* **4OH** plus a free OH^-; table 3.4 clearly indicates that

Species	Total Bonding Energy [kJ mol^{-1}]
$[OH]^-$	-847
$[UO_2(OH)_4]^{2-}$, **4OH**	-6787
$[UO_2(OH)_5]^{3-}$, **5OH**	-7127
ΔE (**5OH** - (**4OH** + $[OH]^-$))	507

Table 3.4: Total bonding energies of $[UO_2(OH)_5]^{3-}$ *vs.* ($[UO_2(OH)_4]^{2-}$ + $[OH]^-$) from ADF/PBE/gas phase calculations (Häller's data)

4OH + OH^- is much more stable than **5OH**, and I am inclined to agree with Vallet *et al*[39] that the four hydroxide species will predominate in highly alkaline solutions.

Bond lengths

I will now turn to a more detailed examination of the calculated structures, and compare bond length data with previous experimental and theoretical studies.

Table 3.5 shows that for all methods there is a gradual lengthening of the U–O_{yl} bond as water ligands are replaced by OH^- around the uranyl ion. Selected data from table 3.5 are plotted in figure 3.8, together with some of the previous experimental and theoretical results.

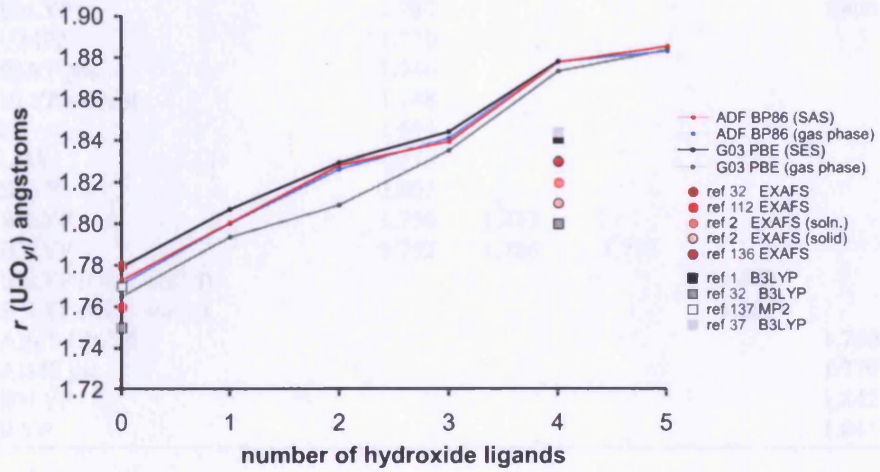

Figure 3.8: Selected calculated r(U–O_{yl}) /Å as a function of the number of coordinated OH^-, including selected previous experimental and theoretical results

The **5W** results presented here (both gas and solvent, ADF and G03, BP86 and PW91 as well as Häller's PBE results) show good agreement with recent experiment, the differences between the three most recent experimental results (refs 32, 39, 112 in table 3.5)

Code	Functional	5W	4W1OH	2W2OH	1W3OH	4OH	5OH
ADF Gas Phase	PBE	1.768	1.797	1.822	1.839	1.875	1.879
	BP86	1.771	1.800	1.826	1.841	1.878	1.883
G03 Gas Phase	PBE	1.765	1.794	1.809	1.835	1.873	1.884
	BP86	1.768	-	1.812	-	1.877	-
	PW91	1.766	-	1.810	-	1.874	-
ADF COSMO (SAS)	PBE	1.770	1.798	1.825	1.836	1.873	1.881
	BP86	1.773	1.801	1.828	1.840	1.878	1.886
	PW91	1.770	-	-	-	1.876	-
G03 CPCM (SES)	PBE	1.779	1.807	1.829	1.844	1.878	not converged
Experimental Results							
ref 32 EXAFS		1.780					
ref 39 EXAFS		1.770					
ref 40 XRD (solid)		1.710					
ref 11 XRD (soln.)		1.700					
ref 112 EXAFS		1.760					
ref 2 XRD						1.820	
ref 2 EXAFS (solid)						1.810	
ref 2 EXAFS (soln.)						1.790	
ref 136 EXAFS						1.830	
Previous Theoretical Results							
ref 32 B3LYP		1.780				1.800	
ref 137 MP2		1.770					
ref 35 BLYP gas		1.746					
ref 35 BLYP solvent		1.748					
ref 33 HF		1.694					
ref 33 LDA		1.778					
ref 33 BLYP		1.803					
ref 33 B3LYP		1.756	1.783				
ref 34 B3LYP		1.752	1.786	1.795			
ref 36 B3LYP (OH^- *ortho*)					1.800		
ref 36 B3LYP (OH^- *meta*)					1.801		
ref 39 AIMP CPCM						1.760	
ref 39 AIMP gas						1.770	
ref 37 B3LYP						1.842	
ref 1 B3LYP						1.841	1.835

Table 3.5: Calculated $r(U–O_{yl})$ /Å as a function of the number of coordinated OH , including previous experimental and theoretical results

being larger than the differences between the results reported here. The only other species for which there are experimental data is **4OH**. Table 3.5 and figure 3.8 show that this work overestimates r(U–O_{yl}) of **4OH** by *ca.* 0.06 Å compared with experiment. It is notable that other workers[1,32] have achieved better agreement with experiment for **4OH** using the B3LYP functional. Häller therefore reoptimized **4OH** using B3LYP (as implemented in Gaussian 03) and found 1.846 Å for r(U–O_{yl}) in gas phase and 1.854 Å in aqueous solution, a shortening of 0.02-0.03 Å in comparison with my G03 results. This compares well with Sonnenberg *et al*'s 1.841 Å in the gas phase.[1] It would therefore appear that the hybrid B3LYP method performs rather better than the pure density functionals for **4OH**; although as table 3.5 shows, this isn't true of the **5W** complex.

Code	Functional	**5W**	**4W1OH**	**2W2OH**	**1W3OH**
ADF Gas Phase	PBE	2.499	2.595	2.610	2.803
	BP86	2.499	2.592	2.604	2.797
G03 Gas Phase	PBE	2.474	2.562	2.583	2.735
	BP86	2.474	-	2.582	-
	PW91	2.469	-	2.576	-
ADF COSMO (SAS)	PBE	2.476	2.584	2.593	2.750
	BP86	2.475	2.586	2.591	2.744
	PW91	2.471	-	-	-
G03 CPCM (SES)	PBE	2.432	2.524	2.520	2.638
Experimental Results					
ref 32 EXAFS		2.410			
ref 39 EXAFS		2.410			
ref 40 XRD (solid)		2.450			
ref 117 XRD (soln.)		2.420			
ref 112 EXAFS		2.410			
Previous Theoretical Results					
ref 32 B3LYP		2.570			
ref 138 MP2 CPCM		2.470			
ref 138 MP2 gas		2.530			
ref 137 MP2		2.460			
ref 33 HF		2.545			
ref 33 LDA		2.423			
ref 33 BLYP		2.516			
ref 33 B3LYP		2.516			
ref 35 BLYP gas		2.550			
ref 35 BLYP solvent		2.500			
ref 34 B3LYP		2.522	2.577	2.620	
ref 36 B3LYP (OH^- *ortho*)					2.670
ref 36 B3LYP (OH^- *meta*)					2.650

Table 3.6: Calculated values for r(U–O_{water}) /Å as a function of the number of coordinated OH^-, including previous experimental and theoretical results

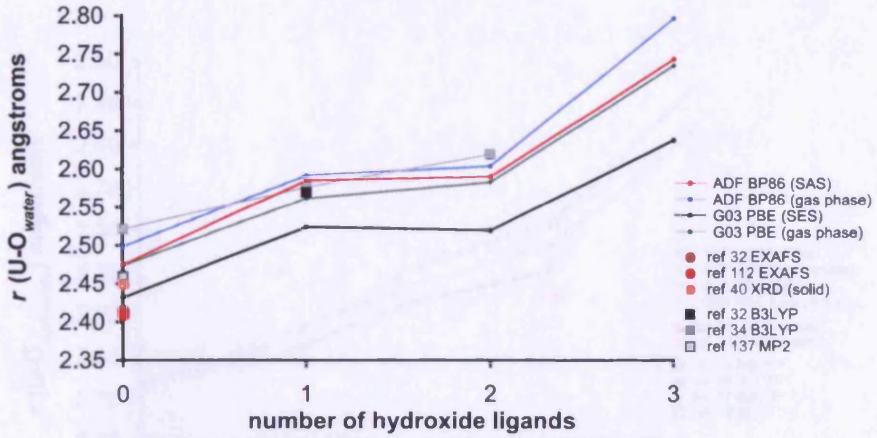

Figure 3.9: Selected calculated r(U–O$_{water}$) /Å as a function of the number of coordinated OH^-, including selected previous experimental and theoretical results

Code	Functional	4W1OH	2W2OH	1W3OH	4OH	5OH
ADF Gas Phase	PBE	2.113	2.164	2.252	2.309	2.465
	BP86	2.116	2.165	2.256	2.311	2.465
G03 Gas Phase	PBE	2.109	2.177	2.235	2.283	2.415
	BP86	-	-	-	2.285	-
	PW91	-	-	-	2.280	-
ADF COSMO (SAS)	PBE	2.116	2.163	2.255	2.294	2.421
	BP86	2.123	2.165	2.255	2.311	2.424
	PW91	-	-	-	2.290	-
G03 CPCM (SES)	PBE	2.118	2.152	2.216	2.251	not converged
Experimental Results						
ref 2 XRD					2.260	
ref 2 EXAFS (solid)					2.210	
ref 2 EXAFS (soln.)					2.220	
ref 136 EXAFS					2.260	
Previous Theoretical Results						
ref 39 AIMP CPCM					2.300	
ref 39 AIMP gas					2.336	
ref 37 B3LYP					2.334	
ref 1 B3LYP					2.309	2.462
ref 33 B3LYP		2.162				
ref 36 B3LYP (OH^- *ortho*)				2.230		
ref 36 B3LYP (OH^- *meta*)				2.250		

Table 3.7: Calculated values for r(U–O$_{hydroxide}$) /Å as a function of the number of coordinated OH^-, including previous experimental and theoretical results

Table 3.6 presents this work's calculated r(U–O$_{water}$), together with previous experimental and calculated data, and selected data are presented in figure 3.9. As with r(U–O$_{yl}$), the gradual addition of OH^- to uranyl produces a lengthening in r(U–O$_{water}$). The

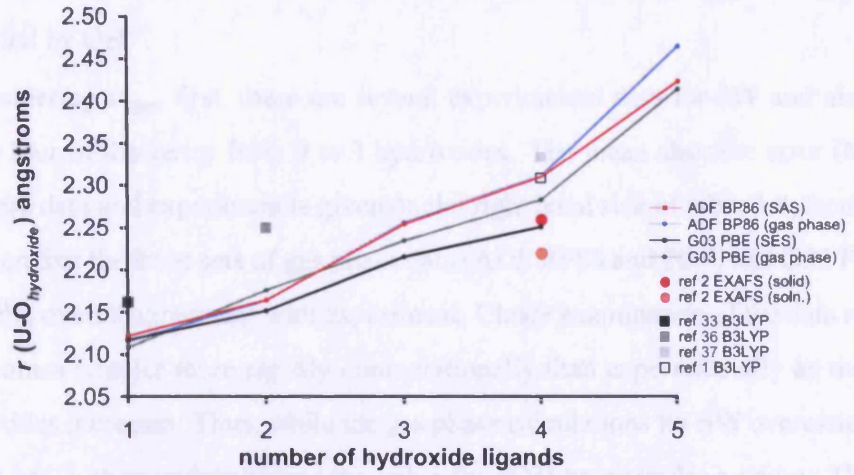

Figure 3.10: Selected calculated r(U–$O_{hydroxide}$) as a function of the number of coordinated OH^-, including selected previous experimental and theoretical results

agreement between my r(U–O_{water}) in **5W** and experiment is good, with these results generally *ca.* 0.05 Å longer than experiment; the value of 2.432 Å obtained by Häller using PBE/SES in G03 is particularly pleasing. The majority of the previous calculations significantly overestimate r(U–O_{water}), discrepancies with experiment of >0.1 Å are typical.

Table 3.7 collects the r(U–$O_{hydroxide}$) data from this work along with previous results, and some of these are displayed in figure 3.10. As for r(U–O_{yl}) and r(U–O_{water}), there is an increase in r(U–$O_{hydroxide}$) with increasing number of coordinated hydroxides. Experimental data are available only for **4OH**, and there is good agreement between theory and experiment. The ADF/PW91/solvent as well as all my G03 calculations achieve better agreement with experiment than any previous calculations for r(U–$O_{hydroxide}$) in **4OH**, as do Häller's PBE calculations.

3.4.2 Uranyl vibrations

The wavenumbers for the symmetric ($\overline{\nu}_{sym}$) and asymmetric ($\overline{\nu}_{asym}$) stretching vibrations of the uranyl ion (or more correctly, the molecular modes with predominant uranyl stretching character) are collected in tables 3.8 and 3.9 respectively, and selected data are shown in figures 3.11 and 3.12. It is normally the case that increases in bond length are accompanied by a decrease in stretching frequency, and figures 3.11 and 3.12 reveal that this is

true in the present study; all of the complexes show a decrease in $\overline{\nu}_{sym}$ and $\overline{\nu}_{asym}$ as H_2O are replaced by OH^-.

Considering $\overline{\nu}_{sym}$ first, there are several experimental data for **5W** and also one set spanning four of the series from 0 to 3 hydroxides. The mean absolute error (MAE) between these data and experiment is given on the right hand side of table 3.8, from which it can be seen that the three sets of gas phase data (ADF BP86 and PBE, and G03 PBE) have very similar overall agreement with experiment. Closer examination of the data reveal that $\overline{\nu}_{sym}$ becomes smaller more rapidly computationally than experimentally as the number of hydroxides increases. Thus, while the gas phase calculations for **5W** overestimate $\overline{\nu}_{sym}$ by 40-50 cm^{-1}, they underestimate the value for **4OH** by a similar amount. This is presumably a reflection of the calculated overestimation in $r(U–O_{yl})$ with increasing number of hydroxides, noted in section 3.4.1.

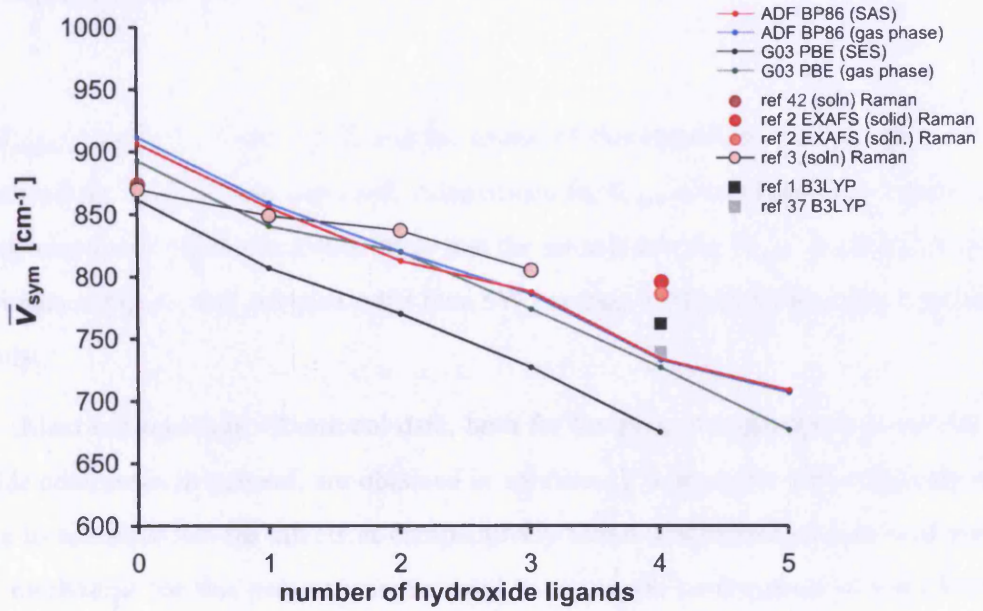

Figure 3.11: Selected calculated values for $\overline{\nu}_{sym}(U–O_{yl})$ compared with selected previous experimental and theoretical results

For $\overline{\nu}_{asym}$ there are experimental data only for the **5W** complex. The agreement between these gas phase calculations and experiment is mixed, with G03 performing better than ADF. As with $\overline{\nu}_{sym}$, increasing the number of hydroxides leads to a steady decrease

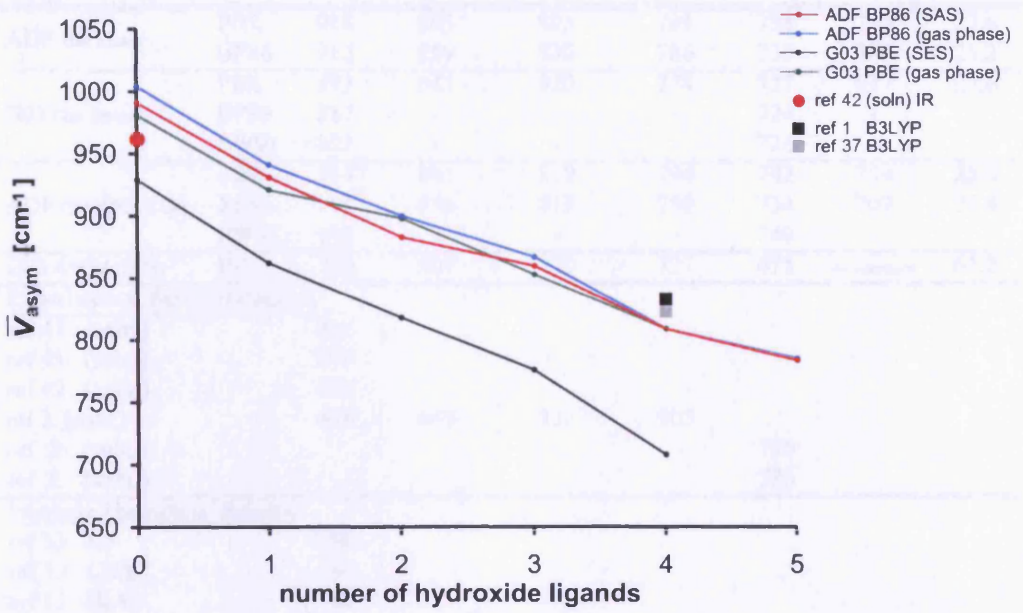

Figure 3.12: Selected calculated values for $\overline{\nu}_{asym}$(U–O_{yl}) compared with selected previous experimental and theoretical results

in $\overline{\nu}_{asym}$ (figures 3.11 and 3.12), and the extent of this reduction is very similar to that observed for $\overline{\nu}_{sym}$. Given that these calculations for $\overline{\nu}_{sym}$ overestimate the reduction in comparison with experiment, it is likely that the same is true for $\overline{\nu}_{asym}$, but the lack of experimental data for any complex other than **5W** prevents me from drawing this conclusion firmly.

Most experimental vibrational data, both for the present target systems and for actinide complexes in general, are obtained in solution. It is therefore very desirable to be able to calculate solvent effects at comparatively minor computational cost, and part of the motivation for this project was the need to assess the performance of the COSMO (ADF) and CPCM (G03) continuum models. In ADF, the use of the esurf approach produced reasonable geometries, but subsequent frequencies calculations generated one or more imaginary vibrations of small magnitude. Adjusting the solvent model parameters did not eliminate these imaginary modes and so Häller attempted analogous calculations in G03 using the SES method. However, these calculations also produced 1-2 imaginary wavenumbers of small magnitude for the positively charged and neutral complexes.

$\overline{\nu}_{sym}$(U–O_{yl})		5W	4W1OH	2W2OH	1W3OH	4OH	5OH	MAE
ADF Gas Phase	PBE	918	865	825	791	738	713	27.6
	BP86	912	859	830	786	733	707	26.2
G03 Gas Phase	PBE	893	841	820	774	727	677	27.6
	BP86	887	-	-	-	724	-	
	PW91	891	-	-	-	726	-	
ADF COSMO (SAS)	PBE	914	861	819	794	742	709	25.8
	BP86	907	856	813	788	734	709	27.4
	PW91	912	-	-	-	740	-	
G03 CPCM (SES)	PBE	862	807	770	727	675	not converged	61.2
Experimental Results (Raman)								
ref 41 (soln.)		869						
ref 43 (soln.)		870						
ref 42 (soln.)		874						
ref 3 (soln.)		870	849	837	805			
ref 2 (solid)						796		
ref 2 (soln.)						786		
Previous Theoretical Results								
ref 33 HF		1091						
ref 33 LDA		854						
ref 33 BLYP		787						
ref 33 B3LYP		910						
ref 34 B3LYP		902	848	831				
ref 37 B3LYP						739		
ref 1 B3LYP						762	750	

Table 3.8: Calculated values for $\overline{\nu}_{sym}$(U–O_{yl}) /cm^{-1} as a function of the number of OH^-, including previous results. MAE = Mean Absolute Error of calculated values compared with experimental data from refs 2[2] and 3[3]

Single points, geometry optimizations along the imaginary modes and Intrinsic Reaction Coordinate calculations were performed by Häller to determine if new minimum energy structures could be located, but they all resulted in structures with higher energies. We therefore concluded that the small imaginary wavenumbers do not indicate the presence of structures with lower energies, but rather are artefacts of the solvent model, most likely caused by the charge discretization on the cavity, i.e. the tesserae. An investigation of the tesserae parameters was performed by Häller on the **5W** complex to see if this was the case. The results of this study have already been reported[139] and will not be discussed in detail here. We concluded that only the TSARE and OFAC parameters significantly affect the magnitude of the imaginary wavenumbers, but no combination of these parameters could eliminate the two small imaginary modes found for **5W**. Thus the esurf/SES approach in both ADF and G03 produces unsatisfactory imaginary modes. I then em-

$\overline{\nu}_{asym}$(U–O_{yl})		5W	4W1OH	2W2OH	1W3OH	4OH	5OH
ADF Gas Phase	PBE	1011	948	904	871	814	789
	BP86	1004	941	900	867	809	785
G03 Gas Phase	PBE	981	921	898	853	809	-
	BP86	976	-	-	-	807	-
	PW91	980	-	-	-	808	-
ADF COSMO (SAS)	PBE	997	942	888	867	810	789
	BP86	991	931	883	860	809	784
	PW91	997	-	-	-	809	-
G03 CPCM (SES)	PBE	929	862	818	776	708	not converged
Experimental Results (I.R.)							
ref 43 (soln.)		961					
ref 42 (soln.)		962					
Previous Theoretical Results							
ref 33 HF		1149					
ref 33 LDA		945					
ref 33 BLYP		893					
ref 33 B3LYP		1003					
ref 37 B3LYP						823	
ref 1 B3LYP						833	822

Table 3.9: Calculated values for $\overline{\nu}_{asym}$(U–O_{yl}) /cm^{-1} as a function of the number of OH^-, including previous results

ployed the asurf (solvent accessible surface) in ADF. This approach certainly produced fewer imaginary modes (in most cases zero) but the structural and vibrational data from this method are so similar to the gas phase results that there is questionable merit in using it. For example, the MAEs for $\overline{\nu}_{sym}$ using the ADF/COSMO/SAS method are essentially the same as the gas phase values (table 3.8), as are the absolute values for $\overline{\nu}_{sym}$.

We wondered if the SES method would give good values for $\overline{\nu}_{sym}$ and $\overline{\nu}_{asym}$, in spite of the presence of imaginary modes. Table 3.8 shows, however, that the inclusion of solvent effects in G03 in this way gives a MAE which is much worse than the other data. Although the value for **5W** is essentially the same as experiment, the agreement for **4OH** is very poor, with a difference of more than 100 cm^{-1}. These data suggest that the inclusion of solvent effects via G03/SES worsens agreement with experiment, and that its application to other (uranyl) systems should be approached with caution.

It may be the case, of course, that better agreement with experiment and removal of imaginary modes could be achieved by the inclusion of explicit solvent molecules. A shell of explicit water molecules around the target systems, perhaps in conjunction with a continuum model for subsequent shells, may well be the way forward for better

modelling of the uranyl vibrations. Such an approach, however, will greatly increase the computational cost, and will be impractical for larger molecules, so it is likely that gas phase calculations will remain the best option for such studies in the short - medium term.

3.4.3 Bond Strengths

Energy Decomposition Scheme

The structural and vibrational data presented in sections 3.4.1 and 3.4.2 strongly suggest that the uranyl bond weakens as water molecules are replaced by hydroxide ions in the equatorial plane. I was interested in obtaining a more quantitative measure of this effect, and attempted to compute the U–O_{yl} bond strength using the energy decomposition scheme implemented in the ADF code. This approach breaks molecules down into fragments, and calculates the interaction energy between them. The choice of fragments is clearly crucial to this process, and difficulties can arise when studying a series of molecules with differing overall charges (as in the present case). The most straightforward approach in this case is to calculate the interaction between O_{yl}^{2-} and the uranium-containing fragment, but it was found that the varying charge on the latter produces data which seem unphysical (U–O_{yl} bond energies of many thousands of kJ mol^{-1} in some cases, see table 3.10).

	5W	4W1OH	2W2OH	1W3OH	4OH	5OH
O_{yl}^{2-} and $fragment^{x+}$ ($x = 4 \rightarrow -1$)						
Bonding Energy	-5506	-4516	-3720	-2807	-1834	-1051
Coulomb Attraction Energy	-6276	-4631	-3043	-1509	0	1476
Bonding Energy - Coulomb Attraction Energy	770	115	-677	-1298	-1834	-2527
O_{yl}^{0} and $fragment^{0}$						
Bonding Energy	186	-606	-1024	-1170	-984	-702

Table 3.10: Calculated bonding energies using charged and neutral fragments along with calculated Coulomb attraction energies

In an attempt to remove the purely ionic component of the bonding I calculated the Coulombic Attraction energy between the two charged fragments for each species (using Coulomb's law, $E_C = \frac{q_a q_d}{4\pi\epsilon_0 d}$) and subtracted it from the bonding energy, as shown in table 3.10; these data do not give chemically useful results either. An alternative method of removing the large ionic interaction energy is to use neutral fragments, and so I converged

each fragment with zero charge before bringing them together for a single point calculation on the charged complex. The bottom row of table 3.10 presents these data, they do not seem chemically sensible and so I conclude that the energy decomposition scheme is not a useful tool for calculating bond strengths in un-like charged complexes such as the ones studied here. Next I turned to other methods of assessing the strength of the U–O_{yl} bond.

Mayer Bond Orders

The Mayer Bond Order (MBO),[104] an extension of the Wiberg index,[140] has previously been used here at UCL,[141] and elsewhere[142] to probe the An-O_{yl} bond. In $[MOX_5]^{n-}$ (M=Pa, n=2; M=U, n=1; M=Np, n=0; X=F,Cl,Br)[141] O'Grady calculated An-O_{yl} bond orders of around 1.9 in all cases, while Cavigliasso and Bridgeman computed 2.11 for U–O_{yl} in **5W**.[142] Both of these values are significantly reduced from the formal value of 3 in UO_2^{2+}, partly due to the involvement of the actinide orbitals in the bonding to the equatorial ligands, and also because MBOs are often underestimated in multiply bonded systems calculated with ADF frozen core basis sets.[143]

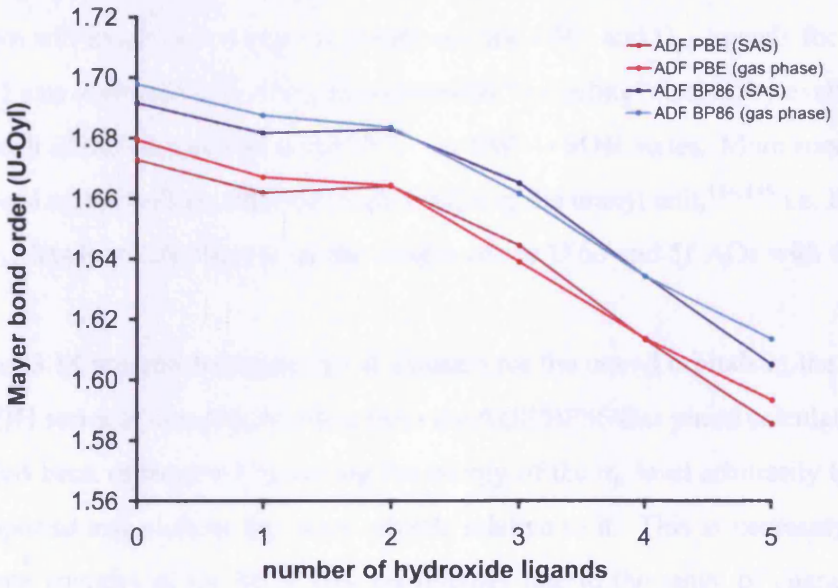

Figure 3.13: Calculated U–O_{yl} MBO as a function of the number of OH^-

I have calculated the MBO of the U–O_{yl} bond in all of the compounds in the **5W** → **5OH** series using the Mayer code developed by Bridgeman[143] in conjunction with wave-functions generated by the ADF code. These data are plotted in figure 3.13. The U–O_{yl}

MBO in **5W** is calculated to be *ca.* 1.7, somewhat reduced from the value reported previously by Bridgeman and Cavigliasso.[142] MBOs are sensitive to computational parameters, and the differing basis sets, geometries and functionals employed in this study will all contribute to the reduced U–O_{yl} MBO*. Figure 3.13 shows that there is a decrease in MBO for the U–O_{yl} bond as the number of hydroxides is increased. The decrease is small to begin with, but then increases such that the MBO of **5OH** is *ca.* 1.6. Thus the MBO data support the structural and vibrational data, and provide further indirect evidence of a decrease in U–O_{yl} bond strength as the **5W** → **5OH** series is crossed.

3.4.4 Molecular orbital analysis

The indirect evidence from geometries, vibrational frequencies and MBOs strongly suggests that the U–O_{yl} bond becomes progressively weaker as H_2O is replaced by OH^-. Clark *et al* have previously speculated as to the origin of this weakening in **4OH**. They suggest that the weakening may be *partially explained by the strong σ-donating ability of the OH^- ligands*[2] but also that partial π bonding between the π-donor OH^- ligands and the U atom will result in a competition between the OH^- and O_{yl} ligands for the U 6*d* orbitals.[2] I was interested in probing this equatorial "π-loading" further, by examining the MOs of each of the compounds in the UO_2^{2+} → **5W** → **5OH** series. More specifically, I have focused on the well established valence MOs of the uranyl unit,[144,145] i.e. the π_g, π_u, σ_g, and σ_u, levels which result from the mixing of the U 6*d* and 5*f* AOs with the O_{yl} 2*p* levels.

Figure 3.14 presents an energy level diagram for the uranyl orbitals in the UO_2^{2+} → **5W** → **5OH** series of complexes, taken from the ADF/BP86/Gas phase calculations. The diagram has been constructed by setting the energy of the σ_u level arbitrarily to 0 eV in each compound and plotting the other orbitals relative to it. This is necessary because the absolute energies of the MOs vary enormously due to the range of charges on the complexes. In many cases it is easy to identify the uranyl orbitals upon examination of 3-dimensional representations of the valence MOs, but for certain MOs in certain complexes, orbital character was smeared over as many as five or six different MOs and so a weighted

*As a check Häller recalculated the MBO of the U–O_{yl} bond in **5W** using the TZ2P basis set on all atoms at the ADF/PBE/gas phase geometry and found it to be 2.00, highlighting the sensitivity of MBOs to basis set

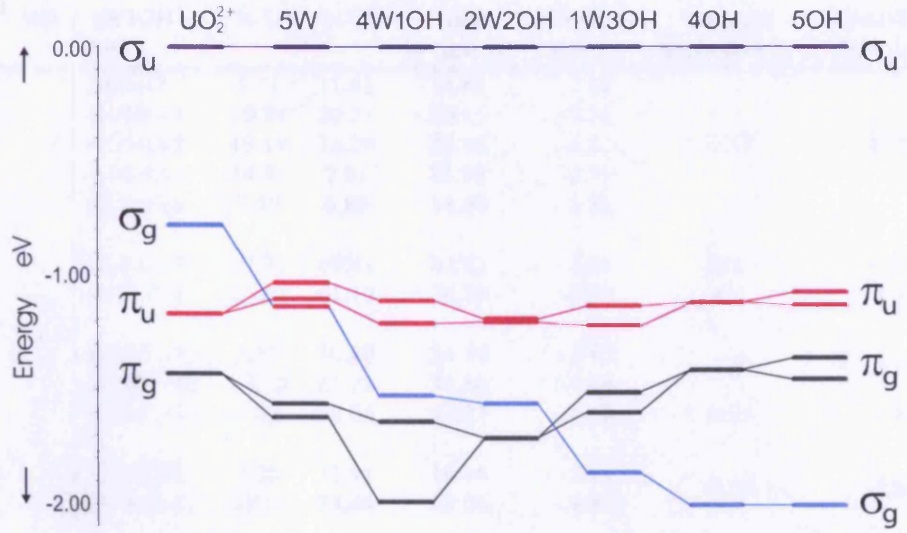

Figure 3.14: MO energy level diagram for species UO_2^{2+}, **5W**, **4W1OH**, **2W2OH**, **1W3OH**, **4OH** and **5OH**. The energies of the σ_u MO for each complex has been set to zero

mean of these orbital energies was calculated to give the orbital energy plotted in figure 3.14. This weighted mean approach is detailed below using the example of the **1W3OH** species.

Constructing the MO diagram

Figures 3.15→3.17 show the thirteen highest energy MOs calculated for the **1W3OH** structure shown in figure 3.5(d). These thirteen MOs span the energy range in which uranyl σ_u, σ_g, π_u, and π_g character were observed. Figure 3.15(a) shows a three-dimensional representation of the uranyl ion HOMO, a σ_u bonding combination of uranium f_{z^3} and oxygen p_z. Figures 3.15(b)→3.15(f) reveal that the HOMO, HOMO-1, HOMO-2, HOMO-3 and HOMO-6 of **1W3OH** all contain similar combinations of uranium *f* and oxygen *p* (as the symmetry is broken this is no longer a pure Uf_{z^3} – Op_z admixture of AOs, but instead a combination of metal *f* and oxygen *p*). Table 3.11 shows the percentage contribution from the σ_u-type orbital to each of the five **1W3OH** MOs, as well as the percentage contribution of σ_g-, π_u-, and π_g- type orbitals to the high energy MOs of **1W3OH**.

The π_u orbitals are fairly well reproduced by the HOMO-7 and HOMO-8 of **1W3OH**, although in this molecule there is a localization of electron density onto one of the two U–

UO_2^{2+} MO	1W3OH MO	% U	% O	Total % 'uranyl'	Absolute Energy	Weighted Mean Energy	Normalised Mean Energy
σ_u :	HOMO	5.21	11.62	16.83	-2.02		
	HOMO-1	19.94	20.21	40.15	-2.18		
	HOMO-2	19.19	16.29	35.48	-2.52	-2.48	0.00
	HOMO-3	14.01	7.91	21.92	-2.74		
	HOMO-6	7.19	6.80	14.00	-3.35		
π_u :	HOMO-7	17.91	69.41	87.32	-3.61	n/a	-1.13
	HOMO-8	15.63	61.12	76.75	-3.69	n/a	-1.22
π_g :	HOMO-9	3.55	30.89	34.44	-3.93	-3.99	-1.51
	HOMO-10	15.50	61.29	76.80	-4.04		
	HOMO-11	9.22	38.05	47.27	-4.10	-4.08	-1.60
σ_g :	HOMO-9	3.25	11.91	16.16	-3.93	-4.34	-1.86
	HOMO-12	12.17	28.44	69.06	-4.43		

Table 3.11: Calculated percentage contributions of U and O_{yl} (i.e. the uranyl unit) to, and absolute/normalised energies of **1W3OH** MOs, all energies given in eV

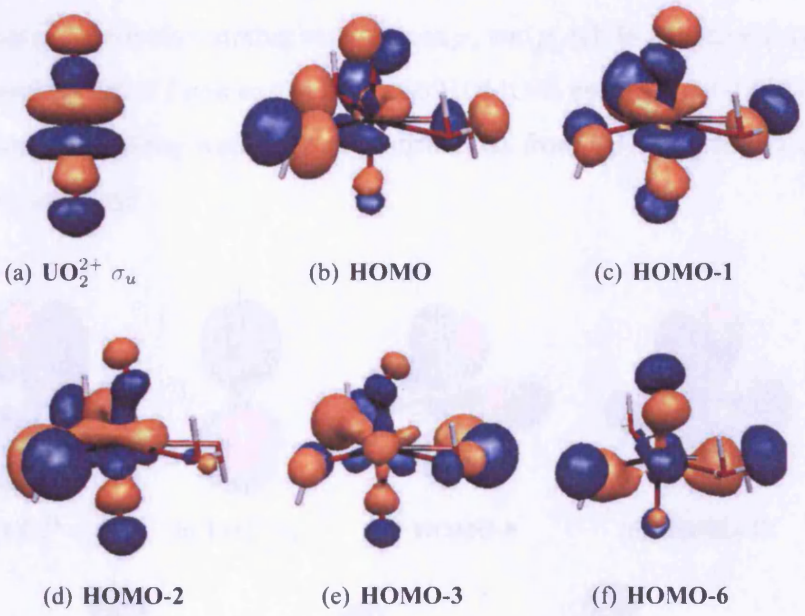

(a) UO_2^{2+} σ_u (b) **HOMO** (c) **HOMO-1**

(d) **HOMO-2** (e) **HOMO-3** (f) **HOMO-6**

Figure 3.15: Three dimensional representations of the UO_2^{2+} HOMO (σ_u) and all **1W3OH** MOs which contain similar uranium–axial oxygen bonding character

O_{yl} bond in each π_u MO rather than an equal distribution of density between the two U–O_{yl} bonds, as in the bare uranyl ion (see figure 3.16). As table 3.11 shows, the two components of the π_u orbital are close in energy, although not degenerate (due to the absence of symmetry).

(a) UO_2^{2+} π_u (b) UO_2^{2+} π_u (c) **HOMO-7** (d) **HOMO-8**

Figure 3.16: Three dimensional representations of the UO_2^{2+} HOMO-1 and HOMO-2, a pair of π_u orbitals and the two analogous **1W3OH** MOs π_u MOs

The π_g and σ_g MOs must be discussed together; as figure 3.17 and table 3.11 show, the character of the π_g and σ_g orbitals is blurred in one of the lower energy valence MOs of the **1W3OH** complex. The two lines of data in table 3.11 for the HOMO-9 relate to a division of the total metal and O_{yl} content of this orbital into that which most closely matches each of the pure π_g and the σ_g, shown in figures 3.17(a), 3.17(b) and 3.17(e). The π_g orbitals contain a metal *d* contribution mixing with oxygen p_x and p_y while σ_g comprises a bonding interaction between metal *f* and oxygen p_z, thus HOMO-9, containing a 3.55% U*d* and a 3.25% U*f* component along with various contributions from Op_x, Op_y and Op_z contains both π_g and σ_g character.

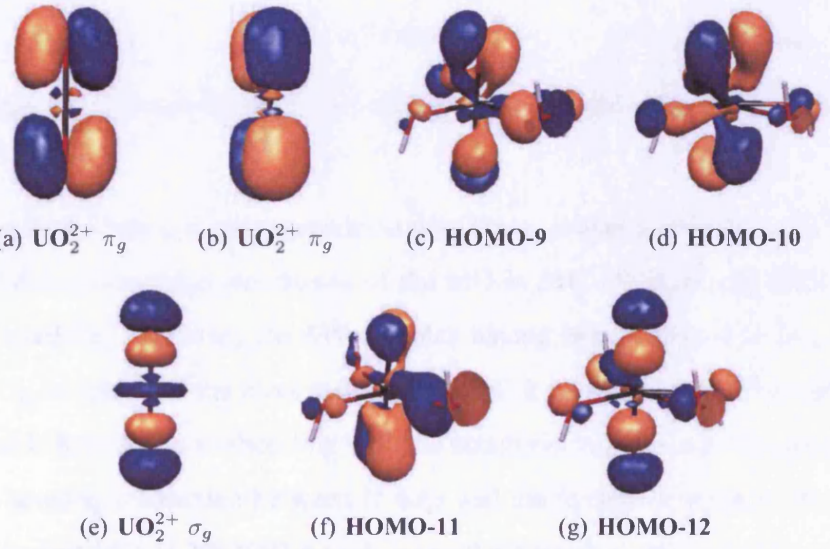

(a) UO_2^{2+} π_g (b) UO_2^{2+} π_g (c) **HOMO-9** (d) **HOMO-10**

(e) UO_2^{2+} σ_g (f) **HOMO-11** (g) **HOMO-12**

Figure 3.17: Three dimensional representations of the UO_2^{2+} HOMO-3, HOMO-4, and HOMO-5, a pair of π_g orbitals and a σ_g orbital respectively, along with four similar **1W3OH** MOs, note how (c) contains a combination of π_g and σ_g character

Analysis of the MO diagram

The UO_2^{2+} and **4OH** systems are the most straightforward to interpret, as their point groups preserve the degeneracy of the π_g and π_u MOs. It is noticeable that the energy of these π orbitals, relative to one another and to the σ_u level, is very similar in UO_2^{2+} and **4OH**. The degeneracy is lost in the intermediate complexes, but even so the energies of the components of the π_u level do not significantly change across the series. There is somewhat more variation in the π_g levels, with a general decrease in energy to **2W2OH** and then a gradual rise again to the **4OH** system.

Much the most striking aspect of figure 3.14 is the pronounced stabilization of the σ_g level with increasing number of hydroxides. The *ca.* 1.2 eV stabilization in this level from UO_2^{2+} → **4OH** is much larger than any other energy change, and is in marked contrast to the essentially unaltered energy of the π MOs between UO_2^{2+} and **4OH**.

(a) **5W** σ_g (b) **2W2OH** σ_g (c) **4OH** σ_g

Figure 3.18: Three-dimensional representations of the σ_g orbital of **5W** (D_{5h}) and **4OH**

Figure 3.18 offers an explanation as to why the σ_g orbital is so stabilized. The figure presents 3-dimensional representations of the MO in **5W**, **2W2OH** and **4OH** with predominant uranyl σ_g character, the **5W** complex having been idealized to D_{5h} symmetry from the C_{2v} structure of the most stable geometry. It is clear that the interaction of the torus of the U $6d_{z^2}$ AO is antibonding with the equatorial ligands in **5W**, but that in **4OH** there is a bonding interaction between U $6d_{z^2}$ and the hydroxide ligands. Examination of the equivalent MO of **2W2OH** reveals a small antibonding interaction between the U and O_{water}, with a non-bonding interaction between U and $O_{hydroxide}$. The stabilization of the σ_g level across the series is therefore most likely to be the result of the changing

interaction between the U and the equatorial ligands in this MO.

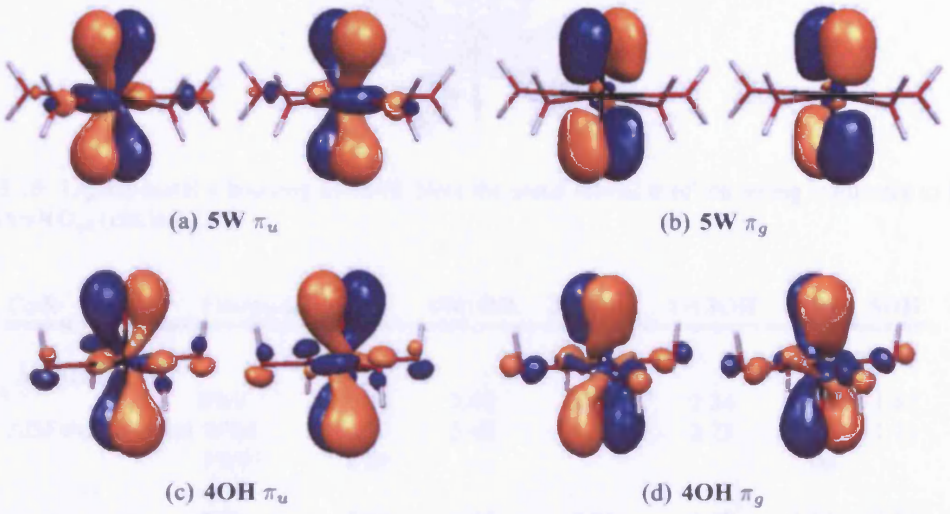

(a) **5W** π_u (b) **5W** π_g

(c) **4OH** π_u (d) **4OH** π_g

Figure 3.19: Three-dimensional representation of the π_u and π_g orbitals of **5W**(D_{5h}) and **4OH**

As noted above, in some of the target systems there are contributions from the uranyl σ and π levels to several MOs. For **5W** and **4OH**, however, there is much less such mixing, and the uranyl MOs can be clearly identified. Figure 3.19 shows the π_g and π_u MOs in **5W** (D_{5h}) and the four components of the π MOs in **4OH** (in which the lower molecular symmetry, D_{2d}, partially scrambles π_g and π_u character). There is little evidence in this figure of a π-type interaction between the U and the hydroxide ligands in **4OH**, from which we conclude that equatorial and axial π bonding are not in competition in the same MO. Analysis of the other valence MOs of **4OH** also suggests little competition between the $O_{hydroxide}$ and O_{yl} for the same U AOs. The **4OH** MO for which an equatorial π interaction is most clearly present is shown in figure 3.20, from which it may be seen that the U–$O_{hydroxide}$ π interaction involves a U 5*f* AO (not 6*d* as previously suggested[2]), and that the small O_{yl} π contribution to this MO is non-bonding with the metal.

3.4.5 Mulliken and Hirshfeld charges, and Mulliken populations

Mulliken charge analysis was carried out on the ADF stationary points, both in gas phase and in solution. Figures 3.21 and 3.22 along with table 3.12 show the Mulliken charges of uranium and O_{yl} using BP86 and PBE (gas and solvent model) and also PW91 (gas only), from which it can be seen that the differences between the different functionals and

Figure 3.20: Ligand-metal π bonding in **4OH**. Note the metal orbital is of the wrong symmetry to form a π-bond with O_{yl} (circled)

Code	Functional	5W	4W1OH	2W2OH	1W3OH	4OH	5OH
URANIUM							
ADF COSMO (SAS)	PBE	2.63	2.46	2.31	2.26	2.08	1.81
	BP86	2.59	2.42	2.27	2.23	2.04	1.78
	PW91	2.60	–	–	–	2.06	–
ADF Gas Phase	PBE	2.60	2.45	2.30	2.28	2.08	1.74
	BP86	2.56	2.40	2.33	2.25	2.04	1.73
OXYGEN							
ADF COSMO (SAS)	PBE	-0.69	-0.74	-0.77	-0.79	-0.85	-0.87
	BP86	-0.68	-0.73	-0.76	-0.79	-0.84	-0.86
	PW91	-0.68	–	–	–	-0.84	–
ADF Gas Phase	PBE	-0.68	-0.74	-0.76	-0.80	-0.85	-0.86
	BP86	-0.67	-0.73	-0.75	-0.79	-0.84	-0.86

Table 3.12: Calculated charges on U and O using the **Mulliken** charge analysis scheme

between the gas and solvent structures are negligible.

A decrease in $q_{Mull U}$ from e.g. +2.56 to +1.73 (ADF/BP86/gas data) from **5W** → **5OH** accompanies an increased $q_{Mull O_{yl}}$ from -0.67 to -0.86. Thus 0.83e$^-$ of extra charge goes to uranium and a total of 0.38e$^-$ to the two uranyl oxygens, i.e. the uranyl unit gains *ca.* 1.2e$^-$ from the five OH$^-$ ions added to the system. Table 3.13 shows that the increased electron density localized on uranium is composed of *ca.* 0.3e$^-$ into the 6*p*-hole[144] and *ca.* 0.4e$^-$ into the metal *d* orbitals; the *s* and *f* orbitals each show an increase in population of a little less than 0.1e$^-$.

Although widely used, it has long been recognized that the Mulliken procedure has a strong dependence on the basis set;[126,127] although this problem is not important here since consistent basis sets are used for U, O and H in these calculations, so self-comparison

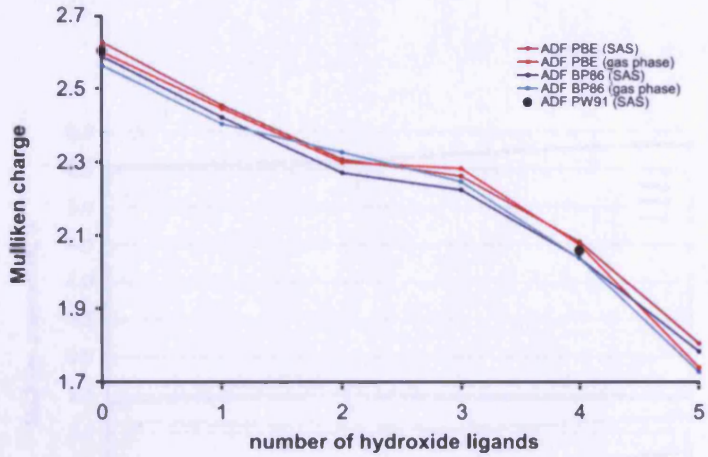

Figure 3.21: Calculated charge on U using the Mulliken charge analysis scheme

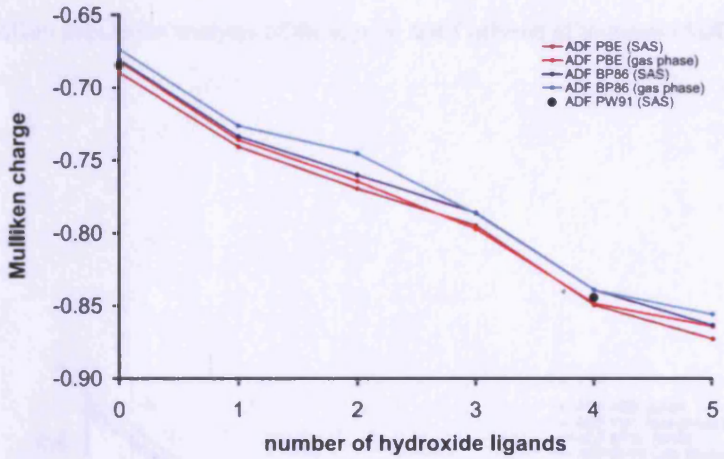

Figure 3.22: Calculated charge on O_{yl} using the Mulliken charge analysis scheme

within this family of complexes gives qualitatively useful results. An alternative approach is the Hirshfeld charge analysis,[94,95] which is less prone to basis set dependencies. The Hirshfeld charge analysis data (table 3.14 and figures 3.24 and 3.25) reveal a decrease in $q_{Hir}U$ from e.g. +0.94 to +0.45 (ADF/BP86/SAS) while each $q_{Hir}O_{yl}$ increases from -0.23 to -0.48. Thus while the absolute numbers are different from those obtained using the Mulliken approach, the trend is the same. The replacement of water ligands by OH^- gradually reduces the positive charge on U and concurrently makes the charge on each O_{yl} more negative.

Table 3.15 gives the charge difference between U and O_{yl} (q_U - $q_{O_{yl}}$) in **5W** and **5OH**,

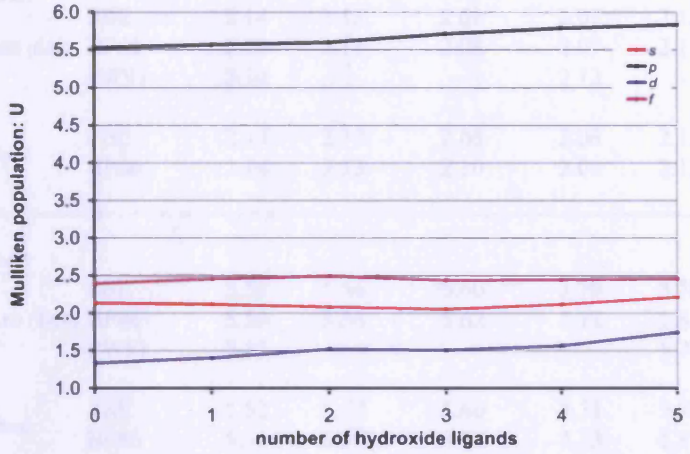

Figure 3.23: Mulliken population analysis of the *s*, *p*, *d*, and *f* orbitals of uranium (ADF/BP86/Gas phase data)

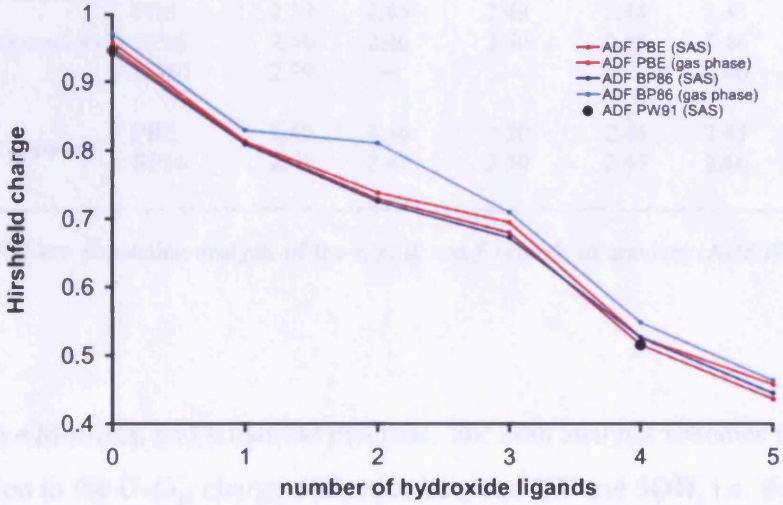

Figure 3.24: Calculated charge on U using the Hirshfeld charge analysis scheme

Code	Functional	5W	4W1OH	2W2OH	1W3OH	4OH	5OH
URANIUM *s*							
ADF COSMO (SAS)	PBE	2.14	2.13	2.08	2.07	2.12	2.21
	BP86	2.14	2.13	2.08	2.07	2.12	2.21
	PW91	2.14	–	–	2.12	–	
ADF Gas phase	PBE	2.14	2.12	2.08	2.06	2.12	2.22
	BP86	2.14	2.13	2.10	2.06	2.12	2.22
URANIUM *p*							
ADF COSMO (SAS)	PBE	5.51	5.56	5.60	5.70	5.78	5.82
	BP86	5.53	5.58	5.62	5.72	5.81	5.83
	PW91	5.52	–	–	–	5.79	–
ADF Gas phase	PBE	5.52	5.57	5.60	5.71	5.79	5.83
	BP86	5.54	5.59	5.59	5.73	5.81	5.85
URANIUM *d*							
ADF COSMO (SAS)	PBE	1.33	1.41	1.52	1.53	1.57	1.71
	BP86	1.34	1.41	1.53	1.53	1.57	1.71
	PW91	1.34	–	–	–	1.57	–
ADF Gas phase	PBE	1.34	1.41	1.52	1.51	1.57	1.74
	BP86	1.34	1.41	1.48	1.52	1.57	1.73
URANIUM *f*							
ADF COSMO (SAS)	PBE	2.39	2.45	2.49	2.44	2.45	2.46
	BP86	2.40	2.46	2.50	2.45	2.46	2.47
	PW91	2.39	–	–	–	2.46	–
ADF Gas phase	PBE	2.40	2.46	2.50	2.44	2.45	2.46
	BP86	2.41	2.47	2.50	2.45	2.46	2.47

Table 3.13: Mulliken population analysis of the *s*, *p*, *d*, and *f* orbitals of uranium (ADF/BP86/Gas phase data)

using both the Mulliken and Hirshfeld methods. For both analysis schemes there is a *ca.* 20% reduction in the U–O_{yl} charge difference between **5W** and **5OH**, i.e. the U and O_{yl} bond becomes significantly less ionic as the **5W** → **5OH** series is crossed. Given the lack of evidence for π competition between O_{yl} and $O_{hydroxide}$ for the U valence AOs, I suggest that the reduction in charge difference between U and O_{yl} is the principal cause of the U–O_{yl} bond weakening with increasing number of OH^- ligands. The reduction

Code	Functional	5W	4W1OH	2W2OH	1W3OH	4OH	5OH
URANIUM							
ADF COSMO (SAS)	PBE	0.95	0.81	0.73	0.68	0.52	0.44
	BP86	0.94	0.81	0.73	0.67	0.53	0.45
	PW91	0.95	–	–	–	0.52	–
ADF Gas Phase	PBE	0.96	0.81	0.74	0.70	0.53	0.46
	BP86	0.97	0.83	0.81	0.71	0.55	0.46
OXYGEN							
ADF COSMO (SAS)	PBE	-0.23	-0.30	-0.36	-0.39	-0.46	-0.48
	BP86	-0.23	-0.30	-0.36	-0.39	-0.46	-0.48
	PW91	-0.23	–	–	–	-0.46	–
ADF Gas Phase	PBE	-0.22	-0.30	-0.36	-0.39	-0.45	-0.47
	BP86	-0.22	-0.30	-0.34	-0.39	-0.46	-0.47

Table 3.14: Calculated charges on U and O using the Hirshfeld charge analysis scheme

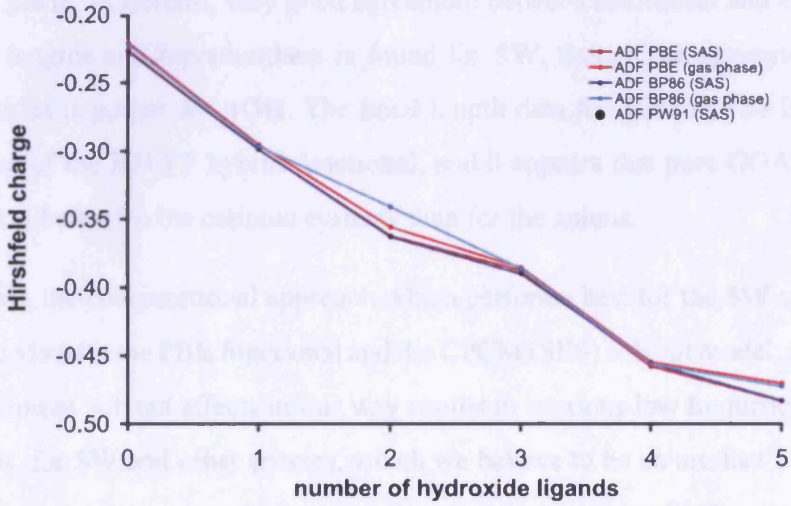

Figure 3.25: Calculated charge on O_{yl} using the Hirshfeld charge analysis scheme

	5W	**5OH**
Mulliken	3.23	2.69
Hirshfeld	1.19	0.92

Table 3.15: Calculated charge difference between uranium and O_{yl} (q_U - $q_{O_{yl}}$) in **5W** and **4OH** using the Mulliken and Hirshfeld charge analysis schemes (ADF/BP86/Gas phase data)

in charge on the U centre as the series is crossed will certainly result from a number of processes, including the change in interaction between the U d_{z^2} AO and the σ functions of the ligands from **5W** → **4OH** (figure 3.18). Thus it is suggested that the U–O_{yl} bond strength reduction arises from a reduction in U–O_{yl} ionic bonding, caused (at least in part) by the σ-donating ability of the OH^- ligands. Hence I conclude that, of two possible causes suggested by Clark *et al*,[2] only the σ mechanism has any substantive effect.

3.5 Conclusions

In this chapter I have reported DFT studies of the series of complexes **5W** → **5OH**. The principal conclusions are:

(i) The uranyl bond length increases and the $\overline{\nu}_{sym}$ and $\overline{\nu}_{asym}$ O_{yl}–U–O_{yl} stretching vibrations decrease as water molecules are replaced by hydroxide ions in the equatorial plane. In general, very good agreement between theoretical and experimental bond lengths and wavenumbers is found for **5W**, though the agreement for both quantities is poorer for **4OH**. The bond length data for **4OH** can be improved by the use of the B3LYP hybrid functional, and it appears that pure GGA functionals perform better for the cationic systems than for the anions.

(ii) Overall, the computational approach which performs best for the **5W** system is the G03 code with the PBE functional and the CPCM (SES) solvent model, although the inclusion of solvent effects in this way results in spurious low frequency imaginary modes, for **5W** and other species, which we believe to be an artefact of the model. Furthermore, the agreement between theory and experiment for $\overline{\nu}_{sym}$ using this approach is significantly worse for the series as a whole than are the gas phase data. We conclude that there is no compelling reason to prefer the CPCM/SES model to gas phase data in these target systems.

(iii) The structural and vibrational data, supported by the calculation of Mayer bond orders, strongly suggest that the U–O_{yl} bond strength decreases as water molecules are replaced by hydroxides. This weakening has previously been attributed to competition between the $O_{hydroxide}$ and O_{yl} for U 6*d* AOs, in which partial U–$O_{hydroxide}$ π bonding weakens the U–O_{yl} π interaction. I see little evidence of such a competition, and suggest that the weakening of U–O_{yl} arises from a reduction in ionic character stemming from charge build up on the U centre.

This work has been published: "Density functional theory investigation of the geometric and electronic structures of $[(UO_2)(OH)_m(H_2O)_n]_q$ ($m + n = 5$; $q = 2m$)" by Kieran I. M. Ingram, L. Jonas L. Häller and Nikolas Kaltsoyannis, *Journal of the Chemical Society, Dalton Transactions*, 2006, 2403 - 2414.

Chapter 4

The performance of Time-Dependent Density Functional Theory (TD-DFT) in the simulation of the electronic spectra of molecular uranium complexes

4.1 Introduction

Time Dependent Density Functional Theory (TD-DFT) has become a useful tool for theoretical chemists. TD-DFT enables the simulation of electronic spectra, and therefore opens another route for comparison between experiment and theory. TD-DFT has been applied in transition metal chemistry where good agreement is seen with experiment,[146,147] but there is a real scarcity of TD-DFT actinide research. The first part of this work uses TD-DFT to test three functionals and six basis set combinations on three uranyl complexes, with the aim of finding a reliable procedure for modelling the electronic spectra of actinide complexes. The second part of this project uses the optimum procedure thus determined to probe the electronic spectra of two further uranyl complexes, $[UO_2(NCN)_2]$ and $[UO_2(NPN)_2]$, the importance of which is discussed below.

I have already discussed in section 1.1.2 how the actinides U → Am in the V/VI oxidation state most commonly exist as linear actinyl ions, uranyl being the most stable. Typical complexes containing actinyl units adopt geometries with the actinyl oxo ligands in the axial sites of bipyramidal systems and ancillary ligands in the equatorial sites, the equatorial plane being perpendicular to the (O–An–O) fragment. Traditionally ligands coordinating to uranyl have been based on hard atoms such as oxygen or chlorine. However, recently there are a growing number of complexes containing non-oxygen based equatorial

ligands, many of which deviate significantly out of the equatorial plane.[148–155]

Studies by Alcock on $[AnO_2(O_2CMe)_2(bipy)]$ (An = U, Np)[154] and Deacon on $[UO_2(O_2(C_6F_5))_2(bipy)]$[150] report severe distortions from the equatorial plane which can be explained by steric and electrostatic considerations, and they thus order the "distortability" of the ligands: $U–O_{axial} < U–O_{equatorial} < U–N_{equatorial}$. Generally significant distortion is observed in uranyl complexes with chelating ligands in a 6-coordinate equatorial plane[148,149,151–155] but Sarsfield *et al* have demonstrated that a distorted equatorial ligand field can be forced with lower coordination numbers. For example $[CH(PH_2P{=}NSiMe_3)_2]^-$ reacts with $[UO_2Cl(thf)_3]$ to give $[UO_2Cl\{CH(Ph_2PNSiMe_3)_2\}thf]$, a red complex which contains an out of plane U–C bond.[148,149] As discussed above, uranium complexes are predominantly yellow/green and so Sarsfield postulates that the unusual electronic absorption characteristics of the aforementioned complex may be a consequence of the out-of-plane equatorial coordination. It is to test this hypothesis that a number of complexes, including $[UO_2(NCN)_2]$ and $[UO_2(NPN)_2]$ where NCN = $(NSiMe_3)_2CPh$ and NPN = $(NSiMe_3)_2PPh_2$, were synthesised;[156] NCN and NPN are defined in figure 4.1. Structural points to note include the U–N distances in each complex; a mean r(U–N) of

(a) NCN (b) NPN

Figure 4.1: NCN and NPN ligands

2.42Å was measured in the NCN complex and a larger r(U–N) value of 2.47Å in the NPN complex. The authors believe this increase in r(U–N) is due to increased charge donation to the metal centre, an idea backed up by their previous work.[157] It is also well established that strongly electron donating ligands can weaken $U–O_{ax}$ bonding and that Raman spectroscopy is a more sensitive probe of bond strength than crystallographic studies; in view of this Raman spectra were taken to investigate bond strength. Compared to $[UO_2Cl_2(thf)_2]_2$ (834 cm^{-1}, for $\overline{\nu}_{sym}(U–O_{ax})$), both $[UO_2(NCN)_2]$ and $[UO_2(NPN)_2]$ have slightly smaller but comparable frequencies, 818 and 824 cm^{-1} respectively, indicat-

ing a slightly weaker U–O_{ax} bond in the NCN and NPN complexes.

Sarsfield's unusual complexes with distorted equatorial ligand fields are investigated computationally using TD-DFT in the second part of this chapter, with an emphasis on why they are coloured orange/red instead of the more usual green/yellow. However these are large systems, and there is as yet little in the literature about performing such calculations. As mentioned in chapter 2, asymptotically correct functionals have been developed for use in TD-DFT due to the importance of the outer regions of a molecule in calculating high-lying excitation states. In this project a range of functionals including the LDA VWN, various GGAs, and two asymptotically correct functionals as well as a range of different quality basis sets were tested on three uranyl complexes for which there are experimental absorption data,[156] $[UO_2Cl_2(TBP)_2]$ (TBP = tri- butylphosphate), $[UO_2Cl_2(THF)_2]$ (THF = tetrahydrofuran), and $[UO_2(NO_3)_2(TBP)_2]$. The optimum basis set/functional combination was subsequently employed for calculations on my target molecules, $[UO_2(NCN)_2]$ and $[UO_2(NPN)_2]$.

4.2 Literature Review

Recent advances in TD-DFT have meant that instead of being restricted to atoms and small molecules, the electronic spectra of larger systems are now able to be studied. Although little has been done in this area in the actinides, numerous transition metal TD-DFT studies have successfully described the electronic spectra of these complexes, a selection of which are summarised below. First I will discuss the spectral history of uranium, and specifically the uranyl ion.

The visible spectrum of the uranyl ion is distinctive and has an extensive past. Although uranium complexes have been used since Roman times,[158,159] the first recognition that they contained an unknown element was in 1789 when Klaproth isolated UO_2^{2+} and named it *uranium*,[160] synthesising *uranium salts* which were actually uranyl complexes. Péligot finally isolated elemental uranium in 1841[161] and rechristened UO_2^{2+} as *uranyl*.[162] The study of the spectroscopy of actinyl ions began in 1846 with Brewster's study of the optical properties of uranium compounds; his study of *canary glass* (in which the species absorbing and emitting light is the uranyl ion) showed that uranium absorbs light in the

blue, transmits in the yellow and has luminescence in the green. Thus uranyl spectroscopy has been known for a long time and has played a role in the coining of the the word fluorescence,[163] the formulation of Stokes law,[163] and the discovery of radioactivity.[164]

More recently Denning has performed a number of spectroscopic studies of UO_2^{2+}, for example to compare the electronic structure of the uranyl ion in $CsUO_2(NO_3)_3$ and $NaUO_2(CH_3COO)_3$[165] , two uranyl salts with similar coordination geometries. The lowest energy absorption bands are found to lie around 21,000 cm^{-1} (the Cs salt slightly below, and the Na, slightly above) and higher energy absorption bands are found to follow similar energetic spacing in each of the compounds. Moreover, when a comparison is made between these trigonally coordinated species and the D_{2h} $[UO_2Cl_4]^{2-}$, Denning *et al* conclude that the ordering of uranyl energy levels is only marginally changed by the change in equatorial coordination. Görller-Warland *et al*[166] probe the influence of solvent on the spectroscopic behaviour of uranyl chloride. Spectra obtained in three organic solvents, acetone, TBP and hexone are compared with single-crystal data for $Cs_2UO_2Cl_4$. The authors again conclude that the main spectroscopic properties of $[UO_2Cl_4]^{2-}$ in solution correspond to those of the $Cs_2UO_2Cl_4$ single crystal, and so the idea begins to form that the electronic structure of the uranyl ion is affected relatively little by external factors, and is principally defined by the strong U-O_{yl} bonding within the ion.

A selection of representative examples of recent TD-DFT calculations follows. In 2005 this group at UCL[69] tested three different XC functionals (revPBE,[68] LB94,[66] SAOP[67]), the latter two of which are asymptotically corrected for use with TD-DFT. The subjects of the paper were the electronic spectra of two tetrahedral metal oxides, RuO_4 and OsO_4. These calculations were performed in ADF with high quality ZORA all electron TZ2P basis sets; the optimised geometries of the complexes were found to be in good agreement with experiment (RuO_4 showed the more impressive agreement of the two). The electronic spectra calculated by Menconi *et al* show very good correlation with experimental energies for the first five excitations of the target molecules; the transitions were all found to be oxygen $p \rightarrow$ metal d LMCTs. Although all three functionals give qualitative results, the LB94 results have the smallest mean absolute error (MAE), 0.23 and 0.24 eV respectively for the lowest energy excitation energies of RuO_4 and OsO_4 respec-

tively (0.25 eV $\sim$ 2000 cm^{-1}). The corresponding MAEs (all eV) with revPBE data, 0.46 (RuO_4) and 0.27 (OsO_4), and SAOP data, 0.56 (RuO_4) and 0.29 (OsO_4), are also impressive. Interestingly, although the optimised geometry of the ruthenium oxide is in better agreement with experiment, the calculated excitation data for the osmium oxide shows better experimental agreement.

In 2005 Neugebauer and Baerends[167] investigated the electronic absorptions of the permanganate ion with ADF's TD-DFT program using the SAOP potential with a variety of (non-relativistic) basis sets, with the aim of assigning the poorly understood second and third transitions. They conclude that for a system such as MnO_4^- with close lying potential energy surfaces, TD-DFT is particularly suitable and they are satisfied that their results have resolved the assignment of the second and third bands as they reproduce experimental features well, though the energetic agreement between theory and experiment is not as good as might be hoped, with discrepancies of between 0.5 and 1 eV. The impressive reproduction of experimental features is an advancement on earlier work[168] by the same group in which they concluded that standard XC functionals performed unreliably and with varying degrees of success on three transition metal complexes, MnO_4^-, $Ni(CO)_4$ and $Mn_2(CO)_{10}$.

A very successful TD-DFT study of Cp_2MCl_2 (M = Ti, Zr, Hf; Cp = C_5H_5) illustrates some of the analyses for which computational chemistry is so useful. Wang *et al*[169] carried out sets of calculations using G03 (B3LYP with LANLZDZ relativistic basis sets) and ADF (PW91 with TZP ZORA basis sets) in an attempt to investigate why Cp_2TiCl_2 shows a red luminescence but Cp_2ZrCl_2 and Cp_2HfCl_2 both give strong green/blue luminescence, and whether the lowest energy LMCT excitations are Cl→M or Cp→M based. Furthermore the low-energy section of the experimental electronic absorption spectrum of the Ti complex is sharp and narrow while the other two are broad and more poorly structured (the Hf peaks come at higher energy). The optimised geometries of the three complexes were isostructural wedge-like sandwiches with non-parallel rings and distorted tetrahedral geometry around the metal centre. Moving from Ti to Zr an increase in r(M–L) (L = Cp, Cl) was calculated, however there was a small decrease from Zr to Hf, a result of the lanthanide contraction. The highest energy occupied MOs (HOMOs) consist of Cp

and Cl AOs in varying ratios, generally the Cp_2TiCl_2 HOMOs contain more Cl than Cp, Cp_2HfCl_2 HOMOs more Cp than Cl, and Cp_2ZrCl_2 similar percentages of AO from each. The lowest energy unoccupied MOs (LUMOs) contain a large metal *d* component with an additional Cp contribution; Cp_2TiCl_2 has the highest percentage of metallic character and the smallest Cp component over the three LUMOs listed while Cp_2HfCl_2 contains the lowest metallic contribution and a higher Cp content. The higher energy valence orbitals of the heavier metals result in a larger HOMO-LUMO gap for Cp_2HfCl_2 decreasing through Cp_2ZrCl_2 to Cp_2TiCl_2, with the smallest HOMO-LUMO gap. Therefore the low-lying excitations were ligand $\pi \rightarrow$ metal *d*; examination of the ground state (*g.s.*) and excited state (*e.s.*) charges and dipole moments lead the group to conclude that the transition is associated with redistribution of electron density from the Cp rings onto the metal centre in each complex.

The electronic absorption spectrum of Cp_2MCl_2 shows a first weak band and a second stronger in the near UV/Vis.[170] The results of this group are in good agreement with experiment, with errors of 0.05 - 0.3eV (B3LYP) and 0.1 - 0.5eV (PW91). The superiority of the B3LYP results they attribute to the energetic advantage of G03's LANL2DZ treatment of relativity over ADF's ZORA for these systems. This idea is supported by the data; the results agree better for the Ti complex (relativity not a significant consideration) but diverge moving onto the Zr and Hf complexes (relativity more important). Wang *et al* conclude that with the *g.s.* $\rightarrow$ *e.s.* transition electron density is transferred from Cp to M, and this is accompanied by a lengthening of M–Cl. Their predicted energy level patterns agree well with the phosphorescence data available.

To summarise, TD-DFT would seem a promising tool for simulating the UV/Vis spectra of organometallic complexes, particularly since the advent of asymptotically correct functionals which outperform GGA functionals in the examples mentioned above. Previous work suggests that an agreement of $\sim$0.5 eV (4000 cm^{-1}) between our results and experimental data would be an impressive result, especially given that actinides have not been modelled by these methods before the work presented below.

4.3 Computational Details

ADF2004 was used to carry out the initial geometry optimisations of $[UO_2Cl_2(TBP)_2]$ (**A**), $[UO_2Cl_2(THF)_2]$ (**B**), and $[UO_2(NO_3)_2(TBP)_2]$ (**C**), as well as subsequent geometry optimisations of $[UO_2(NCN)_2]$ (**D**) and $[UO_2(NPN)_2]$ (**E**). For the geometry optimisations the PW91 functional was used with a TZP basis set for uranium and DZP for the remaining atoms; the ZORA approach was used to account for relativistic effects. First row elements (excluding hydrogen) were given a $1s$ frozen core, second row $2p$, and uranium $5d$.

TD-DFT calculations were performed to simulate the electronic spectra of **A**, **B**, and **C**. VWN[45] (LDA), PBE,[47,48] rev-PBE,[68] PW91[46] (all GGA), LB94[66] and SAOP[67] (asymptotically correct) functionals were trialled on **A**. As the results for PBE, rev-PBE, PW91 and VWN were in very close agreement, and LB94 and SAOP gave different sets of results, three functionals were chosen to perform the production calculations on complexes **A**, **B**, and **C**: the GGA PW91, and the asymptotically correct LB94 and SAOP.

For increased accuracy the following TD-DFT parameters were specified above default values:- vectors: 400, lowest: 250, tolerance: 10^{-8} orthonormality: 10^{-10} and only symmetry-allowed dipole-active transitions were calculated to cut computational cost. Six different basis set combinations were used in conjunction with the PW91 and LB94 functionals, these are given in table 4.1. In combinations 4 and 5 the 'inner' atoms include the first coordination sphere (see figure 4.2 below): O_{yl}, $O_{TBP/THF}$, Cl and all atoms in the NO_3 groups.

Basis set number	Basis set combination
1	QZ4P (all-electron) all atoms
2	TZ2P (all-electron) all atoms
3	TZ2P all atoms
4	TZ2P U & 'inner' atoms, TZP remaining atoms
5	TZP U & 'inner' atoms, DZP remaining atoms
6	TZP U, DZP remaining atoms

Table 4.1: Basis set combinations used, 'inner' atoms includes O_{yl}, $O_{TBP/THF}$, Cl, NO_3 (see figure 4.2)

The SAOP functional can be used only with all-electron basis sets and therefore only combinations 1 and 2 are directly comparable between SAOP and PW91 / LB94 calcu-

lations. For SAOP, basis set combinations 4, 5 and 6 as described in table 4.1 were used without frozen cores.

4.4 Results

4.4.1 Optimised geometries: $[UO_2Cl_2(TBP)_2]$, $[UO_2Cl_2(THF)_2]$, and $[UO_2(NO_3)_2(TBP)_2]$.

A variety of initial geometries for **A**, **B**, and **C** were explored, both with and without symmetry constraints; I will discuss the lowest energy structure in each case. The calculated structures for **A**, **B**, and **C** are presented in figure 4.2. **A** and **C** were found to have a C_{2h} structure and **B** a D_2 structure, although all complexes have a pseudo-octahedral geometry around the uranium metal centre.

Bond lengths- Å	A	B	C
r(U-O_{yl})	1.802	1.799	1.798
r(U-Cl)	2.632	2.622	-
r(U-N_{NO_3})	-	-	2.96
r(U-O_{TBP})	2.450	-	2.493
r(U-O_{THF})	-	2.453	-

Table 4.2: Selected bond length data for complexes **A**, **B**, and **C**

Table 4.2 compares selected bond length data of the three molecules (there are no experimental bond length data for these complexes in the literature). There is negligible difference between the uranyl U–O_{yl} bond lengths in the three species, furthermore r(U–O_{yl}) is in good agreement with previously computed bond lengths for neutral uranyl species.[171,172] There is however an appreciable difference between r(U-O_{TBP}) in **A** and **C**. I attribute this to repulsive interactions between the NO_3 groups and the TBP ligands in **C**; the similarity between the r(U-O_{TBP}) and r(U-O_{THF}) in **A** and **B** respectively supports this suggestion.

4.4.2 Electronic spectra: $[UO_2Cl_2(TBP)_2]$, $[UO_2Cl_2(THF)_2]$, and $[UO_2(NO_3)_2(TBP)_2]$.

For each of the three target systems, experimental data are available for the lowest energy transition[166] (a ligand $\rightarrow$ metal charge transfer), this will be the focus of my initial

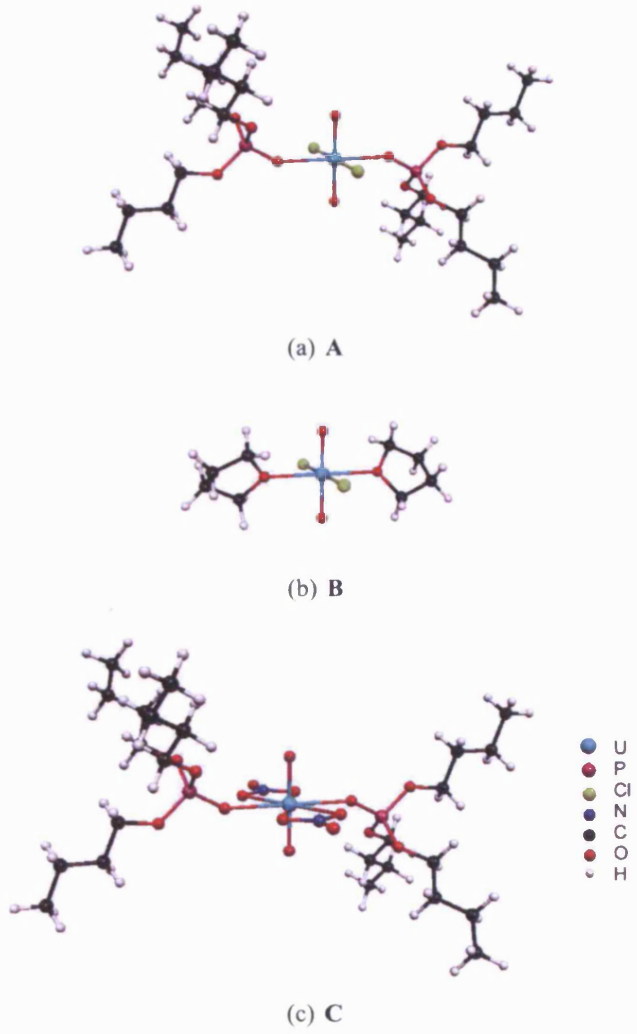

(a) **A**

(b) **B**

(c) **C**

Figure 4.2: Ball and stick representations of the optimised geometries of complexes **A**, **B**, and **C**

investigation.

Table 4.3 presents the absorption data for complex **A**; using each of the six basis set combinations with PW91, the first absorption peak ($\mathbf{A}_1$) is found between 20,330 cm^{-1} and 20,826 cm^{-1}. Using LB94, this range spans 14,711 cm^{-1} $\rightarrow$ 15,038 cm^{-1}, and using SAOP a range of 24,048 cm^{-1} $\rightarrow$ 24,524 cm^{-1} is calculated. The experimental first absorption peak is centred around 23,000 cm^{-1}, indicating that the SAOP data agree best with experiment for this complex. Errors of approx. 1000 - 1500 cm^{-1}, i.e. 0.12 - 0.19 eV, indicate that this work shows similarly impressive agreement with experimental data as the better results in the literature.

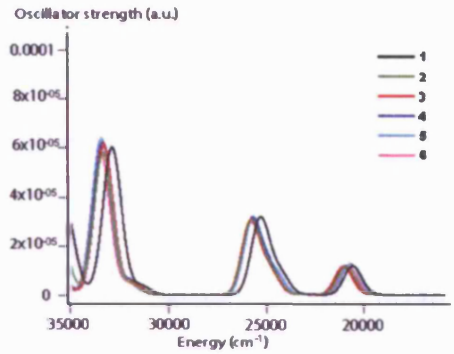

(a) **PW91**

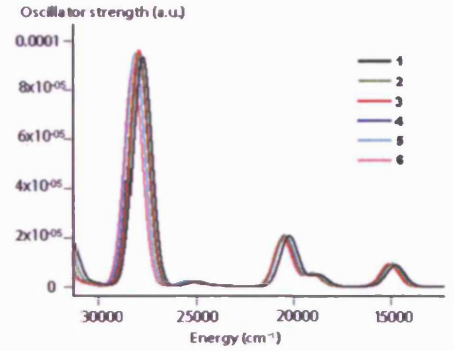

(b) **LB94**

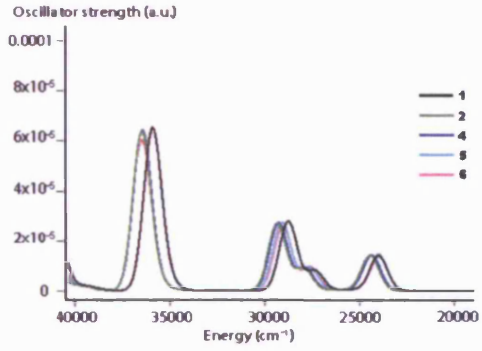

(c) **SAOP**

Figure 4.3: Calculated absorption spectra for **A** using PW91, LB94 and SAOP, 1-6 refer to the basis set combination used, as defined in table 4.1

Figure 4.3* illustrates the excellent agreement between the excitation data for **A** using the six (five for SAOP) basis set combinations. For each of the three functionals, the form

*The y-scale is missing as it is arbitrary and varies with the peak width. All figures presented for **A**, **B** and **C** are on the same scale, and the numbers given in tables 4.3, 4.4, and 4.5 refer to the calculated oscillator strengths at a default peak width, which is not used here for aesthetic reasons.

of the calculated spectrum changes little as the basis sets are altered, a small energy shift separates them from each other. Furthermore the shape of the spectra are very similar on moving between the functionals. The shoulder on $\mathbf{A}_2$ is less pronounced with the PW91 data (figure 4.3(a)), and $\mathbf{A}_x$ located between $\mathbf{A}_2$ and $\mathbf{A}_3$ with PW91 and LB94 is hidden by $\mathbf{A}_3$ with the SAOP data (figure 4.3(c)). However these differences are small compared to the striking similarities between the form of the spectra using each of the three functionals. A further feature observed in all three sets of data is that the basis set affects the energy of the bands more significantly at higher energies. Overall, although the agreement between these results and the experimental data is impressive, it would seem that the extremely small changes to the spectra caused by the basis set quality are negligible in comparison to the discrepancy between theory and experiment.

Functional	PW91		LB94		SAOP	
Basis set	E / cm^{-1}	Oscillator strength x10 ^{3}	E / cm^{-1}	Oscillator strength x10 ^{3}	E / cm^{-1}	Oscillator strength x10 ^{3}
1	20330	13.6	14711	8.2	24048	13.7
2	20710	13.7	14936	8.5	24524	12.7
3	20826	13.9	15029	6.8	-	-
4	20749	13.9	14971	6.5	24458	11.6
5	20444	14.4	14983	6.6	24085	12.3
6	20516	13.4	15038	6.0	24074	12.3
Expt.	**23000**[156]					

Table 4.3: Calculated and experimental absorption data for **A**

Experimentally the first absorption peak for complex **B** is at 24,000 cm ^{1}, a red shift of $\sim$1000 cm^{-1} with respect to **A**. Table 4.4 shows that as for **A**, the best agreement with experiment for **B** is given by SAOP. Indeed the agreement between these results and experimental data is very impressive for all six basis set combinations using SAOP, <0.1 eV difference.

Figure 4.4 shows the calculated absorption spectra for **B** using each functional with the six (five for SAOP) basis set combinations. As for **A**, very good agreement is seen between the different basis sets for each functional. The figure suggests that **B** has a more complicated electronic spectrum than **A**. A comparison of the spectra of **B** and **A** indicates that the two asymptotically correct functionals predict a similar pattern of absorption in

Functional	PW91		LB94		SAOP	
Basis set	E / cm^{-1}	Oscillator strength x10^{-3}	E / cm^{-1}	Oscillator strength x10^{-3}	E / cm^{-1}	Oscillator strength x10^{-3}
1	20126	16.7	14671	13.0	23563	19.2
2	20511	16.8	14858	13.1	24050	19.3
3	20598	17.0	14942	13.2	-	-
4	20643	17.1	14946	13.2	24072	19.5
5	20272	17.3	14757	13.5	23679	19.8
6	20283	16.7	14838	13.0	23662	18.8
Expt.	**24000**[156]					

Table 4.4: Calculated and experimental absorption data for **B**, 1-6 refer to the basis set combination used, as defined in table 4.1

both complexes. Absorption bands centred at approx. 15,000, 21,000 and 28,000cm^{-1} (LB94 data) and 24,000, 29,000 and 37,000 cm^{-1} (SAOP data) are calculated in the spectra of both complexes. However, for **B**, both LB94 and SAOP predict two small absorptions ($\mathbf{B}_{x1}$ and $\mathbf{B}_{x2}$) between $\mathbf{B}_2$ and $\mathbf{B}_3$. The PW91 data show remarkably good agreement between the basis sets for $\mathbf{B}_1$ (~20,000 cm^{-1}) and $\mathbf{B}_3$ (~34,000 cm^{-1}) peaks, but poorer agreement for the peaks between these, although the same approximate spectra shape is seen for PW91 compared with the LB94 and SAOP data.

Functional	PW91		LB94		SAOP	
Basis set	E / cm^{-1}	Oscillator strength x10^{-3}	E / cm^{-1}	Oscillator strength x10^{-3}	E / cm^{-1}	Oscillator strength x10^{-3}
1	19923	9.2	not converged	n/a	28172	11.8
2	20516	9.7	not converged	n/a	29001	12.6
3	20533	9.7	17259	8.4	-	-
4	20409	9.6	17131	8.6	28870	12.6
5	20307	9.0	17079	7.6	28622	12.0
6	20398	9.7	16848	8.1	28492	12.3
Expt.	**24000**[156]					

Table 4.5: Calculated and experimental absorption data for **C**, 1-6 refer to the basis set combination used, as defined in table 4.1

Complex **C** contains an NO_3^- ligand in place of the Cl^- in **A** and **B**. Experimentally the energy of the first absorption peak for **C** is similar to that of **B**, i.e. 24000 cm^{-1}. Table 4.5 shows that although the PW91 data for **C** give similar results to **A** and **B**, the same is not true for either of the other functionals. The LB94 numbers are shifted by approximately +2000 cm^{-1} and the SAOP data by > +4000 cm^{-1}. Thus for **C**, PW91 and SAOP both

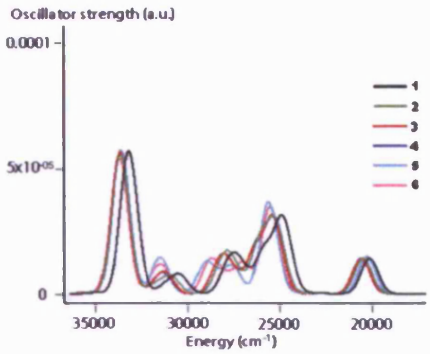

(a) **PW91**

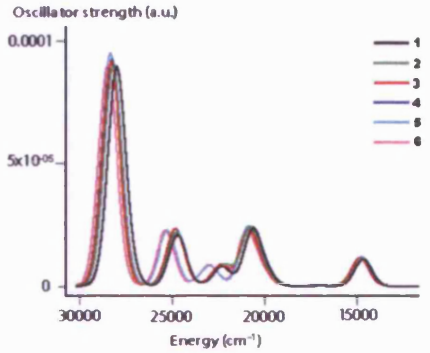

(b) **LB94**

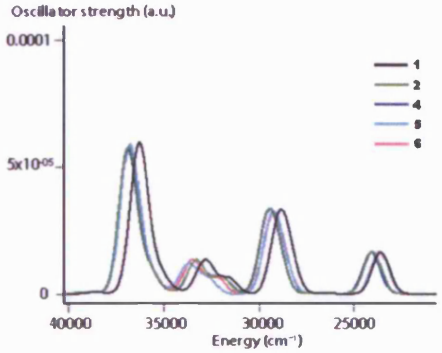

(c) **SAOP**

Figure 4.4: Calculated absorption spectra for **B** using PW91, LB94 and SAOP.

show discrepancies of ~4000 cm^{-1} between theory and experiment, translating to 0.5 eV which is within an acceptable error range as defined on the basis of similar research (see literature review).

Figures 4.5(a) – 4.5(c) show the calculated absorption spectra of complex **C**. There are some not inconsiderable differences between these spectra and those of **A** and **B**, pri-

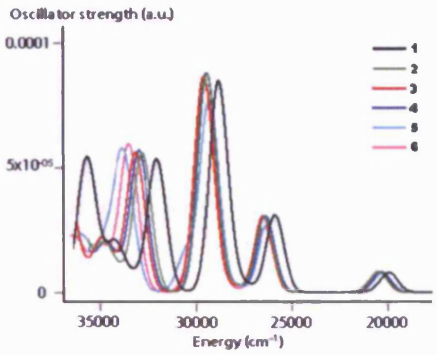

(a) **PW91**

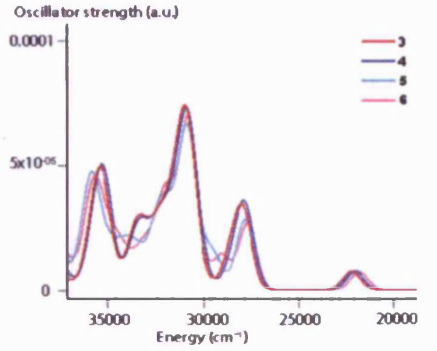

(b) **LB94**

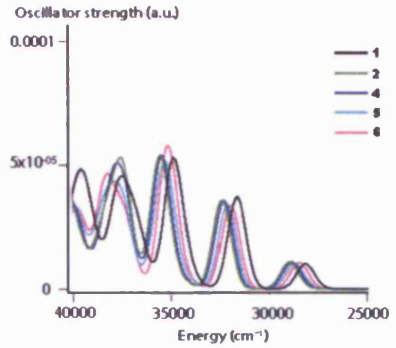

(c) **SAOP**

Figure 4.5: Calculated absorption spectra for **C** using PW91, LB94 and SAOP.

marily that more large absorption peaks are found in the spectrum of **C**.

When comparing the spectra of **A**, **B** and **C** (figures 4.3, 4.4 and 4.5) it is observed that five strong intensity peaks are found for **C**, compared with three in the same energy range for **A** and **B**. The reason for this interesting difference is not known, but the two

delocalised NO_3^- groups replacing the Cl^- groups may explain the increased complexity in the spectrum of **C**, although analysis of this kind is beyond the scope of this project as **A**, **B** and **C** are only of interest to test functional and basis set performance for use on complexes **D** and **E**, see below.

4.4.3 Conclusions: $[UO_2Cl_2(TBP)_2]$, $[UO_2Cl_2(THF)_2]$, and $[UO_2(NO_3)_2(TBP)_2]$

The performance of three density functionals and six basis set combinations in the simulation of the electronic spectra of three uranium compounds, **A**, **B** and **C**, has been evaluated. I conclude that the use of large basis sets is not warranted in these systems; combination 6 consisting of TZP for U and DZP for all other atoms is adequate to produce results of near-identical accuracy to combination 1, QZ4P for all atoms. Furthermore having compared the results obtained from three functionals, I conclude that SAOP is the best of the functionals for reproducing the (limited) experimental data available.

4.4.4 Geometries: $[UO_2(NCN)_2]$ and $[UO_2(NPN)_2]$

Table 4.6 presents selected bond lengths and angles from the optimised structures of $[UO_2(NCN)_2]$ (**D**) and $[UO_2(NPN)_2]$ (**E**), also pictured in figure 4.6, together with selected experimental data.[156] Experimentally, $r(U\text{-}O_{yl})$ is longer in **E** than in **D** and this is reproduced by my calculations, although the calculations underestimate this difference significantly and as a result, although my calculated $r(U\text{-}O_{yl})$ in **E** agrees well with experiment, $r(U\text{-}O_{yl})$ in **D** is underbound. $r(U\text{–}N)$ are calculated ~0.03Å (**D**) or 0.02Å (**E**) too long, a systematic underbinding, although the difference between $r(U\text{–}N)$ in **D** and **E** is well reproduced. All the calculated bond angles are in very good agreement with experiment.

4.4.5 Electronic spectra: $[UO_2(NCN)_2]$ and $[UO_2(NPN)_2]$

Having evaluated the performance of three different functionals and six basis set combinations for use on similar complexes in the last section, TD-DFT calculations were carried out using SAOP, with an all-electron TZP basis set for U and all-electron DZP basis sets for the other atoms. The calculated electronic absorption spectra of **D** and **E** are presented in figure 4.7(a); the main peaks as well as their oscillator strengths and corresponding

	$[UO_2(NCN)_2]$ (**D**)		$[UO_2(NPN)_2]$ (**E**)	
	PW91	expt	PW91	expt
Bond lengths / Å				
r(U–O_{yl})	1.805	1.750	1.808	1.781
r(U–N)	2.447	2.419	2.487	2.467
Bond angles / °				
O–U–O	180.0	179.4	180.0	177.5
N_1–U–N_{2a}	174.6	175.9	172.1	not given
N_1–U–N_{1a}	55.9	56.1	62.4	61.9
N_1–C–N_{1a}	118.6	120	n/a	n/a
N_1–P–N_{1a}	n/a	n/a	105.7	104.9

Table 4.6: Calculated bond lengths and angles for **D** and **E**, for definitions of N_1, N_{1a}, and N_2 see figure 4.6.

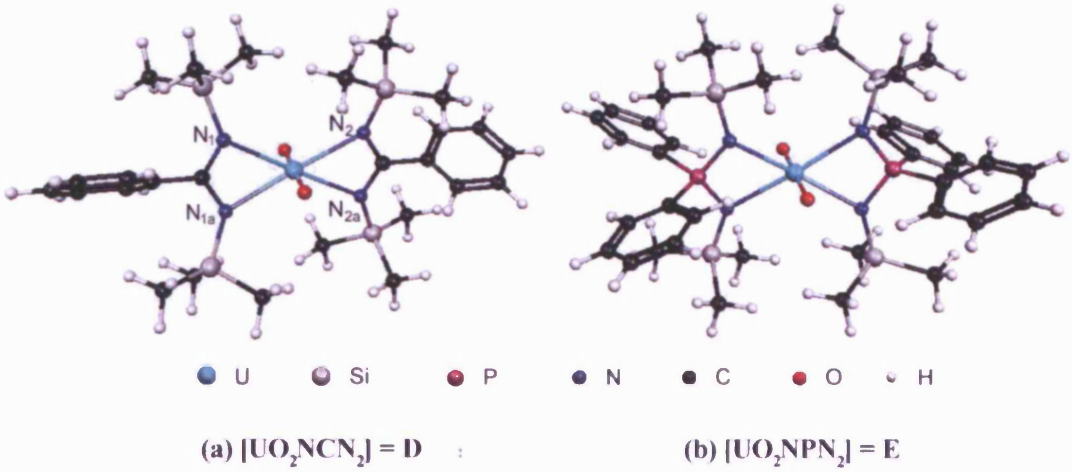

Figure 4.6: Ball and stick representations of $[UO_2(NCN)_2]$ and $[UO_2(NPN)_2]$

transitions are tabulated in table 4.7. The experimental absorption spectra for complexes **D** (red) and **E** (blue) are shown below my calculated spectra in figure 4.7(b)[†]. The experimental spectra for both **D** and **E** show structure on each absorption band. These features are most likely due to vibronic coupling, which occurs when a vertical transition results in multiple vibrational levels of the excited state being populated. As the vibrational manifold is quantised, a fine structure is seen at the absorption band apex rather than a smooth peak, as illustrated in figure 4.8. The present implementation of TD-DFT is only capable

[†]The y-scale is missing from my calculated spectra as it is arbitrary and varies with the peak width. The figures presented for **D**, and **E** are on the same scale, and the numbers given in table 4.7 refer to the calculated oscillator strengths at a default peak width, which is not used here for aesthetic reasons.

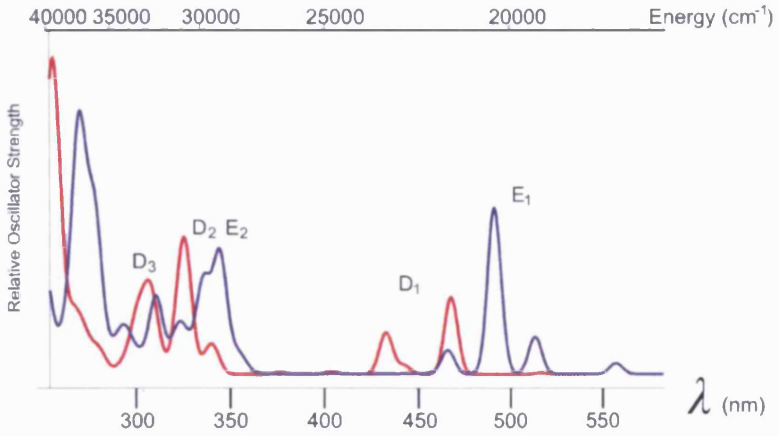

(a) **Calculated electronic absorption spectra for $[UO_2(NCN)_2]$ and $[UO_2(NPN)_2]$**

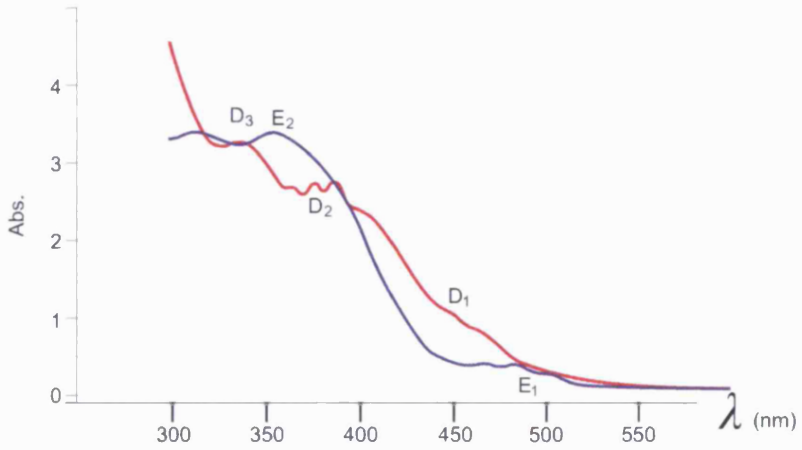

(b) **Experimental electronic absorption spectra for $[UO_2(NCN)_2]$ and $[UO_2(NPN)_2]$**[156]

Figure 4.7: Calculated (a) and experimental (b) absorption spectra of D (red lines) and E (blue lines); all energies are given in nm and the cm^{-1} scale has been included to enable comparison with A, B, and C.

$[UO_2(NCN)_2]$							$[UO_2(NPN)_2]$						
E nm	Oscillator Strength	Transition peak			Contribution	Experimental	E/nm	Oscillator Strength	Transition peak			Contribution	Experimental
468	4.22×10^{-2}	HOMO	→	LUMO+2	94%	$\mathbf{D}_1$	558	6.00×10^{-3}	HOMO	→	LUMO	99%	$\mathbf{E}_1$
433	2.27×10^{-2}	HOMO-2	→	LUMO+2	97%	$\mathbf{D}_1$	514	2.04×10^{-2}	HOMO	→	LUMO+2	66%	$\mathbf{E}_1$
									HOMO-2	→	LUMO	32%	
341	1.17×10^{-2}	HOMO-5	→	LUMO+1	96%	$\mathbf{D}_2$							
							492	8.96×10^{-2}	HOMO-2	→	LUMO	63%	$\mathbf{E}_1$
338	6.40×10^{-3}	HOMO-9	→	LUMO	95%	$\mathbf{D}_2$			HOMO	→	LUMO+2	33%	
326	5.73×10^{-2}	HOMO-4	→	LUMO+3	98%	$\mathbf{D}_2$	467	1.29×10^{-2}	HOMO-2	→	LUMO+2	98%	$\mathbf{E}_1$
323	9.71×10^{-3}	HOMO-5	→	LUMO+3	59%	$\mathbf{D}_2$	345	5.74×10^{-2}	HOMO-6	→	LUMO+3	99%	$\mathbf{E}_2$
		HOMO-8	→	LUMO+1	25%								
		HOMO	→	LUMO+4	7%		337	2.90×10^{-2}	HOMO-1	→	LUMO+4	84%	$\mathbf{E}_2$
									HOMO	→	LUMO+5	9%	
323	4.41×10^{-3}	HOMO-11	→	LUMO	99%	$\mathbf{D}_2$							
							336	1.50×10^{-2}	HOMO-11	→	LUMO+3	94%	$\mathbf{E}_2$
323	1.09×10^{-2}	HOMO-8	→	LUMO+1	62%	$\mathbf{D}_2$							
		HOMO-5	→	LUMO+3	12%								
		HOMO-9	→	LUMO+2	11%		334	3.59×10^{-3}	HOMO-14	→	LUMO+2	95%	$\mathbf{E}_2$
		HOMO	→	LUMO+4	6%								
							322	9.87×10^{-3}	HOMO-3	→	LUMO+5	68%	$\mathbf{E}_{2shoulder}$
311	1.23×10^{-2}	HOMO	→	LUMO+6	99%	$\mathbf{D}_3$			HOMO	→	LUMO+7	10%	
									HOMO-1	→	LUMO+6	9%	
307	3.16×10^{-2}	HOMO-8	→	LUMO+3	95%	$\mathbf{D}_3$			HOMO-2	→	LUMO+4	7%	
									HOMO-14	→	LUMO+3	5%	
301	2.00×10^{-2}	HOMO-2	→	LUMO+4	47%	$\mathbf{D}_3$							
		HOMO-1	→	LUMO+5	41%		311	3.66×10^{-2}	HOMO-1	→	LUMO+6	84%	$\mathbf{E}_{2shoulder}$
									HOMO	→	LUMO+7	6%	

Table 4.7: Selected calculated electronic transition data for **D** and **E**

of modelling the electronic components of the absorption spectrum and so I cannot simulate this fine structure, but I emphasise that the fine shape of the experimental spectra are unlikely to be due to each absorption comprising multiple different electronic transitions; vibronic coupling has been seen before for uranyl complexes[149] and seems the most likely reason.

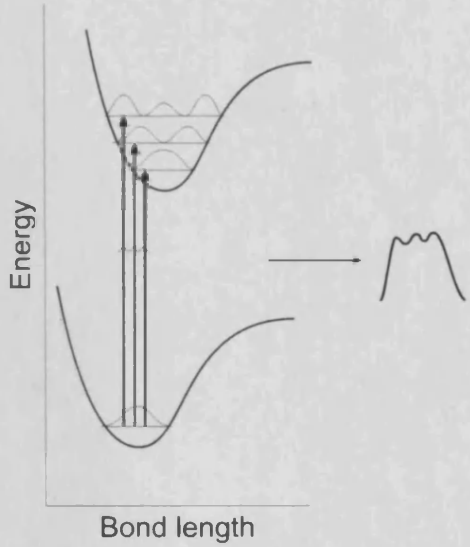

Figure 4.8: Schematic showing vibronic coupling; the quantised energies of the excited vibrational levels in the excited state lead to fine structure on the absorption band

Sarsfield *et al* quote experimental bands for **D** at 449nm ($\mathbf{D}_1$), 388nm ($\mathbf{D}_2$) and 345nm ($\mathbf{D}_3$), and for **E** at 483nm ($\mathbf{E}_1$) and 357nm ($\mathbf{E}_2$). As figure 4.7 shows, the theoretical spectra show significantly more detail than the experimental spectra; certainly the absorption bands in the latter are broad and may therefore arise from more than one electronic transition. Experimentally these peaks are unlikely to be distinguishable from one another, thus merging to form a broad peak such as those seen in the experimental spectra. By comparing the experimental and theoretical spectra for **D** I propose the following assignment of peaks: the theoretical 468 and 433nm form $\mathbf{D}_1$ (in an approx 2 : 1 ratio); 341, 338, 326, 323, 323, and 323nm form the broad $\mathbf{D}_2$ band (approx. 2 : 1 : 10 : 2 : 1 : 2) and the theoretical 311, 307 and 301 give $\mathbf{D}_3$ (approx. 4 : 11 : 7). This assignment is supported further by the higher energy end of the two spectra for **D**; a large unidentified absorption can be seen beginning around 300nm in the experimental spectrum and this matches the

strong absorption seen in my theoretical data centred around 250nm. My results indicate a maximum error of 50 - 60nm between theory and experiment, i.e. 0.56 eV (nm and eV are inversely proportional, 0.56 eV relates to the difference between 388nm and ~330nm, as seen for $\mathbf{D}_2$).

Figure 4.9 illustrates the main component transitions (> 4%) of each excitation which comprise the three absorption bands. Electronic excitations relating to $\mathbf{D}_1$ are shown in red, those relating to $\mathbf{D}_2$ in turquoise and the excitations which comprise the third absorption, $\mathbf{D}_3$ in green. The first absorption results from an electron promotion from ligand based nitrogen p-combinations to metallic f-levels, a typical ligand → metal charge transfer. The second transition is distinctly different from this and is composed of higher energy electron promotions, predominantly from a ligand-ring π MO but also from other ligand based combinations (see figure 4.9) into metal f-levels. The third transition contains an approximately 50/50 mixture of uranyl σ_u → metal f along with ligand based nitrogen/carbon p → ligand ring π^* orbitals.

As in the spectrum of **D**, the experiment spectrum of **E** contains broad absorption peaks and so multiple transitions can be assigned to each band. Again, by comparing the theoretical and experimental spectra, I suggest the following assignments: the theoretical 558, 514, 492 and 467nm form $\mathbf{E}_1$ (in an approx. 2 : 7 : 30 : 4 ratio), and the second very broad experimental ($\mathbf{E}_2$) peak arises mainly from the following theoretical absorptions: 345, 337, 336, 334nm with a shoulder resulting from two further peaks at 322 and 311nm (in an approx. 12 : 6 : 3 : 1, : 2 : 8 ratio). The maximum error associated with these assignments is in the region of 0.25eV. Figure 4.10 shows the two absorption bands split into the main component transitions. Electronic excitations relating to $\mathbf{E}_1$ are shown in red and those relating to $\mathbf{E}_2$ in turquoise; I have coloured the shoulder of $\mathbf{E}_2$ green as it is unclear whether $\mathbf{E}_2$ should be regarded as one band or two. $\mathbf{E}_1$ shows similarities to $\mathbf{D}_1$ and arises mainly from electronic transitions from ligand nitrogen p-combinations into metallic f-levels. $\mathbf{E}_2$ (including the shoulder) shares similar features with $\mathbf{D}_2$ and $\mathbf{D}_3$, the transitions comprising this absorption band are from a number of complicated ligand based MOs into both metallic f-levels and also ligand ring π^* orbitals, and relate to a higher energy increase than the transitions involved in $\mathbf{E}_1$.

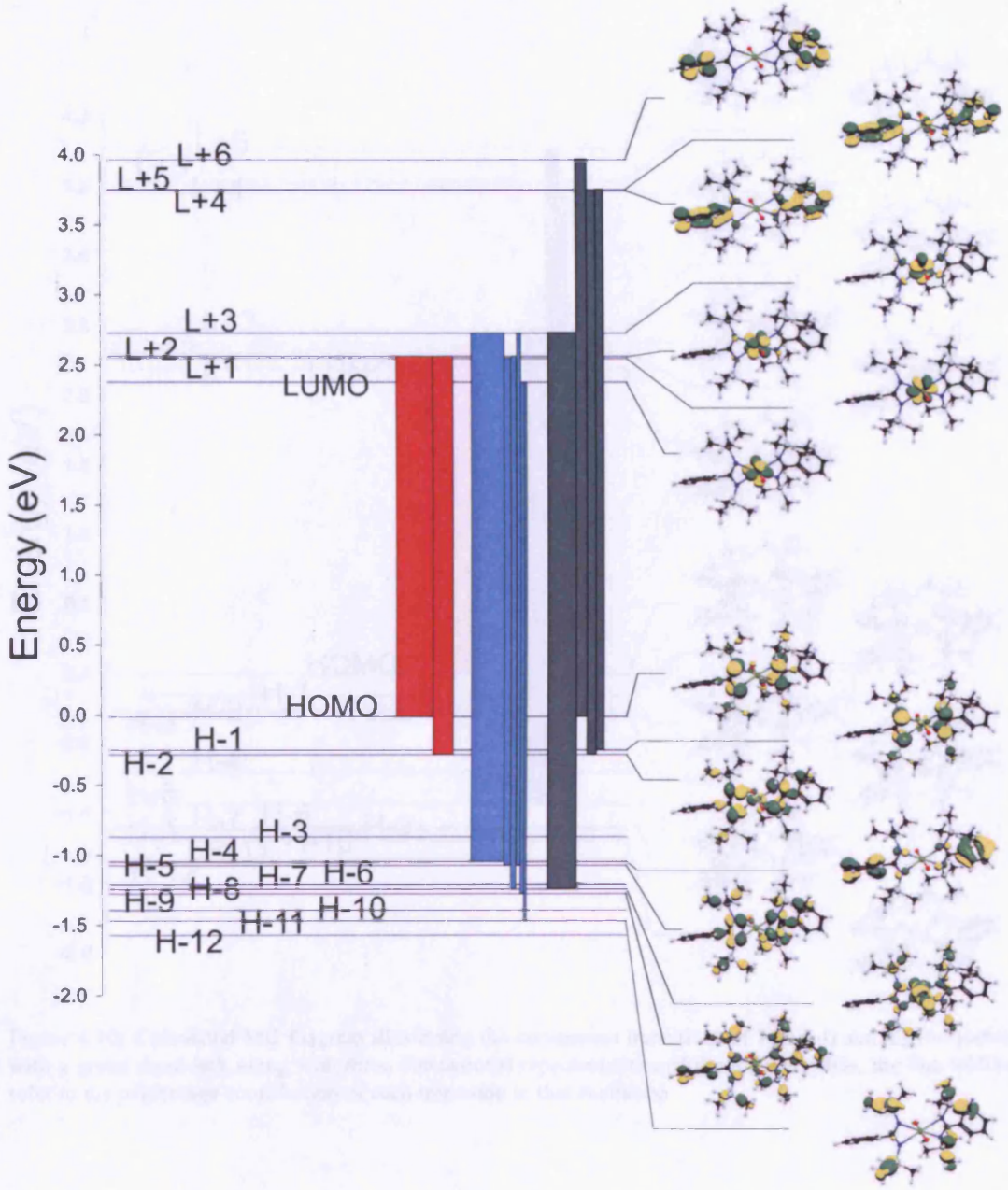

Figure 4.9: Calculated MO diagram illustrating the component transitions of $\mathbf{D}_1$ (red), $\mathbf{D}_2$ (turquoise) and $\mathbf{D}_3$ (green), along with three dimensional representations of the relevant MOs, the line widths refer to the percentage contribution of each transition to that excitation

Figure 4.11 presents an MO diagram showing the component transitions which comprise the first three absorption bands of **B**, $[UO_2Cl_2(thf)_2]$, for comparison with **D** and **E** (**A** and **C**, not shown, give similar results to **B**). From this diagram it can be seen that the

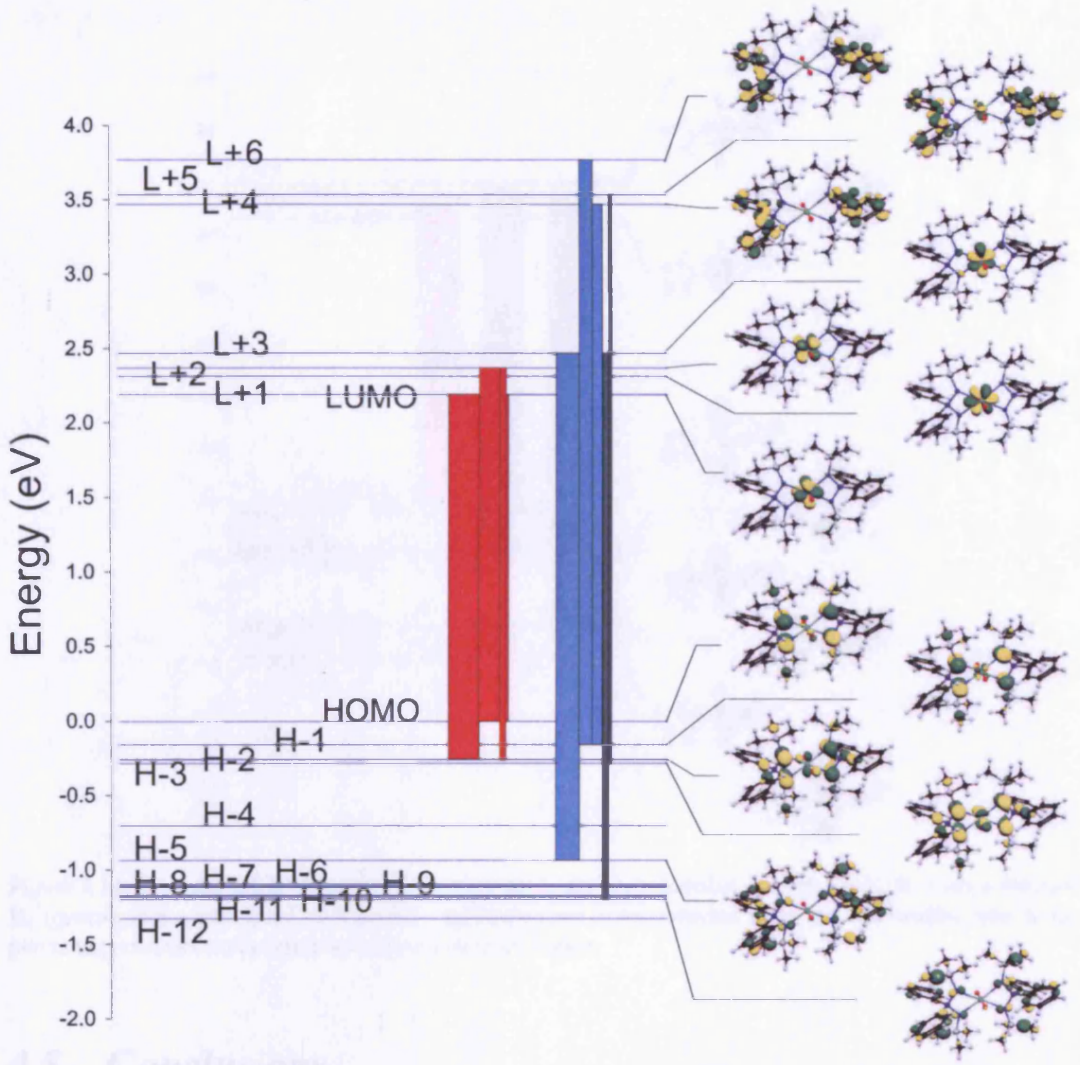

Figure 4.10: Calculated MO diagram illustrating the component transitions of $\mathbf{E}_1$ (red) and $\mathbf{E}_2$ (turquoise with a green shoulder), along with three dimensional representations of the relevant MOs, the line widths refer to the percentage contribution of each transition to that excitation

HOMO-LUMO gaps for **D** (2.4eV) and **E** (2.2eV) are smaller than for **B** (2.7eV). The first absorption band results from a single HOMO → LUMO+1 excitation, i.e. ligand Cl p → U f (see figure 4.11), and is of a similar nature to the transitions relating to $\mathbf{D}_1$ and $\mathbf{E}_1$. The component transitions of $\mathbf{B}_2$ and $\mathbf{B}_3$ are also shown in figure 4.11, although a detailed discussion of these is not presented here.

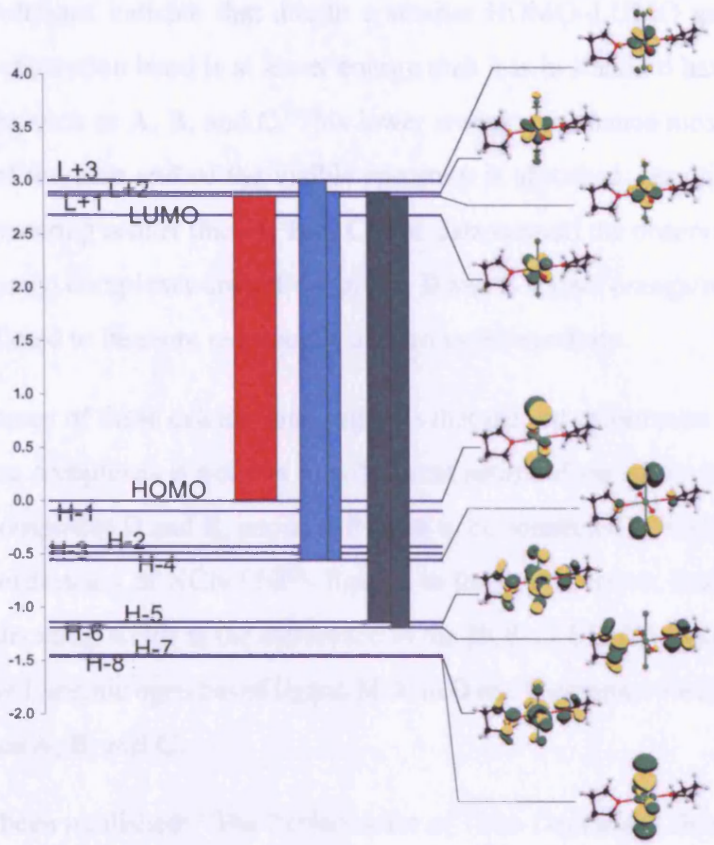

Figure 4.11: Calculated MO diagram illustrating the component transitions of $\mathbf{B}_1$ (red), $\mathbf{B}_2$ (turquoise) and $\mathbf{B}_3$ (green), along with three dimensional representations of the relevant MOs, the line widths refer to the percentage contribution of each transition to that excitation

4.5 Conclusions

(i) On the evidence of these calculations, the SAOP potential performs best for complexes containing uranyl, producing good agreement between theory and experiment; these results show errors of similar magnitude to the 'target error' of 0.5eV. Furthermore no advantage is seen in using high quality QZ4P basis sets over the standard basis sets used for geometry optimisations in this thesis, TZP for the metal and DZP for other atoms.

(ii) The first absorption band is due to a similar transition in each of the complexes studied here: a ligand-binding atom (Cl for **A**, **B**, **C**; N for **D**, **E**) $p \rightarrow$ metal f transition.

(iii) The calculations indicate that due to a smaller HOMO–LUMO gap in **D** and **E**, this first absorption band is at lower energy than it is in standard hard donor uranyl complexes such as **A**, **B**, and **C**. This lower energy absorbance means that a larger portion of the blue end of the visible spectrum is absorbed, resulting in the complexes appearing redder than **A**, **B** or **C**. The data support the observation that while typical uranyl complexes are yellow-green, **D** and **E** appear orange/red; furthermore **E** is predicted to be more red than **D**, as seen experimentally.

(iv) The evidence of these calculations suggests that the red colouration of the N-donor containing complexes is not due to a different nature of excitation in nitrogen containing complexes **D** and **E**, nor does it seem to be connected to the distorted out-of-plane coordination of NCN / NPN ligands to the uranyl centre. Instead I conclude that the deciding factor is the difference in the HOMO-LUMO gap due to the relatively low-lying nitrogen based ligand MOs in **D** and **E** compared with typical uranyl complexes **A**, **B**, and **C**.

This work has been published: "The Performance of Time-Dependent Density Functional Theory (TD-DFT) in the simulation of the Electronic Spectra of Molecular Uranium Complexes" by Kieran I. M. Ingram and Nikolas Kaltsoyannis.*Recent Advances in Actinide Science*, Royal Society of Chemistry 2006, 258 - 260.

Chapter 5

Covalency in the *f*-element – chalcogen bond; computational studies of $[M(N(EPR_2)_2)_3]$, M = Ln (Ln = La, Ce, Pr, Pm, Eu), An (An = U, Np, Pu, Am, Cm); E = O, S, Se, Te; R = H, Me, ^{i}Pr

5.1 Introduction

The separation of U(III) and Pu(III) isotopes as well as the minor actinides Am(III) and Cm(III), from Ln(III) is an important process in many areas including reprocessing spent fuel, storing radiotoxic waste, and transmutation of harmful isotopes.[173] Separation of An(III) from Ln(III) is a challenge because there are many similarities between the properties of the trivalent ions from the two series of homologous elements; both are strongly hydrated in aqueous solution, both bind directly with a variable number of electron-donor atoms forming from 6 to 12 bonds, and they have similar ionic radii. In addition Ln(III) and An(III) are hard acids, therefore reacting with hard bases such as groups which bind through oxygen. Such interactions are understood to be mainly electrostatic and therefore Ln(III) and An(III) have very similar reactivities with a given hard ligand.

The 5*f* shell is known to be more spatially diffuse than the 4*f* (see chapter 1) and it is hoped that this difference can be exploited to obtain a difference in bonding between Ln(III) and An(III) by selecting ligands with softer electron-donor atoms (e.g. Cl, N, S) which are thus more capable of separating these two series of metals from one another. For similar sized Ln(III) and An(III) (e.g. Pm and Am, Sm and Cm, Eu and Cf[25,26]) separation factors of approx. 10 can be achieved using Cl^- ligands in a two-phase separation,[174] N-binding ligands can reach a separation factor of around 100,[175] and a thousandfold pref-

erence for An(III) over Ln(III) has been seen using softer sulphur-bonding ligands.[176,177]

Recent experimental work at the Los Alamos National Laboratory has focused on the synthesis and characterization of a range of homoleptic, trivalent lanthanum and uranium complexes with imidodiphosphinochalcogenide ligands $[N(EPPh_2)_2]^-$ (E = S, Se)[178] and $[N(TeP^iPr_2)_2]^-$.[179] The principal aim of the research is to explore the differences in *f*-element–ligand bonding between Ln(III) and An(III) with soft donor ligands such as S, Se, Te in the anticipation that the actinide bond with heavier chalcogens will be more covalent than the analogous lanthanide bond. Structural data suggest that this is indeed the case, with significantly shorter *r*(U–Te) than *r*(La–Te), despite the ionic radii of La^{3+} and U^{3+} being essentially identical.[180]

This chapter focuses on the use of four different tridentate ligands, $N(EPR_2)_2$ where E = O, S, Se and Te, to investigate the differences between Ln(III) and An(III). The work in this chapter systematically probes complexes of the formula $[M(N(EPR_2)_2)_3]$ (M = Ln (Ln = La, Ce, Pr, Pm, Eu), An (An = U, Np, Pu, Am, Cm); E = O, S, Se, Te, R = H, Me) to see what trends are observed in the M–E bond, with the hope that small differences in bonding character between Ln and An, i.e. the tendency of early actinides to form chemical bonds with some covalent character whereas lanthanides form ionic bonds, might be exaggerated by ligands that contain softer, heavier chalcogens such as S, Se and Te.

I will now present a selection of previous studies comparing An–E with Ln–E, with a view to emphasising the similarities and differences between bonding in the complexes of each type of metal, and furthermore to survey the magnitude of the differences I can expect in my study.

5.2 Literature Review

In 2005 Roger *et al* carried out a joint experimental/computational comparison of $[Ce(Cp^*)_2(dddt)]^-$ and $[U(Cp^*)_2(dddt)]^-$ (also $[U(Cp^*)_2(dddt)]^0$; dddt = 5,6-dihydro-1,4-dithiine-2,3-dithiolate).[24] The optimised geometries showed reasonable agreement with experiment, although the calculations tended to overestimate the differences between the two metals in *r*(M–Cp*) (experimentally U–Cp* is 0.03Å longer than Ce–Cp*, computationally 0.1Å) and *r*(M–S) (experimentally U–S is 0.02Å longer than Ce–S, computa-

tionally 0.08Å). As the ionic radius of U(III) is only 0.01Å larger than that of Ce(III),[25,26] clearly other influences are involved in M–Cp* and M–S bonding in these complexes. Also of interest, it was observed that the calculated ring C–C (Cp*) and C=C (dithiolene) are shorter in the cerium complex than the uranium.

Roger *et al* present an elegant MO diagram, from which the following points are a summary: in the cerium complex almost all the high energy occupied MOs have less than 5% metal character, therefore implying a small covalent interaction. Furthermore, the 5*d* contribution is significantly larger than the 4*f*. In contrast with this the high energy MOs in the uranium complex generally contain between 6 and 10% metal character, with approximately half of the high energy MOs having a larger metal *f* contribution than *d*. This analysis suggests that the contraction of U–S compared to Ce–S may be related to U 5*f* mixing with ligand σ and π as this mixing is greater in the uranium complex than the cerium. Covalency appears more marked in the U complex than in the Ce, both in L→M donation and M→L back donation interactions. Mulliken analysis of $[U(Cp^*)_2(dddt)]^-$ and $[Ce(Cp^*)_2(dddt)]^-$ reveals that the net charge on each M is lower than the formal charge, and furthermore that q_U is considerably lower than q_{Ce}, 0.7 *vs.* 1.3 respectively for the formally +3 metals. This is consistent with the idea of U having an increased covalent component to its bonding, L→M donation lowers the atomic charge on M, although the authors note that these are Mulliken charges which are known to be very basis set dependent and so the large discrepancy in q_M could be (partially) due to basis set differences. Mulliken overlap populations reveal U–Cp* and U–S have greater covalent components to their bonding than do Ce–Cp* and Ce–S, but the latter still have non-negligible covalent contributions. The overlap populations between M and Cp* particularly indicate a significantly larger Cp*→U(III) donation than Cp*→Ce(III) which leads to the reduced charge on U *vs.* Ce. Prominent back donation from U(III)→L compared with Ce(III)→L means that the $\pi*$ antibonding orbitals of the ligand are more populated in the U complex and this is seen in longer C–C (Cp*) and C=C (dithiolene) bonds in the ligands; these data are supported by the Mulliken overlap populations.

Recently Cao *et al* have been investigating the motexafins of the trivalent lanthanides and actinides[181] (see figure 5.1). Ln(III)–motexafins, $(Ln–motex)^{2+}$, have been found to

have significant medical uses, especially in the diagnosis and treatment of cancer and related conditions.[182–184] These important uses of lanthanide motexafins, coupled with

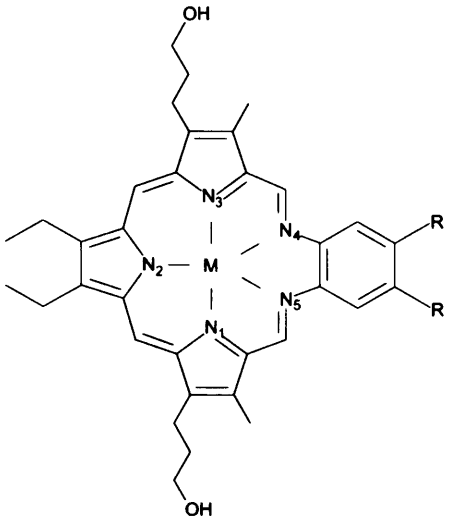

Figure 5.1: Structure for Ln(III) and An(III) motexaphyrins, $(M\text{-motex})^{2+}$, R = $O(CH_2CH_2O)_3CH_3$

a knowledge of the need for ligands capable of achieving good Ln(III)/An(III) separation factors has lead to (so far unsuccessful) attempts to synthesise $(An\text{–motex})^{2+}$ analogues,[185] and Cao *et al*'s theoretical investigation calculates geometric parameters as well as charge data and binding energies to shed some light on the synthetic problem. The calculations show that $r(An\text{–}N_i) > r(Ln\text{–}N_i)$ (i = 1, 2, 3, 4, 5) for each i, typically by ~0.05Å. Furthermore for $r(Ln\text{–}N_i)$, La $>^{0.1\mathring{A}}$ Gd $>^{0.06\mathring{A}}$ Lu and Ac $>^{0.1\mathring{A}}$ Cm $>^{0.07\mathring{A}}$ Lr. A metal–ring-plane distance was also calculated and the actinides each sit further from the plane of the nitrogen ring than their isoelectronic valence Ln.

Mulliken charge and population data suggest that the orbital stabilisation accompanying the lanthanide/actinide contraction favours ligand → metal s and p charge transfer, evidenced by the increasingly oxidised ligand as atomic number increases along each series of metals. Small HOMO–LUMO gaps (~0.4eV) were calculated for all $(Ln\text{–motex})^{2+}$ and $(An\text{–motex})^{2+}$ indicating that these complexes easily absorb electrons in an electron-rich environment, this is supported by experimental data for the lanthanide complexes.[186] The experimental instability of $(An\text{-motex})^{2+}$ compared with $(Ln\text{–motex})^{2+}$ are also predicted by the binding energies, values of ~10eV was calculated for the latter, around 1.5eV

higher than for the former.

In a 2006 paper[187] Petit *et al* mention that population and orbital analysis fail to adequately describe Am(III) systems, and so by using Quantum Chemical Topologies (QCT) try a different approach to the problem, investigating F_3MCO, M = Nd, U, Am (also I_3MCO, M = U, Am, not discussed here). A standard G03/B3LYP DFT approach was used for geometry optimisations and Mulliken/Natural charge analysis, and further calculations (AIM[188] and ELF[189,190]) were made using the Topmod package.[191] Analysis of the M–C bond lengths showed that r(U–C) (2.43Å) was considerably shorter than r(Nd–C) (2.88Å) and r(Am–C) is in between (2.66Å). Mulliken, Natural and AIM and ELF charges all predicted $q_U > q_{Nd}$ (the numbers for the latter three methods were similar, Mulliken charges were significantly smaller), but while Mulliken analysis calculated q_{Am} approx. halfway between q_U and q_{Nd}, the other three methods all predicted similar q_{Am} and q_{Nd}. In addition to this Natural, AIM and ELF methods all calculated a sizable negative charge on the CO fragment (between -0.33 and -0.48); Mulliken analysis did not. The Natural and QCT data support the idea of a backbonding interaction from U to CO leading to a surplus of electron density on the carbonyl ligand and a surfeit on the metal centre, but show no real difference between Nd(III) and Am(III).

The QCT methods also calculate a direct measure of backbonding. The difference between the Nd–C and U–C bond lengths is attributed to a U $5f \rightarrow$ CO π^* back bonding interaction of approx. $0.5e^-$; a significantly smaller back donation of $0.1e^-$ was calculated from Am $5f$ to CO π^*, and a trivial $0.01e^-$ from Nd (with both AIM and ELF methods). Further QCT data gives δ(M,C), a measure of the number of electrons between the M and C atoms. The AIM numbers show $0.2e^-$ are shared between Nd and C, 0.4 for Am and C and 0.94 between U and C, ELF predicts a similar pattern with ~20% smaller numbers. The authors conclude that the Am(III) exhibits a low magnitude covalent interaction, compared with the negligible covalency in F_3NdCO and the significant covalency seen in F_3UCO.

Guillaumont (2004)[62] details a quantum chemistry investigation of the difference between Ln(III) and An(III) (Ln = La, Ce, Nd; An = U, Pu, Am, Cm) with tridentate nitrogen ligands in the complex $[M(L)(H_2O)_6]^{3+}$ for L = Terpy, MeBtp (see figure 5.2) and also

$[M(H_2O)_6]^{3+}$, as a hard-ligand only comparison. Separation factors of over 100 have been obtained with RBtp ligands.[192] However, although several tridentate N-donor ligands give rise to high separation factors, some other ligands of the same family present very poor separation properties[193,194] and so an in depth understanding of the bonding mechanism of these ligands with trivalent lanthanide and actinide ions is essential to advance separation techniques. Guillaumont's paper presents a thorough analysis of the bond lengths and MO compositions and I will concentrate on the pertinent points.

The three metal–ligand bonds, $r(M–N_a)$, $r(M–N_b)$ and $r(M–O_{H_2O})$ decrease (typically by ~0.05-0.06Å across the series) from M = La to M = Nd, in line with the decreasing ionic radii of the lanthanides. For the actinides, $r(M–O_{H_2O})$ decreases from U to Cm, again a range of ~0.05Å is calculated across the series. However, in the terpy and MeBtp complexes, $r(M–N_a)$ and $r(M–N_b)$ *increase* from U to Am, and only from Am to Cm do $r(An–N_a)$ / $r(M–N_b)$ decrease. This suggests that Ln(III) and An(III) form similar ionic bonds with hard ligands, but that there is a difference in the bonding between Ln and An with softer ligands such as MeBtp and terpy.

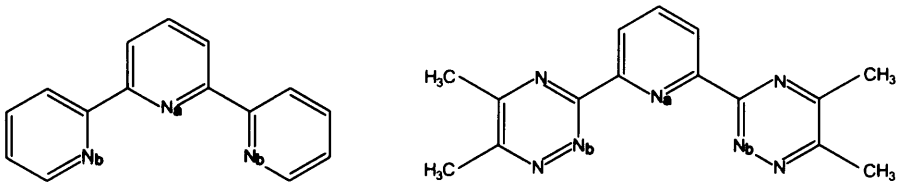

(a) **Terpy** (b) **MeBtp**

Figure 5.2: Terpy and MeBtp ligands

Mulliken charge analysis predicts q_{Ln} are all similar but q_{An} are considerably smaller and decrease with increasing atomic number (although $q_{Cm_{Mull}} < q_{Am_{Mull}}$). Hirshfeld charges do not indicate any bonding trends within either series of metals. Guillaumont summarises by finding that metal–ligand bonding in both series is predominantly ionic, but that covalency is seen in ligand-to-metal donation, and is slightly more pronounced for the actinides than the lanthanides. The author further concludes that the differences between the two series reach the limits of calculational error and approximations for americium and curium and therefore no firm conclusions can be drawn about these two metals, although

the data seem to imply that covalency in actinide(III) is mainly limited to U and Pu, with Am(III) and Cm(III) behaving more like Ln(III).

Given that Guillaumont's calculations put one soft ligand onto a metal centre coordinated to six water molecules, I am hopeful that by comparing homoleptic complexes with three bidentate chalcogen-binding ligands around a metal centre, and by increasing the softness of the chalcogen, this might exaggerate the differences seen between Ln(III) and An(III) and give more insight into how to separate these chemically similar species.

5.3 Computational Details

All calculations were carried out using gradient corrected DFT, as implemented in the Gaussian 03[82] (G03) and Amsterdam Density Functional[78–80] (ADF) quantum chemical codes. Spin-unrestricted calculations were performed on all except the f^0 La complexes, to account for the formal f^n configurations of Ln^{3+} and An^{3+} (n = 1(Ce), 2(Pr), 3(U), 4(Pm, Np), 5(Pu), 6(Eu, Am) and 7(Cm)).

The GGA functional PBE[47,48] was used for all G03 calculations. (14*s* 13*p* 10*d* 8*f*)/[10*s* 9*p* 5*d* 4*f*] segmented valence basis sets with Stuttgart-Bonn variety[128] relativistic effective core potentials (RECPs) were used for the actinides, and a (14*s* 13*p* 10*d* 8*f*)/[10*s* 8*p* 5*d* 4*f*] segmented valence basis set with a Stuttgart-Bonn RECP[128] was used for each lanthanide. 6-31G* basis sets were used for the O, S, Se, N, and P atoms, and the smaller 6-31G was used for H. Te was described with a (4*s* 5*p*)/[2*s* 3*p*] Stuttgart basis set[195] augmented to (4*s* 5*p* 7*d*)/[2*s* 3*p* 3*d*] with STO-3G*[196,197] polarisation functions (for consistency, as 6-31G* includes polarisation functions on O, S and Se); a Stuttgart RECP was also used for Te.[195] The validity of this augmented Te basis set was checked by constructing an analogous Se basis set - a Stuttgart (4*s* 5*p*)/[2*s* 3*p*] augmented to (4*s* 5*p* 4*d*)/[2*s* 3*p* 2*d*] - and performing test geometry optimisations on $[M(N(SePH_2)_2)_3]$ for M = La, U; similar geometries were found with both methods.

The default values for the integration grid ("fine") and the convergence criteria were used for all geometry optimisations (max. force = 4.5×10^{-4} au $Å^{-1}$, SCF = 10^{-8}) with a few exceptions; the praseodymium and plutonium calculations were more problematic and the convergence criteria listed in table 5.1 were used.

Species	Max. Force (au Å^{-1})	SCF
$[Pu(N(OPH_2)_2)_3]$	7×10^{-4}	10^{-7}
$[Pu(N(SPH_2)_2)_3]$	8×10^{-4}	10^{-5}
$[Pu(N(SePH_2)_2)_3]$	5×10^{-4}	default
$[Pu(N(TePH_2)_2)_3]$	8×10^{-4}	10^{-5}
$[Pr(N(SPH_2)_2)_3]$	8×10^{-4}	10^{-7}
$[Pr(N(SePH_2)_2)_3]$	8.5×10^{-4}	10^{-6}
$[Pr(N(TePH_2)_2)_3]$	10×10^{-4}	10^{-5}

Table 5.1: Non-default convergence criteria used for some $[M(N(EPH_2)_2)_3]$

A Natural charge and population analysis[96–102] was carried out on all G03 optimised structures.

Little spin contamination was found for any of the non-zero nf^n complexes, as evidenced by the fact that the values of $\langle S^2\rangle$ were close to the ideal $S(S+1)$ ($S = n/2$) in all cases, with 6.0067 for $[Pm(N(TePH_2)_2)_3]$ being the largest deviation from the ideal, 6.00 for the f^4 Pm^{3+}.

5.3.1 ADF

Single point calculations on optimised G03 structures were carried out in ADF. As with G03 the PBE functional was used. TZP Zero Order Regular Approximation (ZORA) basis sets were used for each of the f-elements together with DZP ZORA basis sets for O, S, Se, P, and N; DZ was used for H. ADF does not have a DZP basis set for Te and so TZP polarisation functions were added to the DZ basis. The frozen core approximation was used. A $5d$ core was used for each actinide, $4d$ for the lanthanides and Te, $3d$ for Se, $2p$ for S, P, and $1s$ for O, N. Mulliken[126,127] population and overlap population[126,127] analyses were carried out.

5.4 Results

5.4.1 Geometries of the La and U complexes

The first part of this chapter focuses on calculations of the lanthanum and uranium complexes of formula $[M(N(EPR_2)_2)_3]$ (E = O, S, Se, Te; R = H, Me). Before extending this work to cover more of the lanthanide and actinide series, various approximations were tested to see if it would be possible to cut computational cost, and the results of these tests are reported first. Sections 5.4.4 onwards report the results of extending this study to include Ln = Ce, Pr, Pm, Eu and An = Np, Pu, Am, Cm for $[Ln/An(N(EPR_2)_2)_3]$ (E = O, S, Se, Te; R = H).

Crystallographic data for the structures of $[M(N(SP^iPr_2)_2)_3]$ and $[M(N(SeP^iPr_2)_2)_3]$ (M = La, U) provided the initial conformations for the geometry optimisations. The ^{i}Pr fragments were replaced with smaller R groups (R = H, Me) and geometry optimisations were carried out on the four complexes obtained. Calculations on further complexes were then carried out starting from these optimised structures: S was substituted by O for each metal and Se by Te. In this way a complete set of 16 geometry optimised were obtained: four for each metal with the H approximation to the ligands' ^{i}Pr groups and four for each metal with the Me approximation.

After the geometry had been optimised, the symmetry of each complex was idealised to D_3 and a further geometry optimisation was carried out. In each case the energy of the D_3 complex was very close to that of the C_1 complex (table 5.2); indeed, in six cases the idealised D_3 structures were actually lower in energy than their non-symmetry counterparts, although such small differences are not significant. The structures of the symmetrised and non-symmetrised complexes were also very similar, see table 5.3, suggesting that idealising the symmetry to D_3 (with its favourable consequences for electronic structure analysis) is not a significant perturbation.

Figures 5.3, 5.4, 5.6 and 5.7 show ball + stick representations of the structures of $[M(N(EPR_2)_2)_3]$; figure 5.3 shows M = La, R = H; figure 5.4 shows M = La, R = Me, figure 5.6 shows M = U, R = H , and figure 5.7 shows M = U, R = Me, all structures with D_3 symmetry. Selected bond lengths and bond angles are given in table 5.3, and figures 5.5 and 5.8 illustrate r(M–E) down group 16 for both metals. Figures 5.3–5.8 show that

Species	Lanthanum Energy	ΔE	Uranium Energy	ΔE
O $R = H, D_3$	-8152547.2		-8261081.6	
O $R = H, C_1$	-8152552.9	-5.8	-8261101.8	-20.2
O $R = Me, D_3$	-9389755.7		-9498294.9	
O $R = Me, C_1$	-9389758.6	-2.8	-9498307.0	-12.1
S $R = H, D_3$	-13238196.7		-13346763.4	
S $R = H, C_1$	-13238194.9	1.7	-13346761.0	2.4
S $R = Me, D_3$	-14475398.6		-14583961.1	
S $R = Me, C_1$	-14475399.0	-0.3	-14583962.4	-1.3
Se $R = H, D_3$	-44752760.9		-44861332.7	
Se $R = H, C_1$	-44752761.3	-0.3	-44861329.9	2.8
Se $R = Me, D_3$	-45989954.5		-46098533.4	
Se $R = Me, C_1$	-45989955.8	-1.3	-46098535.5	-2.1
Te $R = H, D_3$	-7095913.6		-7204478.9	
Te $R = H, C_1$	-7095914.1	-0.5	-7204478.1	0.8
Te $R = Me, D_3$	-8333090.9		-8441656.0	
Te $R = Me, C_1$	-8333089.6	1.3	-8441653.3	2.7

Table 5.2: The total energies (kJ/mol) of the La and U complexes calculated with (D_3) and without (C_1) symmetry constraints. $\Delta E = E(C_1) - E(D_3)$

as the chalcogen is changed from oxygen to tellurium, r(M–E) lengthens significantly (for both the H and Me approximations), the increase being largest between oxygen and sulphur, followed by a smaller increase from sulphur through selenium to tellurium. The calculated r(M–E) agree very well with experiment in all cases (the maximum discrepancy between theory and experiment is *ca.* 0.04 Å) regardless of the level of approximation to the R groups, supporting the use of H or Me as structural models for the experimental ^{i}Pr group in the ligands.

Figure 5.9 shows that while r(M–O) is very similar for uranium and lanthanum, the difference between r(La–E) and r(U–E) increases down group 16. This agrees well with experiment, and suggests that the U–E bonding for the heavier chalcogens is different from the analogous La complexes. This is probed further in sections **5.4.2 – 5.4.9**.

LANTHANUM

	Oxygen				Sulphur					Selenium					Tellurium				
	H approx		Me approx		H approx		Me approx		Expt.	H approx		Me approx		Expt.	H approx		Me approx		Expt.
	D_3	C_1	D_3	C_1	D_3	C_1	D_3	C_1	C_1	D_3	C_1	D_3	C_1	C_1	D_3	C_1	D_3	C_1	C_1
Bond Lengths/Å																			
La-E	2.417	2.422	2.414	2.419	2.916	2.920	2.914	2.914	2.892	3.027	3.026	3.021	3.024	3.019	3.232	3.230	3.223	3.223	3.224
P-E	1.553	1.554	1.560	1.564	2.043	2.044	2.060	2.060	2.022	2.198	2.198	2.219	2.217	2.185	2.443	2.443	2.461	2.462	2.445
P-N	1.612	1.621	1.624	1.624	1.636	1.635	1.633	1.635	1.587	1.638	1.639	1.637	1.636	1.595	1.643	1.644	1.637	1.638	1.594
Bond Angles/°																			
E-La-E (α)	81.7	82.1	81.2	80.1	89.4	88.7	85.7	86.1	86.1	91.3	90.3	87.8	88.2	88.6	92.2	92.1	90.6	90.6	90.9
P-E-La (β)	134.3	133.4	131.3	132.7	105.9	106.3	113.6	112.7	117.8	103.4	102.5	109.2	109.7	114.7	101.7	101.9	106.7	106.8	111.1
N-P-E (γ)	120.0	119.5	118.0	118.0	120.8	121.2	118.9	118.8	119.4	121.5	121.0	118.6	119.1	118.7	120.4	120.3	119.3	119.6	120.8

URANIUM

	Oxygen				Sulphur					Selenium					Tellurium				
	H approx		Me approx		H approx		Me approx		Expt.	H approx		Me approx		Expt.	H approx		Me approx		Expt.
	D_3	C_1	D_3	C_1	D_3	C_1	D_3	C_1	C_1	D_3	C_1	D_3	C_1	C_1	D_3	C_1	D_3	C_1	C_1
Bond Lengths/Å																			
U-E	2.393	2.395	2.397	2.394	2.849	2.842	2.826	2.837	2.853	2.955	2.948	2.928	2.925	2.963	3.126	3.125	3.125	3.124	3.164
P-E	1.555	1.556	1.566	1.566	2.048	2.050	2.066	2.067	2.025	2.206	2.208	2.230	2.228	2.176	2.461	2.461	2.475	2.477	2.438
P-N	1.612	1.621	1.624	1.624	1.636	1.635	1.633	1.633	1.582	1.638	1.640	1.637	1.637	1.591	1.643	1.643	1.637	1.637	1.586
Bond Angles/°																			
E-U-E (α)	81.7	82.1	81.2	80.1	89.4	88.7	85.7	86.1	86.3	91.3	90.3	87.8	88.2	88.7	92.2	92.1	90.6	90.6	90.9
P-E-U (β)	134.3	133.4	131.3	132.7	105.9	106.3	113.6	112.7	118.3	103.4	102.5	109.2	109.7	114.9	101.7	101.9	106.7	106.8	111.7
N-P-E (γ)	120.0	119.5	118.0	118.0	120.8	121.2	118.9	118.8	119.2	121.5	121.0	118.6	119.1	119.4	120.4	120.3	119.3	119.6	120.4

Table 5.3: Selected bond lengths and angles (see figure 5.3(d) for definitions of α, β, γ) from the D_3 and C_1 optimised geometries of $[M(N(EPR_2)_2)_3]$ (M = La, U; E = O, s, Se, Te; R = H, Me), together with experimental data (M = La, U, E = S, Se, Te; R = ^{i}Pr)

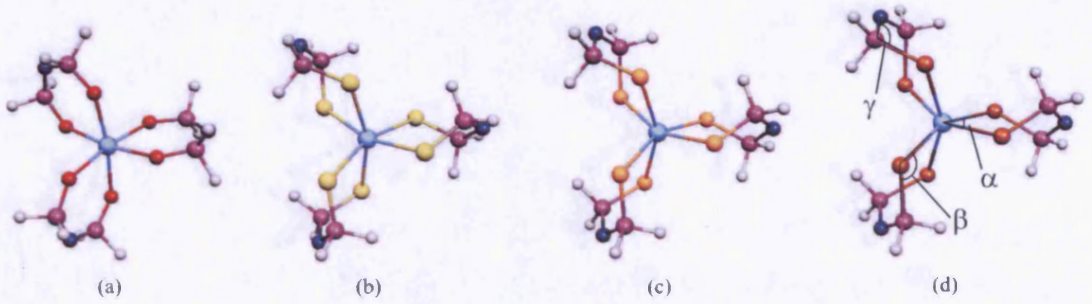

Figure 5.3: Ball and stick representations of the D_3 optimised geometries of $[La(N(EPH_2)_2)_3]$; E = O (a), S (b), Se (c), Te (d)

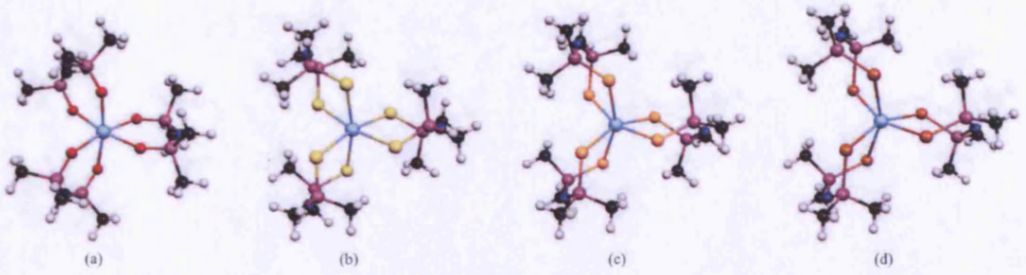

Figure 5.4: Ball and stick representations of the D_3 optimised geometries of $[La(N(EPMe_2)_2)_3]$; E = O (a), S (b), Se (c), Te (d)

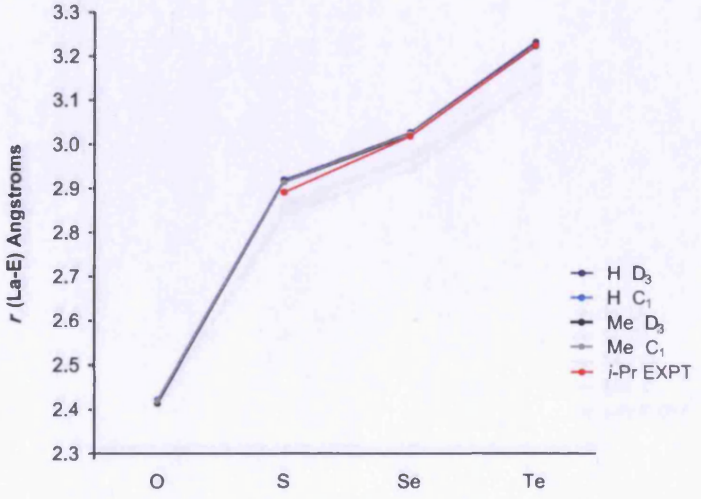

Figure 5.5: Calculated r(La–E) in $[La(N(EPR_2)_2)_3]$ for E = O, S, Se, Te; R = H, Me; both C_1 and D_3, together with the experimental data for $[La(N(EP^iPr_2)_2)_3]$

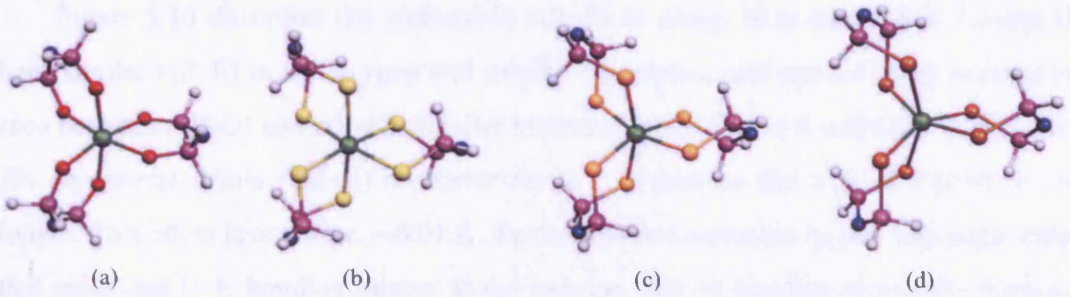

Figure 5.6: Ball and stick representations of the D_3 optimised geometries of $[U(N(EPH_2)_2)_3]$; E = O (a), S (b), Se (c), Te (d) (D_3)

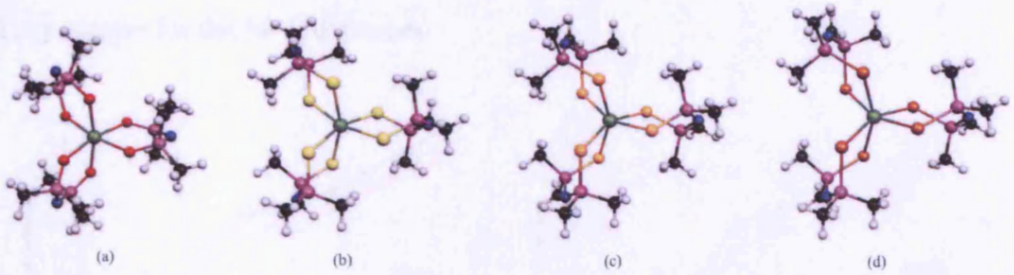

Figure 5.7: Ball and stick representations of the D_3 optimised geometries of $[U(N(EPMe_2)_2)_3]$; E = O (a), S (b), Se (c), Te (d) (D_3)

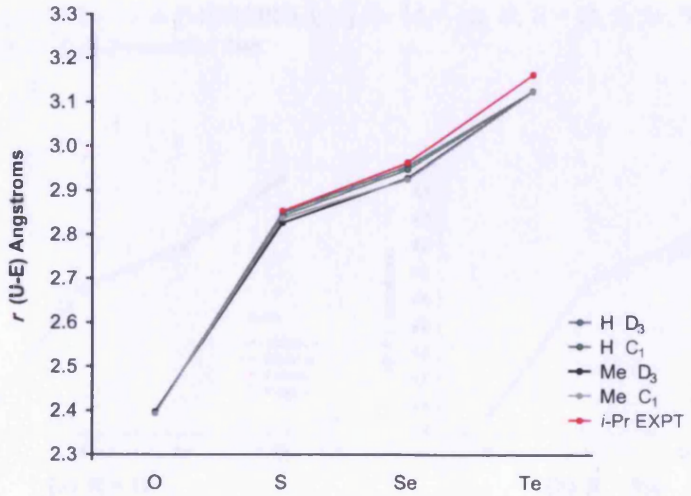

Figure 5.8: Calculated r(U–E) in $[U(N(EPR_2)_2)_3]$ for E = O, S, Se, Te; R = H, Me; both C_1 and D_3 together with the experimental data for $[U(N(EP^iPr_2)_2)_3]$

Figure 5.10 illustrates the increase in r(P–E) as group 16 is descended. La and U have similar r(P–E) in the oxygen and sulphur complexes, and again a large increase is seen between r(P–O) and r(P–S). Smaller increases in r(P–E) are found from S to Se and Te. In general, while r(M–E) is shorter for M = U than La (for a given E), r(P–E) is longer. This effect is not large, ~0.01 Å , but it is present consistently, possibly suggesting that enhanced U–E bonding occurs at the expense of P–E bonding within the ligands. The P–N bond lengths are not reproduced perfectly by these calculations; a systematic overestimation of *ca.* 0.05 Å is present. While this discrepancy is larger than is ideal, it is not a major concern, particularly given the generally excellent agreement between theory and experiment for the M–E distances.

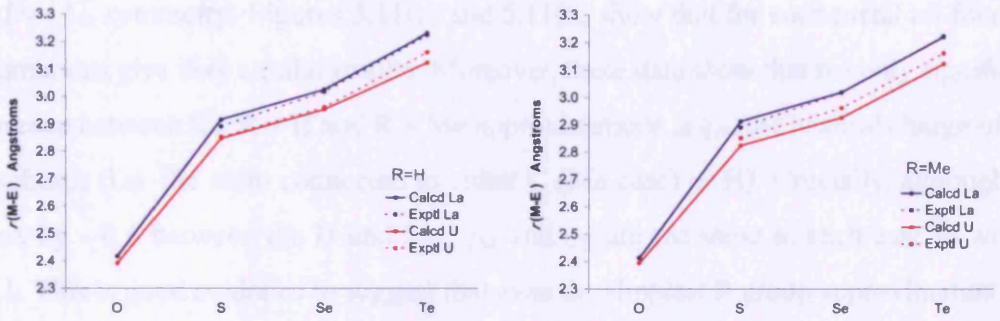

(a) **R = H** (b) **R = Me**

Figure 5.9: Calculated r(M–E) in [M(N(EPR)$_2$)$_2$)$_3$] for M = La, U; E = O, S, Se, Te; R = H, Me; D_3 symmetry, compared with experimental data

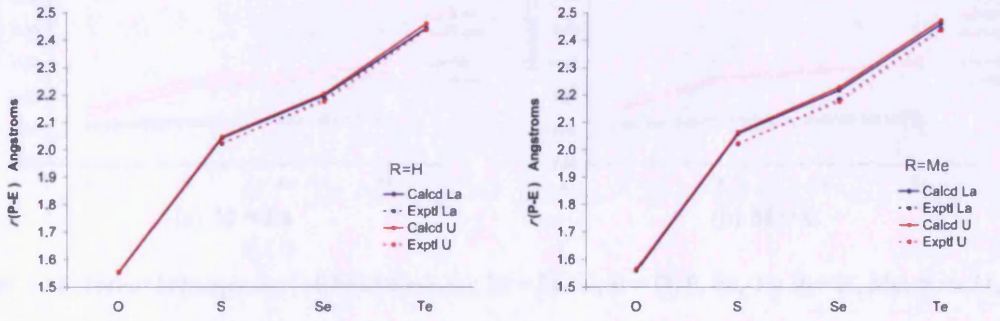

(a) **R = H** (b) **R = Me**

Figure 5.10: Calculated r(P–E) in [M(N(EPR)$_2$)$_2$)$_3$] for M = La, U; E = O, S, Se, Te; R = H, Me; D_3 symmetry compared with experimental data

The $\angle EME$ bite angles, α defined in figure 5.3(d), agree well with experimental

results for both metals. More specifically, the correct trend is seen; as the chalcogen gets bigger so too does $\angle EME$. Once again a large jump is seen on moving from O to S, and then a smaller gradual increase from S, through Se to Te. The $\angle NPE$ angle (γ) is essentially constant in all the complexes, barely deviating from 120°. The $\angle PEM$ angle (β) is underestimated computationally by *ca.* 5° (Me approx) or 10° (H approx). The reasons for this are unclear, but as when considering r(P–N), I do not believe that these minor angular deviations will adversely affect the analyses of the M–E bonding.

5.4.2 Charge analysis of the La / U complexes

Natural charge analysis was carried out on the optimised geometries of all 32 complexes, i.e. for both La and U, with E = O, S, Se and Te, with H and Me approximations to ^{i}Pr and D_3 / C_1 symmetry. Figures 5.11(a) and 5.11(b) show that for each metal all four approximations give very similar results. Moreover, these data show that the only significant difference between the R = H and R = Me approximations is q_P, the Natural charge of the phosphorus (i.e. the atom connected to either C (Me case) or H). Crucially, although q_P differs by ~0.6 between the H and Me, q_M and q_E are the same in each case to within $\ll$0.1. This is good evidence to suggest that even the simplest R group approximation (H) provides a valid description of the metal–chalcogen charge distribution in these systems.

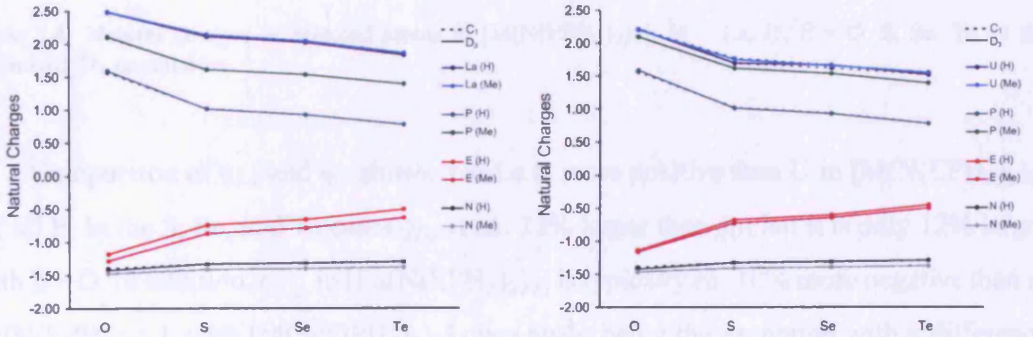

(a) **M = La** (b) **M = U**

Figure 5.11: Natural charges for [M(N(EPR$_2$)$_2$)$_3$]; M = La, U; E = O, S, Se, Te; R = H, Me; both D_3 and C_1

The Natural charges for all [M(N(EPR$_2$)$_2$)$_3$] are collected in table 5.4. Using the D_3 [M(N(EPH$_2$)$_2$)$_3$] numbers as an example, a decrease in q_U from 2.218(O) to 1.524(Te) is seen, a drop of 0.694, accompanied by an increase in q_{E_U} from -1.132(O) to -0.444(Te),

an increase of 0.688. For La, there is a decrease in q_{La} from 2.490(O) to 1.834(Te), a drop of 0.656, accompanied by an increase in $q_{E_{La}}$ from -1.174(O) to -0.494(Te), a rise of 0.68. Both La and U analogues see a decrease of ~0.81 for q_P and a small rise of 0.13 for q_N.

LANTHANUM	O	S	Se	Te	URANIUM	O	S	Se	Te
q_{La}					q_U				
C_1 R = H	2.483	2.120	2.027	1.834	C_1 R = H	2.215	1.696	1.624	1.524
D_3 R = H	2.490	2.117	2.027	1.834	D_3 R = H	2.218	1.701	1.670	1.524
C_1 R = Me	2.486	2.139	2.047	1.865	C_1 R = Me	2.219	1.770	1.666	1.556
D_3 R = Me	2.497	2.141	2.046	1.863	D_3 R = Me	2.205	1.756	1.659	1.555
q_E					q_E				
C_1 R = H	-1.171	-0.737	-0.649	-0.494	C_1 R = H	-1.128	-0.673	-0.596	-0.444
D_3 R = H	-1.174	-0.731	-0.649	-0.494	D_3 R = H	-1.132	-0.670	-0.597	-0.444
C_1 R = Me	-1.196	-0.777	-0.699	-0.543	C_1 R = Me	-1.153	-0.724	-0.637	-0.493
D_3 R = Me	-1.195	-0.779	-0.695	-0.543	D_3 R = Me	-1.153	-0.718	-0.634	-0.492
q_P					q_P				
C_1 R = H	1.571	1.020	0.930	0.779	C_1 R = H	1.569	1.023	0.936	0.782
D_3 R = H	1.596	1.018	0.929	0.779	D_3 R = H	1.592	1.017	0.932	0.782
C_1 R = Me	2.105	1.616	1.541	1.395	C_1 R = Me	2.101	1.621	1.542	1.396
D_3 R = Me	2.114	1.617	1.538	1.395	D_3 R = Me	2.102	1.621	1.540	1.396
q_N					q_N				
C_1 R = H	-1.396	-1.327	-1.313	-1.294	C_1 R = H	-1.395	-1.326	-1.309	-1.290
D_3 R = H	-1.424	-1.327	-1.312	-1.293	D_3 R = H	-1.421	-1.323	-1.308	-1.289
C_1 R = Me	-1.467	-1.411	-1.398	-1.378	C_1 R = Me	-1.464	-1.408	-1.395	-1.374
D_3 R = Me	-1.475	-1.410	-1.397	-1.378	D_3 R = Me	-1.464	-1.409	-1.393	-1.375

Table 5.4: Natural charges of selected atoms in $[M(N(EPH_2)_2)_3]$, M = La, U; E = O, S, Se, Te, at the optimised D_3 geometries

Comparison of q_{La} and q_U shows that La is more positive than U in $[M(N(EPH_2)_2)_3]$ for all E. In the S, Se, and Te cases q_{La} is *ca.* 22% larger than q_U, but it is only 12% larger with E = O. In addition, q_{E_M} in $[La(N(EPH_2)_2)_3]$ is typically *ca.* 10% more negative than in $[U(N(EPH_2)_2)_3]$, with $[M(N(OPH_2)_2)_3]$ once again being the exception with a difference between $q_{O_{La}}$ and q_{O_U} of 4%.

The charge difference between M and E, $\Delta(q_M - q_{E_M})$ can be calculated from the data in table 5.4. This quantity indicates that there is a significant reduction in the M–E charge difference between E = O and E = Te, i.e the M–E bond becomes significantly less polar as the O → Te group is descended; $\Delta(q_U - q_{E_U})$ decreases by 41% from O → Te which compares with 36% for $\Delta(q_{La} - q_{E_{La}})$, suggesting ionicity decreases more quickly in the

uranium-chalcogen bonds than lanthanum-chalcogen.

5.4.3 Conclusions from the initial La / U comparison

In this section I have reported DFT studies of the series of complexes $[M(N(EPH_2)_2)_3]$, M = La, U; E = O, S, Se, Te; R = H, Me. The principal conclusions are:

(i) In general, very good agreement between theoretical and experimental geometries is found. In particular, the experimental observation that metal – chalcogen distances in analogous La and U complexes with S-, Se- and Te- based ligands are shorter in the actinide systems, is reproduced computationally. Furthermore, the difference between r(La–E) and r(U–E) is larger for the heavier E, again agreeing with experimental data.

(ii) Natural charge analysis reveals a significant reduction in both q_M and q_E as the chalcogens are descended, and therefore a decrease also in the M–E charge difference on moving from E = O and E = Te. This suggests the M–E bond becomes less ionic as group 16 is descended. Furthermore the decrease in ionicity is greater in U–E than in La–E.

(iii) The agreement between experimental and calculated geometries, together with the Natural charges, leads me to conclude that it is appropriate to approximate these complexes as D_3 symmetric, with $N(EPH_2)_2$ ligands instead of the bulkier $N(EP^iPr_2)_2$ ligands used experimentally. Therefore all further analysis has been carried out on only the D_3 H-approximation complexes.

5.4.4 Extending the project to $[M(N(EPH_2)_2)_3]$, M = Ce, Pr, Pm, Eu; Np, Pu, Am, Cm

In the first part of this chapter I have reported the results of computational studies on $[M(N(EPH_2)_2)_3]$ (M = La, U; E = O, S, Se, Te), models for the experimentally-characterised ^{i}Pr systems.[178,180,198] The second part of this chapter focuses on a further study to extend the computational work to the M = Ln (Ce, Pr, Pm, Eu), An (Np, Pu, Am, Cm) systems with the hope of observing trends in the bonding along the lanthanides and the actinides, and furthermore with the view of comparing Eu with Am and Cm, three

crucial metals in nuclear separation chemistry[199] about which little is known of the latter two due to the high cost of suitable experimental facilities.

5.4.5 Geometries of $[M(N(EPH_2)_2)_3]$, M = La, Ce, Pr, Pm, Eu; U, Np, Pu, Am, Cm

Structures with the formula $[Ln(N(EPH_2)_2)_3]$ (Ln = Ce, Pr, Pm, Eu; E = O, S, Se, Te) were constructed by replacing La with the appropriate metal and re-optimising; similarly the actinide complexes were constructed by replacing U by each of Np, Pu, Am, and Cm and performing further re-optimisations. In this way a complete set of geometry optimised $[M(N(EPH_2)_2)_3]$ for M = La, Ce, Pr, Pm, Eu, U, Np, Pu, Am, Cm; E = O, S, Se, Te; all D_3, was achieved.

All ten metals converged to similar structures as those shown in figures 5.3 and 5.6. Selected bond lengths and angles for all $[M(N(EPH_2)_2)_3]$ are presented in table 5.5 and figure 5.12. Examination of the actinide data reveal that for the oxygen complexes, r(An–O) decreases U > Np > Pu > Am > Cm, in agreement with the decreasing ionic radii[25,26] (a result of the actinide contraction), although the difference between the largest (U) and smallest (Cm) r(An–O) is small, 0.04 Å. This result agrees well with the difference between the trivalent ionic radii of U and Cm, 0.05 Å. This trend is reversed in the tellurium complexes; U–Te is the shortest of the An–Te bonds, and the heavier actinides have progressively larger r(An–Te), although Am and Cm are inverted; U–Te, Np–Te, Pu–Te and Cm–Te are all similar lengths with <0.01Å separating them. Am–Te is the longest by some margin, 0.023 Å longer than U–Te. These observations are emphasised in figure 5.13, in which r(An–E) have been normalised by setting all r(An–O) to zero. While r(An–E) increases for all metals as group 16 is descended, this increase is smaller for lighter actinides, and progressively larger for each heavier actinide (again Am and Cm are inverted). So while U–Te is 0.73 Å longer than U–O, Am–Te is 0.79 Å longer than Am–O, and Cm–Te, 0.78 Å.

This implies there is a change in the nature of the An–E bond for heavier E across the five actinides studied here. The lengthening of the An–Te bond *vs.* An–O appears to be largest for the mid-series actinides than for the three earlier actinides, with U–E showing the smallest lengthening, echoing the result found by Guillaumont *et al.*

LANTHANIDES

	Lanthanum				Cerium				Praseodynium				Promethium				Europium			
	O	S	Se	Te	O	S	Se	Te	O	S	Se	Te	O	S	Se	Te	O	S	Se	Te
Bond Lengths/Å																				
Ln–E	2.417	2.916	3.027	3.232	2.390	2.890	2.996	3.202	2.373	2.870	2.979	3.187	2.348	2.851	2.961	3.173	2.335	2.873	2.985	3.205
P–E	1.553	2.043	2.198	2.443	1.553	2.043	2.200	2.445	1.553	2.044	2.201	2.447	1.553	2.044	2.200	2.448	1.552	2.041	2.197	2.441
P–N	1.612	1.634	1.639	1.642	1.612	1.634	1.639	1.642	1.612	1.635	1.638	1.642	1.612	1.635	1.639	1.642	1.613	1.636	1.639	1.642
Bond Angles/°																				
E–Ln–E (α)	80.5	87.0	90.1	92.7	81.4	88.0	90.9	93.3	81.9	88.0	90.9	93.4	81.5	88.1	90.9	95.0	83.4	88.5	90.2	92.2
P–E–Ln (β)	135.6	107.5	102.8	99.0	135.2	107.1	102.8	99.0	135.0	107.4	103.0	99.2	135.9	107.8	103.6	98.3	134.3	105.8	103.5	100.0
N–P–E (γ)	119.9	121.3	121.4	121.2	120.0	121.3	121.4	121.2	119.9	121.1	121.2	121.1	119.8	121.1	121.1	121.8	120.1	120.5	121.2	121.2

ACTINIDES

	Uranium				Neptunium				Plutonium				Americium				Curium			
	O	S	Se	Te	O	S	Se	Te	O	S	Se	Te	O	S	Se	Te	O	S	Se	Te
Bond Lengths/Å																				
An–E	2.393	2.849	2.955	3.126	2.381	2.840	2.931	3.132	2.364	2.830	2.932	3.135	2.358	2.835	2.940	3.149	2.355	2.826	2.931	3.134
P–E	1.555	2.048	2.206	2.461	1.555	2.046	2.207	2.454	1.555	2.044	2.202	2.451	1.554	2.043	2.200	2.445	1.554	2.044	2.203	2.449
P–N	1.612	1.636	1.638	1.643	1.612	1.635	1.639	1.643	1.611	1.635	1.639	1.643	1.611	1.635	1.638	1.642	1.612	1.634	1.639	1.643
Bond Angles/°																				
E–An–E (α)	81.7	89.4	91.3	92.1	80.4	90.2	90.2	92.3	82.9	88.2	90.5	92.1	83.0	88.6	90.1	92.1	82.7	89.6	91.4	93.4
P–E–An (β)	134.3	105.9	103.4	101.8	136.0	105.7	104.6	101.2	134.3	107.6	104.5	101.3	134.3	106.3	104.7	101.1	134.5	106.9	103.6	100.3
N–P–E (γ)	120.0	120.8	121.5	120.4	119.8	121.0	120.5	120.3	120.0	120.8	121.0	120.5	120.0	120.2	121.0	120.9	119.9	121.2	121.1	121.0

Table 5.5: Selected bond lengths and angles (see figure 5.3(d) for definitions of α, β, γ) from the optimised geometries of the target molecules, together with experimental data in italics (from ref 4)

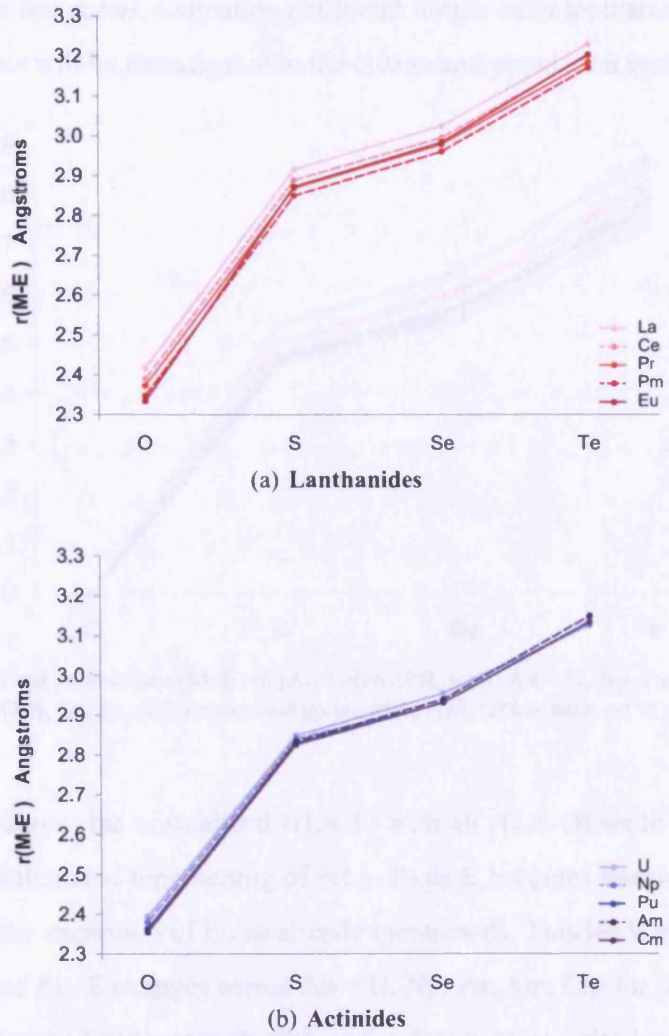

Figure 5.12: Calculated r(M-E) in [Ln/An(N(EPH$_2$)$_2$)$_3$]; An = U, Np, Pu, Am, Cm; Ln = La, Ce, Pr, Pm, Eu; E = O, S, Se, Te, at the optimised geometries

Next I turn to the lanthanides, is such a trend evident in this series of metals? Table 5.5 and figure 5.12(a) reveal that as with the actinides, r(Ln–O) decreases in line with the decreasing ionic radii[25,26] due to the lanthanide contraction; Ln–O > Ce–O >Pr–O > Pm–O > Eu–O. However unlike the actinides, this ordering is largely retained in the Ln–Te complexes (the only exception being r(Eu–Te), which is similar to r(Ce–Te)), and so the structural data suggest Ln–Te are more ionic than An–Te, while both Ln–O and An–O are similarly ionic. The reasons for the anomalous Eu behaviour are unclear, although I note that due to the electronic configuration of europium, [Xe]4$f^7$6s^2, Eu^{2+} is an accessible

oxidation state for this metal, a situation not found for the other lanthanides. The possible implications of this will be investigated in the charge and population sections.

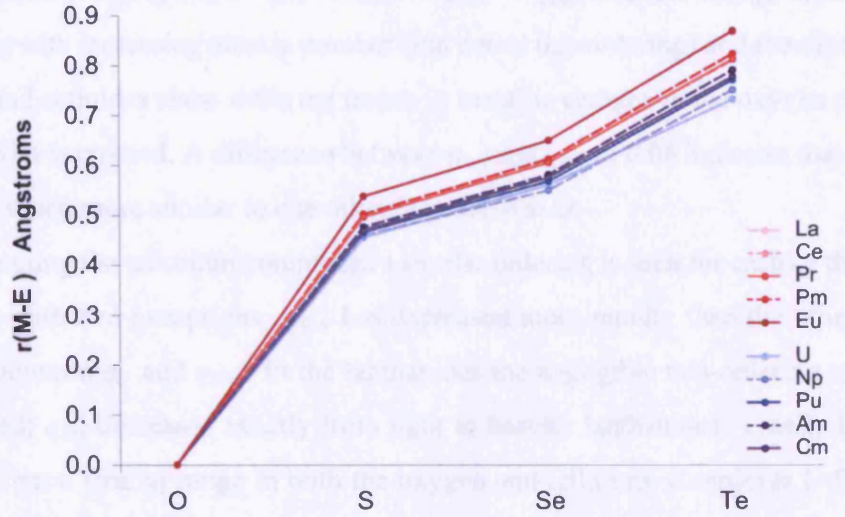

Figure 5.13: Normalised calculated r(M–E) in [An/Ln(N(EPH$_2$)$_2$)$_3$]; An = U, Np, Pu, Am, Cm; Ln = La, Ce, Pr, Pm, Eu; E = O, S, Se, Te, at the optimised geometries. r(M–O) has been set to zero for each metal

Figure 5.13 shows the normalized r(Ln–E) with all r(Ln–O) set to zero. In contrast to r(An–E), the calculated lengthening of r(Ln–E) as E becomes heavier is very similar for all Ln, (with the exception of Eu as already mentioned). This leads me to suggest that while the nature of An–E changes across An = U, Np, Pu, Am, Cm for heavier E, there is little change across the lanthanides studied, so the data suggest a similar Ln–E interaction in Ln = La, Ce, Pr, and Pm complexes for a given E. Furthermore a comparison of the actinide (blue) and lanthanide (red) data shows that An–E is more like Ln–E for heavier An: δ[(An–Te)-(An–O)] is 0.79/0.78 for An = Am/Cm and ~0.81-0.82 for all Ln except Eu, while a value of 0.73 is found for the uranium complexes. A value of 0.87 is found for δ[(Eu–Te)-(Eu–O)].

5.4.6 Natural Charge Analysis of [M(N(EPH$_2$)$_2$)$_3$] M = La, Ce, Pr, Pm, Eu, U, Np, Pu, Am, Cm; E = O, S, Se, Te

Table 5.6 and figure 5.14 present the Natural charge data for the lanthanide and actinide complexes. For both the lanthanides and the actinides a significant decrease in q_M is seen on moving from E = O to E = Te. Examination of q_{An} reveals that for the oxygen com-

plexes, $q_U < q_{Np} < q_{Pu} < q_{Am} < q_{Cm}$, so the metallic charge increases with atomic number, and the difference between q_U and q_{Cm} is ~0.3 charge units. In contrast with this q_{Ln} follow the ordering $q_{Eu} < q_{Pr} < q_{Ce} < q_{Pm} < q_{La}$, with the charge approximately decreasing with increasing atomic number (Pm defies this ordering) and therefore the lanthanides and actinides show differing trends in metallic charges in the oxygen complexes as each series is crossed. A difference between q_{La} and q_{Eu} of 0.08 indicates that the Ln–O bonds are much more similar to one other than are An–O.

Examining the tellurium complexes a similar ordering is seen for each of the q_{An} and q_{Ln} series with two exceptions; q_{Am} has decreased more rapidly than the other q_{An} and now sits between q_U and q_{Np}. In the lanthanides the negligible mis-ordering of q_{Pm} has disappeared; q_{Ln} decreases exactly from light to heavier lanthanides. Finally I note that while q_{An} has a similar range in both the oxygen and tellurium complexes (~0.3 charge units), q_{Ln} has a significantly larger range in the tellurium complexes, nearly 0.2 charge units (Te) *vs.* 0.08 charge units (O).

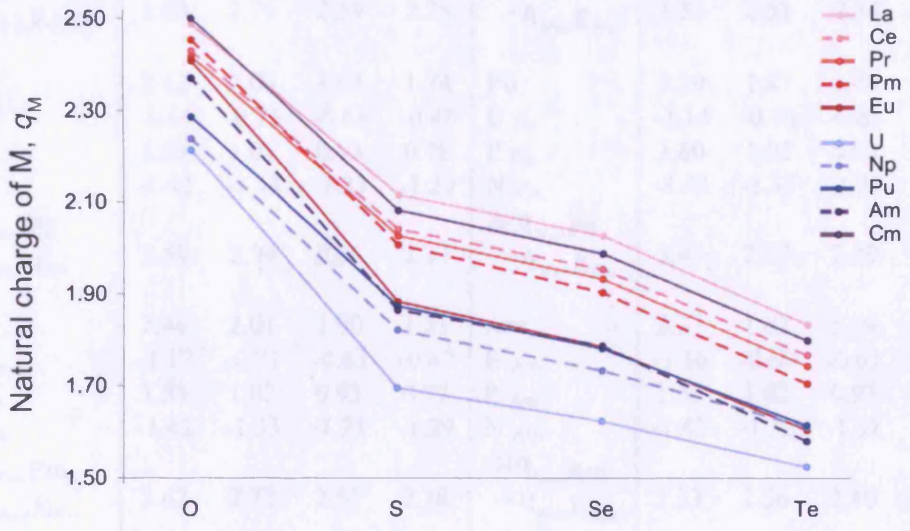

Figure 5.14: Natural charges of $[M(N(EPH_2)_2)_3]$ for M = La, Ce, Pr, Pm, Eu, U, Np, Pu, Am, Cm; E = O, S, Se, Te at the optimised geometries

Figure 5.14 reveals that the enlarged range of charges in the lanthanide complexes is largely a result of change in q_{Eu}, excluding the europium data gives a q_M charge range of 0.12 charge units for the lanthanide tellurium complexes, much closer to the 0.08 range between q_{Ln} in the oxygen complexes. Again these data imply that europium shows dif-

ferent bonding with the softer chalcogens than the other lanthanides studied; figure 5.14 also shows that the q_{Am} data are very similar to q_{Eu} down group 16, so do these data suggest that to some extent the $nf^7(n+2)s^2$ (Eu n=4, Am n=5) configuration affects the metallic charge by partially favouring a +2 oxidation state in complexes with the heavier chalcogens?

LANTHANIDE	O	S	Se	Te	ACTINIDE	O	S	Se	Te
La	2.49	2.12	2.03	1.83	**U**	2.21	1.70	1.62	1.52
E $_{La}$	-1.17	-0.73	-0.65	-0.49	E $_{U}$	-1.13	-0.67	-0.60	-0.44
P $_{La}$	1.60	1.02	0.93	0.78	P $_{U}$	1.59	1.02	0.93	0.78
N $_{La}$	-1.42	-1.33	-1.31	-1.29	N $_{U}$	-1.42	-1.32	-1.31	-1.29
$\Delta(\mathbf{q}_{Nat}\mathbf{La} - \mathbf{q}_{Nat}\mathbf{E}_{La}$	3.66	2.85	2.68	2.33	$\Delta(\mathbf{q}_{Nat}\mathbf{U} - \mathbf{q}_{Nat}\mathbf{E}_{U}$	3.35	2.37	2.22	1.97
Ce	2.43	2.04	1.95	1.77	**Np**	2.24	1.82	1.73	1.61
E $_{Ce}$	-1.17	-0.72	-0.64	-0.48	E $_{Np}$	-1.14	-0.69	-0.60	-0.46
P $_{Ce}$	1.60	1.02	0.93	0.78	P $_{Np}$	1.60	1.02	0.93	0.78
N $_{Ce}$	-1.42	-1.33	-1.31	-1.29	N $_{Np}$	-1.42	-1.33	-1.31	-1.29
$\Delta(\mathbf{q}_{Nat}\mathbf{Ce} - \mathbf{q}_{Nat}\mathbf{E}_{Ce}$	3.60	2.76	2.59	2.25	$\Delta(\mathbf{q}_{Nat}\mathbf{Np} - \mathbf{q}_{Nat}\mathbf{E}_{Np}$	3.38	2.51	2.34	2.07
Pr	2.42	2.03	1.93	1.74	**Pu**	2.29	1.87	1.78	1.61
E $_{Pr}$	-1.16	-0.71	-0.63	-0.48	E $_{Pu}$	-1.14	-0.70	-0.61	-0.46
P $_{Pr}$	1.59	1.01	0.93	0.78	P $_{Pu}$	1.60	1.02	0.93	0.78
N $_{Pr}$	-1.42	-1.33	-1.31	-1.29	N $_{Pu}$	-1.42	-1.32	-1.31	-1.29
$\Delta(\mathbf{q}_{Nat}\mathbf{Pr} - \mathbf{q}_{Nat}\mathbf{E}_{Pr}$	3.58	2.74	2.56	2.22	$\Delta(\mathbf{q}_{Nat}\mathbf{Pu} - \mathbf{q}_{Nat}\mathbf{E}_{Pu}$	3.43	2.57	2.39	2.07
Pm	2.46	2.01	1.90	1.71	**Am**	2.37	1.87	1.79	1.58
E $_{Pm}$	-1.17	-0.71	-0.63	-0.47	E $_{Am}$	-1.16	-0.69	-0.61	-0.45
P $_{Pm}$	1.59	1.02	0.93	0.77	P $_{Am}$	1.59	1.02	0.93	0.78
N $_{Pm}$	-1.42	-1.33	-1.31	-1.29	N $_{Am}$	-1.42	-1.32	-1.31	-1.29
$\Delta(\mathbf{q}_{Nat}\mathbf{Pm} - \mathbf{q}_{Nat}\mathbf{E}_{Pm}$	3.62	2.72	2.53	2.18	$\Delta(\mathbf{q}_{Nat}\mathbf{Am} - \mathbf{q}_{Nat}\mathbf{E}_{Am}$	3.53	2.56	2.40	2.03
Eu	2.41	1.88	1.79	1.60	**Cm**	2.50	2.08	1.99	1.80
E $_{Eu}$	-1.16	-0.69	-0.61	-0.45	E $_{Cm}$	-1.18	-0.73	-0.65	-0.49
P $_{Eu}$	1.59	1.01	0.93	0.78	P $_{Cm}$	1.60	1.02	0.93	0.78
N $_{Eu}$	-1.42	-1.32	-1.31	-1.29	N $_{Cm}$	-1.42	-1.33	-1.31	-1.29
$\Delta(\mathbf{q}_{Nat}\mathbf{Eu} - \mathbf{q}_{Nat}\mathbf{E}_{Eu}$	3.57	2.58	2.39	2.06	$\Delta(\mathbf{q}_{Nat}\mathbf{Cm} - \mathbf{q}_{Nat}\mathbf{E}_{Cm}$	3.68	2.81	2.63	2.29

Table 5.6: Natural charges of [Ln/An(N(EPH$_2$)$_2$)$_3$] Ln = La, Ce, Pr, Pm, Eu; An = U, Np, Pu, Am, Cm; E = O, S, Se, Te

To further probe the An–E and Ln–E bonds I have calculated $\Delta(q_M - q_{E_M})$, a measure of the polarity of An–E and Ln–E, hereafter referred to as $\Delta_{(An-E)}$ and $\Delta_{(Ln-E)}$ respectively; figure 5.15 and table 5.6 present the polarity data for these complexes. $\Delta_{(Ln-O)}$ is similar for all Ln, indicating a similarly ionic interaction between the metal and oxygen for all five lanthanides. Down group 16 $\Delta_{(Ln-E)}$ is generally smaller (less ionicity) as the lanthanides become heavier, but this progression is small and does not indicate a significant difference between the lanthanides (with the exception of europium, showing a significantly smaller $\Delta_{(Ln-E)}$ than any of the other lanthanides in complexes with the three heavier chalcogens, S, Se, and Te).

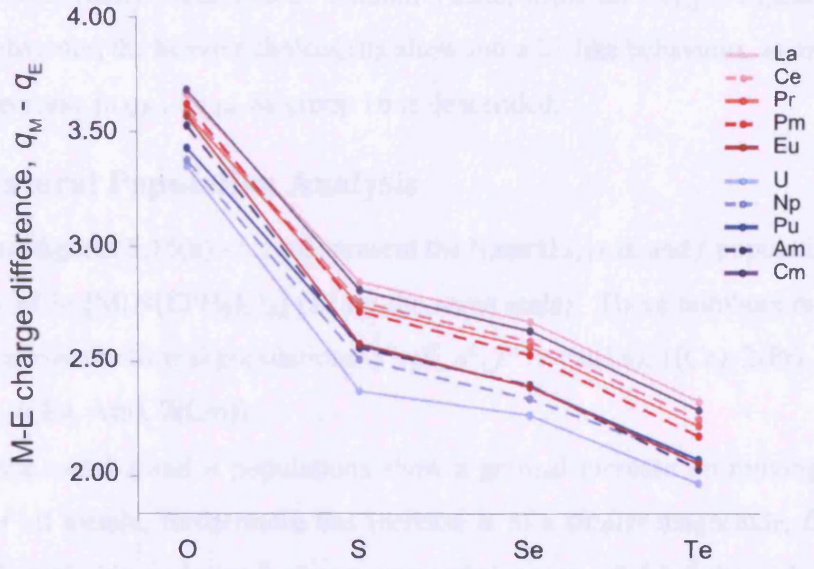

Figure 5.15: $\Delta(q_M - q_{E_M})$ in $[M(N(EPH_2)_2)_3]$ for M = La, Ce, Pr, Pm, Eu, U, Np, Pu, Am, Cm; E = O, S, Se, Te at the optimised geometries

Down the four chalcogens $\Delta_{(An-E)}$ is smallest for An = U (less ionic) becoming progressively larger (increasing ionicity) as the actinide series is crossed. Of the two heavier actinides, $\Delta_{(Am-E)}$ is very similar to $\Delta_{(Eu-E)}$ in complexes with all four chalcogens, while $\Delta_{(Cm-E)}$ is similar to the $\Delta_{(Ln-E)}$ calculated in complexes of the lighter lanthanides.

In summary, La, Ce, Pr and Pm have similarly polar metal-chalcogen interactions. The actinides generally have less polarity in their metal-chalcogen interactions than the lanthanides, with the exception of Cm, which is very lanthanide-like. Excluding Am and

Eu for a moment, the differences between the lanthanides+Cm and the early actinides becomes more pronounced as group 16 is descended, as seen in figure 5.15 where the metals split into two groups upon complexation with S, Se and Te. Furthermore as the actinide series is crossed the polarity of An–E increases, while as the lanthanides are crossed the polarity of Ln–E decreases for each E.

q_{Eu} and q_{Am}, and therefore $\Delta_{(Eu-E)}$ and $\Delta_{(Am-E)}$ are very similar in complexes with each of the four chalcogens. Neither metal 'fits' with the trends shown by the elements in their respective series, instead defining what I will call a $nf^7(n+2)s^2$ (Eu n=4, Am n=5) trend, separate from the other lanthanides or the actinides. I suggest that as both metals have a relatively easily accessible 2+ oxidation state, while the oxygen ligand complexes force 3+ behaviour, the heavier chalcogens allow more 2+ like behaviour, as evidenced by the steep decrease in q_{Eu} / q_{Am} as group 16 is descended.

5.4.7 Natural Population Analysis

Table 5.7 and figures 5.16(a) - 5.16(d) present the Natural *s, p, d,* and *f* population analysis data for all M in $[M(N(EPH_2)_2)_3]$ (all on the same scale). These numbers represent the population above the formal populations: s^0, p^0, d^0, f^n (n= 0(La), 1(Ce), 2(Pr), 3(U), 4(Pr, Np), 5(Pu), 6(Eu, Am), 7(Cm)).

Both the metal *s* and *d* populations show a gradual increase on moving from E = O to Te for all metals; furthermore this increase is of a similar magnitude, from ~0.15 above the formal *s/d* population in the oxygen complexes to ~0.4-0.6 above the formal *s/d* population in the tellurium complexes. Closer examination of the *s* populations reveals a clear difference between the behaviour of the actinide and lanthanide *s* orbitals, both as each metal series is crossed and also as group 16 is descended. The metal *s* populations in the oxygen ligand complexes increase with increasing atomic number for both series of metals, from La to Eu and also from U to Cm. However on moving from oxygen to sulphur ligands a difference appears between the lanthanides and the actinides: while the metal *s* population has increased for all metals, the increase for each of the actinides is steeper than for the lanthanides. This trend continues as the chalcogen becomes heavier and so a divergence in the behaviour of the two metal series is seen. Figure 5.17(a) emphasises this point with a plot of *s* population as a function of the formal number of *f*-electrons.

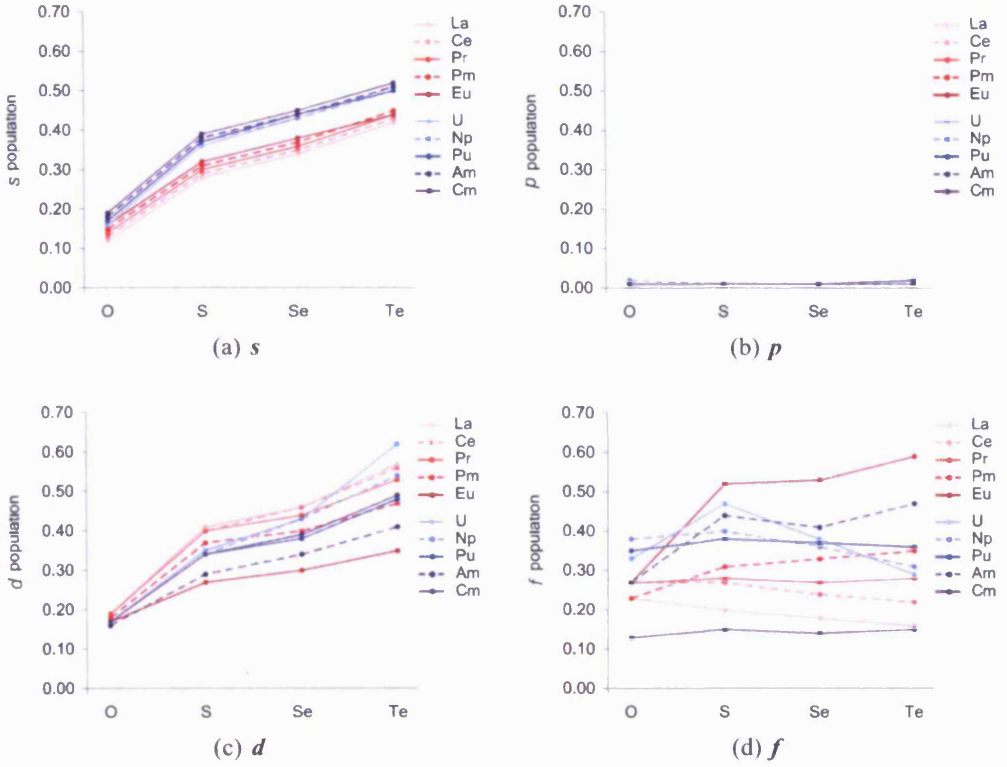

Figure 5.16: Natural populations of $[An/Ln(N(EPH_2)_2)_3]$ for Ln = La, Ce, Pr, Pm, Eu; An = U, Np, Pu, Am, Cm; E = O, S, Se, Te, at the optimised geometries

In this figure negligible difference is seen between the lanthanides and actinides for the oxygen complexes (data for Pm & Np (f^4) and Eu & Am (f^6) are similar), but there is a marked difference between Ln and An in the sulphur, selenium and tellurium complexes, as indicated by the different trends seen along the lanthanide and actinide data and the difference between Pm & Np and Eu & Am data for S, Se, and Te.

As mentioned previously, a similar overall increase is seen in metallic *d* population as *s*. However the *d* trends within each series of metals, and the difference between the two series are not so clear cut. In the complexes with oxygen ligands all ten lanthanide and actinide complexes have very similar *d* populations, but moving to sulphur a pattern begins to emerge. With the exception of europium, the lanthanides have consistently larger metallic *d* populations than the actinides (see also table 5.7). This general pattern continues to selenium and tellurium, although the *d* population of U in $[U(N(TePH_2)_2)_3]$ is higher than any other metal studied, similarly Np has a higher *d* population in $[Np(N(TePH_2)_2)_3]$ than

Pr, Pm or Eu in their tellurium analogues.

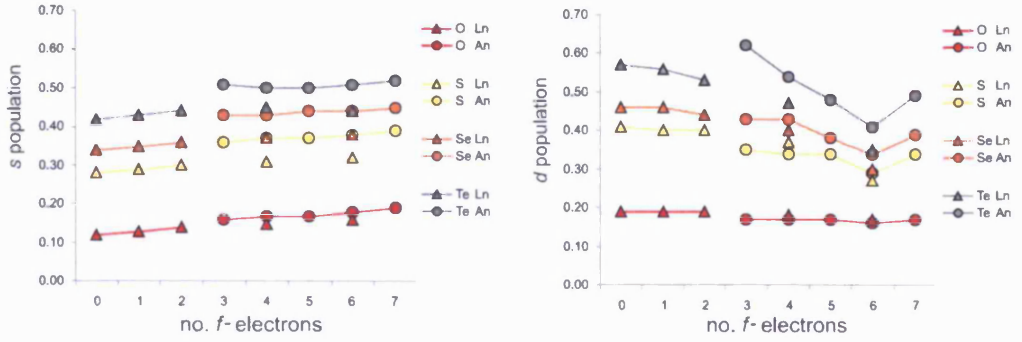

Figure 5.17: Natural *s*- and *d*- populations of [An/Ln(N(EPH$_2$)$_2$)$_3$] for Ln = La, Ce, Pr, Pm, Eu; An = U, Np, Pu, Am, Cm; E = O, S, Se, Te, at the optimised geometries *plotted as a function of the formal number of f-electrons*. Triangles indicate lanthanide data, circles indicate actinides

Figure 5.17(b) shows these data as a function of the formal number of *f*-electrons. These data show that within each of the oxygen and sulphur complexes, the metal *d* population is largely dependent on the formal number of *f*-electrons, and shows little difference between the actinides and lanthanides. In complexes with the two heavier chalcogens some divergence of the lanthanide and actinide behaviour is seen; while the *d* population of Pm & Np and Eu & Am are similar in the oxygen and sulphur complexes, both these actinides have a ~10% larger *d* population than their lanthanide analogues in the selenium complexes. The difference between Ln and An is larger still in the tellurium complexes, Np has a 15% larger *d* population than Pm, and Am 17% larger than Eu.

The metallic *f* populations are illustrated in figure 5.16(d), from which I conclude that in general the *f* population of each metal is fairly constant across the four chalcogens, with the exception of Eu, and to a lesser extent Pm, Am, and U. All five lanthanides have similar *f* populations in the oxygen complexes, diverging as group 16 is descended to give a wider spread of *f* populations in the tellurium complexes. These are ordered with the lightest lanthanide having the smallest *f* population, and the progressively heavier lanthanides having progressively larger *f* populations. Among the actinides there is a large spread of *f* populations in all four chalcogen complexes. In general the *f* population of the actinides increases with the heavier actinides, with the exception of Cm, which has a consistently smaller *f* population than any of the other actinides.

The actinides generally have higher f populations than the lanthanides; europium and curium (as mentioned above) are the two exceptions to this. I suggest an explanation for this involves the electronic structures of Eu and Cm; to achieve the half-full f^7 shell Eu^{3+} must gain an electron while Cm^{3+} is f^7 already, hence europium's enhanced f-population is in contrast to curium's reluctance to accept more density into the f orbitals. Similarly La has a low f-population which may be due to the La^{3+} f^0 also being particularly stable, but it is just as likely to arise from the poor lanthanum f-orbital/ligand energy match (see section 5.4.9 later).

LANTHANIDE		O	S	Se	Te	ACTINIDE		O	S	Se	Te
La	*s*	0.12	0.28	0.34	0.42	U	*s*	0.16	0.36	0.43	0.51
	p	0.01	0.01	0.01	0.02		*p*	0.01	0.01	0.01	0.01
	d	0.19	0.41	0.46	0.57		*d*	0.17	0.35	0.43	0.62
	f	0.23	0.2	0.18	0.16		*f*	0.33	0.47	0.38	0.29
Ce	*s*	0.13	0.29	0.35	0.43	Np	*s*	0.17	0.37	0.43	0.5
	p	0.01	0.01	0.01	0.02		*p*	0.02	0.01	0.01	0.01
	d	0.19	0.4	0.46	0.56		*d*	0.17	0.34	0.43	0.54
	f	0.27	0.27	0.24	0.22		*f*	0.38	0.40	0.36	0.31
Pr	*s*	0.14	0.3	0.36	0.44	Pu	*s*	0.17	0.37	0.44	0.5
	p	0.01	0.01	0.01	0.02		*p*	0.01	0.01	0.01	0.02
	d	0.19	0.4	0.44	0.53		*d*	0.17	0.34	0.38	0.48
	f	0.27	0.28	0.27	0.28		*f*	0.35	0.38	0.37	0.36
Pm	*s*	0.15	0.31	0.37	0.45	Am	*s*	0.18	0.38	0.44	0.51
	p	0.01	0.01	0.01	0.02		*p*	0.01	0.01	0.01	0.01
	d	0.18	0.37	0.40	0.47		*d*	0.16	0.29	0.34	0.41
	f	0.23	0.31	0.33	0.35		*f*	0.27	0.44	0.41	0.47
Eu	*s*	0.16	0.32	0.38	0.44	Cm	*s*	0.19	0.39	0.45	0.52
	p	0.01	0.01	0.01	0.02		*p*	0.01	0.01	0.01	0.02
	d	0.17	0.27	0.30	0.35		*d*	0.17	0.34	0.39	0.49
	f	0.27	0.52	0.53	0.59		*f*	0.13	0.15	0.14	0.15

Table 5.7: Natural population data for Ln, An in $[Ln/An(N(EPH_2)_2)_3]$ Ln = La, Ce, Pr, Pm, Eu; An = U, Np, Pu, Am, Cm; E = O, S, Se, Te

Both these population data and the q_M show that the amount of 'extra' metallic electron density, that is to say the total metallic population above the formal population of each metal in the +3 oxidation state, is generally higher in complexes of the actinides than

of the lanthanides. Each metal carries progressively more extra electron density when complexed with the heavier chalcogens. Focusing on the sulphur, selenium, and tellurium complex data, the metal with most extra electron density is uranium. This electron density is found primarily in the *d* shell, especially in the Se and Te complexes. The second most electron rich metals are Eu and Am, both of which have this density entering the *f* orbitals predominantly. After Eu and Am come Np and Pu, the data indicate that the extra electron density on these two actinides enters the *d* orbitals more than the *f*. Pm, Pr, and Ce come next, all showing significantly less extra electron density than the metals mentioned above. La and Cm have the smallest amount of extra electron density, the stable f^0 and f^7 electronic configurations found respectively on their 3+ ions suggests that this might be expected, although the poor La *f*-manifold / ligand energy match may be more responsible for this in the lanthanum case.

5.4.8 Mulliken Overlap Populations

Mulliken overlap populations can be considered as the number of electrons covalently bonding between two atoms; figures 5.18(a) and 5.18(b) show the overlap population between M — E and M^{3+}— L_3^{3-} respectively and the data are tabulated in table 5.8.

A significant increase in overlap population is seen on moving from E = O to E = Te. In the oxygen complexes of the actinides, the calculated overlap populations are ordered such that U shows the smallest overlap populations and Cm the largest, although the range of values is small (U — O = 0.08, Cm — O = 0.10 and U^{3+}— L_3^{3-} = 0.26, Cm^{3+}— L_3^{3-} = 0.42). However on moving to the heavier chalcogens this order is reversed, and furthermore the spread of values is increased such that the overlap populations between U — Te and U^{3+}— L_3^{3-} are 0.25 and 1.3 respectively, compared with 0.19 and 1.0 for Cm — E and Cm^{3+}— L_3^3 . So as the chalcogens are descended, the ordering of the actinide overlap populations reverses and diverges so that while Cm has the greatest overlap population with oxygen, uranium has the largest overlap population with Te.

Next I will look at the Mulliken overlap populations of the lanthanide complexes. Figure 5.18 shows that unlike the actinides, the ordering of the lanthanide overlap populations is the same in the oxygen complexes as in the tellurium complexes. Except for a small disordering in the sulphur complexes, a consistent but small decrease in Mulliken

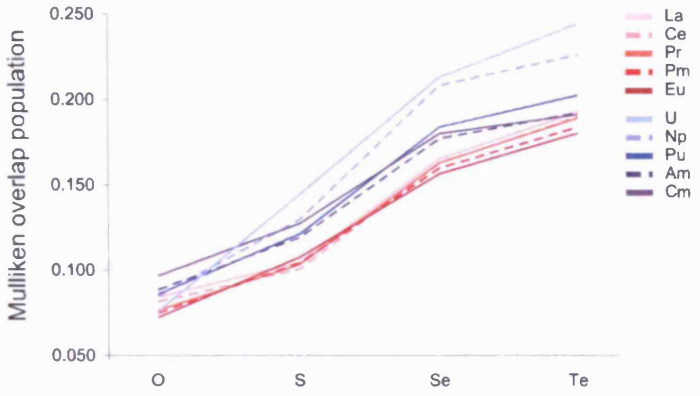

(a) **M — E overlap populations**

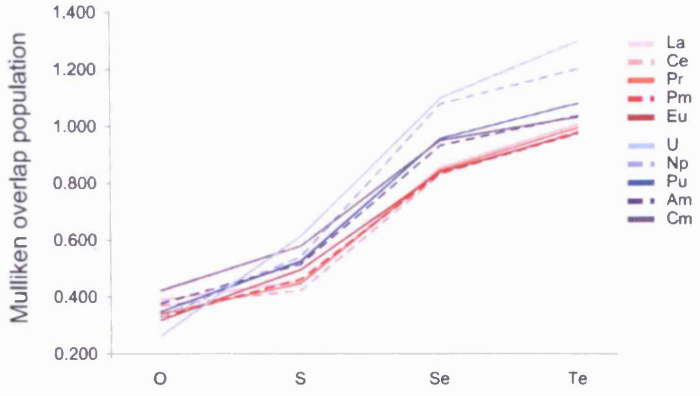

(b) **M^{3+}— L_3^{3-} overlap populations**

Figure 5.18: Mulliken M — E and M^{3+}— L_3^{3-} overlap populations in $[An/Ln(N(EPH_2)_2)_3]$ for Ln = La, Ce, Pr, Pm, Eu; An = U, Np, Pu, Am, Cm; E = O, S, Se, Te

overlap population from La to Eu is seen for a given E. Also contrasting with the actinides, the range of overlap populations is similar in both the oxygen and tellurium complexes, and furthermore this range is small, *ca.* 0.01 across Ln—E and *ca.* 0.03 across Ln^{3+}—L_3^{3-} *vs. ca.* 0.05 across the An—E and *ca.* 0.25 across all An^{3+}—L_3^{3-}.

Comparing the lanthanides with the actinides I can see that three of the actinides, Pu, Np and U have progressively larger overlap populations between M and E and also M^{3+} and L_3^{3-} for E = S, Se, Te than the other two actinides, Am and Cm. Furthermore although Am and Cm show larger overlap populations than any of the lanthanides for E = S and Se, in the tellurium complexes the five lanthanides have similar overlaps to Am and Cm.

The data suggest enhanced covalency in the compounds of the heavier chalcogens, and also greater covalency in analogous actinide complexes *vs.* the lanthanide equivalents

LANTHANIDE	O	S	Se	Te	ACTINIDE	O	S	Se	Te
La — E	0.085	0.105	0.166	0.193	U — E	0.075	0.144	0.213	0.245
La^{3+}— L_3^3	0.391	0.456	0.857	1.009	U^{3+}— L_3^3	0.262	0.617	1.102	1.303
Ce — E	0.082	0.101	0.163	0.190	Np — E	0.085	0.130	0.209	0.227
Ce^{3+}— L_3^3	0.371	0.425	0.833	0.985	Np^{3+}— L_3^3	0.330	0.544	1.081	1.203
Pr — E	0.077	0.104	0.163	0.190	Pu — E	0.086	0.121	0.184	0.203
Pr^{3+}— L_3^3	0.344	0.449	0.848	0.997	Pu^{3+}— L_3^3	0.349	0.526	0.958	1.083
Pm — E	0.075	0.105	0.160	0.184	Am — E	0.089	0.119	0.178	0.193
Pm^{3+}— L_3^3	0.332	0.464	0.837	0.977	Am^{3+}— L_3^3	0.378	0.517	0.934	1.039
Eu — E	0.073	0.108	0.157	0.181	Cm — E	0.097	0.128	0.180	0.192
Eu^{3+}— L_3^3	0.320	0.498	0.841	0.979	Cm^{3+}— L_3^3	0.424	0.581	0.952	1.035

Table 5.8: Selected Mulliken overlap populations in $[An/Ln(N(EPH_2)_2)_3]$ for Ln = La, Ce, Pr, Pm, Eu, U, Np, Pu, Am, Cm; E = O, S, Se, Te

(for E = S, Se). For the tellurium complexes Pu, Np and U show progressively enhanced covalent interactions, while Am and Cm behave more like the lanthanides, the data indicating relatively less covalency compared with the lighter actinides.

5.4.9 Molecular Orbital Analysis

In order to further probe the effect of the four different chalcogen based ligands on the lanthanides and the actinides a detailed examination of the molecular orbitals (MOs) has been made.

Molecular orbital energy level diagrams for the $[An/Ln(N(EPH_2)_2)_3]$ systems are presented in figures 5.19 and 5.20. For each complex the energy of the lowest lying *f* orbital has been set to zero and the other energies adjusted accordingly, so for the lanthanum complexes orbitals 52 and 53 are the highest occupied and lowest unoccupied molecular orbitals (HOMO and LUMO) respectively, while for e.g. the uranium complexes, orbitals 52 and 53 are the highest occupied ligand based molecular orbital ($HO_{LB}MO$) and lowest lying *f* electron (LL_{fe}) respectively. ADF's unrestricted calculations provide the energies of both α and β components of all orbitals and the energies presented in figures 5.19 and 5.20 are the mean of these.

As can be seen in figures 5.19 and 5.20, a similar energetic pattern of molecular orbitals is present in each of the complexes, with a remarkable similarity between the

metals for a given E. I have chosen to investigate orbitals 35 → 52 because these orbitals form a group that is typically separated by 2 eV from the next most stable level (although this is closer to 1 eV in the oxygen complexes).

The most obvious immediate difference between the molecular orbital diagrams of each metal is the energy gap between orbitals 52 and 53, the HOMO — LUMO gap of the lanthanum complexes and the $HO_{LB}MO$ — LL_{f_e} gap for the other lanthanide and actinide complexes. Figures 5.19 and 5.20 and table 5.9 show that as each of the lanthanide and actinide series are crossed, this energy gap decreases. This is due to the

Oxygen				Sulphur			
Lanthanide		Actinide		Lanthanide		Actinide	
La	-5.20	U	-4.41	La	-3.78	U	-2.84
Ce	-3.85	Np	-3.54	Ce	-2.72	Np	-2.31
Pr	-2.97	Pu	-2.61	Pr	-2.02	Pu	-1.50
Pm	-1.24	Am	-1.50	Pm	-0.75	Am	-0.66
Eu	0.00	Cm	-0.52	Eu	0.10	Cm	1.28

Selenium				Tellurium			
Lanthanide		Actinide		Lanthanide		Actinide	
La	-3.42	U	-2.66	La	-2.67	U	-2.07
Ce	-2.51	Np	-2.00	Ce	-2.51	Np	-1.52
Pr	-1.77	Pu	-1.27	Pr	-1.49	Pu	-0.98
Pm	-0.73	Am	-0.54	Pm	-0.54	Am	-0.37
Eu	0.14	Cm	1.45	Eu	0.12	Cm	1.55

Table 5.9: $\Delta(E_{HO_{LB}MO} - E_{LL_{f_e}})$ for $[Ln/An(N(EPH_2)_2)_3]$ Ln = La, Ce, Pr, Pm, Eu; An = U, Np, Pu, Am, Cm; E = O, S, Se, Te

f levels becoming increasingly stabilised as both the lanthanide and actinide series are crossed; so great is the stabilisation in europium and curium that for both metals, the *f* electrons are found at lower energy than the $HO_{LB}MO$s (see figures 5.19(e) and 5.20(e)), shown in table 5.9 as positive $\Delta(E_{HO_{LB}MO} - E_{LL_{f_e}})$.

To complement the orbital energies, orbital compositions were analysed. The 18 highest energy ligand-based orbitals are largely chalcogen-*p* based with some phosphorus and nitrogen *p* character, with an admixture of metal in some cases. The magnitude and character of this metal contribution will be examined next. Visual analysis of 3-dimensional representations of the valence MOs reveal some covalent interactions be-

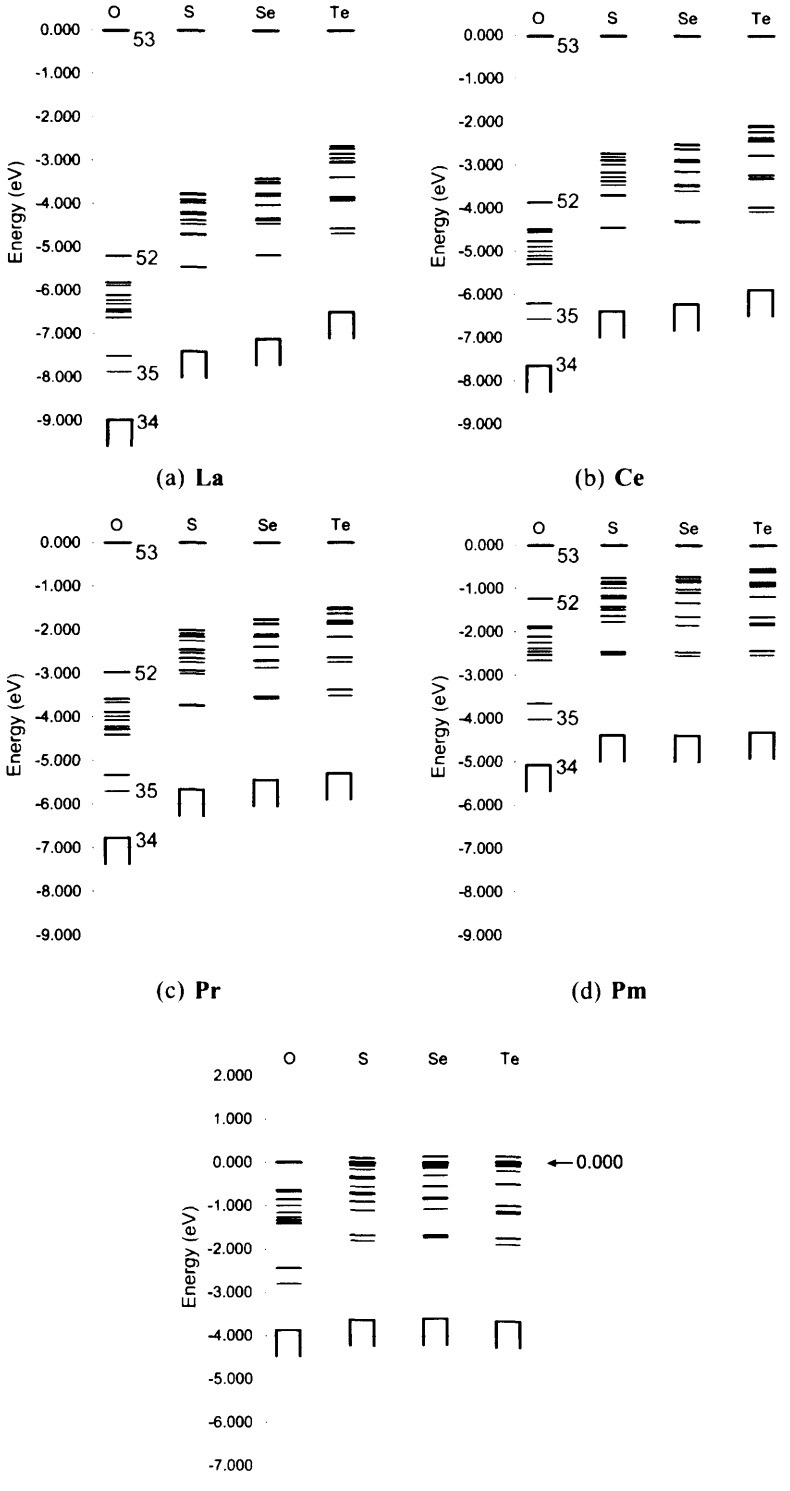

Figure 5.19: MO energy level diagram for $[Ln(N(EPH_2)_2)_3]$ Ln = La, Ce, Pr, Pm, Eu; E = O, S, Se, Te at the optimised D_3 geometries. The energies of orbitals 34 → 52 have been normalised to that of MO 53, which has been arbitrarily set to 0eV in all cases. Orbitals with a_1 symmetry are shown in red, a_2 in blue and e in black

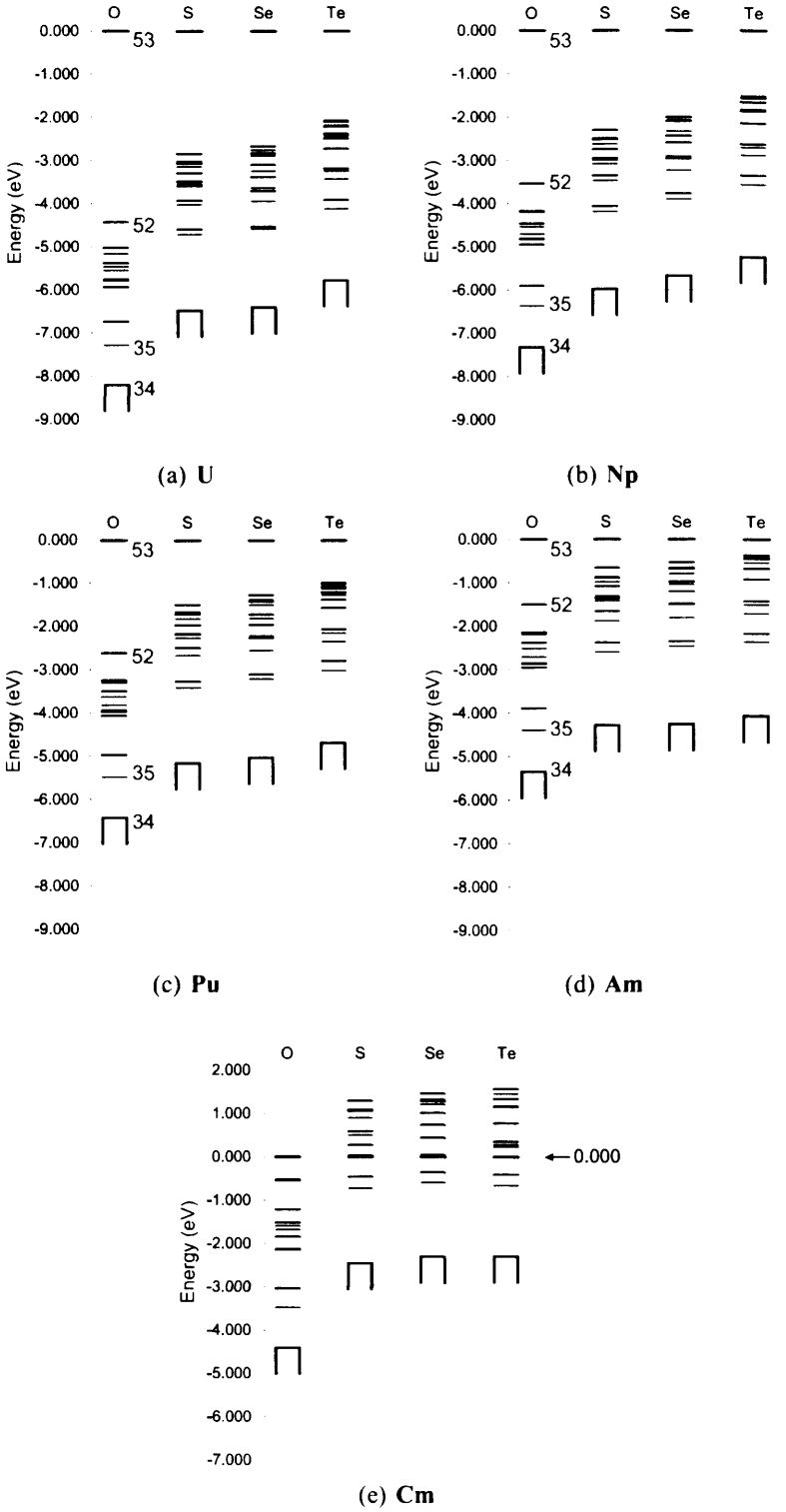

Figure 5.20: MO energy level diagram for $[An(N(EPH_2)_2)_3]$ An = U, Np, Pu, Am, Cm; E = O, S, Se, Te at the optimised D_3 geometries. The energies of orbitals 34 – 52 have been normalised to that of MO 53, which has been arbitrarily set to 0eV in all cases. Orbitals with a_1 symmetry are shown in red, a_2 in blue and e in black

	LANTHANIDE			ACTINIDE	
	% metal *d*	Normalised E(eV)		% metal *d*	Normalised E(eV)
La	8.78%	-4.70	U	11.06%	-3.95
Ce	9.31%	-3.68	Np	10.17%	-3.36
Pr	8.44%	-2.94	Pu	8.79%	-2.49
Pm	7.51%	-1.64	Am	9.58%	-1.66
Eu	8.61%	-0.66	Cm	8.11%	0.15

Table 5.10: % metal *d* contribution to, and normalised energy of e orbitals 39 and 40 in [Ln/An(N(SPH$_2$)$_2$)$_3$] Ln = La, Ce, Pr, Pm, Eu; An = U, Np, Pu, Am, Cm

tween metallic AOs and ligand-based MOs in each complex. Evidence of such covalent interactions is seen predominantly in MOs of a_1 and e symmetry. Using the calculated MO compositions to guide the visual analysis, the sulphur complexes were examined first and the MO with the most significant covalent interaction between M and S was identified. Occupying positions 39 and 40 in the energetic ordering of the valence MOs, this is a relatively low-lying orbital. Table 5.10 presents the % metal content of this set of e orbitals across both metal series (for the sulphur-ligand complexes); the main metal contributor to these MOs is *d*.

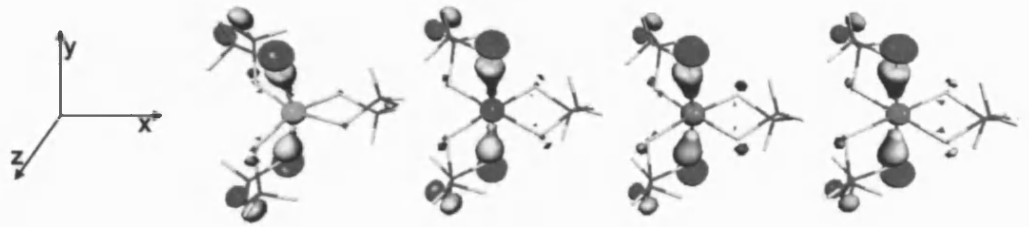

(a) **Orbital 39**

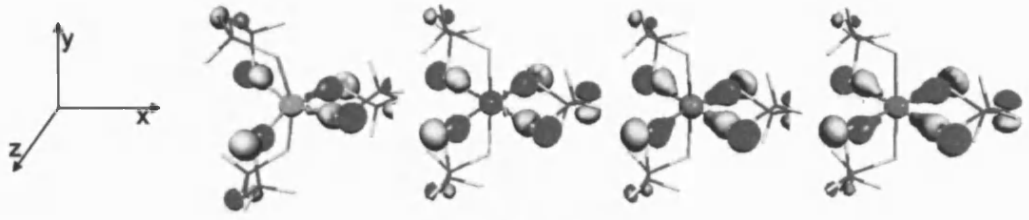

(b) **Orbital 40**

Figure 5.21: Three dimensional representations (at the same space value, 0.375) of orbitals 39 and 40 in selected [Ln/An(N(SPH$_2$)$_2$)$_3$] Ln = Pr (turquoise), Eu (blue); An = U (green), Am (red)

Generally the lanthanides show a smaller *d* content in this orbital than the actinides,

the average across the five Lns being 8.5% compared with 9.5% for the actinides. However examination of the data reveal that this difference is a result of enhanced *d* content in the U and Np complexes; the mean *d* contribution of Pu, Am, and Cm is 8.8%, much closer to that of the lanthanides. Figure 5.21 shows the three-dimensional representations of orbitals 39 and 40 in a selection of four of the complexes: $[M(N(SPH_2)_2)_3]$ with M = Pr (turquoise), Eu (blue), U (green), Am (red). A covalent σ type interaction can be seen between the metallic AO pairs (d_{xy} + d_{xz}) and (d_{yz} + $d_{x^2-y^2}$) and the ligand sulphur *p* orbitals, furthermore this interaction is larger in the actinide complexes compared with the lanthanides. These pictures, coupled with table 5.10, suggest that enhanced covalency in the U and Np sulphur complexes over Pu, Am and Cm and also over all five lanthanides arises partially as a result of chalcogen *p* σ-donation into metallic *d* levels.

I have established that in the sulphur ligand complexes a pair of e orbitals is a factor in the bonding differences between $[An(N(SPH_2)_2)_3]$ and $[Ln(N(SPH_2)_2)_3]$ as well as differentiating to some extent between actinides in $[An(N(SPH_2)_2)_3]$. Next I will investigate if there are analogous MOs in the complexes of the heavier chalcogens.

Visual and numerical analysis of orbitals 39 and 40 reveals that the metallic *d* contribution is significantly smaller in the selenium complexes (about half that of the S complexes, i.e. ~5-6%) and negligible in the tellurium complexes (between 0% and 3%). However a full examination of e symmetry MOs in the Se and Te complexes reveals that enhanced *d* character is present in higher energy MOs of these complexes. Figures 5.22(a) - 5.22(d) present two degenerate pairs of e symmetry MOs, 42 & 43 and 45 & 46 in four example complexes: $[M(N(TePH_2)_2)_3]$ with M = Pr (turquoise), Ce (yellow), U (green) and Np (black).

Referring back to figure 5.21, a similarity can be seen between orbitals 39 & 40 and these two pairs; the orbital composition analysis reveals that they all contain the same combination of metallic *d* orbitals, ($d_{yz} + d_{x^2-y^2}$) to one component of the degenerate pair (39, 42, 45) and ($d_{xy} + d_{xz}$) to the other (40, 43, 46). The diagrams clearly show an enhanced overlap of metal-*d* with tellurium-*p* in the actinide complexes compared with the two lanthanides.

A further σ interaction has been identified in orbital 44. Of a_1 symmetry, this MO

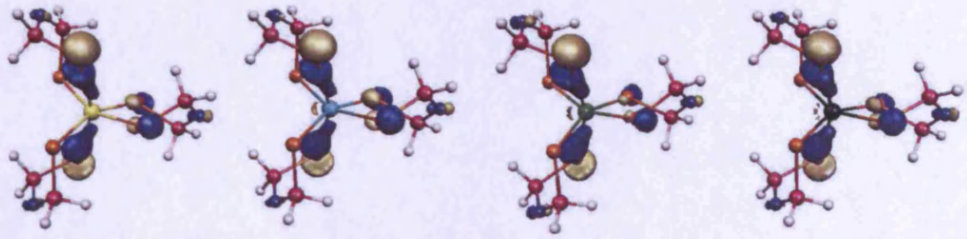

(a) **Orbital 42**

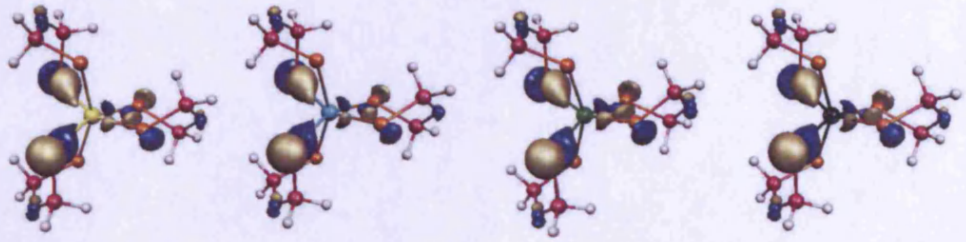

(b) **Orbital 43**

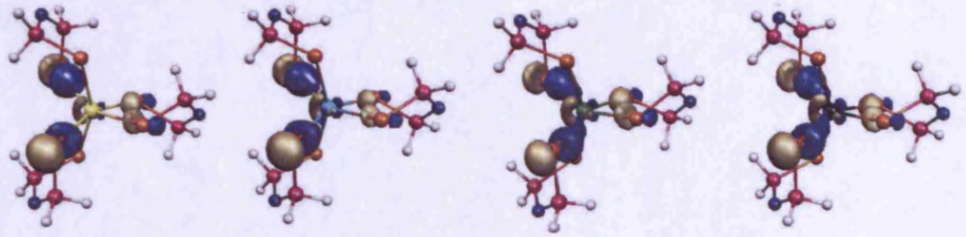

(c) **Orbital 45**

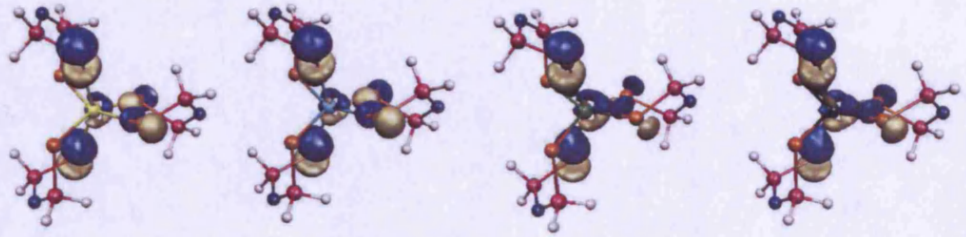

(d) **Orbital 46**

Figure 5.22: Three dimensional representations (at the same space value, 0.375) of e symmetry orbital pairs 42 & 43 and 45 & 46 in selected [Ln/An($N(TePH_2)_2)_3$] Ln = Pr (turquoise), Ce (yellow); An = U (green), Np (black)

is composed largely of a σ bonding interaction between chalcogen-p orbitals with metal d_{z^2}. Figure 5.23 presents three-dimensional representations of this orbital in two typical molecules, [$M(N(SePH_2)_2)_3$] for M = Pr (turquoise) and U (green). An enhanced covalent

overlap can be seen in the latter *vs.* the former. Figure 5.24 presents the data for this orbital in all ten metal complexes with all four chalcogens, and from this it can be seen that the uranium complexes have the largest metal content in this orbital, and furthermore that An MO 44 generally has a greater metallic content than Ln. The *d* contribution to a_1 orbital 44 is low in the oxygen complexes, maximises in the sulphur complexes and decreases slightly upon complexation with selenium and tellurium.

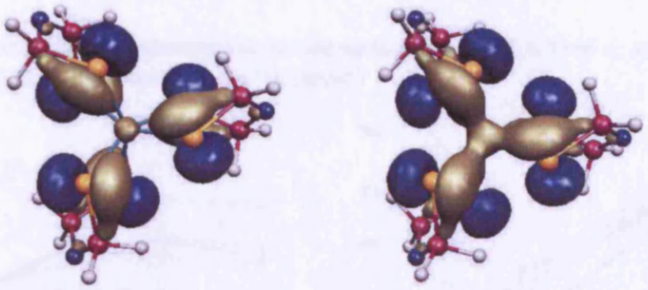

(a) **Orbital 44 Pr** (b) **Orbital 44 U**

Figure 5.23: Three dimensional representations (at same space value, 0.375) of a_1 orbital 44 in selected [Ln/An(N($SePH_2$)$_2$)$_3$] Ln = Pr(turquoise), An = U(green)

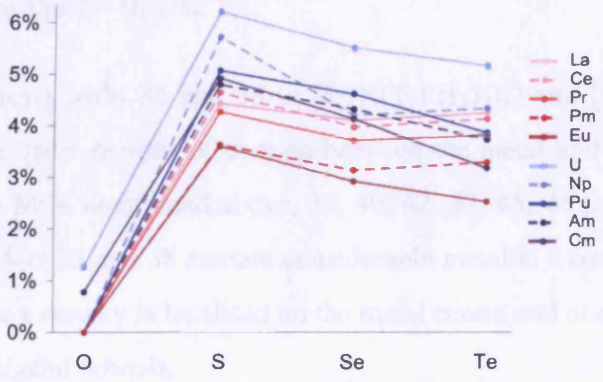

Figure 5.24: % metal *d* contribution to a_1 symmetry orbital 44 in [Ln/An(N(EPH_2)$_2$)$_3$] Ln = La, Ce, Pr, Pm, Eu; An = U, Np, Pu, Am, Cm; E = O, S, Se, Te

Two further MOs of a_1 symmetry were also examined. Orbitals 35 and 38 lie lower in energy than 44 mentioned above and they are of interest as they contain significant metallic *s* content. Section 5.4.7 described how the increase in metal *s* population as group 16 is descended was significant, and furthermore how the An *s* populations increased more steeply from E = O to E = Te than the Ln *s* populations.

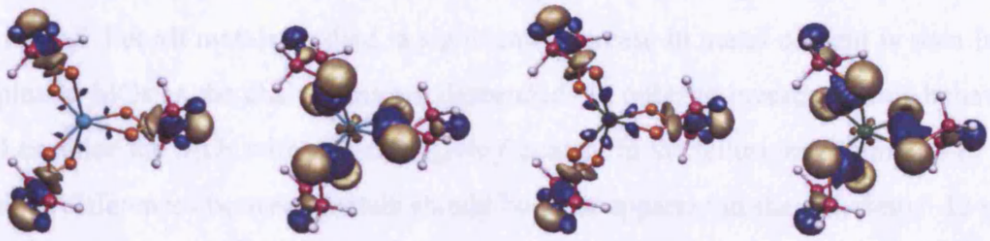

(a) **Orbital 35 Pr** (b) **Orbital 38 Pr** (c) **Orbital 35 U** (d) **Orbital 38 U**

Figure 5.25: Three dimensional representations (at the same space value, 0.4) of a_1 symmetry orbital 38 in $[Ln/An(N(TePH_2)_2)_3]$ Ln = Pr(turquoise), An = U(green)

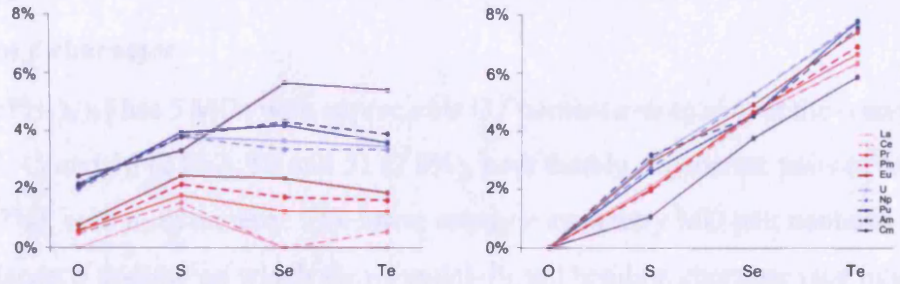

(a) **Orbital 35** (b) **Orbital 38**

Figure 5.26: % metal *s* contribution to a_1 symmetry orbitals in $[Ln/An(N(EPH_2)_2)_3]$ Ln = La, Ce, Pr, Pm, Eu; An = U, Np, Pu, Am, Cm; E = O, S, Se, Te

Figure 5.25 shows MOs 35 and 38 in $[Pr(N(TePH_2)_2)_3]$ and $[U(N(TePH_2)_2)_3]$, in neither complex are there regions of overlap between the metal and the ligand. This is in contrast with the MOs mentioned above, 39, 40, 42, 43, 45, 46 (e symmetry) and 44 (a_1). So although MOs 35 and 38 contain considerable metallic *s* contributions, my data suggest that metallic *s* density is localised on the metal centre and does not form bonding combinations with ligand orbitals.

5.4.10 MOs containing *f*-electrons

The *f* contribution to the MOs of $[Ln/An(N(EPH_2)_2)_3]$ are significantly more complicated than either the *s* or *d* contributions. As a result of competing factors such as the stabilisation and contraction of the *f* levels as both the lanthanides and actinides are crossed, paired with the enhanced spatial extension of the 5*f* shell over the 4*f* shell, and also the more 2+ behaviour of the two f^6 metals with the heavier chalcogens, I will discuss the fe^- MO contributions for each actinide separately. In general the oxygen complexes show very

little covalency in the M–O bond and contain negligible percentage contributions of metal *s*, *p*, *d*, or *f*. For all metals studied, a significant increase in metal content is seen in the complexes' MOs as the chalcogens are descended. In order to investigate this behaviour I will examine the MOs with non-negligible *f* content in the tellurium complexes of each metal, as differences between metals should be most apparent in these systems. In every 3-D MO representation below, the α component of the MO is shown as in each case the *f* contribution to the α component is considerably higher than to the β component and therefore emphasises the differences between the metals for illustrative purposes. However all percentages mentioned relate to the mean of the α and β components.

Uranium *f* character

$[U(N(TePH_2)_2)_3]$ has 5 MOs with appreciable U *f* content averaged over the α and β components: 45 and 46 (2.8%), 50 and 51 (2.8%), both doubly degenerate pairs of MOs, and 52 (*ca.* 7%), with a_2 symmetry. The lower energy e symmetry MO pair contains a significantly larger *d* population which shows metal–ligand bonding character (see figure 5.22) so the small *f* contribution is hidden; this orbital will be examined further later. Figure 5.27 presents MOs 50, 51, and 52. With the aid of the two views in figure 5.27, it is clear

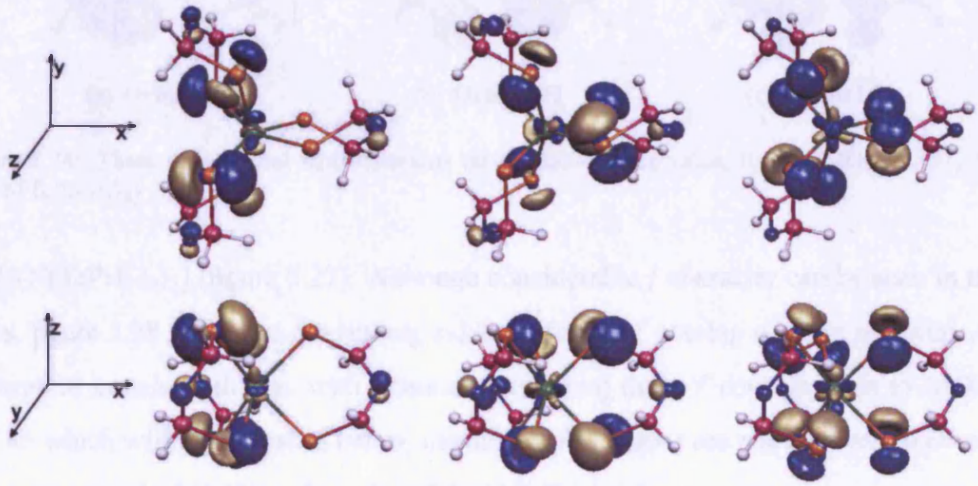

(a) **Orbital 50** (b) **Orbital 51** (c) **Orbital 52**

Figure 5.27: Three dimensional representations (at the same space value, 0.4) of MOs 50, 51, 52 in $[U(N(TePH_2)_2)_3]$

that there is no evidence of a bonding interaction between the metal *f* and tellurium *p*

orbitals in MOs 50, 51 or 52, so I conclude that with the possible exception of the degenerate orbitals 45 and 46, uranium *f* density does not contribute to metal–ligand bonding combinations in these complexes.

Neptunium *f* character

The neptunium–tellurium complex has similar MOs containing *f* character to the uranium–tellurium complex; MOs 45 and 46 (4% *f*), 50 and 51 (3.4% *f*) and 52 (6.4% *f*). As with the uranium analogue, MOs 45-46 show some metal–ligand bonding interaction, and as this orbital pair also contains considerable *d* character it will be discussed later. MOs 50-52 are very similar in $[Np(N(TePH_2)_2)_3]$ (see figure 5.28) to those seen above

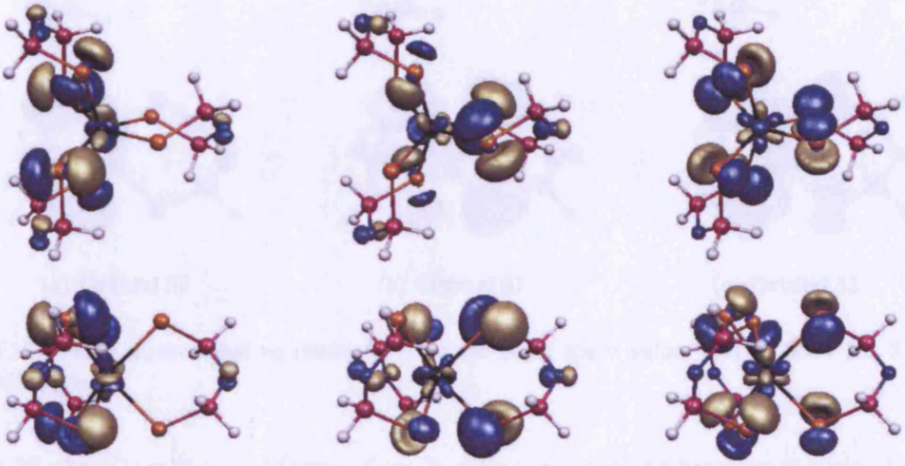

(a) **Orbital 50** (b) **Orbital 51** (c) **Orbital 52**

Figure 5.28: Three dimensional representations (at the same space value, 0.4) of MOs 50, 51, 52 in $[Np(N(TePH_2)_2)_3]$

in $[U(N(TePH_2)_2)_3]$ (figure 5.27). Although considerable *f* character can be seen in these MOs, figure 5.28 shows no convincing evidence for Np *f* overlap with Te *p* orbitals, and I therefore conclude that as with uranium, excluding those *f* contributions to MOs 45 and 46 which will be discussed below, neptunium *f* electrons are not involved in covalent interactions with $N(TePH_2)_2$ ligands in $[Np(N(TePH_2)_2)_3]$.

Plutonium *f* character

In $[Pu(N(TePH_2)_2)_3]$ the same five *f*-containing MOs are seen, 44 and 45 (6% *f*), 50 and 51 (5.8% *f*) and 52 (8.2% *f*). Comparing these percentages with $[U(N(TePH_2)_2)_3]$ and $[Np(N(TePH_2)_2)_3]$ an increase in *f* contribution as the actinides are crossed can be seen.

It is not clear why this increase is observed, the most likely explanation is the improved energy match between the *f* electrons and tellurium *p*; as the actinide series is crossed the *f* levels are stabilised and are therefore closer in energy to the lower energy Te *p* shell. MOs 44 and 45 will be discussed below, and figure 5.29 shows top and side views of MOs 50 – 52. Although the increase in %*f* character over the two previous actinides can be seen in

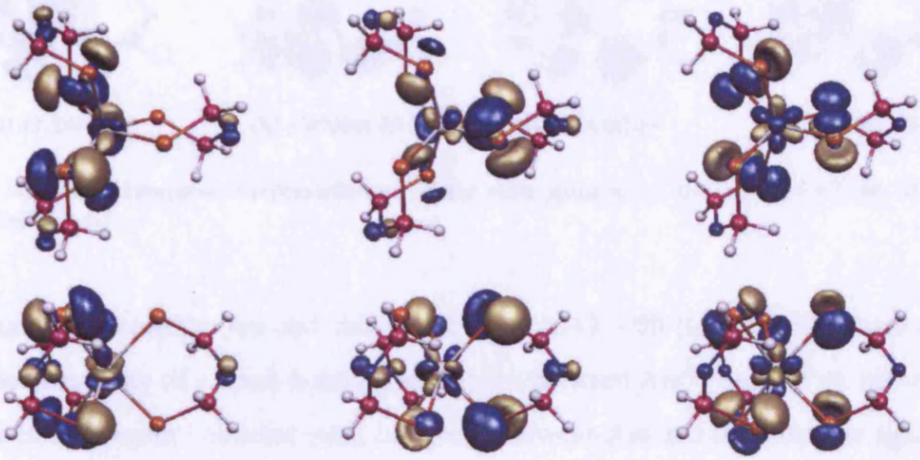

(a) **Orbital 50** (b) **Orbital 51** (c) **Orbital 52**

Figure 5.29: Three dimensional representations (at the same space value, 0.4) of MOs 50, 51, 52 in $[Pu(N(TePH_2)_2)_3]$

figure 5.29, there is still no evidence of any bonding interactions between the metal and the ligands, so again I conclude that apart from the possibility of some *f* covalency in MOs 45 and 46, the *f* orbital content of the predominantly ligand-based MOs in $[Pu(N(TePH_2)_2)_3]$ is metal based and does not participate in metal–ligand covalency.

Americium *f* character

In the americium–tellurium complex, $[Am(N(TePH_2)_2)_3]$, significantly elevated percentages of *f* electron are observed in the ten highest energy MOs. Because the $HO_{LB}MO - LL_{fe}$- gap is negligible (see figure 5.20(d)), there is a much better energy match between metal *f* and tellurium *p*. This results in metal *f* character being found in many of the MOs around the $HO_{LB}MO$. MOs 45 and 46 (4.65% *f*), 47 (12.34% *f*), 48 (14.02% *f*), and 49 and 50 (15.11% *f*) all contain significant percentages of metal *f*, as well as being analogous to MOs 45 and 46, 50 and 51 and 52 (both 47 and 48 match the shape of 52) in $[U(N(TePH_2)_2)_3]$, $[Np(N(TePH_2)_2)_3]$ and $[Pu(N(TePH_2)_2)_3]$.

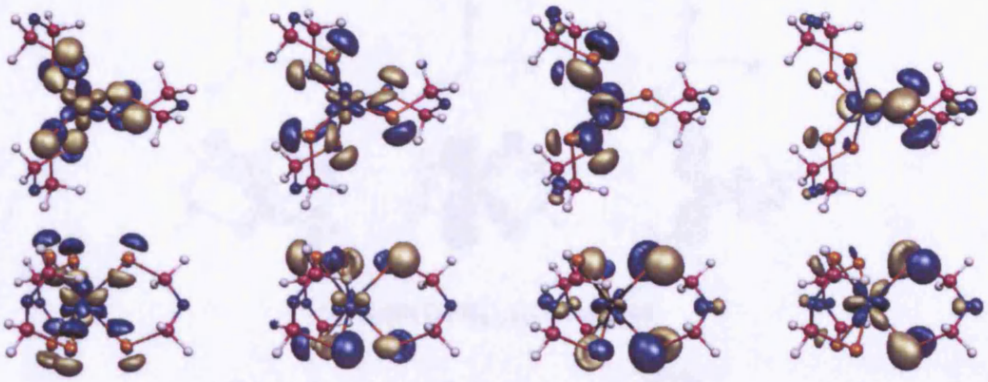

(a) **Orbital 47** (b) **Orbital 48** (c) **Orbital 49** (d) **Orbital 50**

Figure 5.30: Three dimensional representations (at the same space value, 0.4) of MOs 47, 48, 49, 50 in $[Am(N(TePH_2)_2)_3]$

Examining both the top and side views of MOs 47 – 50 (figure 5.30), there seems to be the possibility of a small bonding interaction between Am^{3+} and L_3^{3-} in MO 47 but nothing else, so again I conclude that covalency between Am and the tellurium ligands is unlikely to be seen in other than the lower energy MOs 45 and 46. These will be examined below in greater detail.

MOs 45 and 46 in $[An(N(TePH_2)_2)_3]$, An = U, Np, Pu, Am

Table 5.11 shows the mean % *d* and % *f* contributions to the pair of orbitals 45 and 46. The *d* content has already been discussed in section 5.4.9 and illustrated in diagram 5.22, and it can be seen from table 5.11 that as the actinides are crossed the *d* character decreases in this orbital pair. Concurrent with the %*d* decrease, an increase in %*f* is seen. As demonstrated above, there is no bonding interaction between the *f* electron contributions to MOs 50, 51 or 52 (i.e. the three highest energy ligand-based MOs) and the ligand-chalcogen *p* orbitals. To investigate if *f* electrons are involved in the enhanced covalency seen in An over Ln, and more specifically in U, Np and Pu over any other heavy metals studied in the project, I have examined the component M^{3+} AOs and L_3^{3-} MOs of orbital 45 to try and gain a deeper understanding of which specific metal shells are involved in the bonding interaction.

Figure 5.31 shows the six largest components of $[U(N(TePH_2)_2)_3]$'s MO 45, three contributions from the L_3^{3-} fragment and three from M^{3+}. Considering views from along

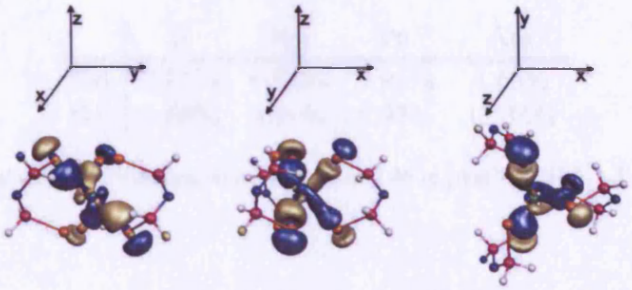

(a) $[U(N(TePH_2)_2)_3]$ Orbital 45

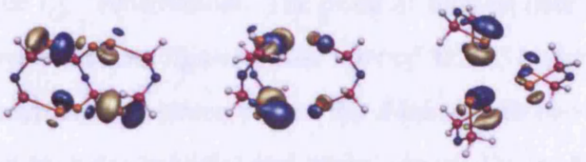

(b) L_3^{3-} = 40% component

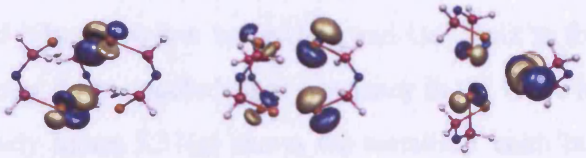

(c) L_3^{3-} = 26 % component

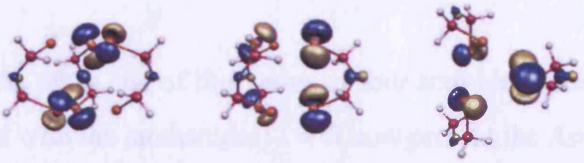

(d) L_3^{3-} = 15 % component

(e) U^{3+} d_{xz} = 4.5% component

(f) U^{3+} d_{xy} = 3.3% component

(g) U^{3+} f_z = 2.8% component

Figure 5.31: Three dimensional representations (at the same space value, 0.4) of the six main U^{3+} and L_3^{3-} components of MO 45 in $[U(N(TePH_2)_2)_3]$, as seen relative to three different Cartesian axes defined in 5.31(a)

	U	Np	Pu	Am
%d	7.81%	6.92%	5.96%	4.65%
%f	2.80%	3.99%	5.97%	12.34%

Table 5.11: % metal *d* and *f* contribution to orbitals 45 and 46 in [An(N(SPH_2)$_2$)$_3$] An = U, Np, Pu, Am

the x, y, and z Cartesian axes helps to explain how the ligand-based part of MO 45 is made up of each of the three L_3^{3-} contributors. The point of interest here is *how do the metal d and f orbitals interact with the ligand-based part of MO 45?* Considering first Ud_{xz}, a possible bonding interaction between two of the *d* lobes with two Te *p* lobes in figure 5.31(b) can be seen in both the 'middle' and 'right' views. Figure 5.31(f) shows the d_{xy} uranium AO, I can see no evidence of a bonding overlap between the lobes of this AO and any ligand based lobes, however since Ud_{xz} and Ud_{xy} mix to form a single irrep in the D_3 symmetry group, I can conclude that covalency in the U–Te bond arises from U*d* participation. Similarly figure 5.31(g) shows the metallic *f* contribution to MO 45 and there seems to be no bonding-type overlap between the *f* lobes and the ligand-based Te *p* lobes.

To investigate the other end of this series of four actinides (Cm behaves differently and will be discussed with the lanthanides) I will now present the Am^{3+} and L_3^{3-} components of orbital 45 in [An(N($TePH_2$)$_2$)$_3$]. As table 5.11 shows, [Am(N($TePH_2$)$_2$)$_3$] contains a considerably higher %*f* contribution than any of the other actinide–tellurium complexes. Furthermore I remind the reader that the percentages given in table 5.11 relate to the mean of the α and β %*f* contribution, while figure 5.32(a) presents a three dimensional representation of the α component of orbital 45, which contains considerably more *f* density than the β.

Examining figure 5.32, the only metal and ligand orbitals which match to give potential bonding overlap are the metallic d_{xz} shown in 5.32(g) and the orbital shown in 5.32(b). There appears to be no overlap potential between any of the ligand-based orbitals and Am f_{xyz}, so again I conclude that metallic *f* contributions have no direct participation in covalent interactions between An(III) and N(EPH_2)$_2^-$ ligands. In addition to the symmetry-allowed mixing investigated above, figures 5.32(f) and 5.32(g), and also 5.31(e), 5.31(f),

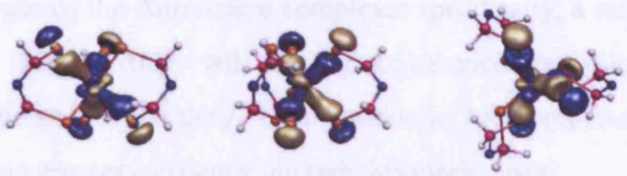

(a) $[Am(N(TePH_2)_2)_3]$ Orbital 45

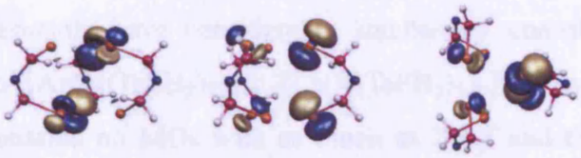

(b) L_3^{3-} = 42% component

(c) L_3^{3-} = 12 % component

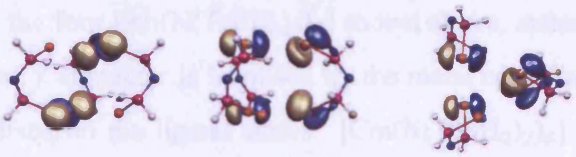

(d) L_3^{3-} = 12 % component

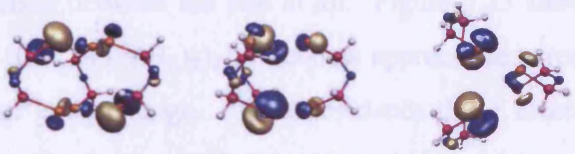

(e) L_3^{3-} = 9 % component

(f) Am^{3+} f_{xyz} = 10.9% component

(g) Am^{3+} d_{xz} = 4.6% component

Figure 5.32: Three dimensional representations (at the same space value, 0.4) of the six main Am^{3+} and L_3^{3-} components of MO 45 in $[Am(N(TePH_2)_2)_3]$, as seen relative to three different Cartesian axes defined in 5.31(a)

and 5.31(g) show that the *d* levels are significantly more diffuse than the *f* levels, and are therefore considerably more likely to overlap with ligand-based MOs thus giving rise to

covalency. In the case of the Americium complexes specifically, a reduction in metallic charge from Am^{3+} towards Am^{2+} will result in an enhanced radial extension of the 6*d* orbitals, and thus the stability of the f^7 configuration in Am complexes could be said to indirectly bring about greater covalency through this mechanism.

***f* electrons in [Ln(N(TePH$_2$)$_2$)$_3$] and [Cm(N(TePH$_2$)$_2$)$_3$]**

[Ln(N(TePH$_2$)$_2$)$_3$] generally have considerably smaller %*f* contributions to their valence MOs than do [An(N(TePH$_2$)$_2$)$_3$]; [La(N(TePH$_2$)$_2$)$_3$] contains no *f* character, [Ce(N(TePH$_2$)$_2$)$_3$] contains no MOs with as much as 2% *f* and the *f* percentages for MOs 45-46, 50-51 and 52 in [Pr(N(TePH$_2$)$_2$)$_3$] are 2.5%, 2.0% and 2.7% respectively. Moving across to Pm and Eu this percentage *f* increases, most likely as a result of the ever-decreasing $HO_{LB}MO - LL_{fe}$ gap (see figures 5.19(d) and 5.19(e)); similarly the *f* contribution to the valence MOs of [Cm(N(TePH$_2$)$_2$)$_3$] is very large. In each of these complexes, just as in the four [An(N(TePH$_2$)$_2$)$_3$] shown above, instead of seeing metallic *f* – ligand interactions, *f* character is localised on the metal centre and ligand chalcogen *p* combinations localised on the ligand atoms. [Cm(N(TePH$_2$)$_2$)$_3$] is the most extreme example of this with the seven Cm^{3+} *f*-electrons embedded in an array of ligand-based MOs with no interaction between the two at all. Figure 5.33 shows the α component of MOs 35 → 59 in [Cm(N(TePH$_2$)$_2$)$_3$], note how appreciable percentages of *f* electron are found over a large energy range. Further evidence that *f* electrons do not seem to participate in bonding interactions with ligand-based chalcogen *p* combinations can be seen in figure 5.33. Figures 5.33(o) & 5.33(p) and 5.33(u) & 5.33(v) are the only MOs to show any metal–ligand interaction, and these are the only two MO pairs to contain considerable metallic *d* contributions, 10% and 8% respectively. The *f* electrons of Cm are too contracted to participate in any bonding interaction with the ligands, even though the energy match for such an interaction is favourable.

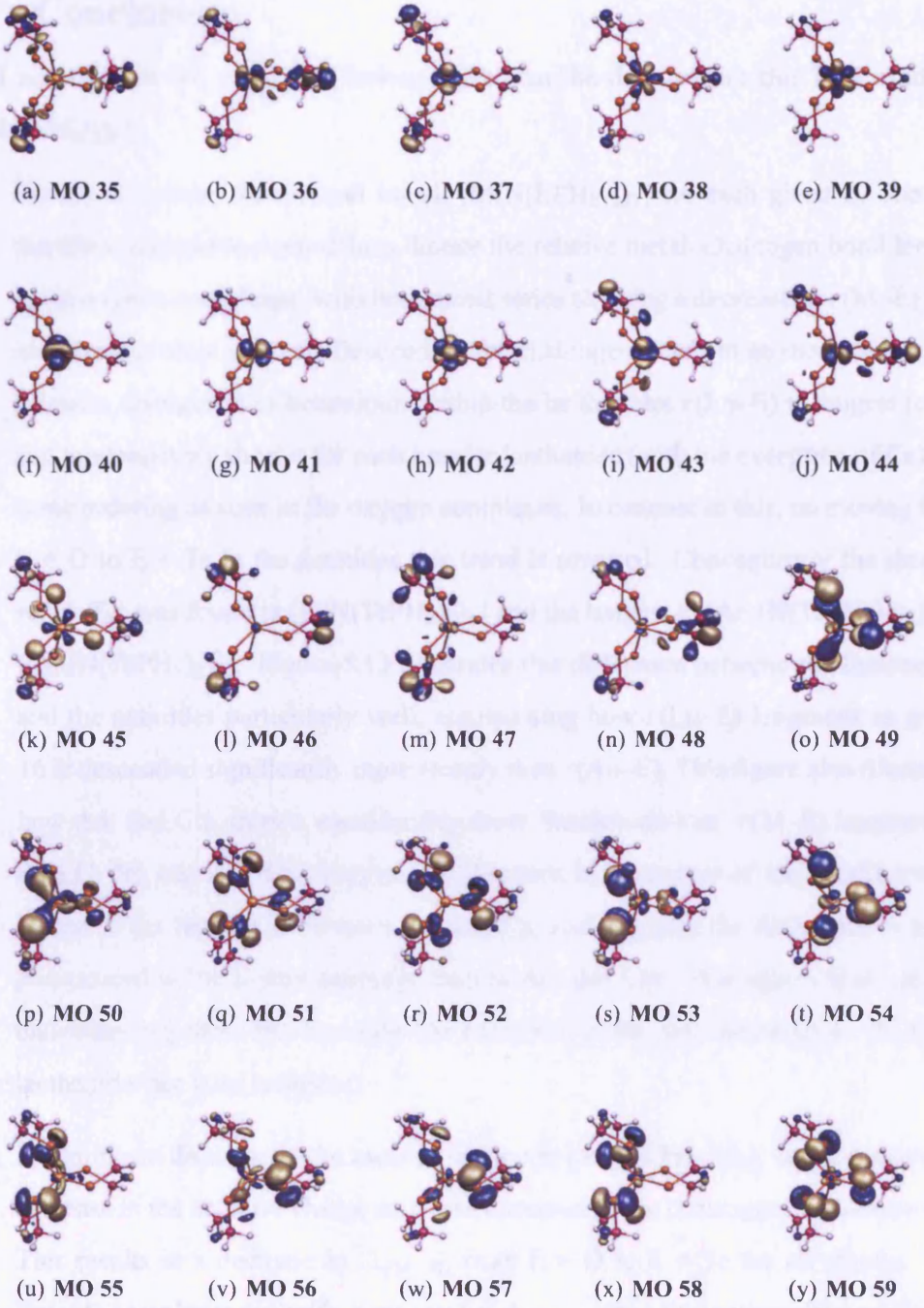

(a) **MO 35** (b) **MO 36** (c) **MO 37** (d) **MO 38** (e) **MO 39**

(f) **MO 40** (g) **MO 41** (h) **MO 42** (i) **MO 43** (j) **MO 44**

(k) **MO 45** (l) **MO 46** (m) **MO 47** (n) **MO 48** (o) **MO 49**

(p) **MO 50** (q) **MO 51** (r) **MO 52** (s) **MO 53** (t) **MO 54**

(u) **MO 55** (v) **MO 56** (w) **MO 57** (x) **MO 58** (y) **MO 59**

Figure 5.33: Three dimensional representations (at same space value, 0.4) of orbitals 35 → 59 in $[Cm(N(TePH_2)_2)_3]$

5.5 Conclusions

I will now discuss the main conclusions which can be drawn from this DFT study of $[M(N(EPH_2)_2)_3]$.

(i) Similar structures were found for all $[M(N(EPH_2)_2)_3]$ for each given E. The lanthanide and actinide contractions dictate the relative metal–chalcogen bond lengths in the oxygen complexes, with both metal series showing a decrease in r(M–E) with increasing atomic number. Descending the chalcogens leads to an increase in r(M–E) and a divergence of behaviour: within the lanthanides r(Ln–E) is longest for La and progressively shorter for each heavier lanthanide (with the exception of Eu), the same ordering as seen in the oxygen complexes. In contrast to this, on moving from E = O to E = Te in the actinides this trend is reversed. Consequently the shortest r(An–Te) was found in $[U(N(TePH_2)_2)_3]$ and the longest in $[Am(N(TePH_2)_2)_3]$ and $[Cm(N(TePH_2)_2)_3]$. Figure 5.13 illustrates this difference between the lanthanides and the actinides particularly well, emphasising how r(Ln–E) lengthens as group 16 is descended significantly more steeply than r(An–E). This figure also illustrates how Am and Cm show a considerably more 'lanthanide-like' r(M–E) lengthening than U, Np and Pu. This suggests a difference in the nature of the bond between M and E for heavier E between An and Ln, and suggests the difference is more pronounced in the lighter actinides than in Am and Cm. This agrees with current understanding about the transition-like behaviour of the early actinides *vs.* the more lanthanide-like later actinides.

(ii) A significant decrease in the metallic charge in $[M(N(EPH_2)_2)_3]$, and a concurrent decrease in the negative charge on E was observed as the chalcogens are descended. This results in a decrease in $\Delta_{(M-E)}$ from E = O to E = Te for all metals. The actinide complexes generally have smaller $\Delta_{(An-E)}$ than the lanthanides complexes, although I note that in this regard europium is very 'actinide-like' whilst curium is 'lanthanide-like'. $\Delta_{(An-E)}$ is consistently smallest in the uranium complexes, increasing as the actinide becomes heavier; the reverse trend is seen among the lanthanides, with $\Delta_{(La-E)}$ largest, decreasing with increasingly heavier lanthanides. $\Delta_{(M-E)}$ can be taken as a measure of the ionicity of the metal-chalcogen bond, and

so a decrease in ionicity was calculated as E becomes heavier, with an additional decrease in ionicity for the actinides *vs.* the lanthanides for a given E. Further to this, the least ionic M–E bonds were observed in the lighter actinide complexes for each E.

(iii) Negligible metallic *p* population above the formal p^0 is seen in any of the complexes studied. Metallic *s* and *d* populations increase as group 16 is descended for each metal. Within the lanthanides and actinides the *s* populations are larger for progressively heavier Ln and An respectively. Actinide *s* populations were systematically larger than those of the lanthanides, and a divergence of lanthanide and actinide behaviour at E = S was observed: *s* population increases significantly more steeply for M = An than M = Ln. All ten metals have a similar *d* population in their oxygen complexes, these populations changing at different rates down group 16, so that within the tellurium complexes a wide range of *d* populations are seen. Generally Ln have larger *d* populations than An, although comparing the metals with iso-electronic valence shells, in each case the actinide (Np and Am) has a higher *d* population than the lanthanide (Pm and Eu). In this regard a divergence of behaviour between M = Ln and M = An is seen at E = Se, contrasting with E = S for the *s* populations.

Further to this I note that the metallic *d* population in $[U(N(TePH_2)_2)_3]$ is particularly high, and furthermore the metallic *d* populations in $[Eu(N(EPH_2)_2)_3]$ and $[Am(N(EPH_2)_2)_3]$ (E = S, Se, Te) are particularly low, which is interesting in light of the observation that there is a steeper decrease in q_{Eu} / q_{Am} as group 16 is descended than for any other metal.

The *f* populations go some way to explaining this observation. Both Eu and Am have considerably higher *f* populations in their heavier chalcogen complexes than any other metals. This suggests that the lower than expected charges on these two metals are due to electron density entering the *f* shell and not the *d* shell. Ignoring these two anomalous metals in the comparison of *f* populations across the lanthanide and actinide series, I note that generally a constant *f* population was found in all four chalcogen complexes of $[M(N(EPH_2)_2)_3]$ for each metal, with the largest deviation

from this being uranium. It is unclear why the *f* population in $[U(N(SPH_2)_2)_3]$ is so elevated. Excluding this result, larger *f* populations were generally seen for progressively heavier Ln/An, and the *f* populations for An are in most cases larger than those of Ln.

Summing the *s*, *p*, *d*, and *f* show that the metal with most 'extra' electron density is uranium. This electron density is found primarily in the *d* shell, especially in the Se and Te complexes. The remaining metals are ordered in groups; Am and Eu, (extra density into the *f* orbitals mainly), Np and Pu (the extra density into the *d* orbitals more than the *f*), Pm, Pr, and Ce, all showing significantly less extra electron density than the previous metals, and La and Cm with the smallest amount of extra electron density. The stable f^0 and f^7 electronic configurations found respectively on La^{3+} and Cm^{3+} suggest that this might be expected, although the poor 4*f*-manifold / ligand energy match may be more responsible for this in the lanthanum case.

(iv) Mulliken overlap populations between both M^{3+} and E^{2-} and also M^{3+} and L_3^{3-} increase as group 16 is descended. In complexes of the heavier chalcogens the overlap population is greatest for the lighter actinides, decreasing for the heavier actinides and decreasing further for the lanthanides. This suggests enhanced covalency in the compounds of the heavier chalcogens, and also greater covalency in analogous actinide complexes *vs.* the lanthanide equivalents (for E = S, Se). For the tellurium complexes Pu, Np and U show progressively enhanced covalent interactions, while Am and Cm behave more like the lanthanides, showing relatively less covalency compared with the lighter actinides.

This conclusion is especially important if coupled with the charge data above. Both Eu and Am have smaller q_M than anticipated, an indicator of potential covalency. The overlap population data show that the reason for the reduced charges is not covalency in Eu / Am complexes, thus supporting the idea that it is due to the metals to some extent favouring a +2 oxidation state when complexed by S, Se or Te. Contrast this with U, Np and Pu which all have reduced charges and elevated M–E overlap populations, therefore supporting the idea of covalency in the M–E bond.

(v) Covalency in the sulphur complexes seems to arise from e and a_1 symmetry ligand based chalcogen-*p* combinations into metal-*d* donation. In the selenium and tellurium complexes this same interaction is higher in energy and contains a higher percentage of metal character. Furthermore the e symmetry combination is smeared over a range of MOs. Increasing amounts of metal *f* character can be seen in the valence MOs of [Ln/An(N(EPH_2)$_2$)$_3$] as Ln and An become heavier, i.e. as the $HO_{LB}MO - LL_{fe}$ gap decreases and there is a better energetic match between metallic *f* and ligand-based orbitals. However an extensive examination of all the *f* character seen in each complex leads me to conclude that covalency between M^{3+} and L_3^{3-} does not result from metallic *f* electron density, but is exclusively a result of metallic *d* orbitals accepting electron density from ligand chalcogen *p* orbitals.

This situation is reminiscent of Bruce Bursten's *FEUDAL* description of the electronic structure of (early) actinide complexes, the acronym standing for "*f*s essentially unaltered, *d*s accomodate ligands".[200]

The results of this study lead me to conclude that chalcogen donor ligands are extremely promising for the successful separation of Cm from Am and Eu, however there is no evidence to suggest that they would lead to good separation factors of Am from Eu. The heavy chalcogen ligands studied here would seem to distinguish between the f^6 and f^7 actinides as a result of electronic structure differences, similarly they do not seem to distinguish between the valence isoelectronic Am and Eu. My results show little evidence of covalency in the M–E bonds of Eu, Am or Cm.

La and U were used initially as models for Eu and Am/Cm respectively, but for the reasons mentioned above I must conclude that this approximation has little validity. Evidence of significant covalent interactions between U and S, Se and Te has been seen, yet the interactions between Am and Cm with these chalcogens seem to be predominantly ionic. La shows no signs of covalency with any of the chalcogens and behaves like a hard 3^+ ion, while there is strong evidence to suggest the charge on Eu is $(3\text{-}x)^+$ with a non-negligible value for x.

Ligands of the sort studied here may be useful as part of a two-step separation process, but I conclude that to separate Am from Eu different kinds of ligands are neces-

sary. Furthermore the QCT results presented by Petit *et al*[187] show promising insights into americium bonding, so this is a possible alternative method for future research into this problem.

Two papers are being published from this work:

1. "Covalency in the f elementchalcogen bond. Computational studies of $[M(N(EPR_2)_2)_3]$ (M = Pu, U, La; E = O, S, Se, Te; R = H)" by Kieran I. M. Ingram, Nikolas Kaltsoyannis, Andrew J. Gaunt and Mary P. Neu, *Journal of Alloys Compounds*, in press.

2. "Experimental and Theoretical Comparison of Bonding Differences Between An(III) and Ln(III) Ions of Similar Radii in $M[(N(EPPh_2)_2)]_3$ (M = U, Pu, La, Ce; E = S, Se), $M[N(EP^iPr_2)_2]_3$ (M = U, Pu, La, Ce; E = S, Se, Te) and Model Systems" by Andrew J. Gaunt, Brian L. Scott, Sean D. Reilly, Alejandro E. Enriquez, Mary P. Neu, James. A. Ibers, Kieran I. M. Ingram and Nikolas Kaltsoyannis, *Journal of the American Chemical Society*, submitted.

References

[1] J. L. Sonnenberg, P. J. Hay, R. L. Martin, and B. E. Bursten, *Inorg. Chem.*, 2005, **44**, 2255–2262.

[2] D. L. Clark, S. D. Conradson, R. J. Donohoe, D. W. Keogh, D. E. Morris, P. D. Palmer, R. D. Rogers, and C. D. Tait, *Inorg. Chem.*, 1999, **38**, 1456–1466.

[3] C. Nguyen-Trung, G. M. Begun, and D. A. Palmer, *Inorg. Chem.*, 1992, **31**, 5280–5287.

[4] K. C. Jantunen, R. J. Batchelor, and D. B. Leznoff, *Organometallics*, 2004, **23 (9)**, 2186–2193.

[5] J. C. Berthet, M. Nierlich, and M. Ephritikhine, *Chem. Commun.*, 2004, **7**, 870–871.

[6] I. Ijjali, K. Mitchell, F. Q. Huang, and J. A. Ibers, *J. Solid State Chem.*, 2004, **177**, 257–261.

[7] Please visit http://periodic.lanl.gov/elements/93.html and http://periodic.lanl.gov/elements/94.html.

[8] Please visit http://www.theodoregray.com/PeriodicTable/Elements/094/.

[9] IAEA Technical Report 445, STI/DOC/010/445 p 42-44 (2006).

[10] N. Kaltsoyannis, *J. Chem. Soc., Dalton Trans.*, 1997, **1**, 1–11.

[11] N. Kaltsoyannis, *Chem. Soc. Rev.*, 2003, **32**, 9–16.

[12] Please visit http://www.radiochemistry.org/periodictable/la_series/.

[13] P. Pyykko, *Inorg. Chim. Acta.*, 1987, **139**, 243–245.

[14] J. Qu, L. Wang, Y. Liu, Y. Song, Y. Wang, and X. Ji, *J. Rare Earths*, 2006, **24**, 15–19.

[15] R. G. Jones, G. Karmas, G. A. J. Martin, and H. Gilman, *J. Am. Chem. Soc.*, 1956, **78**, 4285.

[16] K. Tatsumi, I. Matsubara, Y. Inoue, A. Nakamura, R. E. Cramer, G. J. Tagoshi, J. A. Golen, and J. W. Gilje, *Inorg. Chem.*, 1990, **29**, 4928.

[17] L. P. C, M. Ephritikhine, M. Lance, J. Vigner, and M. Nierlich, *J. Organomet. Chem.*, 1996, **507**, 229–237.

[18] L. Ventelon, C. Lescop, T. Arliguie, M. Ephritikhine, P. C. Leverd, M. Lance, and M. Nierlich, *Chem. Comm*, .

[19] T. Arliguie, M. Fourmigué, and M. Ephritikhine, *Organometallics*, 2000, **19**, 109–111.

[20] P. C. Leverd, T. Arliguie, M. Lance, M. Nierlich, J. Vigner, and M. Ephritikhine, *J. Chem. Soc., Dalton Trans.*, 1994, **24**, 501–504.

[21] C. Lescop, T. Arliguie, M. Lance, M. Nierlich, and M. Ephritikhine, *J. Organomet. Chem.*, 1999, **580**, 137–144.

[22] T. Arliguie, P. Thuéry, M. Fourmigué, and M. Ephritikhine, *Eur. J. Inorg. Chem.*, 2004, **22**, 4502–4509.

[23] T. Arliguie, P. Thuéry, M. Fourmigué, and M. Ephritikhine, *Organometallics*, 2003, **22**, 3000–3003.

[24] M. Roger, L. Belkhiri, P. Thuéry, T. Arliguie, M. Fourmigué, A. Boucekkine, and M. Ephritikhine, *Organometallics*, 2005, **24**, 4940–4952.

[25] Database of ionic radii, http://abulafia.mt.ic.ac.uk/shannon/.

[26] R. D. Shannon, *Acta Cryst.*, 1976, **A32**, 751–767.

[27] R. Pocha, M. Tampier, R. D. Hoffmann, B. D. Mosel, R. Pottgen, and D. Johrendt, *Z. Anorg. Allg. Chem.*, 2003, **629**, 1379–1384.

[28] F. Lissner and T. Schleid, *Z. Anorg. Allg. Chem.*, 2005, **631**, 427–432.

[29] F. Lissner and T. Schleid, *Z. Anorg. Allg. Chem.*, 2003, **629**, 1027–1032.

[30] S. Strobel and T. Schleid, *Z. Anorg. Allg. Chem.*, 2004, **630**, 706–711.

[31] A. J. Gaunt, B. L. Scott, and M. P. Neu, *Inorg. Chem.*, 2006, **45**, 7401–7407.

[32] U. Wahlgren, H. Moll, I. Grenthe, B. Schimmelphennig, L. Maroni, V. Vallet, and O. Gropen, *J. Phys. Chem. A*, 1999, **103**, 8257–8264.

[33] P. J. Hay, R. L. Martin, and G. Schreckenbach, *J. Phys. Chem. A*, 2000, **104**, 6259–6270.

[34] Y. Oda and A. Aoshima, *J. Nuc. Sci. Tech.*, 2002, **39**, 647–654.

[35] S. Spencer, L. Gagliardi, N. C. Handy, A. G. Ioannou, C. K. Skylaris, and A. Willetts, *J. Phys. Chem. A*, 1999, **103**, 1831–1837.

[36] S. Tsushima and T. Reich, *Chem. Phys. Lett.*, 2001, **347**, 127–132.

[37] G. Schreckenbach, P. J. Hay, and R. L. Martin, *Inorg. Chem.*, 1998, **37**, 4442–4451.

[38] V. Vallet, L. Maron, B. Schimmelpfennig, T. Leininger, C. Teichteil, O. Gropen, I. Grenthe, and U. Wahlgren, *J. Phys. Chem.*, 1999, **103**, 9285–9289.

[39] V. Vallet, U. Wahlgren, B. Schimmelpfennig, H. Moll, Z. Szabó, and I. Grenthe, *Inorg. Chem.*, 2001, **40**, 3516–3525.

[40] N. W. Alcock and S. Esperas, *J. Chem. Soc., Dalton Trans.*, 1977, 893–896.

[41] L. M. Toth and G. M. Begun, *J. Phys. Chem.*, 1981, **85**, 547–549.

[42] M. Gál, P. L. Goggin, and J. Mink, *Spectrochimica Acta A*, 1992, **48**, 121–132.

[43] F. Quilés and A. Burneau, *Vib. Spectr.*, 2000, **23**, 231–241.

[44] P. Hohenberg and W. Kohn, *Phys. Rev.*, 1964, **136**, B864.

[45] S. H. Vosko, L. Wilk, and M. Nusair, *Can. J. Phys.*, 1980, **58**, 1200.

[46] J. P. Perdew, J. A. Chevary, S. H. Visko, K. A. Jackson, M. R. Pederson, D. J. Singh, and C. Fiolhais, *Phys. Rev. B*, 1992, **46**, 6671–6687.

[47] J. P. Perdew, K. Burke, and M.Ernzerhof, *Phys. Rev. Lett.*, 1996, **77**, 3865–3868.

[48] J. P. Perdew, K. Burke, and M.Ernzerhof, *Phys. Rev. Lett.*, 1997, **78**, 1396.

[49] J. P. Perdew, *Phys. Rev. Lett*, 1985, **55**, 1665.

[50] A. D. Becke, *J. Phys. Chem.*, 1993, **98**, 7.

[51] P. J. Stephens, F. J. Devlin, C. F. Chablowski, and M. J. Frisch, *J. Phys. Chem.*, 1994, **98**, 11623–11627.

[52] W. Koch and M. C. Holthausen, *A Chemist's Guide to Density Functional Theory*, Wiley VCH.

[53] S. K. Ghosh and R. G. Parr, *Phys. Rev. A.*, 1986, **34**, 785.

[54] A. D. Becke and M. R. Roussel, *Phys. Rev. A.*, 1989, **39**, 3761.

[55] A. D. Becke, *J. Chem. Phys.*, 1992, **98**, 1372.

[56] O. Gunnarsson, *Solid State Commun.*, 1977, **24**, 765.

[57] C. Clavaguéra-Sarrio, N. Ismail, C. J. Marsden, D. Begue, and C. Pouchan, *Chem. Phys.*, 2004, **302**, 1–11.

[58] H. Heiberg, O. Gropen, J. Laerdahl, O. Swang, and U. Wahlgren, *Theor. Chem. Acc.*, 2003, **110**, 118–125.

[59] Z.-F. Xu, Y. Xie, W.-L. Feng, and H. F. S. III, *J. Phys. Chem. A*, 2003, **107**, 2716–2729.

[60] M. Swart, *Theor. Chem. Acc.*, 2003, **110**, 34–41.

[61] C. Clavaguéra-Sarrio, V. Vallet, D. Maynau, and C. J. Marsden, *J. Chem. Phys.*, 2004, **121**, 5312–5321.

[62] D. Guillaumont, *Chem. Phys. A*, 2004, **108**, 6893–6900.

[63] G. Schreckenbach, *Int. J. Quantum Chem*, 2005, **101**, 372–380.

[64] G. A. Shamov and G. Schreckenbach, *J. Phys. Chem. A.*, 2005, **109**, 10961–10974.

[65] O. Gunnarsson, *Phys. Lett.*, 1976, **59A**, 177.

[66] R. van Leeuwen and E. J. Baerends, *Phys. Rev. A*, 1994, **49**, 2421–2431.

[67] P. R. T. Schipper, O. V. Gritsenko, S. J. A. van Gisbergen, and E. J. Baerends, *J. Chem. Phys.*, 2000, **112**, 1344–1352.

[68] Y. Zhang and W. Yang, *Phys. Rev. Lett.*, 1998, **80**, 890.

[69] G. Menconi and N. Kaltsoyannis, *Chem. Phys. Lett.*, **415**.

[70] E. R. Batista, R. L. Martin, P. J. Hay, J. E. Paralta, and E. Scuseria, *J. Chem. Phys*, 2004, **121**, 2144–2150.

[71] M. Garciá-Hernández, C. Lauterbach, S. Krüger, A. Matveev, and N. Rösch, *J. Comput. Chem.*, 2002, **23**, 834–846.

[72] F. Jensen, *Introduction to Computational Chemistry*, John Wiley & Sons.

[73] E. van Lenthe, R. van Leeuwen, E. J. Baerends, and J. G. Snijders, *Int. J. Quantum Chem.*, 1996, **57**, 281.

[74] J. G. Snijder and A. D. Sadlej, *Chem. Phys. Lett.*, 1996, **252**, 51.

[75] E. van Lenthe, E. J. Baerends, and J. G. Snijders, *J. Chem. Phys.*, 1993, **99**, 4597.

[76] E. van Lenthe, E. J. Baerends, and J. G. Snijders, *J. Chem. Phys.*, 1994, **101**, 9783.

[77] E. van Lenthe, E. J. Baerends, and J. G. Snijders, *J. Chem. Phys.*, 1996, **105**, 6505.

[78] ADF2004.01, SCM, Theoretical Chemistry, Vrije Universiteit, Amsterdam, The Netherlands, http://www.scm.com.

[79] G. te Velde, F. Bickelhaupt, S. van Gisbergen, C. F. Guerra, E. J. Baerends, J. Snijders, and T. Ziegler, *J. Comput. Chem.*, 2001, **22**, 931–967.

[80] C. F. Guerra, J. Snijders, G. te Velde, and E. J. Baerends, *Theor. Chem. Acc.*, 1998, **99**, 391.

[81] C. Fonseca Guerra, O. Visser, J.G. Snijders, G. te Velde and E. J. Baerends in: Methods and Techniques for Computational Chemistry, E. Clementi and C. Corongiu, eds, p. 303-395, STEF, Cagliari, 1995.

[82] Gaussian 03, Revision C.02, M. J. Frisch, G. W. Trucks, H. B. Schlegel, G. E. Scuseria, M. A. Robb, J. R. Cheeseman, J. A. Montgomery, Jr., T. Vreven, K. N. Kudin, J. C. Burant, J. M. Millam, S. S. Iyengar, J. Tomasi, V. Barone, B. Mennucci, M. Cossi, G. Scalmani, N. Rega, G. A. Petersson, H. Nakatsuji, M. Hada, M. Ehara, K. Toyota, R. Fukuda, J. Hasegawa, M. Ishida, T. Nakajima, Y. Honda, O. Kitao, H. Nakai, M. Klene, X. Li, J. E. Knox, H. P. Hratchian, J. B. Cross, V. Bakken, C. Adamo, J. Jaramillo, R. Gomperts, R. E. Stratmann, O. Yazyev, A. J. Austin, R. Cammi, C. Pomelli, J. W. Ochterski, P. Y. Ayala, K. Morokuma, G. A. Voth, P. Salvador, J. J. Dannenberg, V. G. Zakrzewski, S. Dapprich, A. D. Daniels, M. C. Strain, O. Farkas, D. K. Malick, A. D. Rabuck, K. Raghavachari, J. B. Foresman, J. V. Ortiz, Q. Cui, A. G. Baboul, S. Clifford, J. Cioslowski, B. B. Stefanov, G. Liu, A. Liashenko, P. Piskorz, I. Komaromi, R. L. Martin, D. J. Fox, T. Keith, M. A. Al-Laham, C. Y. Peng, A. Nanayakkara, M. Challacombe, P. M. W. Gill, B. Johnson, W. Chen, M. W. Wong, C. Gonzalez, and J. A. Pople, Gaussian, Inc., Wallingford CT, 2004.

[83] L. Versluis and T. Ziegler, *J. Chem. Phys.*, 1988, **88**, 322.

[84] L. Fan and T. Ziegler, *J. Chem. Phys.*, 1991, **95**, 7401.

[85] L. Wersluis, *PhD Thesis*, University of Calgary, 1989.

[86] C. G. Broyden, The convergence of a class of double-rank minimization algorithms 2. the new algorithm., *J. Inst. Math. Appl.*, 1970, **6**, 222–231.

[87] R. Fletcher, A new approach to variable metric algorithms., *The Comp. J.*, 1970, **13**, 317–322.

[88] R. Fletcher, A family of variable-metric methods derived by variational means., *Math. of Computation*, 1970, **24**, 23–26.

[89] R. Fletcher, Conditioning of quasi-newton methods for function minimization., *Math. of Computation*, 1970, **24**, 647–656.

[90] H. B. Schlegel, *J. Comp. Chem.*, 1982, **3**, 214.

[91] G. te Velde, *PhD Thesis*, Vrije Universiteit, AMsterdam, 1990.

[92] F. Bickelhaupt, N. J. R. van Eikema Hommes, C. F. Guerra, and E. J. Baerends, *Organometallics*, 1996, **15**, 2923.

[93] C. F. Guerra, J. W. Handgraaf, E. J. Baerends, and F. Bickelhaupt, *J. Comput. Chem*, 2004, **25**, 189–210.

[94] F. L. Hirshfeld, *J. Theo. Chim. Act.*, 1977, **44**, 129–138.

[95] K. B. Wiberg and R. B. Rablen, *J. Comput. Chem*, 1993, **14**, 1504.

[96] J. E. Carpenter and F. Weinhold, *J. Mol. Struct. (Theochem)*, 1988, **169**, 41–62.

[97] J. E. Carpenter, *PhD Thesis*, University of Wisconsin, Madison, WI, 1987.

[98] J. P. Foster and F. Weinhold, *J. Am. Chem. Soc.*, 1980, **102**, 7211.

[99] A. E. Reed and F. Weinhold, *J. Chem. Phys.*, 1983, **78**, 4066.

[100] A. E. Reed, R. B. Weinstock, and F. Weinhold, *J. Chem. Phys.*, 1985, **83**, 735.

[101] A. E. Reed, L. A. Curtiss, and F. Weinhold, *Chem. Rev.*, 1988, **88**, 899.

[102] F. Weinhold and J. E. Carpenter, *The Structure of Small Molecules and Ions*, Plenum, 227, (1988).

[103] C. J. Cramer, *Essentials of Computational Chemistry (2nd Edition)*, John Wiley & Sons, 2004.

[104] I. Mayer, *Chem. Phys. Lett.*, 1983, **97**, 270–274.

[105] T. Ziegler and A. Rauk, *Theor. Chim. Acta.*, 1977, **46**, 1.

[106] T. Ziegler and A. Rauk, *Inorg. Chem.*, 1979, **18**, 1558.

[107] J. L. Pascual-Ahuir, E. Silla, and I. Tunon, *J. Comput. Chem.*, 1994, **15**, 1127–1138.

[108] P. Scarlin, R. Battino, E. Silla, I.Tunon, and J. L. Pascual-Ahuir, *Pure & Appl. Chem.*, 1998, **70**, 1895–1904.

[109] CRC, *Handbook of Chemistry and Physics*, Boca Raton.

[110] Gaussian 98, Revision A.7, M. J. Frisch, G. W. Trucks, H. B. Schlegel, G. E. Scuseria, M. A. Robb, J. R. Cheeseman, V. G. Zakrzewski, J. A. Montgomery, Jr., R. E. Stratmann, J. C. Burrant, S. Dapprich, J. M. Millam, A. D. Daniels, K. N. Kudin, M. C. Strain, O. Farkas, J. Tomasi, V. Barone, M. Cossi,R. Cammi, B. Menucci, C. Pomelli, S. Clifford, J. W. Ochterski, A. Petersson, P. Y. Ayala, Q. Cui, K. Morokuma, D. K. Malick, A. D. Rabuck, K. Raghavachari, J. B. Foresman, J. Cioslowski, J. V. Ortiz, A. G. Baboul, B. B. Stefanov, G. Liu, A. Liashenko, P. Piskorz, I. Komaromi, R. Gomperts, R. L. Martin, D. J. Fox, T. Keith, M. A. Al-Laham, C. Y. Peng, A. Nanayakkara, M. Gonzalez, M. Challacombe, P. M. W. Gill, B. Johnson, W. Chen, M. W. Wong, C. Gonzalez, E. S. Replogle and J. A. Pople, Gaussian, Inc., Pittsburgh, PA, 1995.

[111] P. J. Hay, *J. Chem. Phys. A*, 1983, **79**, 5469.

[112] P. G. Allen, J. J. Butcher, D. K. Shuh, N. M. Edelstein, and T. Reich, *Inorg. Chem.*, 1997, **36**, 4676–4683.

[113] L. J. Basile, J. C. Sullivan, J. R. Ferrato, and P. LaBonville, *Appl. Spectrosc.*, 1974, **28**, 142.

[114] L. H. Jones and R. A. Penneman, *J. Chem. Phys.*, 1953, **21**, 542.

[115] C. D. Tait, Presented at the Symposium on Heavy Element Complexes: The convergence of Theory and Experiment, 217th ACS National Meeting, 1999, Anaheim, CA.

[116] D. L. Clark, Presented at the Symposium on Heavy Element Complexes: The convergence of Theory and Experiment, 217th ACS National Meeting, 1999, Anaheim, CA.

[117] M. Aberg, D. Ferri, J. Glaser, and I. Grenthe, *Inorg. Chem.*, 1983, **22**, 3986–3989.

[118] C. Madic, G. M. Begun, D. E. Hobart, and R. L. Hahn, *Inorg. Chem.*, 1984, **23**, 1914.

[119] S. D. Conradson, *Appl. Spectrosc*, 1998, **52**, 252.

[120] Y. Oda and A. Aoshima, *J. Nucl. Sci. and Tech.*, 2002, **39**, 647–654.

[121] L. Gagliardi, N. C. Handy, A. G. Ioannou, C. K. Skylaris, S. Spencer, A. Willetts, and A. Simper, *Chem. Phys. Lett.*, 1998, **283**, 187.

[122] Gaussian 94, Revision E.1, M. J. Frisch, G. W. Trucks, H. B. Schlegel, P. M. W. Gill, B. G. Johnson, M. A. Robb, J. R. Cheeseman, T. Keith, G. A. Petersson, J. A. Montgomery, K. Raghavachari, M. A. Al-Laham, V. G. Zakrzewski, J. V. Ortiz, J. B. Foresman, J. Cioslowski, B. B. Stefanov, A. Nanayakkara, M. Challacombe, C. Y. Peng, P. Y. Ayala, W. Chen, M. W. Wong, J. L. Andres, E. S. Replogle, R. Gomperts, R. L. Martin, D. J. Fox, J. S. Binckley, D. J. Defrees, J. Baker, J. P. Stewart, M. Head-Gordon, C. Gonzalez, and J. A. Pople, Gaussian, Inc., Pittsburgh, PA, 1995.

[123] A. D. Becke, *Phys. Rev. A*, 1988, **38**, 3098–3100.

[124] J. P. Perdew, *Phys. Rev. B*, 1986, **33**, 8822–8824.

[125] MAYER version 1.2.3, A. J. Bridgeman and C. J. Empson, University of Hull (2004). Freely available on the worldwide web: http://www.hull.ac.uk/php/chsajb/mayer/.

[126] P. Politzer and R. S. Mulliken, *J. Chem. Phys.*, 1971, **55**, 5135–5136.

[127] D. L. Grier and J. A. Streitwieser, *J. Am. Chem. Soc.*, 1982, **104**, 3556–3564.

[128] X. Cao and M. Dolg, *J. Mol. Struct. (Theochem)*, 2004, **673**, 203–209.

[129] V. Barone and M. Cossi, *J. Phys. Chem. A*, 1998, **102**, 1995–2001.

[130] V. Barone, M. Cossi, and J. Tomasi, *J. Chem. Phys.*, 1997, **107**, 3210–3221.

[131] J. L. Pascual-Ahuir and E. Silla, *J. Comput. Chem.*, 1987, **8**, 778–787.

[132] A. Klamt and G. Schuurmann, *J. Chem. Soc. Perkin Trans 2*, 1993, **5**, 799–805.

[133] A. Klamt, *J. Phys. Chem.*, 1995, **99**, 2224–2235.

[134] MOLEKEL 4.0, P. Flükiger, H. P. Lüthi, S. Portmann, J. Weber, Swiss Center for Scientific Computing, Manno (Switzerland), 2000, http://www.cscs.ch/molekel/.

[135] S. Portmann and H. P. Lüthi, Molekel: An interactive molecular graphics tool., *Chimia*, 2000, **54**, 766–770.

[136] H. Moll, T. Reich, and Z. Szabó, *Radiochim. Acta*, 2000, **88**, 411–415.

[137] C. Clavaguéra-Sarrio, V. Brenner, S. Hoyau, C. J. Marsden, P. Millié, and J. P. Dognon, *J. Phys. Chem. B*, 2003, **107**, 3051–3060.

[138] V. Vallet, U. Wahlgren, B. Schimmelpfennig, Z. Szabó, and I. Grenthe, *J. Am. Chem. Soc.*, 2001, **123**, 11999–12008.

[139] J. Häller and N. Kaltsoyannis, *Recent Advances in Actinide Science, The Effect of Solvent on the Modelling of the Geomtry and Vibrations of* $UO_2(H_2O)_5^{2+}$, Royal Society of Chemistry, 2006.

[140] K. B. Wiberg, *Tetrahedron*, 1968, **24**, 1083–1096.

[141] E. O'Grady and N. Kaltsoyannis, *J. Chem. Soc., Dalton Trans.*, 2002, 1233–1239.

[142] A. J. Bridgeman and G. Cavigliasso, *Faraday Discuss.*, 2003, **124**, 239–258.

[143] A. J. Bridgeman, G. Cavigliasso, L. R. Ireland, and J. Rothery, *J. Chem. Soc., Dalton Trans.*, 2001, 2095–2108.

[144] N. Kaltsoyannis, *Inorg. Chem.*, 2000, **39**, 6009–6017.

[145] R. G. Denning, J. C. Green, T. E. Hutchings, C. Dallera, A. Tagliaferri, K. Giarda, N. B. Brookes, and L. Braicovich, *J. Chem. Phys.*, 2002, **117**, 8008.

[146] B. Machura, M. Jaworska, and R. Kruszynski, *Polyhedron*, 2005, **24**, 267–279.

[147] J. M. Villegas, S. R. Stoyanov, W. Huang, and D. P. Rillema, *J. Chem. Soc., Dalton Trans.*, 2005, **6**, 1042–1051.

[148] M. J. Sarsfield, M. Helliwell, and D. Collinson, *Chem. Comm.*, 2002, 2264.

[149] M. J. Sarsfield, M. Helliwell, H. Steele, and S. Teat, *J. Chem. Soc., Dalton Trans.*, 2003, 3443.

[150] G. B. Deacon, P. I. Makinnon, and J. C. Taylor, *Polyhedron*, 1985, **4**, 1036.

[151] J. L. Sessler, D. Seidel, A. E. Vivian, B. Lynch, B. L. Scott, and W. Keogh, *Angew. Chem. Int. Ed.*, 2001, **40**, 591.

[152] G. Paolucci, G. Marangoni, G. Bandoli, and D. A. Clemente, *J. Chem. Soc., Dalton Trans.*, 1979, 459.

[153] A. Navara, F. Villain, and P. Charpin, *Polyhedron*, 1984, **3**, 247.

[154] N. W. Alcock, D. J. Flanders, M. Pennington, and D. Brown, *J. Chem. Soc., Dalton Trans.*, 1985, 1001.

[155] J. C. Berthet, M. Nierlich, and M. Ephritikhine, *Chem. Comm.*, 2003, 1660.

[156] M. J. Sarsfield, M. Helliwell, and J. Raftery, *Inorg. Chem.*, 2004, **43**, 3170–3179.

[157] M. J. Sarsfield, M. Helliwell, H. Steele, and S. Teat, *J. Am. Chem. Soc.*, 2004, **126**, 1036.

[158] R. T. Günther, *Archaeologia*, 1912, **63**, 99–105.

[159] E. R. Caley, *Isis*, 1948, **38**, 190–193.

[160] M. H. Klaproth, *Ann. Freunde. Naturl*, 1789, **2**, 387–403.

[161] E. Péligot, *J. Pharm. Sci. Accessoires*, 1841, **27**, 525–535.

[162] E. Péligot, *Ann. Chim. Phys.*, 1842, **5**, 35.

[163] G. G. Stokes, *Trans. R. Soc. London*, 1852, 463–562.

[164] H. Becquerel, *Hebd. Seances Acad. Sci.*, 1896, **122**, 420–421.

[165] R. G. Denning, N. P. Foster, T. R. Snellgrove, and D. R. Woodwark, *Mol. Phys.*, 1979, **37**, 1089–1107.

[166] C. Görller-Walrand, S. D. Houwer, L. Fluyt, and K. Binnemans, *Phys. Chem. Chem. Phys.*, 2004, **6**, 3292–3298.

[167] J. Neugebauer, E. J. Baerends, and M. Nooijen, *J. Phys. Chem. A*, 2005, **109**, 1168–1179.

[168] S. J. A. Gisbergen, J. A. Groeneveld, A. Rosa, J. G. Snijders, and E. J. Baerends, *J. Phys. Chem. A*, 2005, **109**, 1168–1179.

[169] X. Wang, L. Chen, A. Endou, M. Kubo, and A. Miyamoto, *J. Organomet. Chem.*, 2003, **678**, 156–165.

[170] G. Loukova and V. A. Smirnov, *Chem. Phys. Lett.*, 2000, **329**, 437.

[171] K. Ingram, J. Häller, and N. Kaltsoyannis, *J. Chem. Soc., Dalton Trans.*, 2006, 2403–2414.

[172] E. van Besien, K. Pierloot, and C. Görller-Walrand, *Phys. Chem. Chem. Phys.*, 2006, **8**, 4311–43191.

[173] Http://www.world-nuclear.org/info/inf69.htm.

[174] R. M. Diamond, K. Street, and G. T. Seaborg, *J. Am. Chem. Soc.*, 1954, **76**, 1461.

[175] M. P. Jensen, L. R. Morss, J. V. Beitz, and D. D. Ensor, *J. Alloys Compd.*, 2000, **303/304**, 137.

[176] Y. Zhu, J. Chen, and R. Jiao, *Solvent Extr. Ion Exch,*, 1996, **14**, 61.

[177] M. P. Jensen and A. H. Bond, *J. Am. Chem. Soc.*, 2002, **124**, 9870–9877.

[178] A. J. Gaunt, B. L. Scott, and M. P. Neu, *Chem. Comm.*, 2005, **255**, 3215–3217.

[179] A. J. Gaunt, B. L. Scott, and M. P. Neu, *Angew. Chem. Int. Ed.*, 2006, **45**, 1638–1641.

[180] A. J. Gaunt, unpublished results.

[181] X. Cao, Q. Li, A. Moritz, Z. Xie, M. Dolg, X. Chen, and W. Fangstuff, *Inorg. Chem.*, 2006, **45**, 3444–3451.

[182] S. W. Young, F. Qing, A. Harriman, J. L. Sessler, W. C. Dow, T. D. Mody, G. W. Hemmi, Y. P. Hao, and R. A. Miller, *Proc. Natl. Acad. Sci. U.S.A.*, 1996, **93**, 6610–6615.

[183] D. I. Rosenthal, P. Nurenberg, C. R. Becerra, E. P. Frenkel, D. P. Carbone, B. L. Lum, R. Miller, J. Engel, S. W. Young, D. Miles, and M. F. Renschler, *Clin. Cancer Res.*, 1999, **5**, 739–745.

[184] S. G. Rockson, P. Kramer, M. Razavi, A. Szuba, S. Filardo, and D. C. Adelman, *Circulation*, 2000, **102**, 2322–2324.

[185] J. L. Sessler, A. E. Vivian, D. Seidel, A. K. Burrell, M. Hoehner, T. D. Mody, A. Gebauer, S. J. Weghorn, and V. Lynch, *Coord. Chem. Rev.*, **216**.

[186] T. D. Mody, L. Fu, J. L. Sessler, and K. D. Karlin, *Progress in Inorganic Chemistry*, John Wiley & Sons: New York.

[187] L. Petit, L. Joubert, P. Maldivi, and C. Adamo, *J. Am. Chem. Soc.*, 2006, **128**, 2190.

[188] R. F. Bader, *Atoms in Molecules: A Quantum Theory*, Oxford University Press: Oxford, U.K., 1990.

[189] A. D. Becke and K. E. Edgecombe, *J. Chem. Phys.*, 1990, **92**, 5397.

[190] B. Silvi and A. Savin, *Nature.*, 1994, **371**, 683.

[191] S. Noury, X. Krokidis, F. Fuster and B. Silvi, *ToPMoD Package*, Laboratoire de Chemie Thèoretique de l'Universitè Pierre et Marie Curie, Paris, France, 1997.

[192] Z. Kolarik, U. Müllich, and F. Gassner, *Solvent Extr. Ion exch.*, 1999, **17**, 23–32.

[193] N. Boubals, M. G. B. Drew, C. Hill, M. J. Hudson, P. B. Iveson, C. Madic, M. L. Russell, and T. G. A. Youngs, *J. Chem. Soc., Dalton Trans.*, 2002, 55.

[194] P. Y. Cordier, C. Hill, P. Baron, C. Madic, M. J. Hudson, and J. O. Liljenzin, *J. Alloys Compd.*, 1998, **271**, 738.

[195] A. Bergner, M. Dolg, W. Kuechle, H. Stoll, and H. Preuss, *Mol. Phys.*, 1993, **80**, 1431.

[196] W. J. Hehre, R. F. Stewart, and J. A. Pople, *J. Chem. Phys.*, 1969, **59**, 2657.

[197] J. B. Collins, P. v. R. Schleyer, J. S. Binkley, and J. A. Pople, *J. Chem. Phys.*, 1976, **64**, 5142.

[198] A. J. Gaunt, *Recent Advances in Actinide Science, 5f Element Complexes with 'Soft' Donor Atom Ligands: Eight Coordinate Pu(III) Pyrazinyl and Thioether Complexes*, Royal Society of Chemistry, 2005, in press.

[199] G. R. Choppin and K. L. Nash, *Radiochimica Acta*, 1995, 225.

[200] C. J. Burns and B. E. Bursten, *Comments Inorg. Chem.*, 1989, **9**, 61.